UNIVERSITÄT ZU LÜBECK

Institute for human genetics

Of the university of Lübeck

Director: Prof. Dr. Malte Spielmann

microRNAs – size doesn't matter!

The role of miR-149-5p in regulating metabolic pathways in metabolic dysfunction-associated steatotic liver disease

Dissertation

for Fulfillment of Requirements

for the Doctoral Degree

of the University of Lübeck

From the Department of Natural Sciences

Submitted by

Jan Hendric Britsemmer

From Wiesbaden, Germany

Lübeck, 2024

First referee:	Prof. Dr. Henriette Kirchner
Second referee:	Prof. Dr. Lars Redecke
Date of oral examination:	10.09.2024
Approved for printing:	12.09.2024

Eigenständigkeitserklärung

Hiermit versichere ich, Jan Hendric Britsemmer, dass die Anfertigung dieser Dissertation ohne fremde Hilfe durchgeführt wurde und keine anderen Hilfsmittel als die angegebenen verwendet wurden. Ich habe weder vorher noch parallel andernorts einen Zulassungsantrag gestellt oder diese Doktorarbeit vorgelegt. Zuvor bin ich noch zu keinem Promotionsverfahren angetreten.

Lübeck, ……

(Jan Hendric Britsemmer)

Danksagung

Now that my PhD journey has come to an end, I want to thank everyone that has contributed to the work and has supported me throughout all the four years. Its been an incredible time with emotional up and downs, a lot of stress and work, but it was worth every minute of it. I gained a lot of knowledge, wisdom and I could feel myself growing as a person. But all of this would not be possible without the help of many people, colleagues, my family, friends and colleagues that became friends.
As first, I want to thank my supervisor Prof. Dr. Henriette Kirchner for all the great support and trust she gave me. For always believing in my ideas and giving me valuable feedback. It was an amazing time and I never felt a single day uncomfortable going to work, which is greatly attributed to her exceptional mentorship and leadership of the working group that creates a thriving atmosphere. I want to thank you for always remaining considerate even though many experiments did not work out as planned.
Second, I want to thank Prof. Dr. Henrik Oster as my second supervisor for thesis and spokesperson of the GRK 1957, of which I was part of. I appreciated the meetings discussing the data and for always offering me help.
I also want to thank my mentor Dr. Christin Krause that taught me everything I know about programming and supporting me throughout the four years. Further, I want to thank all the GRK-members, which made the GRK meetings and progress reports way more enjoyable. Also a big thank you to Dr. Sonja Schriever for all the amazing feedback in our meetings.
Next, many thanks to my amazing friend and office and lab partner Natalie Taege for all the shared laughter, cheering ups, emotional support and scientific input.
Even though you leave the lab, the PhD work follows you home very often. Therefore I want to thank my parents, sister, family, and girlfriend, which always supported me in trying to reduce my stress levels. I know it was a hard time.
And many thanks to all the people that I can not all write down here, but I appreciated your support.

And last but not least:

Publications

1. **Britsemmer, Jan** & Krause, Christin & Taege, Natalie & Geißler, Cathleen & López-Alcántara, Nuria & Schmidtke, Linda & Naujack, Alison-Michelle & Wagner, Jonas & Wolter, Stefan & Mann, Oliver & Kirchner, Henriette. (2023). Fatty Acid Induced Hypermethylation in the Slc2a4 Gene in Visceral Adipose Tissue Is Associated to Insulin-Resistance and Obesity. International Journal of Molecular Sciences. 24. 6417. 10.3390/ijms24076417.

2. Krause Christin, **Britsemmer Jan H**., Bernecker Miriam, Molenaar Anna, Taege Natalie, Geißler Cathleen, Kaehler Meike, Iben Katharina, Judycka Anna, Wagner Jonas, Wolter Stefan, Mann Oliver, Pfluger Paul T., Cascorbi Ingolf, Lehnert Hendrik, Stemmer Kerstin, Schriever Sonja C., Kirchner Henriette (2023) Liver microRNA transcriptome reveals miR-182 as link between type 2 diabetes and fatty liver disease in obesity eLife 12:RP92075
https://doi.org/10.7554/eLife.92075.1

3. Geißler C, Krause C, Neumann AM, **Britsemmer JH**, Taege N, Grohs M, Kaehler M, Cascorbi I, Lewis AG, Seeley RJ, Oster H, Kirchner H. Dietary induction of obesity and insulin resistance is associated with changes in Fgf21 DNA methylation in liver of mice. J Nutr Biochem. 2022 Feb;100:108907. doi: 10.1016/j.jnutbio.2021.108907. Epub 2021 Nov 18. PMID: 34801693.

Zusammenfassung

Die weltweite Pandemie der Adipositas erreicht ein verheerendes Ausmaß und erhöht das Risiko für eine Vielzahl von Begleiterkrankungen wie Insulinresistenz, Typ-2-Diabetes oder Metabolismus-assoziierte Lebererkrankung (*engl.* MASLD). Beide Begleiterkrankungen sind mit einer verminderten Lebenserwartung und einer Einschränkung der Lebensqualität verbunden und stellen somit eine enorme Belastung für die globalen Gesundheitssysteme dar. Daher ist die Entwicklung neuer Behandlungsstrategien dringend erforderlich, aber die zugrunde liegende Komplexität des Krankheitsverlaufs erschwert diesen Prozess, insbesondere da viele beteiligte molekulare Mechanismen nur unvollständig verstanden sind. Epigenetische Veränderungen in der DNA-Methylierung oder der microRNA-Expression beeinflussen die Expression krankheitsbezogener Gene und spielen somit eine entscheidende Rolle bei der Entstehung dieser Krankheiten. Die Identifizierung neuer epigenetischer krankheitsauslösender Modifikationen kann neue Wirkstoffkandidaten oder diagnostische Marker aufdecken.

Daher liegt der Fokus dieser Arbeit darauf, eine Masterregulator-MicroRNA zu identifizieren, welche übermäßig am Fortschreiten der MASLD beteiligt ist. Um diese Forschungsfrage zu beantworten, werden *in silico* Vorhersagen von Zielgenen mit realen hepatischen Transkriptom- und Metabolom-Daten aus einem Mausmodell für ernährungsbedingte Adipositas, einer Vielzahl von Interventions-Mausmodellen und einem in vitro Zellkulturmodell unter Verwendung von HepG2-Zellen kombiniert. Um eine Übertragung der Ergebnisse auf den Menschen zu gewährleisten, werden auch hepatische, Transkriptom-Daten einer adipösen menschlichen Kohorte verwendet. Die Analyse identifizierte miR-149-5p als einen konservierten, potenziellen zentralen Regulator metabolischer Stoffwechselwege, die den Trichloressigsäure Zyklus, den GABA-Shunt, den Ein-Kohlenstoff-Stoffwechsel (Methionin/Folsäurezyklus) und den Harnstoffzyklus umfassen. Darüber hinaus ist miR-149-5p in der Leber von DIO-Mäusen und in der Leber von übergewichtigen Personen mit Typ-2-Diabetes hochreguliert, was mit einer verminderten Genexpression der Stoffwechselweg-assoziierten Gene einhergeht.

Zusätzlich wird in dieser Arbeit eine neuartige Verbindung zwischen DNA-Hypermethylierung im *SLC2A4*-Gen und der durch Adipositas verursachten *SLC2A4*-Repression im viszeralen Fettgewebe entdeckt, die zur Entwicklung einer systemischen Insulinresistenz und Typ-2-Diabetes beiträgt. *SLC2A4* kodiert für den Hauptinsulin-abhängigen Glukosetransporter im Fettgewebe, der die systemische Insulinsensitivität reguliert, indem er die Kapazität der De novo Lipogenese im Fettgewebe durch Glukoseaufnahme ausbalanciert. Diese Studie zeigt, dass die DNA-Methylierung an einer spezifischen Enhancer-Stelle bei adipösen Personen mit Typ-2-Diabetes und bei DIO-Mäusen zunimmt.

Zusammenfassend liefert diese Arbeit neue und wertvolle Erkenntnisse zum Fortschreiten der MASLD und zur Entwicklung von Insulinresistenz, die für die Gestaltung neuer Behandlungstherapien nützlich sein könnten.

Abstract

The global pandemic of obesity reaches a devastating magnitude and increases the risk for a variety of comorbidities, such as insulin resistance, type 2 diabetes or metabolic-associated steatotic liver disease (MASLD). Both comorbidities are associated with a decreased life expectancy and reduction in quality of life, therefore displaying a huge burden on global health care systems. Therefore, the development of new treatment strategies is urgent, but the underlying complexity of the disease progressions keeps this process challenging, especially since many involved molecular mechanisms rare incompletely understood. Epigenetic changes in DNA methylation or microRNA expression alter the expression of disease-related genes and thereby play a crucial role in the emergence of those diseases. Identifying novel molecular epigenetic disease-driving modifications may unravel new drug candidates or diagnostic markers.

Therefore, the focus of this work is to identify a master regulator microRNA that is excessively involved in the progression of MASLD. To address this research question, *in silico* target gene predictions are combined with real-world hepatic transcriptomic and metabolomic data from a mouse model for diet-induced obesity, a variety of intervention mouse models, and *in vitro* cell culture model utilizing HepG2 cells. To guarantee a translation of the findings into human, also hepatic transcriptomic data of an obese human cohort is employed. The analysis identified the miR-149-5p as a conserved, potential central regulator of metabolic pathways, involving the trichloroacetic acid cycle, GABA shunt, one-carbon metabolism (methionine/folate cycle), and urea cycle. Furthermore, miR-149-5p is upregulated in the liver of DIO mice and in the liver of obese subjects with type 2 diabetes, which is accompanied by decreased gene expression of metabolic pathway genes.

Additionally, in this work a novel link between DNA hypermethylation in the *SLC2A4* gene and obesity-associated *SLC2A4* downregulation in the visceral adipose tissue is discovered that contributes to the development of systemic insulin resistance and type 2 diabetes. *SLC2A4* encodes the main insulin-dependent glucose transporter in the adipose tissue, which regulates systemic insulin sensitivity by balancing the de novo lipogenesis capacity in the adipose tissue through glucose uptake. This study shows that DNA methylation at a specific enhancer site increases in the VAT of obese subjects with type 2 diabetes and in DIO mice.

Taken together, this work provides novel and valuable findings in the progression of MASLD and the development of insulin resistance, which could be of use for the design of new therapies.

Table of Contents

1. Introduction

The term *epigenetics* was firstly coined by Conrad H. Waddington in the year 1942 and was originally used to describe the complex development process between the genotype and phenotype, also referred to as the epigenotype (Felsenfeld 2014; Ospelt 2022; C H Waddington 2011). Conrad H. Waddington forged this neologism from the Greek word ‚epigenesis', meaning ‚new formation', and genetics, meaning ‚generative' (Conrad H Waddington 1953). With this term, embryologists were able to define the process from the fertilized zygote developing into an adult organism. With advances in molecular technologies and better understanding of gene regulation, the term epigenetic was reinterpreted. The Greek prefix ‚*epi-*' implied a mechanism lying ‚*above*' the genetic information carried within a cell of an organism, regulating morphology and the cell fate. Consequently, the term epigenetic nowadays describes all regulatory mechanisms of gene expression, which do not entail changes in the DNA sequence (C. -t. Wu and Morris 2001). To date, three major categories of molecular epigenetic mechanisms are best characterized - histone modifications, DNA methylation and non-coding RNAs (Fitz-James and Cavalli 2022). The entirety of all epigenetic modifications of a cell is summarized by the term *epigenome* (Smith 2015). The epigenome is cell-type specific and is by no means a static, inflexible entity (Rahmani et al. 2019). Throughout a lifetime it can change and thereby promote and contribute to the pathogenesis of a variety of diseases, such as neurological diseases, cancer, insulin resistances, obesity and metabolic-associated steatotic liver disease (MASLD) (Cheng et al. 2019; Jakovcevski and Akbarian 2012; Y.-L. Wu et al. 2023). This flexibility is inherently needed for the pivotal role of the epigenome to adapt to environmental factors and also to integrate those external stimuli into a cellular response (Toraño et al. 2016). Environmental factors affecting our epigenome are for instance diet, physical activity or the exposure to hazardous material (Alegría-Torres, Baccarelli, and Bollati 2011). Malign changes in the epigenome induced by environmental factors can be cause or consequence for disease development.
Especially with the ongoing pandemic of obesity and its comorbidities, researchers shed light upon the crucial role of epigenetic in these diseases. The global increase in prevalence of obesity is disproportional to the global changes in genetic information, but matches with the switch to a more sedative lifestyle and nutritional oversupply.
Understanding those fundamental processes of how epigenetics are involved in obesity and MASLD may pave the way for new therapeutics and diagnostic- or biomarkers. The scope of this work is to contribute to this matter by generating new knowledge.

1.1. Obesity and its comorbidities – one strikes, the other kills

1.1.1. Characteristics and diagnostic of obesity

Obesity is generally defined by the guidelines of the World Health Organization (WHO) as an excessive accumulation of adipose tissue with an increased risk for health complications and is diagnosed at an BMI above 30 kg/m² (Whitlock et al. 2009). Besides its critical burden on the organism, it was just in 2020 that the German government accepted obesity as disease, allowing appropriate medical treatment and approval for obesity-drugs in Germany, according to the European Medicine Agency (EMA). But the trend of increasing incidence knows no boarders and is not restricted exclusively to industrialized countries, but also affects low income countries (Nour 2010). It is estimated that by 2030 approximately 58 % of the world's adult population is either overweight or obese (Kelly et al. 2008). Moreover, in parallel the numbers of overweight in childhood and adolescents are rising likewise (Kansra, Lakkunarajah, and Jay 2021). According to WHO-declarations, in 2022 more than 390 million

children and adolescents are overweighted, accounting for 20 % of the total population group (WHO). Those numbers are alarming and demands tremendous effort to reduce obesity rates globally.

Obesity is a major risk factor for noncommunicable diseases (NCDs), such as cancer, insulin resistances and diabetes mellitus, fatty liver diseases and cardiovascular diseases (Ejigu and Tiruneh 2023). Further, it is associated with a decreased life expectancy of approximately five to 20 years, depending on the degree of severity of the condition and comorbidities (Blüher 2019; Fontaine et al. 2003). Current treatment strategies for obesity aim to reduce the body weight by either lifestyle interventions, bariatric surgery or pharmacotherapy. For a long time, bariatric surgery was the most effective, but also the last option of treatment for obesity achieving up to 20 % long-term body weight reduction (Maciejewski et al. 2016). But recently, the invention of incretin analogs has revolutionized the field and replaces the conventional approaches, since their induction in body weight loss is similar to the bariatric surgery (Kokkinos et al. 2019; Meier and Nauck 2015). Liraglutide and semaglutide mimic the effect of glucagon-like peptide 1 (GLP-1) by GLP-1 receptor agonism (Azuri et al. 2023). Tirzepatide take it a step further, by activating both – the GLP-1 and glucose-dependent insulinotropic polypeptide (GIP) receptor, combining the effect of two incretins (Jastreboff et al. 2022; Lin et al. 2023). Interestingly, those ‚new era' drugs show great improvement in obesity-associated comorbidities and are partially approved for the treatment of type 2 diabetes as well (Ross and Ekoé 2010). Additionally, the safety profiles display subjectively low side effects compared to the benefits, such as nausea and flatulence (Filippatos, Panagiotopoulou, and Elisaf 2014). Moreover, obesity can build up to a multiple-resistant state and especially leptin resistance, the anorexigenic hormone released from the adipose tissue in proportion to the fat mass that suppresses food intake, is commonly observed in obesity (Ahmed, Sultana, and Greene 2021). Therefore obese individuals have high levels of circulating leptin, but the leptin signaling in the brain is impaired, which leads to an improper feed-back signaling of the individual fat reservoirs (Gruzdeva et al. 2019). The disruption of leptin-signaling plays also a role in some genetic causes of obesity. Mutations in the leptin receptor and/or the leptin gene is associated with a predisposition to develop obesity (H. Chen et al. 1996; G.-H. Lee et al. 1996). Further, a mutation in the melanocortin-4 receptor (MC4R), which increases energy expenditure upon stimulation with melanocyte-stimulating hormones (MSH) or adrenocorticotropic hormone (ACTH), is the most common monogenic cause for obesity. Although genetic causes for obesity, either monogenic or polygenic, definitely play a crucial role for increasing the susceptibility for obesity, they can not explain the drastic increase in prevalence, which sheds the light onto epigenetic causes (Rohde et al. 2019; Thaker 2017).
Overall, with the advent of new incretin-based drugs, the fight against obesity has been officially declared. Nevertheless, not every individual is responsive to those drugs, which keeps the demand for alternative treatment strategies high (Austin and Tomas 2023). Additionally, many puzzles in the pathogenesis of obesity are unsolved and a great role of epigenetics in those is assumed. Therefore, further research is needed, to develop new treatment strategies or to unravel the molecular mechanism contributing to obesity and its comorbidities.

1.1.2. The adipose tissue in obesity – Laying a foundation for development of insulin resistance?

In the human body several fat depots exist, which differ in body distribution, structural organization and biological function (Frühbeck 2008). The adipose tissue is a loose connective tissue and was described for a long time as a storage tissue that is exclusively involved in thermoregulation and insulation of the organism during cold exposure (Longo et al. 2019a). With the increasing prevalence

of obesity, also the adipose tissue gained more attention and important functions are discovered in regulating glucose homeostasis, insulin resistance, immune system, food intake and also endocrine functions by secreting adipose tissue specific hormones – adipokines (Luo and Liu 2016).
The adipose tissue is categorized into white adipose tissue (WAT), beige adipose tissue (BeAT) and brown adipose tissue (BAT). The WAT can further be subdivided based on its location in the organism into subcutaneous adipose tissue (SAT), describing the fat depot directly underneath the dermis of the skin, and the visceral adipose tissue (VAT) – the fat depot surrounding the abdominal organs (Bjørndal et al. 2011). Up to 70 % of the predominant cell type across all adipose tissues is the adipocyte, but also immune cells, endothelial cells and adipocyte progenitor cells are located inside the adipose tissue, contributing to its high plasticity (Lenz et al. 2020). Adipocytes greatly differ in morphology and function between WAT and BAT. In the WAT, adipocytes are characterized by a single lipid-storing droplet and a low density of mitochondria, whereas adipocytes of the BAT contain more mitochondria and many small lipid-storing droplets (Park 2014). These characteristics define the BAT as a more ‚metabolic active' tissue involved in shiver-free thermogenesis, since the high mitochondrial content and the expression of the *uncoupling protein 1* (*UCP1*) generates heat by uncoupling the proton gradient within the mitochondrion (Fedorenko, Lishko, and Kirichok 2012). However, this should not imply that WAT is not metabolic active, even though its main function is storage and energy supply. WAT exerts capacity of a process called beiging, which can be induced by cold exposure or norepinephrine stimulation and leads to an increased mitochondrial content and lipid droplet amount similar to BAT (Thyagarajan and Foster 2017).
By surface area the SAT is the largest fat depot, but is assumed to secrete less adipokines, such as leptin or adiponectin compared to the VAT and the VAT is assumed to exert higher endocrine function in healthy conditions (Reneau et al. 2018).
Therefore in this study, the VAT is investigated.

1.1.2.1. The visceral adipose tissue-and de novo lipogenesis in obesity

Under fasted, healthy conditions, the VAT supplies the tissues in its proximity with energy in form of released TAGs or free fatty acids into the circulation by increasing lipolysis (Defour et al. 2020). Due to its location and especially the abdominal VAT, the secreted lipids are transported through the portal vein primarily to the liver (Rytka et al. 2011). In healthy conditions, lipolysis and de novo lipogenesis (DNL) are tightly regulated by insulin among others and are in a equilibrium to maintain the fat content of the VAT (Mottillo et al. 2014). However, during obesity, this equilibrium gets disrupted, since the oversupply of dietary fats exceeds the storing capacity of the VAT, which is also referred to as adipose tissue dysfunction (Longo et al. 2019b). This is followed by expansion (hyperplasia) of the adipose tissue to compensate for increased demand of storage capacity and adipocytes start to enlarge in response to increased fatty acid uptake (hypertrophy) (Horwitz and Birk 2023; Jo et al. 2009). This process is associated with the development of microinflammation of the tissue and impaired vascularization creates a hypoxic microenvironment, which both contribute to the development of insulin resistance of the adipose tissue (S. Sun et al. 2012). Like an overflowing barrel, the VAT tries to get rid off stored lipids to provide space for the persistent uptake of new dietary lipids and henceforth becomes highly lipolytic (Langin 2006), which contributes to the elevated fatty acid and TAG levels in the circulation often observed in obese subjects (Stadler and Marsche 2020). Those secreted lipids first arrive in the liver, where they contribute to the ectopic fat accumulation of hepatocytes (further discussed in 1.1.3). Additionally, the DNL rate of the VAT decreases, which comes with drastic consequences for the whole organism. Adipose tissue-dependent DNL generates a variety of insulin-sensitizing fatty acids, also known as lipokines like palmitoleate (H. Cao et al. 2008a).
DNL is tightly regulated in the VAT on a transcriptional level by the transcription factors carbohydrate

response element binding protein (ChREBP or *MLXIPL* gene), sterol regulatory element binding transcription factor 1 (SREBF1) and liver X receptor (LXR) (Z. Song, Xiaoli, and Yang 2018a). The importance of DNL and ChREBP activity is seen in differentiating adipocytes, which are deficient for ChREBP and therefore lack the capacity for a proper DNL. This leads to impaired differentiation and decreased peroxisome proliferator-activated receptor gamma (*PPARG*) expression. *PPARG* is the master regulator for adipogenesis and differentiation in adipocytes. It is assumed that an unknown metabolite generated in DNL is essential for PPARG activation upon differentiation (Witte et al. 2015). Once glucose is taken up into the adipocyte, glycolysis-derived metabolites activate the ChREBP, which is also the glucose sensor in the adipose tissue (Herman et al. 2012). ChREBP then induces the expression of DNL-related genes, such as *FASN* and *ACACA*, which are also the rate limiting enzymes of DNL (Herman et al. 2012, Figure 1).

Even though the VAT contributes small proportions to postprandial glucose uptake, glucose levels in the adipocyte are essential to stimulate DNL by activation of ChREBP (Z. Song, Xiaoli, and Yang 2018a). Insulin-stimulated glucose uptake is facilitated by the glucose transporter 4 (GLUT4 or *SLC2A4* gene). In response to insulin stimulation, GLUT4 proteins are inserted into the adipocyte membrane, which are stored in vesicles during basal conditions (T. Wang et al. 2020). During obesity, expression levels of GLUT4 as well as translocation of the membrane in the VAT are decreasing, which is linked to increased insulin resistance of adipocytes, as well as muscle tissue (van Gerwen, Shun-Shion, and Fazakerley 2023). Interestingly, adipose tissue specific GLUT4 knock out mice display insulin resistance, especially of the muscle tissue (Abel et al. 2001). Overexpression of GLUT4 in those animals restores muscle tissue insulin resistance (Carvalho et al. 2005).

This underlines the regulatory role of the insulin sensitivity by the VAT. Overall, this suggests that

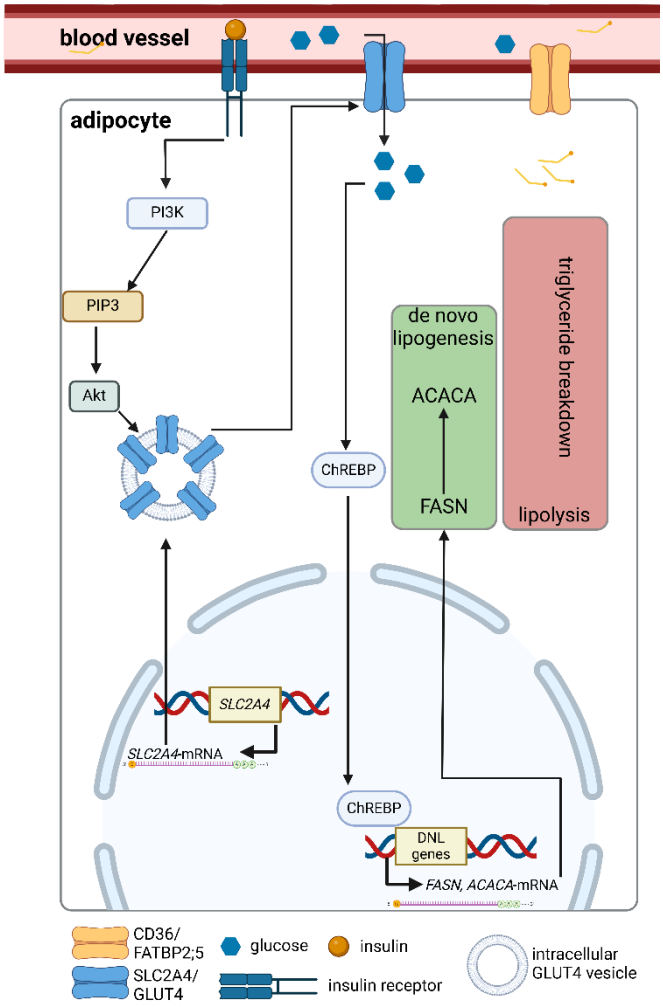

Figure 1: Insulin-mediated glucose uptake in adipocytes. In response to insulin stimulation, the signaling cascade of PI3K/PIP3 and Akt gets activated by phosphorylation. Then, activated Akt induces the translocation of GLUT4 protein, which is stored in intracellular vesicles during basal conditions, into the membrane of the adipocyte. This facilitates the glucose uptake by GLUT4 and consequently activates the ChREBP, which in turn induces the gene expression of de novo lipogenesis genes. PI3K = phosphoinositide 3-kinase, PIP3 = phosphatidylinositol triphosphate, Akt = protein kinase B, ACACA = acetyl-CoA carboxylase alpha, FASN = fatty acid synthase, ChREBP = carbohydrate-responsive element-binding protein, SLC2A4 = solute carrier family 2 member 4, DNL = de novo lipogenesis.

glucose uptake by GLUT4 is essential for DNL and the crucial role of VAT-dependend *SLC2A4* expression for the whole organism. However, the mechanism causing the downregulation of *SLC2A4* are incompletely understood. Therefore, the main hypothesis in this work is to study the mechanism behind the downregulation of *SLC2A4* expression and to study if *SLC2A4* expression is regulated by epigenetics, especially DNA methylation.

1.1.3. Metabolic dysfunction-associated steatotic liver disease in obesity – how to tackle the disease

Metabolic dysfunction-associated steatotic liver disease (MASLD), former non-alcoholic fatty liver disease (NAFLD), is an umbrella term for metabolic driven liver diseases. MASLD is characterized by fatty acid accumulation within at least 5 % of hepatocytes, but also includes a more liberal alcohol consumption and avoids the stigmatization of fatty-related terminology compared to its prior nomenclature of MASLD (Rinella et al. 2023). Additionally, MASLD criteria include also the context of coexisting cardiometabolic risk factors, such as insulin resistance, hypertension or elevated BMI to further emphasize the underlying metabolic condition (C. L. Hsu and Loomba 2024). Since the recent change in terminology in 2023 to MASLD and its more liberal definition towards alcohol consumption, less is actually known about to which degree MASLD and NAFLD differ on a molecular level. That it is not only a difference in nomenclature is supported by latest evidence, that categorizing a human cohort based on MASLD criteria is more accurate at identifying individuals at higher risk for diabetes compared to the traditional MASLD criteria (L. He et al. 2024). Because data is very scarce, in this work MASLD and NAFLD are treated as synonyms and literature referring to NAFLD is regarded accountable for MASLD, however one has to be aware of potential differences on molecular levels as well as pathological.

MASLD can progress into more severe and live threatening conditions, such as metabolic dysfunction-associated steatohepatitis (MASH, former non-alcoholic steatohepatitis or NASH) or hepatocellular carcinoma (HCC) (Anstee, Targher, and Day 2013). Until recently, there was no approved treatment for neither MASLD nor MASH, but with the approval of resmetirom, a selective *thyroid hormone receptor beta* (THRβ) agonist, the latter received its first available drug (Kingwell 2024). Nevertheless, treatment therapies to inhibit MASLD progression into its more severe conditions are still missing, which is owned to the complexity and diversity of the disease (Thiagarajan and Aithal 2019).

A major risk factor to develop MASLD is an increased body weight and obesity, which has been shown that MASLD prevalence increases with BMI and MASLD prevalence is significantly higher in morbidly obese patients when compared to only overweighted patients (J. Li et al. 2019). Obesity-associated adipose tissue dysfunction, where adipose tissue loses its capability to store fatty acids properly, increases adipose tissue lipolysis and decreases de novo lipogenesis. Therefore, excessive lipids are secreted from the adipose tissue, which need to be redistributed throughout the organism (Nishizawa and Shimomura 2019). The ‚portal-hypothesis' describes the liver to be more prone for ectopic lipid accumulation, since it is directly exposed to increased fatty acid secretion from the adipose tissue and therefore acting as a sink for excessive lipids in the blood circulation (Kabir et al. 2005). This is supported by the fact that approximately 59 % of accumulated lipids within hepatocytes during MASLD development is derived from the adipose tissue and not directly dependent on dietary intake (Donnelly et al. 2005). However, besides the increased uptake of circulating fatty acids, increased hepatic de novo lipogenesis, a decrease in hepatic beta-oxidation and reduced lipid export from the hepatocytes are further mechanism causing hepatic lipid accumulation (Geisler and Renquist 2017). The imbalance of fatty acid uptake and lipid export further drives hepatic lipid accumulation.

Mechanisms of lipid accumulation by increased uptake

Circulating lipids are transported into the hepatocytes by fatty acid transporters *cluster of differentiation 36* (*CD36*) or fatty acid transport protein 2 & 5 (FATP2 & FATP5, encoded on the genes *SLC27A2* & *SLC27A5*) (Ipsen, Lykkesfeldt, and Tveden-Nyborg 2018, Figure 2). *CD36* has found to be upregulated in DIO mouse models and adenoviral-mediated overexpression of *CD36* in mice results in increased hepatic lipid accumulation and FATP2/5 liver knock-out mice display reduced levels of hepatic lipid content (Doege et al. 2006; Falcon et al. 2010; Koonen et al. 2007; Wilson et al. 2016). Interestingly, the rs56225452 SNP is a gain-of-function mutation in the FATP5 promoter, which is associated with increased ALT activity, insulin resistance and degree of steatosis in MASLD individuals, adding another layer of genetic predisposition for MASLD (Auinger et al. 2010).
Once fatty acids enter the hepatocyte, a variety of cascades are triggered. First, fatty acids are activated with acyl-CoA by the *acyl-CoA synthetase* (*ACSL*) into fatty acyl-CoA, which is then distributed by fatty acid binding proteins (FABP) within the cytoplasm to either serve as signaling molecule, as substrate for beta oxidation or as substrate for TAG synthesis (FÆRGEMAN and KNUDSEN 1997). The latter is the dominant form of lipid storage in the liver and is synthesized by two pathways, namely the glycerol phosphate pathway or the monoacylglycerol pathway, of which both use fatty acyl-CoA as substrate (Bell and Coleman 1980; Of and Acids 1956). In the former pathway, fatty acyl-CoA is conjugated to glycerol-3-phsophate to form lysophosphatidate (lyso-P) by enzymes of the *glycerol-3-phosphate O-acyltransferases* (*GPATs*) family, followed by a second fatty acyl-CoA transfer to lysophosphatidate to generate phosphatidate (PS) by *acylglycerolphosphate acyltransferases* (*AGPATs*) (Takeuchi and Reue 2009). Then, phosphatidate is dephosphorylated by *phosphatidate phosphohydrolases* (*PAP*s) to produce diacylglycerol (DAG) (Carman and Han 2009). DAG is also the product of the monoacylglycerol pathway arising from the conjugation of monoacylglycerol with fatty acyl-CoA by *acyl-CoA:monoacylglycerol acyltransferases* (*MGATs*). Interestingly, during MASLD progression, DAG accumulate within the cell membranes increasing the DAG-membrane content, which has been associated with an increased protein kinase Cε (PKCε) activity that in turn inactivates the insulin receptor and thereby contributes to hepatic insulin resistance (Samuel et al. 2007). DAG is then conjugated with a third fatty acyl-CoA by *acyl-CoA:diacylglycerol transferases* (*DGATs*) to form triacylglyerols (TAG), the primary storage form of fatty acids within the liver and the one primarily used to measure fatty acid content. TAGs are stored within very-low density lipoprotein vesicles (VLDL vesicle) for secretion into the blood circulation or within cytoplasmic lipid droplets, from where they are consumed for energy supply from beta-oxidation (Nagle, Klett, and Coleman 2009).

Mechanism of lipid accumulation by increased de novo lipogenesis

As mentioned previously, hepatic lipid accumulation in MASLD is also attributed to an increased de novo lipogenesis (DNL). DNL is the conversion process of carbohydrates, predominantly glucose and fructose, into fatty acids from acetyl-CoA, which are then further metabolized to TAGs. Fructose and glucose are mainly imported into the liver by the insulin-independent *solute carrier family 2 member 2* (*SLC2A2*) (Douard and Ferraris 2013). Upon uptake, fructose and glucose are metabolized by two pathways into acetyl-CoA. In the first pathway, pyruvate generated from glycolysis is converted to acetyl-CoA within the mitochondria – the main substrate for the citrate cycle (TCA), which is catalyzed by the pyruvate dehydrogenase complex (assembled from pyruvate dehydrogenase, dihydrolipoamide acetyltransferase & dihydrolipoamide dehydrogenase) (Patel et al. 2014). Then, acetyl-CoA is condensed to oxaloacetate by the *citrate synthase* (*CS*) to form citrate, which is further metabolized in the TCA, or is exported from the mitochondria by a citrate-isocitrate carrier (CIC) in the form of citric acid (Z. Zhu et al. 2023). In the cytosol, citric acid is converted back into oxaloacetate and acetyl-CoA by the *ATP citrate lyase* (*ACLY*) (Chypre, Zaidi, and Smans 2012). In the second pathway, pyruvate

bypasses the mitochondrial conversion into citrate and is directly converted into acetate in the cytosol by keto acid dehydrogenases (KAD) by neutralization of reactive oxygen species to pyruvate (X. Liu et al. 2018). Then acetate is converted into acetyl-CoA by the *acetyl-CoA synthetase* (*ACS*) (S. Zhang et al. 2019) and is used for the formation and elongation process of fatty acids. Therefore, acetyl-CoA undergoes decarboxylation by acetyl-CoA decarboxylases (ACC1/ACC2, encoded on the *ACACA*/*ACACB* genes) to form malonyl-CoA (Y. Wang et al. 2022), which is then converted by the *fatty acid synthase* (*FASN*) into palmitate under the consumption of NADPH (Jensen-Urstad and Semenkovich 2012). Palmitate can be elongated by *fatty acid elongases* (*ELOVLs*) before conjugation to G3P to form TAGs (Xiangyu Wang et al. 2023). During MASLD, many genes involved in DNL in the liver are upregulated, such as *FASN*, *ACACA* and *ELOVL1*, which are regulated by the transcription factors (TF) *carbohydrate-response element binding protein* (ChREBP or *MLXIPL* gene), *sterol regulatory element-binding protein 1* (*SREBF1*) or *peroxisome proliferator-activated receptor gamma* (*PPARG*). Those TFs are activated upon glucose, fructose or fatty acid binding (Chou et al. 2018; Z. Zhu et al. 2023).

Mechanisms of lipid accumulation by decreased beta-oxidation

In periods of nutritional deprivation, TAGs are mobilized from intrahepatic stores to generate energy in form of ATP. Therefore, TAGs are broken down again to win acetyl-CoA, which is needed in the TCA. This process occurs in the mitochondria or peroxisomes and is defined as beta-oxidation (Houten et al. 2016b). Thereby, acyl-CoA groups from fatty acid chains of the TAGs are ‚shortened' stepwise under the release of acetyl-CoA by *acyl-CoA dehydrogenases* (*MCADs*), *enoyl-CoA hydratases* (*ECHs*), 3-hydroxyacyl-CoA dehydrogenases (*HADH*) and *3-ketoacyl-CoA-thiolases* (*KATs*) (Houten et al. 2016a). Interestingly, the number one MASLD-genetic risk factor, SNP rs738409 in the *ptatin-like phospholipase domain-containing protein 3* (*PNPLA3*) gene, results in abnormal accumulation of *PNPLA3* in lipid droplet membranes and thereby seem to interfere with fatty acid secretion and beta-oxidation due to impaired lipid mobilization (BasuRay et al. 2019; Romeo et al. 2008).

Mechanisms of lipid accumulation by decreased VLDL secretion

VLDL secretion is tightly regulated by insulin signaling within the hepatocyte (Choi and Ginsberg 2011). During basal conditions, apolipoprotein-rich VLDL particles export lipids from the liver into the blood flow to provide energy resources of other tissues (van Zwol et al. 2024). After food intake, pancreatic insulin release inhibits VLDL secretion from the liver. Interestingly, patients with MASLD have higher basal rates of VLDL-mediated lipid secretion, which also contribute to elevated lipid concentrations in the blood and indicates an impaired action of insulin-mediated repression of VLDL secretion (Heebøll et al. 2022). Hepatic insulin resistance blunts this pathway and VLDL-lipid secretion is not able to compensate anymore with the increased fatty acid uptake or induced DNL activity causing more and more lipid accumulation.

Overall, lipid accumulation in early stages of MASLD are considered benign (Ipsen, Lykkesfeldt, and Tveden-Nyborg 2018), but with ongoing progression, the excessive amount of lipids induce lipotoxicity, stress responds and oxidative stress in the hepatocyte, which ultimately leads to a failure in liver function (Pouwels et al. 2022). This goes along with a dysregulation of other metabolic pathways and inflammation and activation of Kupffer cells (hepatic macrophages), which finally cause scarring of the liver tissue (fibrosis and cirrhosis) (Dixon et al. 2013).
Since lipid accumulation is the primary step in developing MASLD, many treatment therapies try to reduce lipid accumulation by either increasing beta-oxidation or inhibiting fatty acid uptake (Filipovic et al. 2021). However, alternative treatment strategies are needed.

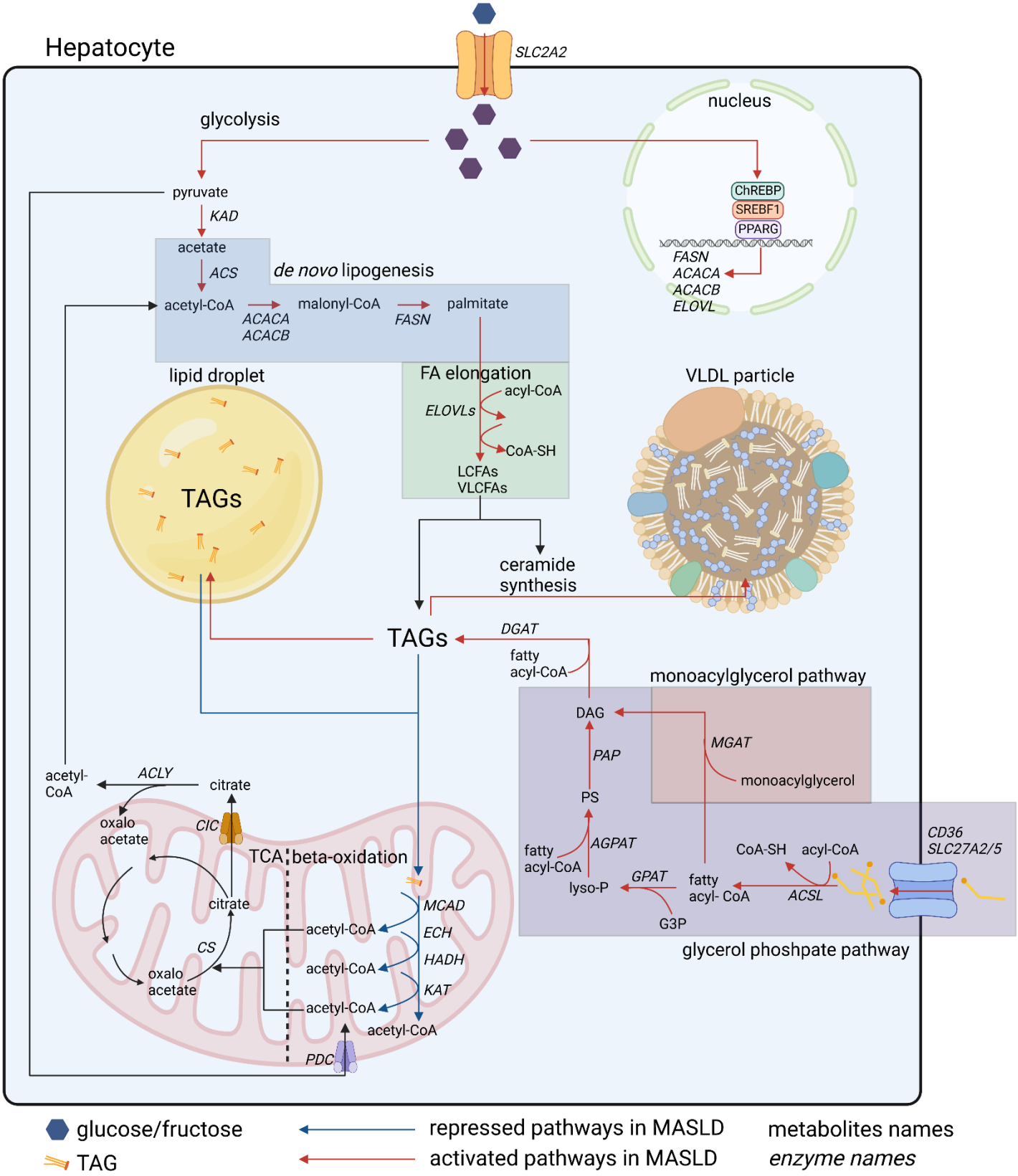
Hepatocyte
SLC2A2
glycolysis
nucleus
pyruvate
KAD
acetate
ACS
de novo lipogenesis
acetyl-CoA
ACACA
ACACB
malonyl-CoA
FASN
palmitate
ChREBP
SREBF1
PPARG
FASN
ACACA
ACACB
ELOVL
lipid droplet
TAGs
FA elongation
ELOVLs
acyl-CoA
CoA-SH
LCFAs
VLCFAs
VLDL particle
ceramide
synthesis
TAGs
DGAT
fatty
acyl-CoA
monoacylglycerol pathway
DAG
PAP
MGAT
monoacylglycerol
PS
AGPAT
fatty
acyl-CoA
lyso-P
GPAT
fatty
acyl- CoA
G3P
CoA-SH
acyl-CoA
ACSL
CD36
SLC27A2/5
glycerol phoshpate pathway
acetyl-
CoA
ACLY
citrate
oxalo
acetate
CIC
citrate
CS
oxalo
acetate
TCA
beta-oxidation
MCAD
ECH
HADH
KAT
acetyl-CoA
acetyl-CoA
acetyl-CoA
acetyl-CoA
PDC
glucose/fructose
TAG
repressed pathways in MASLD
activated pathways in MASLD
metabolites names
enzyme names

Figure 2: Triacylglycerol accumulating pathways in hepatocytes in the progression of MASLD. Increased glucose and fructose uptake by SLC2A2 activates de novo lipogenesis (DNL) pathways and induces the transcription factors ChREBP, SREBF1 and PPARG. Fatty acids synthesized in DNL are elongated in the fatty acid elongation (FA elongation) pathway and are esterified with glycerol 3-phopshate (G3P) to form triacylglycerol (TAG), which is stored either in lipid droplets or in VLDL particles for secretion. Increased fatty acid uptake by fatty acid transporters (CD36/SLC27A2/SLC27A5) leads to TAG production via the monocylglycerol or glycerol phosphate pathway. TAGs are either mobilized from lipid droplets or from previously described pathways into the mitochondria, where they are degraded in beta-oxidation to generate acetyl-CoA. *SLC2A2 = Solute carrier family family 2 member 2, KAD = keto acid dehydrogenases, ACS = acetyl-CoA synthetase, ACACA/ACACB = acetyl-CoA carboxylase A and B, FASN = fatty acid synthase, ELOVL = fatty acid elongases, DGAT = acyl-CoA diacylglycerol transferases, PAP = phosphatidate phosphohydrolases, AGPAT = acylglycerolphosphate acyltransferases, MGAT = acyl-CoA:monoacylglycerol acyltransferases, GPAT = glycerol-3-phosphate O-aceyltransferases, ACSL = acyl-CoA synthetase, MCAT = acyl-CoA dehydrogenases, ECH = enoyl-CoA hydratases, HADH = 3-hydroxyacyl-CoA dehydrogenases*, *KAT = 3-ketoacyl-CoA-thiolases, CIC = citrate-isocitrate carrier, PDC = pyruvate dehydrogenase complex, CS = citrate synthase, ACLY = ATP citrate lyase,* LCFAs = Long chain fatty acids, VLCFAs = very long chain fatty acids, DAG = diacylglycerol, PS = phosphatidate, lyso-P = lysophosphatidate

1.1.4. Dysregulation of metabolic pathways in MASLD

MASLD is often referred as the metabolic syndrome of the liver and thereby comes along with significant changes in the metabolite profile (McGlinchey et al. 2022). Hyperammonemia is a common phenotype observed in subjects with MASLD and MASH (Felipo et al. 2012). The cause of this is assumed to be a dysregulated urea cycle, which is exclusively located within the liver (Neill et al. 2009). Enzymes involved in the urea cycle, such as *ornithine transcarbamylase* (*OTC*), *carbamoylphosphate synthetase* (*CPS1*) and *arginase 1* (*ARG1*) are reported to be downregulated in MASLD (De Chiara et al. 2018) and deficiency of these genes is associated with elevated hepatic citrulline levels, which is also present in urea cycle disorders (UCD) (Matsumoto et al. 2019). The urea cycle is linked to the one-carbon metabolism, which comprises the methionine and folate cycle (Ducker and Rabinowitz 2017, Figure 3). Homocysteine, derived from the one carbon metabolism, is converted into cystathionine by the *cystathionine beta synthase* (*CBS*) under the consumption of serine (EC 4.2.1.22, (Matoba et al. 2017)). The former is degraded into cysteine and ammonia by the *cystathionine gamma-lyase* (*CTH*, EC 4.4.1.1) and ammonia serves as entering substrate to the urea cycle. The one-carbon metabolism is essential to generate and recycle the methyl donor S-adenosylmethionine (SAM) and approved models to study NASH use a methionine deficient high-fat diet (Flessa et al. 2022; Klein Geltink and Pearce 2019). DNA methyltransferase activity transfers the methyl group of SAM onto cytosine residues in the DNA generating S-adenosylhomocysteine (SAH, (Tehlivets et al. 2013)). Decreased hepatic SAH and methionine levels are observed in mouse models for NASH using high-fat/sucrose diet or human subjects with MASLD and are often associated with *methionine adenosyltransferase 1 A depletion* (*MAT1A*, (Quinn et al. 2022; Zubiete-Franco et al. 2016)). A crucial pathway to recycle methionine within the liver is the conversion of homocysteine by the *betaine homocysteine methyltransferase* (*BHMT*), which requires the import of betaine as a substrate. Betaine administration has been shown to improve hepatic steatosis in human subjects and hepatic insulin resistance in mouse (Abdelmalek et al. 2001; Kathirvel et al. 2010). Hepatocytes import betaine by a the *betaine/GABA transporter 1* (*SLC6A12*/*BGT1*) (Ji and Kaplowitz 2003). Gamma-aminobutyric acid (GABA) is degraded in hepatocytes into succinate within the citrate cycle (TCA) salvage pathway GABA shunt, which is then metabolized in the TCA (K. Kim and Yoon 2023; Seok Roh et al. 2016). The key enzyme of the GABA shunt, *4-aminobytyrate aminotransferase* (*ABAT*), degrades GABA into succinate semialdehyde and *ABAT* deficiency is associated with GABA accumulation (Besse et al. 2015). GABA accumulation has shown to promote methionine-choline deficient diet-induced MASH and systemic insulin resistance (Geisler et al. 2021; Seok Roh et al. 2016). *Serine-glyoxylate transaminase* (*AGXT*) catalyzes the detoxification of glyoxylate with serine into glycine and pyruvate (EC 2.6.1.45), of which the latter serves as substrate for the TCA. Recently, *AGXT* downregulation in MASLD has proven to induce liver damage by increasing

oxidative stress accompanied by increased kidney damage as well (Gianmoena et al. 2021).
Mechanisms regulating responsible for the dysregulations in amino acid metabolism are incompletely understood. MicroRNAs (miRNAs) have great potential in treating MASLD, due to their properties of regulating multiple genes or complete pathways (Ben-Hamo and Efroni 2015; Y. Zhu et al. 2023). Identification of a single miRNA involved in regulating a majority of the metabolic pathway-associated genes may have an enormous impact on MASLD progression and may serve as a potential therapeutic target (1.2.1).

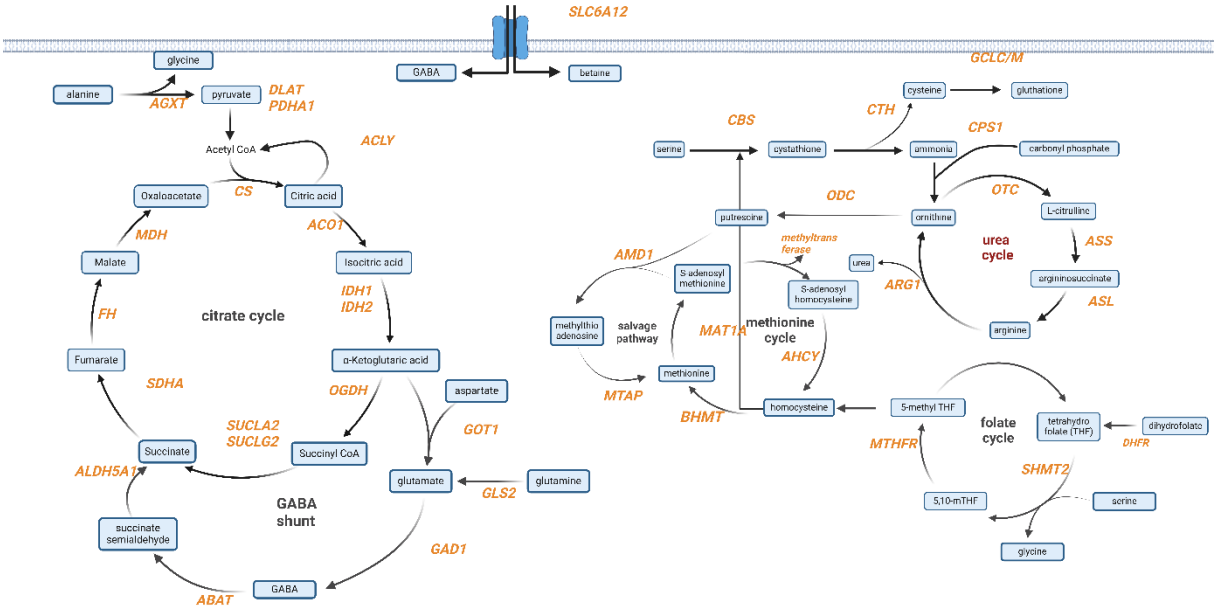

Figure 3: Metabolic pathways associated with MASLD. Dysregulations of the GABA shunt, citrate cycle (TCA), one-carbon metabolism (methionine/folate) and urea cycle are associated with MASLD. The GABA shunt is a recycling pathway of the TCA, where GABA is catabolized into succinate and thereby fed back into the TCA. GABA is transported into the hepatocyte by the SLC6A12 transporter, which also imports betaine. Betaine is a crucial substrate for the methionine cycle and thus SLC6A12 links the GABA shunt/TCA to the one-carbon metabolism. Within the one-carbon metabolism, crucial amino acids are generated and metabolites involved in DNA methylation regulation, such as S-adenosyl methionine (SAM) and S-adenosyl homocysteine (SAH). Also, homocysteine from the methionine cycle is metabolized into cystathionine by *CBS*. A product of cystathionine degradation is ammonia, which enters the urea cycle by condensation with ornithine. Ornithine is further metabolized into urea, which is finally secreted into the blood and excreted via the urine.

1.2. Epigenetics

As mentioned previously, epigenetic describes the sum of mechanisms that regulate gene expression without altering the underlying genetic information. Those mechanisms are cell and tissue specific and are assumed to be inherited (Lacal and Ventura 2018). The epigenetic landscape determines the fate of a cell, but also shows high plasticity in response to external and internal stimuli, allowing the organism to adapt dynamically to specific environmental circumstances (Moosavi and Motevalizadeh Ardekani 2016). Overall, three major epigenetic mechanisms are best understood: Histone modifications, DNA methylation and non-coding RNAs (Figure 4) (Y.-L. Wu et al. 2023). In the scope of this thesis, DNA methylation and small non-coding RNAs, a subclass of non-coding RNAs, are investigated and histone modifications are not studied. Therefore, histone modifications are briefly introduced, but not explained in detail, whereas small non-coding RNAs and DNA methylation are explained in the following chapters. Also, long non-coding RNAs (lncRNAs), an additional subclass of non-coding RNAs, are not in the focus of this project and are only shortly introduced in this chapter.

Histone modifications mostly modulate the chromatin accessibility or recruit transcriptional enhancers or repressors and thereby affect the gene expression. Histone acetylation and phosphorylation reduce the positive histone charge. This disrupts the electrostatic interactions of the negatively charged DNA with the histone proteins causing a less compact chromatin structure and increasing the chromatin accessibility. Acetylation occurs on lysine residues of the histone, whereas phosphorylation predominantly takes place at serines, threonines or tyrosines (Bannister and Kouzarides 2011). Histone methylations are present at lysine and arginine residues of the histone. Histone methylation does not alter the charge of the histone and therefore the chromatin structure is not directly affected. Lysine residues are mono-, di-, or trimethylated and arginine residues mono- or dimethylated (Ng et al. 2009). The effect of histone methylation on the transcription depends on its location (which lysine or arginine of a histone), number of methylations (mono, di, tri) and which factors are recruited. For example, H3K4me3 (Histone 3, Lysine residue 4, trimethylation) is associated with active transcription and is found in promoters (Champagne and Kutateladze 2009), whereas H3K9me3 (Histone 3, Lysine residue 9, trimethylation) is associated with repressive heterochromatin by heterochromatin protein 1 (HP1)-mediated gene silencing (Bannister et al. 2001).
Besides histone acetylation, phosphorylation and methylation, other histone modifications exist (Bannister and Kouzarides 2011; Hassa et al. 2006; Sakabe, Wang, and Hart 2010).

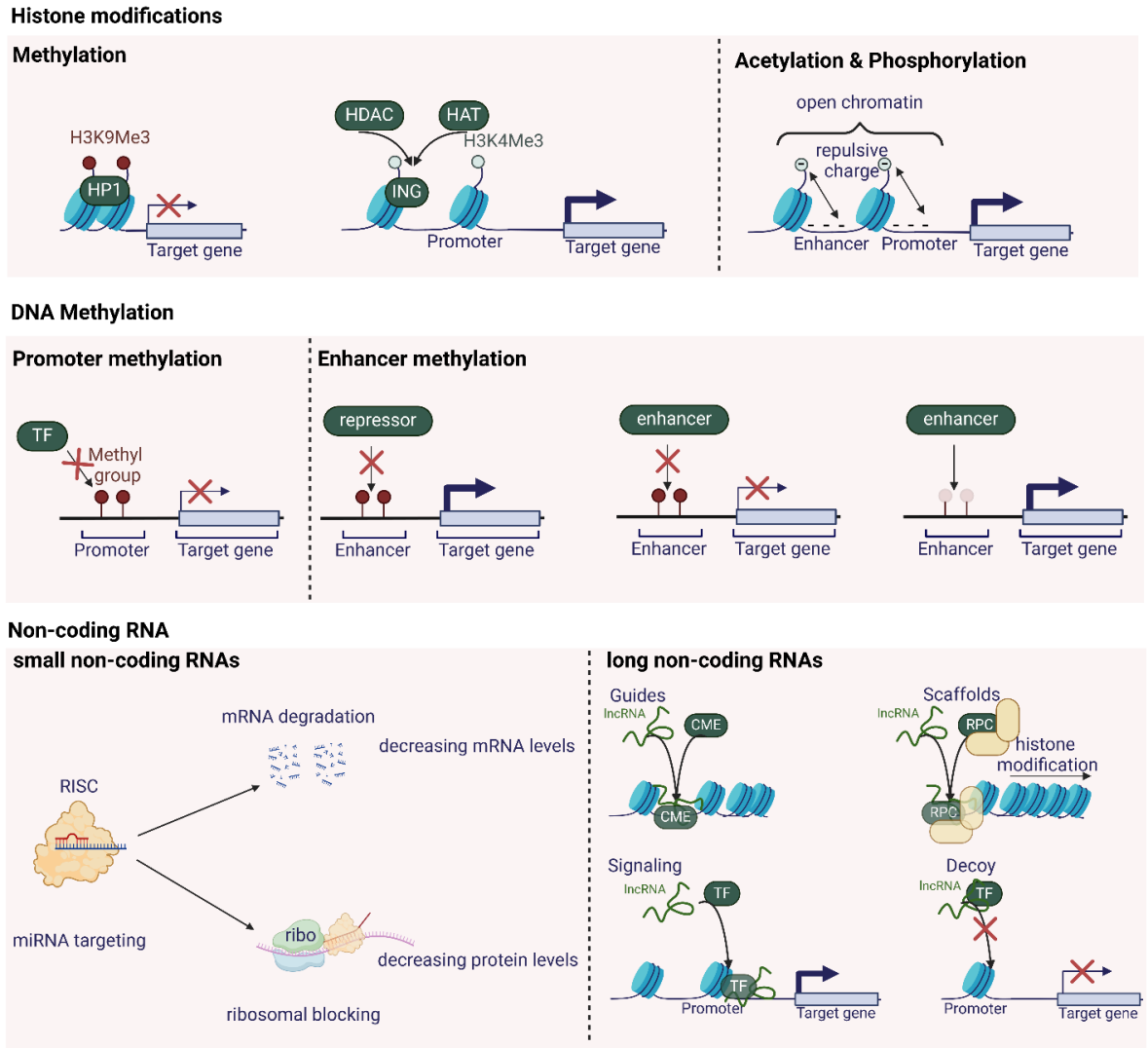

Figure 4: Overview of the three best described epigenetic mechanisms. Histone modifications involve methylation, acetylation and phosphorylation. Since the latter two introduce a negative charge to the histone, repulsive electrostatic effects between negatively charged histone and DNA create an ‚opened' chromatin accessible for transcription factors. Histone methylation either represses gene expression by recruitment of HP1 or enhances gene expression. DNA methylation occurs at CpG sites and promoter methylation is commonly associated with repression of the target gene. In enhancer regions, DNA methylation either enhances gene expression by interfering with repressor binding, or represses gene expression by interfering with enhancer binding. Non-coding RNAs are majorly categorized into small non-coding RNAs to which miRNAs belong to and long non-coding RNAs (lncRNAs). MiRNA binding to a target gene mRNA induces either mRNA degradation or translational inhibition. LncRNAs serve guiding, scaffolding, signaling or decoy functions.

1.2.1. Micro RNAs in health and disease – small friends and foes

Micro RNAs (miRNA) belong to the small non-coding RNAs and are about 22 nucleotides long RNA molecules with a 8-nucleotides long seed sequence commonly starting at first 5'-nucleotide of the mature miRNA. Other members of the small non-coding RNA family are small interference RNAs (siRNAs) and piwi-interacting RNAs (piRNAs) (C. Li and Chen 2015). Since the discovery of the first miRNA *lin-4* in *Caenorhabditis Elegans* in 1993 by Ambros and Ruvkun (R. C. Lee, Feinbaum, and Ambros 1993; O'Brien et al. 2018), approximately 2300 mature miRNAs are predicted for the human genome with roughly ~ 50 % (1115) being experimental validated (Alles et al. 2019). MiRNAs serve as negative-posttranscriptional regulator of gene expression and play a crucial role in development, proliferation, neurogenesis, differentiation, and immune system, where their main purpose is to balance basal expression (O'Brien et al. 2018). Since a single miRNAs can possess over several hundred target genes, miRNAs have a huge potential in regulating complete pathways or cellular processes and approximately 60 % of all coding-mRNAs in the human genome are estimated to be regulated by miRNAs (Kehl et al. 2017). Therefore, dysregulated miRNA expression contributes to a variety of diseases, such as neurodegenerative diseases, cancer and metabolic diseases, among these obesity, MASLD and insulin resistance (Ardekani and Naeini 2010).
MiRNA expression and function is cell and tissue specific, similar to other epigenetic mechanisms. For example, the term myomiRs describes miRNAs preferentially expressed in skeletal muscle tissue (McCarthy 2011). On the other hand, miR-122 is a hepatocyte-specific miRNA, which accounts of up to 75% of total miRNA within the hepatocyte and is essential for liver function but is also responsible for hepatitis C virus (HCV) liver-tropism (Schult et al. 2018; Tsai et al. 2012). Interestingly, HepG2 cells do not express miR-122 natively (Jopling et al. 2005).
Function of the miRNA within the tissue depends on the expression of perspective target genes, co-factors, such as RNA-binding proteins, and abundance of target gene expression. Therefore, a specific miRNA can be benign in the one tissue or cancer type, but also malign in another one. An example for this opposing-function is the miR-18a, where tumor suppressing and oncogenic characteristics have been described (Kolenda et al. 2020; K. Shen et al. 2019; Tsang and Kwok 2009). However, there are still a lot of unsolved mechanisms in miRNA biogenesis, their regulation in diseases and their contribution to disease progression.

1.2.1.1. Biogenesis and regulation of miRNA expression

The transcription of miRNAs and processing into their active, functional single-stranded RNA molecule is categorized into a canonical and a non-canonical pathway. The canonical pathway describes the transcription and processing of the premature miRNA by the RNase III enzymes Drosha and Dicer (Figure 4 & Figure 5). The non-canonical pathway summarizes all alterations to this pathway (O'Brien et al. 2018). Half of the identified miRNAs are transcribed from intragenic regions of their host gene, with the majority from introns and rather few from exons (Y.-K. Kim and Kim 2007; de Rie et al. 2017).

However, latest research indicate intragenic miRNAs regulated by an intragenic miRNA promoter (Monteys et al. 2010). The remaining half of miRNAs are transcribed from intergenic regions and are regulated by their own promoter. This process is independently of a serving host gene (B. Liu et al. 2018).

The canonical pathway starts with the transcription of the miRNA gene into a pri-miRNA by the RNA polymerase II in the nucleus (Y. Lee et al. 2004). In contrast, other short-non coding RNAs, such as transfer-RNAs (tRNAs), U6 small nuclear RNAs (snRNAs) or small interfering RNAs (siRNAs), are transcribed by RNA polymerase III (Arimbasseri and Maraia 2016; Sui et al. 2002). A pri-miRNA is a several kilobases long, partially double-stranded RNA transcript with a characteristic internal hairpin structure (W. Jin et al. 2020). This hairpin structure is crucial for the recognition of the microprocessor complex containing Drosha and Pasha (also known as DGCR8) and resides the prospective mature miRNA. The ribonuclease Drosha recognizes the basal junction between the single-stranded basal region and the lower stem and cleaves the pri-miRNA 11 base pairs (bps) upstream of it (J. Han et al. 2006), whereas Pasha binds as a dimer to the apical junction of the loop (Nguyen et al. 2015). Interestingly, alternative cleavage of the pri-miRNA by Drosha results in the generation of isomiRs, which inhabit a different seed sequence despite the fact that miRNA and isomiR are derived from the same pri-miRNA (Burke et al. 2014). Due to this alternated seed sequence, isomiRs have a distinct subset of target genes and thereby affect disease progression. A famous example is miR-9, where an instability of the stem loop in the pri-miR-9-1 results in the generation of the miR-9-5', which might contribute to tumor progression in the brain tissue (Bofill-De Ros et al. 2019).

The product of the Drosha and Pasha processing of the pri-miRNA is the hairpin-structure with a 2 nucleotide overhang at the 3' end, called the pre-miRNA (Y.-Y. Lee et al. 2023). This pre-miRNA is then transported into the cytoplasm by the exportin 5 (XPO5)/RanGTP complex for further processing (Yi et al. 2003). Once the pre-miRNA reaches the cytoplasm, it is bound by the RNase Dicer. Dicer recruits the double-stranded RNA-binding protein TRBP and cleaves off the loop from the hairpin structure, generating the mature miRNA duplex, consisting of the miR-5p-strand originating from the 5'-end of the pre-miRNA hairpin and the miR-3p-strand from the 3'-end (Kozomara and Griffiths-Jones 2014). This miRNA duplex is recognized and loaded into one of the four Argonaute proteins (AGO), of which AGO2 seems to be the most ubiquitous and abundant expressed Argonaute protein and essential, since AGO2 deletions are lethal (Cheloufi et al. 2010; Fagerberg et al. 2014; Nakanishi 2022). Nevertheless, it seems that each Argonaute protein shows increased specificity for a subset of miRNAs or other small-non coding RNAs, but the underlying mechanism of Argonaute tropism towards a miRNA remains unknown (Turchinovich and Burwinkel 2012; Yamakawa et al. 2014). After the binding of the miRNA duplex to the Argonaute protein, the Argonaute is left with a binary choice of which miRNA strand of the duplex to keep and which to discard (Medley, Panzade, and Zinovyeva 2021). This procedure is referred to as strand selection. The exact mode of selection is incompletely understood, but several factors, such as 5'-end thermodynamic stability, are assumed to affect strand selection by the Argonaute (Khvorova, Reynolds, and Jayasena 2003). Once the Argonaute protein made its selection, further proteins are recruited to form the miRNA-induced silencing complex, or short termed miRISC. Additionally to the Argonaute protein, the miRISC complex in human comprises also GW182, Hsp90β, Hsc70, Hop, Dnaja2 and p23 (Iwakawa and Tomari 2022; Naruse et al. 2018). This complex is guided by the loaded miRNA to its destined target mRNA. Through complementary base pairing of the seed sequence within the miRNA to the 3'UTR of the target mRNA, binding of the miRISC is facilitated. This induces mRNA degradation or inhibit protein translation by ribosomal blocking (O'Brien et al. 2018). Those mechanisms are summarized as RNA interference (Figure 4 & Figure 5).

The non-canonical pathways can be generalized into *Drosha/DGCR8*-independent and *Dicer*-independent mechanisms. Non-canonical processed miRNAs display the minority of the miRNAs within a cell, thus these processes will be explained briefly, to cover the full complexity of miRNA biogenesis. Part of the *Drosha/DGCR8*-independent processed miRNAs are *miRtrons*. In human, there are around

13 *miRtrons* predicted, with only a hand full being validated (Berezikov et al. 2007; Schamberger, Sarkadi, and Orbán 2012). *miRtrons* are intronic miRNAs with the defined length of the encoding intron.(Ruby, Jan, and Bartel 2007) Therefore, biogenesis of *miRtrons* bypasses *Drosha/DGCR8* cleavage, but the pre-miRNA maturation relies on splicing of the mRNA by the spliceosome (Havens et al. 2012). This pre-miRNA is exported into the cytoplasm by *XPO5* and serves directly as *Dicer* product (Stavast and Erkeland 2019). For the Dicer-independent pathway, only one miRNA in human is known to date, namely the miR-451 (Cheloufi et al. 2010). A shortened stem loop of the pre-miR-451 makes *Dicer* cleavage unfeasible. Therefore, the pre-miR-451 is loaded directly into and processed by the AGO2 (Cifuentes et al. 2010).

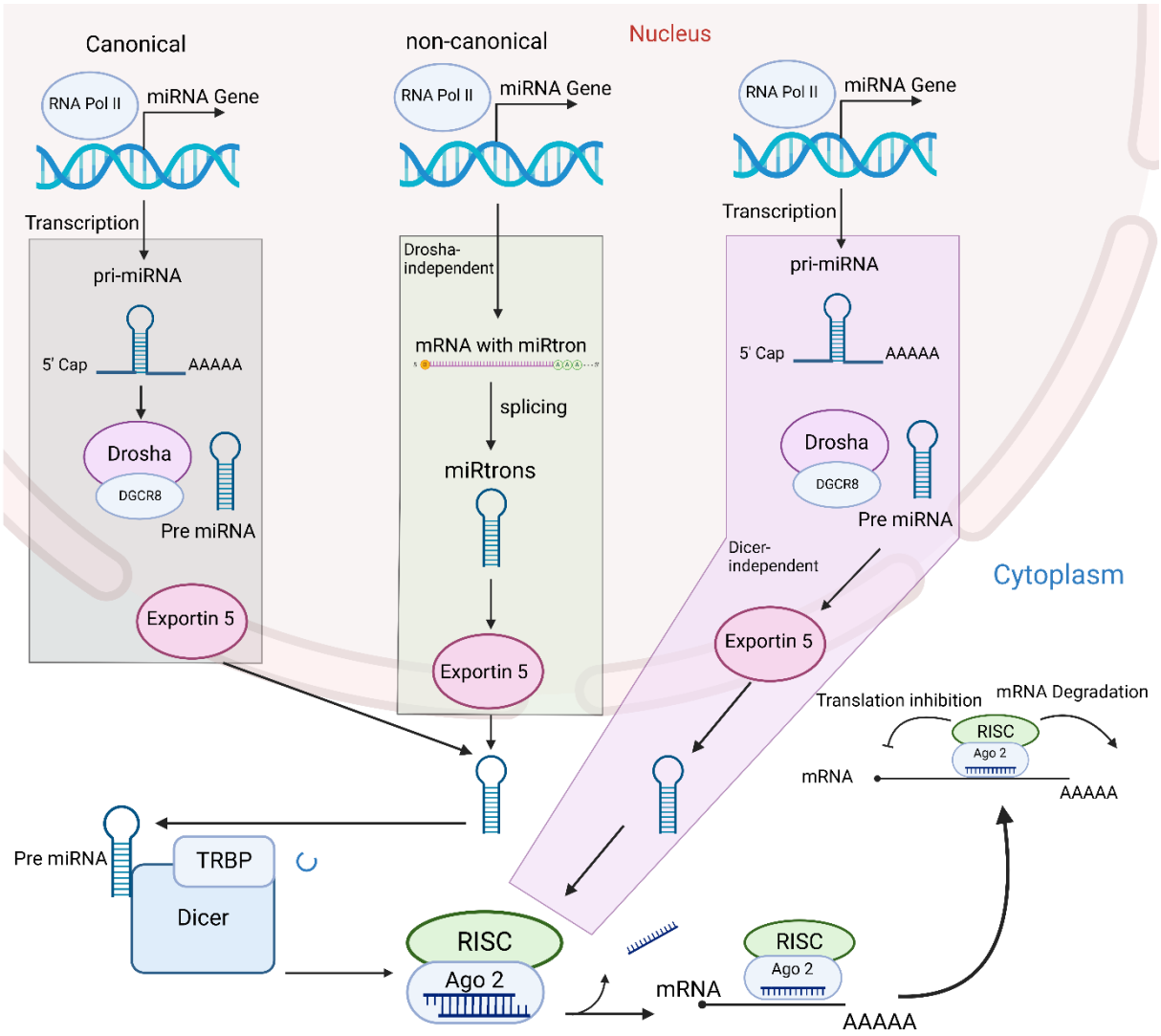

Figure 5: Biogenesis and processing of miRNAs. MiRNAs are processed by a canonical and non-canonical pathway. In the former, miRNAs are transcribed into a pri-miRNA including a characteristic stem loop structure and single-stranded overhangs. The Drosha/DGCR8 RNAse III microprocessor complex cleaves off the single stranded overhangs at the stem of the loop, generating the pre-miRNA transcript, which is exported into the cytosol via Exportin 5. Then, Dicer cleaves off the pre-miRNA stem loop and die miRNA-duplex is loaded into the Argonaute 2 (Ago2) protein, followed by assembly of the miRISC complex. Subsequently, Ago 2 removes one strand of the miRNA-duplex and the miRISC complex is guided to the target mRNA to induce mRNA degradation or translational inhibition. The non-canonical pathway is separated into a Drosha-independent and a Dicer-independent pathway. MiRtrons are commonly processed in the Drosha-independent pathway, since the pre-miRNA is directly generated from mRNA-splicing. The Dicer-independent pathway is utilized for pre-miRNAs with alternative stem loop structure, which makes Dicer-processing infeasible.

1.2.1.2. miRNAs in MASLD

MASLD and its progression goes along with alterations of the transcriptome, metabolome and miRNA expression (Mondal et al. 2023; Shao et al. 2022). It is already established that miRNAs are greatly involved in MASLD pathogenesis and progression by altering the transcriptome and thereby also might be potential therapeutics.

For example, miR-34a is reported to be upregulated in the liver but also serum of subjects with MASLD (Salvoza et al. 2016). Serum levels of miR-34a correlate positively with BMI and blunts fibroblast growth factor 19 and 21 (FGF19 & 21) signaling, which are hepatokines with insulin-sensitizing function (T. H. Kim, Hong, and Yang 2021). Additionally, hepatic miR-34a expression is elevated in mouse models for diet-induced obesity, mouse models for MASH and obese human subjects with type 2 diabetes (Xu et al. 2015) Thereby, miR-34a-mediated hepatocyte nuclear factor 4 alpha (HNF4a) downregulation promotes triglyceride accumulation within the liver. It has been shown that miR-34a promotes MASLD progression through further pathways in mouse and human and its expression increases with severity of MASLD progression into MASH (Hochreuter et al. 2022).

Recently, miR-182-5p was identified to be upregulated in the liver of obese individuals with type 2 diabetes and that it is positively correlated with NAS score, HbA1c, serum triglyceride and glucose levels (Krause et al. 2023). MiR-182-5p directly targets the low-density lipoprotein receptor-related protein 6 (LRP6) and the insulin receptor substrate 1 (IRS1), which play a role in Wnt- and insulin signaling and impaired signaling of those pathways is one of the many components for building up insulin resistance in the liver (S. Li, Brown, and Goldstein 2010). Additionally, high levels of miR-182-5p expression are associated with progression of hepatocellular carcinoma (HCC), the final endpoint of MASLD progression (M.-Q. Cao et al. 2018; Petersen and Shulman 2018).

Interestingly, for the most abundant hepatic miRNA, namely miR-122, the role in MASLD progression is ambiguous. On the one side, hepatic germline knockout mice for the miR-122 show increased liver steatosis, which progressed into fibrosis and also malignant, HCC-like tumors (S. Hsu et al. 2012). Overexpression of miR-122 in the hepatic KO mice rescued steatosis again (Tsai et al. 2012). Those findings suggest a protective role of miR-122 for MASLD. On the other side, treatment of diet-induced obese (DIO) mice with an antisense oligonucleotides for miR-122 reduces liver steatosis and the expression of lipogenic genes in the liver (Esau et al. 2006), which implies a MASLD promoting effect. However, a big difference between the both conducted studies is that the KO mouse model diminishes both mature miRNAs, the miR-122-3p and the miR-122-5p, encoded by the miR-122 gene, whereas the antisense oligonucleotide specifically targets the miR-122-5p. This might be an explanation for the reported ambiguous function and further emphasizes the importance of differentiating between both miRNAs derived from a pre-miRNA.

Also, the miR-21 is found to be upregulated in individuals with MASH and HCC, but is rarely reported to be upregulated in early stages of MASLD (Hochreuter et al. 2022; Loyer et al. 2016). Therefore, it is suggested that miR-21 is primarily involved in MASLD progression rather than in the initiation of the disease. This is also supported by the fact that miR-21 tends to increase in expression with increase in liver inflammation and fibrosis, which is a characteristic of MASH more than MASLD (Loyer et al. 2016). But still, many functions of miR-21 in MASLD remain elusive.

Furthermore, miR-149-5p is described with ambiguous function in human cancer by exerting tumor suppressive and oncogenic properties (Ghafouri-Fard et al. 2021; Y. Shen et al. 2022). But recent studies report that miR-149-5p is upregulated in the liver of DIO mice (S. Chen et al. 2020). MiR-149-5p expression shows weight-cycling patterns, where reduction in body weight of caloric restricted animals after high-fat diet exposure is coupled with a tendency of reduced miR-149-5p expression levels. Refeeding the caloric restricted animals with high-fat diet (hfd) elevates miR-149-5p expression again (Krause et al. 2023).

Interestingly, the miRNA-expression profile in serum of obese human subjects when compared to normal-weight controls shows a distinct pattern of upregulated hepatic-specific and dysregulated adipose tissue-derived miRNAs. For instance, the liver-specific miR-122, miR-885-5p and miR-192 are also upregulated in the serum of obese subjects. Astonishingly, the expression of those liver-specific miRNAs is reversed in a longitudinal measurement of three, six to 12 months post bariatric surgery. Further, in the same cohort, miR-21 expression is significantly decreased in the serum of obese subjects, but is unaltered after bariatric surgery. However, direct hepatic miRNA expression after bariatric surgery is not measured and literature is scarce, but since hepatic-specific miRNA expression in the serum is reversed after bariatric surgery, it can be assumed that the reversal originates from the liver (Sangiao-Alvarellos et al. 2020).
Overall, evidence in the literature support the role of miRNAs in pathogenesis and progression of MASLD and empathize their great potential as therapeutic treatments by either inhibiting them with antisense oligonucleotides or rescue their expression to stop MASLD progression. Additionally, this supports the reversibility of miRNA expression through weight-loss interventions, such as bariatric surgery.

1.2.2. DNA methylation

As the term implies, DNA methylation is a direct modification, in that case a methylation, on the DNA. It is commonly found at CpG-sites, where a cytosine base is directly followed by a guanine base on the same DNA strand (C. P. Walsh and Xu n.d.). This is indicated by the ‚p' in the CpG, which refers to the phosphodiester bond between the both bases. However, also non-CpG site methylation occurs at cytosines followed by any other base of the DNA code (CpA, CpT, CpC) and has also been found to play a major role in cancer progression (Ramasamy et al. 2021). DNA methylation interferes with DNA-protein binding of transcription factors, transcriptional enhancers or repressors and thereby regulates gene expression depending on the location where DNA methylation occurs. But this is only partially true, since DNA methylation-sensitive protein exists, which show a higher affinity of binding towards methylated cytosine and are capable of recruiting complex machineries that induce histone modifications or transcriptional regulators (Clouaire and Stancheva 2008).
Since coding regions within the DNA only account of up to 2 % of the whole genome, intergenic regions are vastly methylated to silence these regions (Sana et al. 2012). Within these intergenic regions transposons or viral elements are located, which harbor potential harm upon activation (Schulz, Steinhoff, and Florl n.d.; Colum P. Walsh, Chaillet, and Bestor 1998). Promoter regions of genes are frequently located within CpG-islands, defined as DNA regions of high CpG content, and promoter methylation is majorly associated with repressed gene expression (Mohn et al. 2008; Saxonov, Berg, and Brutlag 2006). On the other hand, methylation of intragenic regions, also known as the gene body consisting of exons and introns, displays an enhancing effect on the gene expression (Ball et al. 2009). An exception here is the first exon of a gene. Due to its close proximity to the promoter region, methylation of the first exon seems to have similar effects as promoter methylation (Brenet et al. 2011).

DNA methylation is an actively catalyzed process in which a methyl group is transferred to a cytosine. This reaction is carried out by an enzyme family called DNA-methyl transferases (DNMTs). So far, there are three known DNMTs: DNMT1, DNMT2 and DNMT3 (to which DNMT3a, DNMT3b and DNMT3L belong). Despite its binding to the DNA, there is no evidence that proves also methylation activity of DNMT2 and it is theorized that DNMT2 serves as a marker of specific DNA sequences (Dong 2001). Therefore, it is assumed that DNMT1, DNMT3a and DNMT3b are the predominant DNA methyltransferases (Figure 6). DNMT1 has been observed to preferentially methylate hemimethylated

cytosines. Hemimethylation describes a state where only one of the double stranded DNA molecule is methylated and the other strand is unmethylated, which occurs after DNA replication. DNMT1 recognizes the ‚missing' methylation on the unmethylated, newly synthesized strand and transfers a methyl group to restore the methylation pattern on both strands. Therefore, DNMT1 is often referred to as the maintenance DNMT. DNMT3a and DNMT3b are capable of methylating hemimethylated CpGs, but show no preferences for unmethylated or hemimethlyated CpGs. Since they can introduce new methylation on ‚naked', unmethylated DNA, DNMT3a and DNMT3b are referred to as *de novo* DNMTs (Okano et al. 1999). Whereas DNMT3a is expressed ubiquitously, DNMT3b is expressed in the thyroid gland, bone marrow and testes (Xie et al. 1999). How de novo DNA methylation is regulated is currently unknown. Theories about bound transcription factors protecting the DNA from methylation by interfering with DNMT recruitment are one possibility (Moore, Le, and Fan 2013).

To catalyze the methylation reaction of a cytosine by DNMTs, a methyl donor is needed. That methyl donor comes in the form of S-adenosylmethionine (SAM), which is either retrieved from the diet or synthesized in the methionine cycle (Broderick, Broderick, and Hoffman 2023). This reaction is separated into four steps, where deprotonation of a cysteine residue in the catalytic domain of a DNMT takes place, followed by nucleophilic addition of the residue to the aromatic-like ring structure of the cytosine at the 6^{th} carbon position. Subsequently, the methyl group from the methionine residue of SAM is transferred on the 5^{th} carbon of the cytosine ring and in the fourth step a b-elimination releases the cysteine residue of the DNMT (Jerbi et al. 2017). SAM is thereby demethylated into S-adenosyl homocysteine. The methylated cytosine is also referred as 5mC, describing the methylation of the 5^{th} carbon of the cytosine.

However, DNA methylation is neither a persistent nor an inflexible modification and various factors influence the stability of the methylation allowing the cell to adapt to a certain external stimuli, such as stress, diet, physical activity or other environmental factors (Apsley et al. 2023; Lim and Song 2012). Since DNA methylation is actively established by DNMT, there are also DNMT-counterparts, which erase methylation on the DNA actively (Moore, Le, and Fan 2013). There are three enzyme classes, which are involved in demethylation – activation-induced cytidine deaminases/apolipoprotein B mRNA-editing enzyme complex (AID/APOBEC), thymine DNA glycosylase (TDG), and ten-eleven translocation family proteins (TETs) (Cortellino et al. 2011; Rai et al. 2008; X. Zhang et al. 2023). The active demethylation of 5mC is catalyzed in various intermediate states (Figure 6). Besides active demethylation, also passive demethylation occurs, in which methylated cytosine spontaneously deaminizes to thymine, causing a G-T mismatch in the DNA. If not recognized by DNA mismatch repair mechanisms, spontaneous demethylation harbors great mutagenic potential (Holliday and Grigg 1993).

DNA methylation, like other epigenetic mechanisms, is altered by environmental factors and thereby contributes to the development of obesity, insulin resistance or other metabolic diseases by affecting the gene expression of disease-related genes (Kirchner et al. 2013). As explained previously, the adipose tissue plays a crucial role in these diseases as well. Therefore, DNA methylation of one disease-related gene, might promote the development of insulin resistance.

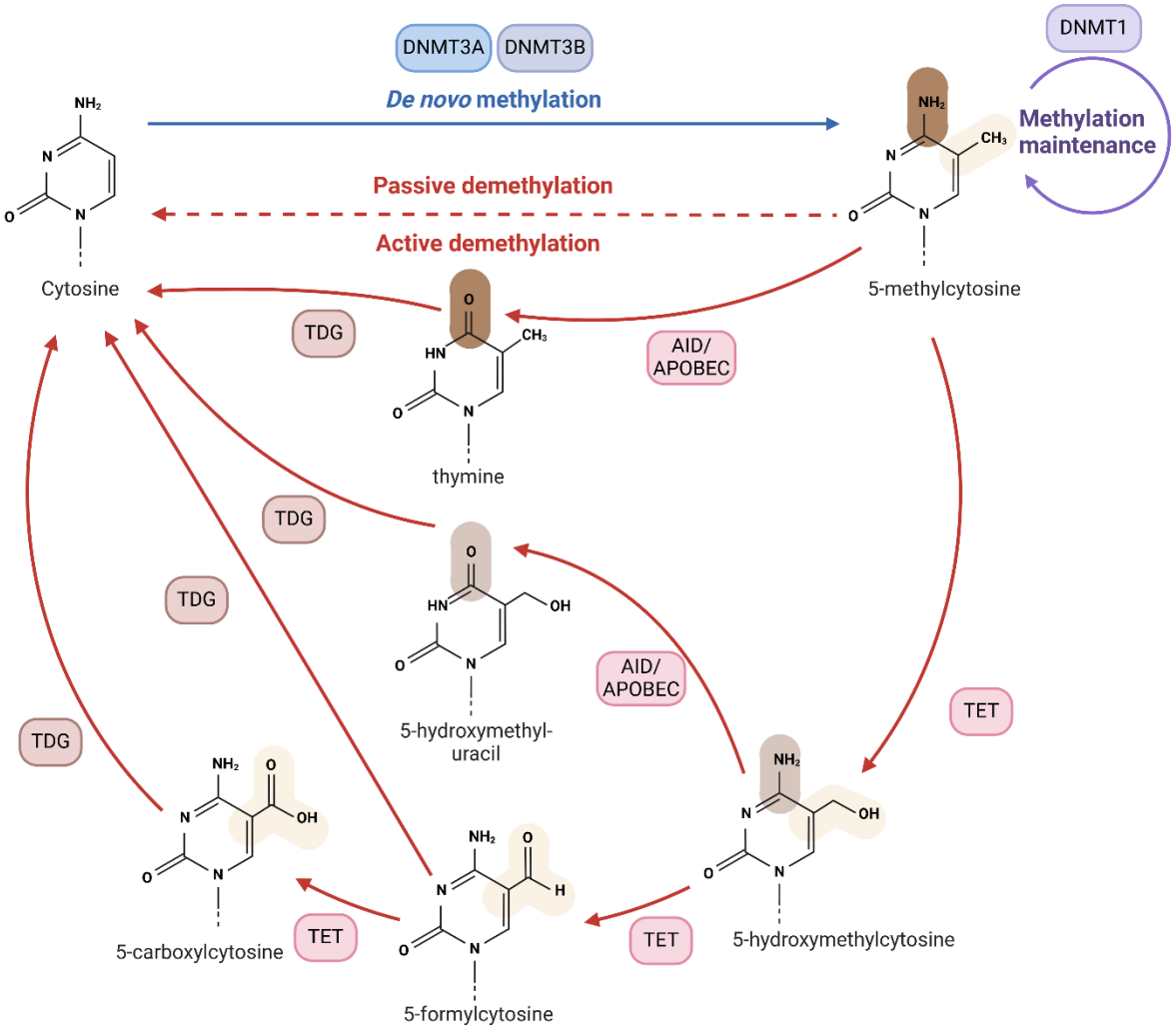

Figure 6: Mechanisms regulating DNA methylation. DNA methylation is either introduced de novo by DNMT3A or DNMT3B or is maintained by DNMT1. DNMTs required a methyl donor as substrate, which is commonly supplied by S-adenosyl methionine (inspired by Moore, Le, and Fan 2013). Demethylation of the DNA either occurs passively or actively. Active demethylation requires a variety of enzymes, which catalyze the demethylation of 5-methylcytosine back into cytosine via different intermediate steps. Currently, enzyme members of the TET family, APOBEC and TDG are identified to catalyze DNA-demethylation.

1.2.3. DNA methylation in metabolic diseases – The methylome of VAT and liver

The technical and computational progression in regards of genome-wide sequencing and micro array hybridization-based methylation analysis, such as whole-genome bisulfite sequencing (WGBS) or the Illumina Infinium Methylation Assay, gained a broad view on the methylome of the liver and the VAT in metabolic diseases. Especially the combination of different OMICS data display a powerful tool in deciphering the interplay between epigenetic changes and their impact on the transcriptional or metabolite level. OMICS data thereby describe the high-throughput profiling of the complete protein (proteomics), epigenetic (epigenomics), transcriptome (transcriptomics), or metabolome (metabolomics) alterations (Allis and Jenuwein 2016; Dai and Shen 2022). This allows the identification of dysregulated pathways under the control of DNA methylation in the steatotic liver (MASLD) or the insulin-resistant adipose tissue.

For instance, methionine-deficient diet induced hypomethylation in the promoter region results in the

upregulation of glucose, fibrosis and lipid metabolism-associated genes in the liver of mice (Tryndyak et al. 2011). Further, supplementation of high-fat diet fed mice with betaine revised promoter DNA methylation in the *microsomal triglyceride transfer protein* (*Mttp*), a protein essential for the assembly of apolipoprotein B-containing lipoproteins, and rescued *Mttp* gene expression, when compared to high-fat diet fed animals without betaine supplementation (Grove et al. 2023; Y. Li et al. 2022). Interestingly, Markus Ahrens and colleagues identified a subset of 9 genes potentially regulated by DNA methylation involved in progression of MASLD, which they termed ‚Epigenetic Disease Driver Genes'. Among them *ACLY* (hypomethylated and induced), *glutamate receptor delta-1* (*GRID1*, hypermethylated and induced), *phospholipase C gamma 1* (*PLCG1*, hypomethylated and induced), and *insulin-like growth factor 1* (*IGF1*, hypermethylated and repressed). Furthermore, the group could show that bariatric surgery normalizes the DNA methylation patterns and gene expression towards a normal-weighted control group in humans. Also, they found that transcription factor binding motifs of SREBP2, ZNF173 and PGC1A are significantly enriched in differentially methylated regions on the DNA, which emphasizes a superior role of DNA methylation on the transcriptomic level by interfering with TF binding and thereby affecting the gene expression of complete regulons (Ahrens et al. 2013). A regulon defines the entirety of genes regulated by a certain transcription factor (Müller-Dott et al. 2023). Those findings indicate that there might be subset of genes, which contribute to a greater extend to MASLD progression and they might also be epigenetically regulated. Additionally, hepatic genome-wide methylation differ between human individuals with MASLD-associated fibrosis when compared to individuals without fibrosis (Johnson et al. 2021). Integration of bulk-mRNA sequencing gene expression data to the genome-wide DNA methylation pattern identified 7 high-risk CpGs associated with liver fibrosis. Furthermore, cell-type specific deconvolution of DNA methylation data provides information about changes in cell type populations between fibrotic and non-fibrotic MASLD individuals. Deconvolution of data generated from bulk sequencing (complete tissue with pooled cell populations) describes a computational approach to retrieve single-cell information by analyzing alterations of cell-type specific reference gene expression or methylation loci without performing single-cell sequencing methods (Momeni et al. 2023; Singh, Pratt, and Aldape 2021).

Aside from the liver, DNA methylation contributes to the development of insulin resistance in the adipose tissue and affects adipogenesis and adipocyte function during obesity. As mentioned previously, the adipose tissue is a highly plastic tissue and during obesity processes such as hyperplasia and hypertrophy of adipocytes occur. Interestingly, a further mechanism has been observed, which is tightly regulated by epigenetic remodeling, namely adipocyte-dedifferentiation (Merrell and Stanger 2016; T. Song and Kuang 2019). Against the traditional dogma that terminally differentiated cells lose the capability to reverse their identity, it seems like adipocytes may undergo a constant cycle of dedifferentiation into progenitor cells and redifferentiation into adipocytes within the adipose tissue (Sakers et al. 2022). The dedifferentiation process from adipocytes into their progenitor cells is thereby accompanied by an increase in lipolysis, at least observed in the subcutaneous adipose tissue (Shook et al. 2020). Single-cell RNA sequencing from human VAT of obese individuals reveals a higher amount of adipocyte precursor cells (APCs) and a lower amount of differentiating preadipocytes, which suggests a disruption of the differentiating cycle of adipocytes tending towards more undifferentiated cells (Hildreth et al. 2021). However, to which extend disrupted DNA methylation is involved in this process remains elusive and no specific loci associated with this process are reported.

In a small cohort of obese non-diabetic and obese diabetic patients, differentially methylated regions (DMR) in the VAT display the greatest difference in methylation in genes associated with T2D, supporting the fact that DNA methylation in the VAT contributes to T2D development in obesity (Baca et al. 2022). Also, in VAT of obese diabetic patients hypomethylation in the promoter of the zinc finger protein 714 (*ZNF714*), a transcription factor potentially involved in insulin resistance and differentiation, is accompanied by an increased *ZNF714* gene expression (Crujeiras et al. 2016; Ramirez et al. 2020). But aberrant DNA methylation in the VAT is not exclusively restricted to processes of

adipocyte differentiation. DNA methylation is reported to regulate gene expression of adipokines, such as leptin or adiponectin (Pham and Lee 2017). For instance, cytokine release (TNFα) from infiltrating macrophages during low-grade inflammation in the VAT of obese subjects seems to mediate site-specific DNA methylation in the adiponectin gene by inducing DNMT1b gene expression, which in turn represses adiponectin gene expression. Administration of a DNMT-inhibitor, in this case RG108, to db/db mice rescues adiponectin gene expression and DNA methylation. Consequently, db/db mice show reduced levels of fasted blood glucose, fasted insulin and serum triglyceride levels (A. Y. Kim et al. 2015). These observations indicate a great impact of DNA methylation within a single gene influencing systemic insulin sensitivity. However, it is noteworthy that RG108 ubiquitously inhibits DNMTs in the VAT and global DNA methylation levels are not measured in the reported study. Therefore, alterations in DNA methylation within other genes that might contribute to this phenotype can not be excluded.

During adipogenesis the leptin promoter is demethylated, which is essential to induce leptin gene (*Lep*) expression within the adipocyte (Melzner et al. 2002). This inverse correlation between *Lep* promoter methylation and gene expression is maintained in the VAT of lean, chow-fed animals, whereas for high-fat diet animals this association gets disrupted and promoter hypermethylation is accompanied by an increased *Lep* gene expression (Wenwen Shen et al. 2014). Intriguingly, recent findings assume that autocrine leptin signaling in the VAT regulates its own gene expression in a negative feedback loop. Thereby, leptin signaling activates the JAK2/STAT3 pathway, which in turn inhibits the DNA-methylation eraser TET2 to retain *Lep* gene promoter hypermethylation (Zeng et al. 2024).

Apart from its tissue-specific regulatory function on gene expression, DNA methylation also excels beyond that role and might serve as diagnostic marker in blood for metabolic diseases (Q.-F. Sun et al. 2022; Willmer et al. 2018).

Those findings highlight the importance of DNA methylation in the development of metabolic diseases. Furthermore, the identification of potential epigenetic disease driver genes, suggests that there might be certain subsets of epigenetically regulated genes that contribute to disease progression. Furthermore, it once again shows how flexible epigenetic mechanisms are in response to interventions (supplementation or bariatric surgery). Identifying common underlying regulatory epigenetic mechanism might display a great potential as therapeutic target.

1.3. Synergistic effects of epigenetics in diseases

Now that epigenetic mechanisms and their separately contribution to metabolic diseases are introduced previously, such as DNA methylation and miRNAs, it is possible that one gene is regulated by several epigenetic mechanisms at the same time, which act in a synergistic manner. Synergistic effects in the epigenetic landscape are also supported by the theory of an epigenetic hierarchy, where researchers try to identify superior and inferior epigenetic modifications – comparable to the question what came first? The hen or the egg? An example for this would be that the histone trimethylation at H3K9 (Histone 3, lysine residue 9), H3K27 (Histone 3, lysine residue 27) and H4K20 (Histone 4, lysine residue 20) is required for subsequent DNA methylation in pericentric heterochromatin regions (Lehnertz et al. 2003). This is orchestrated by the histone lysine methyltransferase *SUV39H1*, which physically interacts and recruits DNMT3b to the locus destined for DNA methylation (B. Jin, Li, and Robertson 2011). In this example, histone modification is the superior mechanism guiding the inferior DNA methylation.

Additionally, DNA methylation can occur in regulatory regions of miRNA genes, defining the DNA methylation as superior mechanism. DNA methylation-associated silencing of tumor suppressor miR-148a, miR-34b/c and miR-9 is for instance found in human cancer metastasis (Lujambio et al. 2008).

Further, the expression of *insulin receptor substrate 2* (*IRS2*) decreases in the liver of obese subjects with high HbA1c levels (> 6.5 %) when compared with obese subjects with low HbA1c levels (< 6.5 %). This downregulation is achieved by an additive regulation of an increased DNA methylation in the *IRS2* gene, which blocks transcription factor binding of SP1 and SREBF, and the additional downregulation on a posttranscriptional level by upregulated let-7-5p miRNA (Krause et al. 2020).
Those studies emphasize that miRNA and DNA methylation do not work independently from each other and combining the research for both mechanisms may unravel the contribution of epigenetics to obesity and MASLD progression or to the development of insulin resistance.

1.4. The local controlling genes of the liver – foundation for the master regulator miRNA hypothesis

As described previously, there might be subsets of epigenetically regulated genes, which contribute to a greater extend to MASLD progression (‚Epigenetic disease driver genes'). Recently, a novel subset called ‚Local controlling genes' (LCGs) has been identified in the liver from integration of multiple different omics data (Klaus et al. 2021). Since the LCGs are in the focus of this work, the identification process is briefly explained (for schematic overview see Figure 7).
The computational approach to identify LCGs is termed ‚Correlation guided network integration', or short CoNI. The primarily goal of CoNI is to combine two different types of omics data within one graphical network to identify transcripts that influence metabolite levels, which in turn contributes to MASH. Therefore, in the first step of the CoNI analysis, random pairs of metabolites (M) from metabolomics data are correlated using Pearsons correlation. The correlation coefficient of metabolite pairs (ρ_{m1m2}) is stored within a symmetrical matrix sized M-rows times M-columns. Subsequently, transcriptomic data are integrated and the linear effect of each gene (t for transcript) on the metabolite pairs is estimated by comparing the metabolite correlation pairs ρ_{m1m2} with the partial correlation after transcriptomic integration ρ_{m1m2*t} and K-numbers of adjacency matrices for each partial correlation (Number of transcripts = K) are generated. Then, significant interactions between metabolite pairs with gene effect are calculated and significant interactions are stored in an individual adjacency matrix for each gene, resulting again in K-numbers of adjacency matrices with significant gene interactions. From those interactions a graphical network is drawn, where the edges indicate genes and the nodes indicate metabolites.
The CoNI analysis is initially performed separately from hepatic transcriptomic and metabolomic data of mice either receiving a chow diet or hfd for 22 weeks. From the chow-network *Ddx3x* and from the hfd-network *Myc*, *Arhgap24*, *Smim13*, *Rapgef4*, *Cd82*, *Inhbe* and *Gk* are identified as LCGs. Subsequently, *Cobll1* and *Appl2* are added as LCG, due to their strong association with diabetic relevant traits, such as hepatic fat content, insulin resistance (based on HOMA-IR) and overweight. Additionally, *Tap1* is identified as LCG, since it is the only gene occurring in the chow and hfd-network, which is also differentially expressed between both groups. Consequently, a list of 11 LCG is generated.
Afterwards, the expression of the 11 LCGs is measured in a human cohort to assess the translational relevance and gene expression is correlated with metabolic traits (BMI, hepatic fat content and HOMA-IR, see Table 1).

Table 1: Correlation analysis of LCGs from human cohort (Klaus et al. 2021)

	BMI		Hepatic fat content		HOMA-IR	
LCG name	**R^2**	**p**	**R^2**	**p**	**R^2**	**p**
GK	0.06	< 0.01	0.02	0.09	0.04	0.1
INHBE	0.09	< 0.01	0.1	< 0.01	0.1	0.01
TAP1	0.05	< 0.01	0.02	0.1	0.03	0.14
MYC	0.05	< 0.01	0.01	0.71	0.02	0.23
SMIM13	0.02	0.07	0.04	0.03	0.03	0.18

Representative gene silencing of *Appl2*, *Cobll1*, *Gk*, *Rapgef3* and *Inhbe* in HepG2 cells using specific siRNAs cause a loss of correlation between metabolites in the siRNA-treated network, when compared to control siRNA-treated network. This confirms the role of LCGs in regulating metabolites involved in liver health and metabolism.
However, due to the novelty of the identified LCGs less is known about their regulation in MASLD.

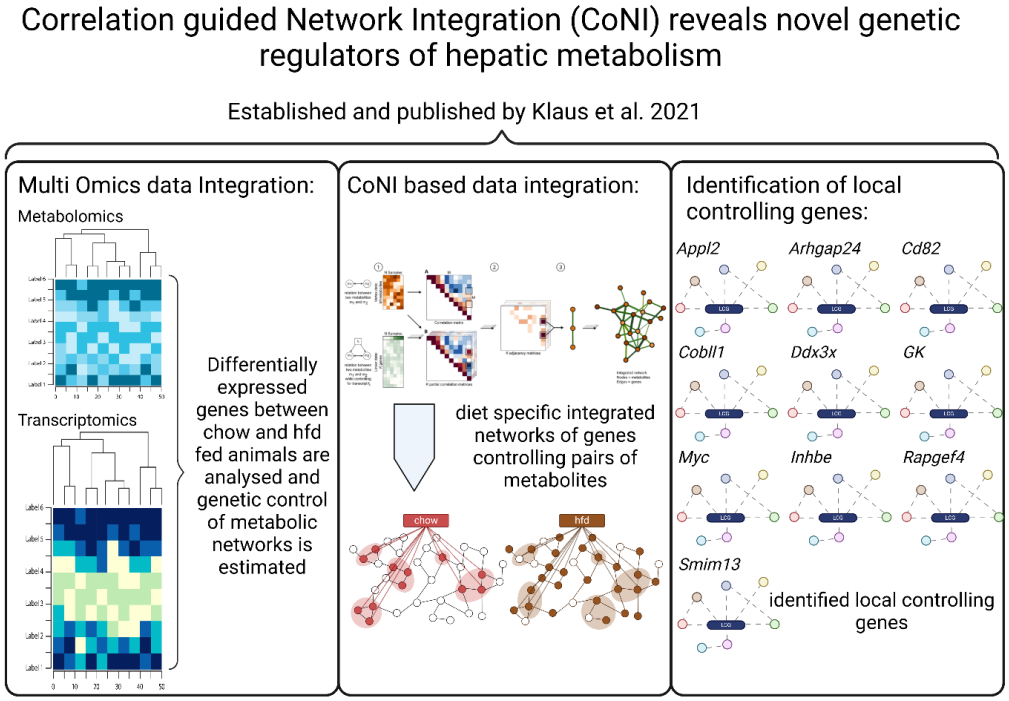

Figure 7: Overview of CoNI to identify local controlling genes (LCGs) in the liver. First, random Pearson correlation of metabolite pairs is performed and the correlation coefficient is saved within a symmetrical matrix. Then, transcriptomic data are integrated and the genetic effect of a gene on the metabolite correlation is estimated. Significant interactions between metabolite pairs and genes are combined in a graphical network and local controlling genes are selected from it. This approach identifies 11 LCGs: Appl2, Arhgap24, Cd82, Cobll1, Ddx3x, *Gk*, *Myc*, *Inhbe*, *Rapgef4* and *Smim13*.

1.5. Hypotheses

Obesity and its comorbidities, such as type 2 diabetes or MASLD, place a great burden on global health care systems and tremendously affect the life of hundred of millions people world wide. Therefore, a better understanding of molecular mechanisms involved in those diseases is required to develop novel treatment strategies. Epigenetic changes in DNA methylation or miRNA expression are associated with disease progression in MASLD and in the development of insulin resistance as described previously. However, many epigenetic mechanisms remain unidentified, which may also harbor potential therapeutic properties.
The main aim of this work is to elucidate novel epigenetic changes, which are involved in disease progression and may also serve as novel therapeutic approaches.

1. The master regulator miRNA regulating LCGs in MASLD progression:

As explained above, a subset of genes is identified that is involved in MASLD and is dysregulated during disease progression, termed LCGs. A common underlying regulatory mechanism, such as miRNAs might be involved in the dysregulation of LCGs.
Therefore, I hypothesize that a specific dysregulated miRNA is causative for the aberrant LCG expression in MASLD. This miRNA is classified as a master regulator miRNA and need to fulfill certain criteria. At first, the master regulator miRNA must show an opposite expression pattern in the liver of DIO mice compared to its target LCGs. For instance, an upregulated LCG must be regulated by a downregulated

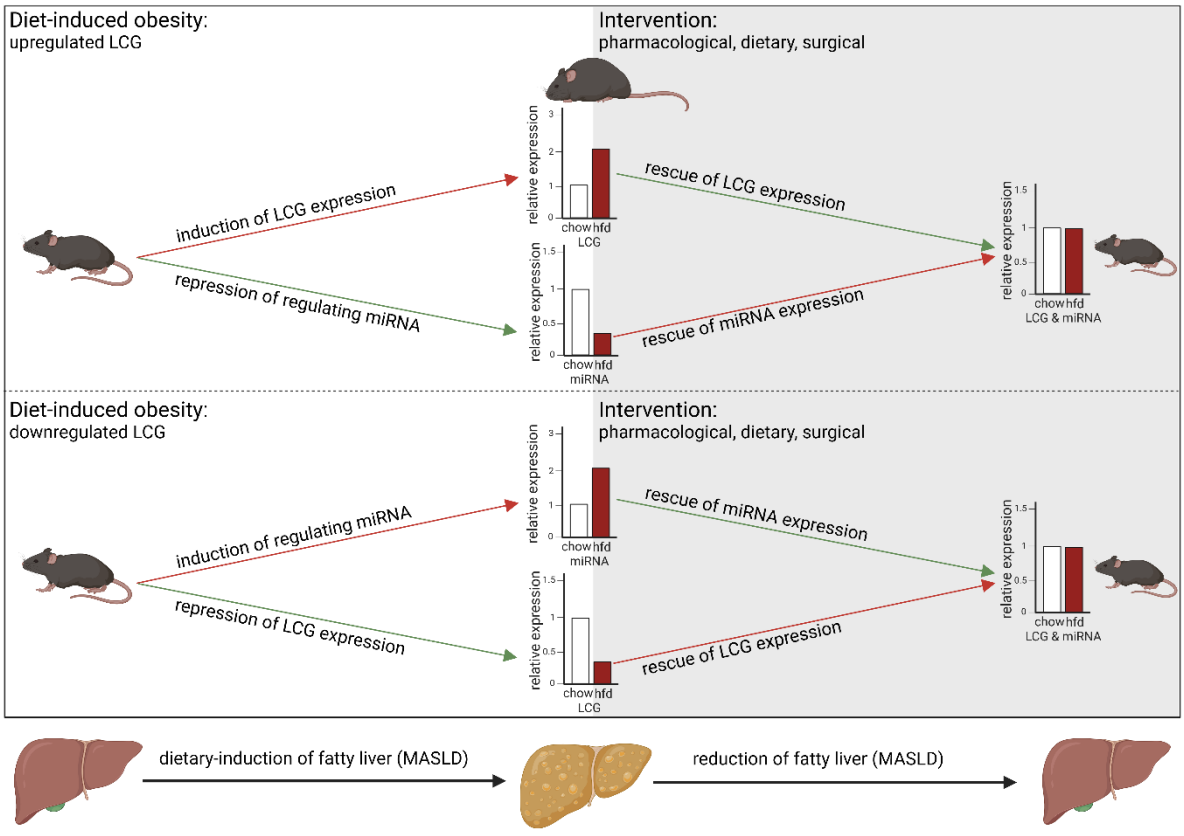

Figure 8: Schematic overview of the master regulator miRNA hypothesis. LCG expression is disrupted during the development of MASLD. Likewise, the master regulator miRNA expression must display an opposite expression pattern compared with the target LCG. Interventions, such as dietary approaches (caloric restriction, diet-switch), pharmacological treatments (exendin-4, metformin) or surgery (vertical sleeve gastrectomy) are associated with MASLD remission and partially lead to reduction in hepatic fat content. Therefore, miRNA-LCG pairs involved in MASLD progression must be reversed in expression.

miRNA to align with the concepts of RNA-interference (miRNA-induced mRNA degradation). Therefore, miRNA-LCG pairs should display a negative correlation in expression (Figure 8).
Secondly, interventions, which achieve a remission of MASLD measured by the hepatic triglyceride content, must affect miRNA and LCG expression towards the control chow-fed mice (grey box in Figure 8). The last criteria of the master regulator miRNA is the translation into the human situation. The experimental approaches use murine models and the complications of interspecies-miRNA studies are described above. Therefore, miRNA-LCG interaction must be conserved between the murine and human organism.

2. Identification of a miRNA regulating metabolic pathways independently of the LCGs

MASLD progression goes along with the dysregulation of several metabolic pathways. Currently, treatment strategies to reduce lipid accumulation in the liver are prioritized, which lead to the approval of resmetirom as first treatment for MASH. However, other metabolic pathways, including amino acid metabolism, methionine and folate cycle, urea cycle or the TCA are underrepresented, despite their known role in MASLD progression. Therefore, the aim of this project is to identify a miRNA that shows the potential in regulating key enzymes involved in those pathways. This study utilizes the knowledge generated from the first project.

3. Epigenetic regulation of the *SLC2A4* gene by DNA methylation in obesogenic VAT

Dysregulated gene expression within a single gene of the VAT, such as the adiponectin gene, contributes to systemic insulin resistance and affects blood glucose homeostasis. The insulin-dependent glucose transporter *SLC2A4* is downregulated in the adipose tissue of obese subjects when compared to normal weighted subjects and its role in regulating insulin sensitivity of the liver and muscle are well established, since *SLC2A4*-dependent glucose uptake is linked with de novo lipogenesis in VAT.
However, the molecular mechanism behind *SLC2A4* downregulation is incompletely understood. Therefore, an epigenetic regulation by DNA methylation within the *SLC2A4* gene is hypothesized that might contribute to the downregulation.

4. Material & Methods

In the following all used chemicals, extraction kits, primer sequences, enzymes and consumables are listed as well as animal models performed. Additionally, a short paragraph summarizing the benefits and of R-packages used in the analysis is supplied.

4.1. Materials

4.1.1. Equipment

Table 2: List of used equipment

Equipment	**manufacturer**
Autoclave, CX-65	Systec GmbH, DE
Cell culture clean bench	Thermo Fisher Scientific Inc., US
Centrifuge 5425	Eppendorf SE, DE
Centrifuge 5430R	Eppendorf SE, DE
ChemiDoc	Bio-Rad Laboratories Inc., US
Criterion™ Cell	Bio-Rad Laboratories Inc., US
Dionex UltiMate 3000 RSLC System	Thermo Fisher Scientific Inc., US
Fisherbrand Bead Mill 24 Homogenizer	Fisher Scientific, DE
Fixed-angle Rotor FA-45-48-11 (for 1.5 ml and 2.0 ml tubes)	Eppendorf SE, DE
Fixed-angled Rotor F-35-6-30 (for 15 ml and 50 ml tubes)	Eppendorf SE, DE
Flake ice maker	Ziegra Eismaschinen GmbH, DE
Incubator Hood TH 30	Edmund Bühler GmbH, DE
Incubator with CO_2 CellXpert	Eppendorf SE, DE
Incubator with CO_2 Hera cell 150	Thermo Fisher Scientific Inc., US
Light microscope Axiovert 40	CFL Zeiss, DE
Magnetic stirrer, MR 2002	Heidolph Instruments, DE
Mastercycler Nexus Gradient	Eppendorf SE, DE
Mastercycler Nexus X2 eco	Eppendorf SE, DE
Microplate reader CLARIOstar Plus	BMG Labtech, DE
Microwave	emens, DE
Mini centrifuges	VWR, US; Sarstedt AG, DE
Minispec LF110	Bruker, US
Multichannel pipette, 10 uL, 300 uL	Eppendorf SE, DE
Multifuge 35A Heraeus	Fisher Scientific, DE
Multistep pipette Multipette E3	Eppendorf SE, DE
Multistep pipette Pipetman P20M, 2-20 uL	Gilson, US
NanoDrop One spectrophotometer	Thermo Fisher Scientific Inc., US
Neubauer counting chamber	VWR, US
NextSeq 2000 System	Illumina, US
PCR Workstation	VWR, US
PerfectBlueTM gel system, Mini L (12 x 14 cm) Peqlab	VWR, US
PerfectBlueTM gel system, Mini S (7 x 8 cm) Peqlab	VWR, US
pH meter PB-11	Sartorius AG, DE

Pipettes, 2.5, 10, 20, 100, 200, 300, 1000 uL	Eppendorf SE, DE
Pipetus Akku	Hirschmann, DE
Plate shaker Titramax 100	Heidolph Instruments, DE
Power supply PowerPac™	Bio-Rad Laboratories Inc., US
Preci on scale, PCB 1000-1	KERN
Preci on scale, SE 203 LR	VWR, US
PyroMark Q48 Autoprep pyrosequencer Quenzy and cartridges	QIAGEN GmbH, NL
Q Exactive Plus Hybrid Quadrupol-Orbitrap™ mass spectrometer	Thermo Fisher Scientific Inc., US
QuantStudio 5 Real-Time PCR System	Applied Biosystems, US
Qubit™ 4 Fluorometer	Thermo Fisher Scientic, US
Surgical instruments	Fine Science Tools, DE
Swing-bucket rotor Rotor A-2-MTP	Eppendorf SE, DE
Swivel roller mixer RS-TR 5	Phoenix Instrument GmbH, DE
ThermoMixer C	Eppendorf SE, DE
Trans-Blot® Turbo™ Transfer System	Bio-Rad Laboratories Inc., US
Veiti Thermal cycler	Applied Biosystems, US
Vortex mixer 7-2020	neoLab Migge, DE
Vortex mixer, mini	Greiner Bio-One, AT
Water bath Grant OLS 200	Grant Instruments, UK

4.1.2. Kits

Table 3: List of used kits

Kit	**manufacturer**
Bio-Plex® Cell lysis Kit	Bio-Rad Laboratories Inc., US
Dual-Glo® Luciferase Assay system	Promega GmbH, US
EpiTect Fast DNA Bisulfite Kit	QIAGEN GmbH, NL
Fast DNA Tissue Kit	QIAGEN GmbH, NL
Fast Sort Universal SYBR Green Master Mix	Roche Applied Science, DE
Fast start advanced Master Mix for TaqMan	Thermo Fisher Scientific Inc., US
Glucose Uptake-Glo™ Assay	Promega GmbH, US
High Capacity cDNA Reverse Kit	Life Technologies, US
miRNeasy Mini Kit	QIAGEN GmbH, NL
Pierce® BCA Protein Assay Kits	Thermo Fisher Scientific Inc., US
Plasmid Midi Kit	QIAGEN GmbH, NL
Plasmid Mini Kit	QIAGEN GmbH, NL
PrimeTime\texttrademark Mastermix	Integrated DNA Technologies, US
PyroMark PCR Kit	QIAGEN GmbH, NL
QIAamp DNA Mini Kit	QIAGEN GmbH, NL
QIAamp Fast DNA Tissue Kit	QIAGEN GmbH, NL
QIAprep spin Miniprep Kit	QIAGEN GmbH, NL
QuantSeq 3’ mRNA-Seq V2 Library Prep Kit FWD with UDI	Lexogen GmbH, AT
Qubit dsDNA BR Assay	Thermo Fisher Scientific Inc., US
Qubit dsDNA HS Assay	Thermo Fisher Scientific Inc., US
Quick Ligation Kit	New England Biolabs, US
Quick-DNA® Microprep Plus Kit	Zymo research GmbH, DE
REPLI-g Mini Kit	QIAGEN GmbH, NL

RevertAid cDNA synthesis Kit	Thermo Fisher Scientific Inc., US
RNase-Free DNase Set	QIAGEN GmbH, NL
SuperScript® IV VILO®	Thermo Fisher Scientific Inc., US
TaqMan TM Advanced miRNA cDNA synthesis Kit	Thermo Fisher Scientific Inc., US
Triglyceride Colorimetric Assay Kit	Cayman Chemical Company, US
WIZARD®SV Gel and PCR Clean-up system	Promega GmbH, US

4.1.3. Consumables

Table 4: List of used consumables

Consumable	**manufacturer**
10 % Criterion™ TGX Stain-Free™ Protein gel, 18 well	Bio-Rad, US
6-well culture plates BF-3001C Collagen I	Flexcell textregistered Inc., US
Adhesive PCR seal MicroAmp™ optical adhesive film	Applied Biosystems, US
Aluminium foil (0.03 mm x 300 mm x 100 m), Labsolute	Th.Geyer GmbH, DE
Biosphere Filter tips 1000, 300, 200, 100, 20, 10, & 2.5 µL	Sarstedt AG, DE
Cell culture flask T50, T75, standard, ventilated cap	Sarstedt AG, DE
Cell culture plates: 6-well, 12-well, 96-well; TC-plates standard	Sarstedt AG, DE
Bulk Beads 1.4 mm Zirconium oxide beads	Precellys, FR
Cell scaper	Sarstedt AG, DE
Combitips advanced/Plus Biopur R 0.1, 0.2, 0.5, 2.5, 5.0, and 10 mL	Eppendorf SE, DE
Falcon tubes 10 mL, 50 mL	Sarstedt AG, DE
Filtropur S 0.2 micro M	Sarstedt AG, DE
Gelloader pipette tips, 200 µL	Sarstedt AG, DE
Microplate, 96-well, F, transparent	Sarstedt AG, DE
Microplate, 96-well, PS, F bottom, transparent	Greiner Bio-One, AT
Microtubes PCR-PT for tissue disruption, 2 mL	Sarstedt AG, DE
Microtubes, low binding,1.5 mL, 2 mL	Sarstedt AG, DE
Pasteur pipettes	Th.Geyer GmbH, DE
PCR 8-stripes, 0.2 mL	Sarstedt AG, DE
PCR plates, 0.2 mL	Th.Geyer GmbH, DE
Petri dish with cams, 100 mm	Sarstedt AG, DE
Plating spatula	Sarstedt AG, DE
PyroMark Q48 Absorber Strips	QIAGEN GmbH, NL
PyroMark Q48 advancedCpG Reagents	QIAGEN GmbH, NL
PyroMark Q48 Discs	QIAGEN GmbH, NL
PyroMark Q48 Magnetic Beads	QIAGEN GmbH, NL
Qubit Assay tubes, 0.5 mL	Life Technologies, US
Reactiontubes SafeSeal 5 mL, 2 mL, 1.5 mL	Sarstedt AG, DE
Scalpel, disposable	Feather Safety Razor Co.Ltd, JP
Serological pipettes 25 mL, 10 mL, 5 mL, 2.5 mL, 1 mL	Sarstedt AG, DE
Trans-Blot Turbo Midi 0.2 µm PVDF Transfer Pack	Bio-Rad, US

4.1.4. Chemicals

Table 5: List of used chemicals

Chemical	manufacturer
2-aminoadipic acid	Sigma Aldrich, US
3-Isobutyl-1-methylxanthin	Sigma Aldrich, US
Acetic acid	Merck KGaA, DE
acetone	Carl Roth, DE
acetonitrile	Sigma Aldrich, US
Agarose Broad Range	Carl Roth, DE
BC isotone saline solution, SI 0.9 per nt	Berlin-Chemie AG, DE
Bovine serum albumin (BSA)	Sigma Aldrich, US
chloroform	Carl Roth, DE
cOmplete™, Mini, EDTA-free Protease-Inhibitor-Cocktail	Roche Applied Science, DE
DEPC treated water	Life Technologies, US
Dexamethasone	Sigma Aldrich, US
Dimethyl sulfoxide (DMSO)	AppliChem GmbH, DE
DNA Away	Thermo Fisher Scientific Inc., US
EDTA solution, pH 8.0	AppliChem GmbH, DE
Ethanol 70 %, denatured	Carl Roth, DE
Ethanol 99.8 %, denatured	Carl Roth, DE
Ethanol 99.8 %, pure	Carl Roth, DE
Gel Loading Dye, Blue	New England Biolabs, US
GeneRuler 100 bp DNA Ladder	Life Technologies, US
GlycoBlue texttrademark	Thermo Fisher Scientific Inc., US
GoTaq G2 Green Master Mix	Promega GmbH, US
IBMX BioUltra 99 % 100mg	Th.Geyer GmbH, DE
insulin: Humalog 100 IE/mL	Eli Lilly and Company, US
Isopropanol, pure	Thermo Fisher Scientific Inc., US
Lipofectamin 2000	Life Technologies, US
Lipofectamin RNAiMAX	Thermo Fisher Scientific Inc., US
Metabolomics Amino Acid Mix Standard	Cambridge Isotope Laboratories, US
methanol	Carl Roth, DE
Penicillin Streptomycin 100 mL (cell culture)	Life Technologies, US
PrimeTime® Gene Expression Master Mix	Integrated DNA Technologies, US
QIAzol Lysis Reagent	QIAGEN GmbH, NL
RNase Inhibitor	Life Technologies, US
RNase ZAP	Th.Geyer GmbH, DE
S-adenosylmethionine (SAM)	New England Biolabs, US
Sodium chloride (NaCl), pure, solid	AppliChem GmbH, DE
sodium dodecyl sulfate	Carl Roth, DE
Sodium oleate, O7501	Sigma Aldrich, US
Sodium palmitate, P9767	Sigma Aldrich, US
SuperScript texttrademark IV VILO texttrademark	Thermo Fisher Scientific Inc., US
SYB texttrademark Safe DNA Gel Stain	Thermo Fisher Scientific Inc., US
TaqMan Fast Advanced Master Mix	Thermo Fisher Scientific Inc., US

Tris-HCl	Carl Roth, DE
Triton-X	Sigma Aldrich, US
Trizma Base, 2-Amino-2-(hydroxymethyl)-1,3-propanediol	Sigma Aldrich, US
Trypan Blue Solution, 0.4 %	Sigma Aldrich, US
trypsin TrypLE Exp.Enzyme (1X) no phenol red	Life Technologies, US

4.1.5. Cell culture media, buffers and solutions

Table 6: List of used cell culture mdia and selection media for bacterial cultures

Name	Ingredients [per 250 ml]	Manufacturer	Catalog number
HepG2-maintenance medium (1.5 g/l glucose, 10 % FBS, 1 % P/S)	139.1 ml DMEM, no glucose 83. 4 ml DMEM GlutaMAX™ 25 ml FBS 2.5 ml penicilline/streptomycin	Life Technologies, US, Gibco™	11966025 10569010
3T3-proliferation medium (4.5 g/l glucose, 10 % FBS, 1 % P/S)	222.5 ml DMEM GlutaMAX™ 25 ml FBS 2.5 ml penicillin/streptomycin	Life Technologies, US, Gibco™	11966025
3T3-initiation medium	3T3-proliferation medium 25 µM dexamethasone 0.5 µM 3-isobutyl methylxanthine 1 µg/mL insulin	See above	See above
3T3-differentiation medium	3T3-proliferation medium 1 µg/mL insulin	See above	See above
HEK-maintenance medium (4.5 g/l glucose, 10 % FBS, 1 % P/S)	222.5 ml DMEM GlutaMAX™ 25 ml FBS 2.5 ml penicillin/streptomycin	Life Technologies, US, Gibco™	10569010
HepG2-transfection medium (1.5 g/l glucose, 10 % FBS)	139.1 ml DMEM, no glucose 83. 4 ml DMEM GlutaMAX™ 25 ml FBS	Life Technologies, US, Gibco™	11966025 10569010
HEK-transfection medium (4.5 g/l glucose, 10 % FBS)	222.5 ml DMEM GlutaMAX™ 25 ml FBS	Life Technologies, US, Gibco™	11966025
Opti-MEM™		Life Technologies, US	31985062
Fast-Media® Zeo Agar	A pouch per 200 mL water with zeocin	InvivoGen, US	fas-zn-1
Fast-Media® Amp Agar	A pouch per 200 mL water with ampicillin	InvivoGen, US	fas-am-1
Fast-Media® Zeo TB	A pouch per 200 mL water with zeocin	InvivoGen, US	fas-zn-s
Fast-Media® Amp TB	A pouch per 200 mL water with ampicillin	InvivoGen, US	fas-am-s

Table 7: List of used commercial buffers

Name	Manufacturer
Phosphate-buffered aline	Thermo Fisher Scientic, US
EDTA solution, pH 8.0	Carl Roth, DE
3x SDS Blue Loading Dye	New England Biolabs, US
NEBuffer 2x	New England Biolabs, US
Restore R PLUS Western Blot Stripping Buffer	Thermo Fisher Scientic, US
TE Buffer (1x, 20x)	Promega GmbH, US

Table 8: List of used self-made buffers

Name	Ingredients
Milk-TBS	5 % milk powder in TBS
RIPA buffer	150 mM NaCl; 50 mM Tris (pH 7.4); 0.25 % Sodium deoxycholate; 1 % NP-40; 1 mM EDTA (pH 8.0)
Running buffer (Western Blot)	0.25 M Tris; 1.92 M Glycin; 1 % SDS
TAE buffer (50x)	2 mM Tris; 0.05 M EDTA (pH 8.0); 5.71 % glacial acetic acid
TBST buffer (10x), pH 7.4	100 mM Tris; 1.5 M NaCl
TBS buffer (1x), pH 7.4	10 x TBS; 0.1 % Tween® 20

4.1.6. Master mixes and enzymes

Table 9: Master mixes and transfection reagents

Buffer/Master Mix name	Ingredients	Final volume
DNA-extraction buffer	- 200 µl AVE Buffer - 40 µl VXL Buffer - 1 µl DX Reagent - 20 µl Proteinase K - 4 µl RNase A (100 mg/ml)	165 µl/sample
High-Capacity RT Master Mix	- 2 µl RT Buffer - 2 µl RT Random Primers - 0.8 µl dNTP Mix (100 mM) - 1 µl MultiScribe RT (50 U/ µl) - 1 µl RNase Inhibitor - 3.2 µl nuclease-free water	10 µl/sample
miRNA Polyadenylation Master Mix	- 0.5 µl 10x Poly A Buffer - 0.5 µl ATp - 0.3 µl Poly A Enzyme - 1.7 µl Nuclease-free water	3 µl/sample
miRNA Adaptor Ligation Master Mix	- 3 µl 5x DNA ligase Buffer - 4.5 µl 50 % PEG 8000 - 0.6 µl 25x Ligation Adaptor - 1.5 µl RNA ligase - 0.4 µl nuclease-free water	10 µl/sample
miRNA Reverse Transcription Master Mix	- 6 µl 5x RT Buffer - 1.2 µl dNTP Mix - 1.5 µl 20x Universal RT Primer	15 µl/sample

	-	3 µl 10x RT Enzyme Mix	
	-	3.3 µl nuclease-free water	
miR-Amp Reaction Master Mix	-	25 µl 2x miR-Amp Master Mix	45 µl/sample
	-	2.5 µl 20x miR-Amp Primer Mix	
	-	17.5 µl nuclease-free water	
mRNA RT-qPCR TaqMan Master Mix	-	5 µl TaqMan™ Fast Advanced Master Mix, no UNG	6 µl/reaction
	-	0.5 µl of TaqMan Assay	
	-	0.5 µl nuclease-free water	
PrimeTime RT-qPCR Master Mix	-	5 µl PrimeTime™ Gene Expression Master Mix	6 µl/reaction
	-	0.5 µl of PrimeTime™ Probe Assay	
	-	0.5 µl nuclease-free water	
SYBR green RT-qPCR Master Mix	-	5 µl FastStart Universal SYBR green Master	6 µl/reaction
	-	0.5 µl forward RT-qPCR primer	
	-	0.5 µl reverse RT-qPCR primer	
MirVana miRNA mimic transfection reagent	-	2.5 µl Lipofectamine® RNAiMAX	500 µl/transfection
	-	2.5 µl 10 mM MirVana miRNA mimic	
	-	495 µl Opti-MEM™	
bis-PCR Master Mix	-	12.5 µl PyroMark PCR MasterMix	24 µl/reaction
	-	2.5 µl CoralLoad concentrate	
	-	0.5 µl forward primer (final 0.2 µM)	
	-	0.5 µl reverse primer (final 0.2 µM)	

Table 10: List of used enzymes

enzyme	**manufacturer**
HindIII-HF	New England Biolabs, US
M.SssI CpG methyltransferase	New England Biolabs, US
NcoI-HF	New England Biolabs, US
Proteinase K	QIAGEN GmbH, NL
Pyrophosphatase inorganic (0.1 U/µl) 10 U	Life Technologies, US
RNase A	QIAGEN GmbH, NL

4.1.7. Antibodies

Table 11: List of used antibodies

Name	**Host organism**	**Reactivity**	**Manufacturer**	**ID**
Anti-Glut4	Mouse	H, M, R, P	Proteintech, USA	66846-1-Ig
Anti-Hsp90	Rabbit	H, R, M, Mk		
Anti-mouse-HRP conjugate	Goat	M	Agilent Technologies (DAKO), USA	P044701
Anti-rabbit-HRP conjugate	Goat	Rb	Agilent Technologies (DAKO), USA	P044801

H = human, M = mouse, R = rat, P = pig, Mk = monkey, Rb = rabbit

4.1.8. Materials used to measure gene expression with RT-qPCR: MirVana miRNA mimics, oligonucleotides for RT-qPCR and bisulfite PCR and PrimeTime/TaqMan assays

Table 12: MirVana miRNA mimic IDs used in HepG2 transfections

Name	Species	Manufacturer	ID
miR-149-5p	hsa/mmu	Thermo Fisher Scientific Inc., US	MC12788
miR-21-5p	hsa/mmu	Thermo Fisher Scientific Inc., US	MC10206
Negative control #1	none	Thermo Fisher Scientific Inc., US	4464058

Table 13: IDT PrimeTime assays used in RT-qPCR

Gene	IDT assay ID	species	Fluorophore
Acaca	Mm.PT.58.12492865	mmu	FAM
Appl2	Mm.PT.58.32451463	mmu	FAM
Arhgap24	Mm.PT.58.10972373	mmu	FAM
Cd82	Mm.PT.58.9412828	mmu	FAM
Cobll1	Mm.PT.58.7661485	mmu	FAM
Ddx3x	Mm.PT.58.32669527	mmu	FAM
DDX3X	Hs.PT.58.4941778	hsa	FAM
Fasn	Mm.PT.58.14276063	mmu	FAM
Gk	Mm.PT.58.32154073	mmu	FAM
HPRT	Hs.PT.58v.45621572	hsa	Cy5
Hprt	Mm.PT.39a.22214828	mmu	Cy5
Inhbe	Mm.PT.58.11376306.g	mmu	FAM
INHBE	Hs.PT.58.40955789.g	hsa	FAM
Mlxipl	Mm.PT.56a.33592172	mmu	FAM
Myc	Mm.PT.58.28494642	mmu	FAM
Rapgef4	Mm.PT.58.19072276	mmu	FAM
Rplp0	Mm.PT.58.43894205	mmu	Cy5
Slc2a1	Mm.PT.58.7590689	mmu	FAM
Slc2a4	Mm.PT.58.9683859	mmu	FAM
Smim13	Mm.PT.58.16124434	mmu	FAM
SMIM13	Hs.PT.58.15690992	hsa	FAM
Tap1	Mm.PT.58.33370832	mmu	FAM

Table 14: SYBR green RT-qPCR primer sequences

Gene	Primer orientation	sequence	species
	forward	CCAGAGGTGATGGGTGACG	mmu
Gpc1	reverse	TGATCTTGAGCTGCATAATCTGC	mmu
	forward	TCTGGCTCCGTGTCTTCACT	mmu
miR-149-5p	reverse	Universal Primer	mmu
	forward	TCGCTGATGCACTGCCTATG	mmu
Pparg	reverse	GAGAGGTCCACAGAGCTGATT	mmu
	forward	GCAGCCACCATCTAGCCTG	mmu
Srebf1	reverse	CAGCAGTGAGTCTGCCTTGAT	mmu

Table 15: TaqMan Assay IDs used in RT-qPCR

Gene	TaqMan ID	species	Fluorophore
ACACA	Hs01046047_m1	hsa	FAM
CASC3	Hs00201226_m1	hsa	VIC
FASN	Hs01005622_m1	hsa	FAM
miR-149-5p	477917_mir	mmu/hsa	FAM
miR-21-5p	477975_mir	mmu/hsa	FAM
miR-24-3p	477992_mir	mmu/hsa	FAM
MLXIPL	HS00975714_m1	hsa	FAM
SLC2A4	HS00168966_m1	hsa	FAM

Table 16: Oligonucleotides used in bis-PCR to amplify Slc2a4 region of interest and sequencing primer used in pyrosequencing

Gene	orientation	5' modification	usage	sequence	Species
Slc2a4	forward	none	bis-PCR	GGAGGGATGGTAGTGAGTGG	mmu
slc2a4	reverse	biotin	bis-PCR	CCCCCCAACTCAAATTTCCT	mmu
Slc2a4		none	pyrosequencing	GTAGTGAGTGGTGTGA	mmu
SLC2A4	forward	none	bis-PCR	AGGGTAGGAAGGTAGTGTGA	hsa
SLC2A4	reverse	biotin	bis-PCR	CCACCCCCACTCCTAACC	hsa
SLC2A4		none	pyrosequencing	GGAAGGTAGTGTGAG	hsa

Table 17: Primer sequences used for amplification of the Slc2a4 from murine genomic DNA and sequencing primer for pCpG-free vector sequencing

Gene	orientation	usage	sequence	Species
Slc2a4_overhang	forward	Genomic PCR	CATAAGCTTGAGGAGGGATGGTAGTGAGTG	mmu
slc2a4_overhang	reverse	Genomic PCR	AGTCCATGGGTGGGTGGAGGGGCAGAG	mmu
vector seq	sense	sequencing	TAAATCTCTTTGTTCAGCTCTCTG	none

4.2. Animal experiments

In the following chapters all used animal models will be explained. Additionally, this serves as giving credit to the researchers and colleagues conducting the work and taking care about the animals. Data that were not collected by myself will be indicated in this method section as well as in the figure caption where the data will be shown.
All animal experiments were conducted to the ethical guidelines.

4.2.1. Longitudinal mouse model of diet-induced obesity (DIO)

Male C57BL/6N mice were ordered from Charles River at 4 weeks of age and were housed under constant temperature (22 ± 1 °C) with a normal 12-h light/dark cycle. Mice had ad libitum access to water and food. After one week of acclimation, mice were randomized into two groups of similar body weights. Mice were fed consistently ad libitum with either a chow diet (=control group; Breeding Diet

1314 obtained from Altromin, Germany) or a 60% high-fat diet (=treated group; HFD, D12492, Research Diets, New Brunswick, NJ, USA) for 1, 2, 4, 5, 6, 7, 8 or 12 weeks (Figure 9). At each indicated time point, an intraperitoneal glucose tolerance (ipGTT) test is performed. On the day of sacrifice, mice were anesthetized with ketamine/xylazine (120 mg/kg ketamine and 16 mg/kg xylazine) and blood was collected by cardiac puncture. Plasma was prepared from EDTA-blood by centrifugation for 15 min at 2000× g and stored at −80 °C. Subsequently, mice were perfused with Krebs-Ringer solution with 1 U/mL heparin. VAT and liver tissue were dissected and immediately frozen and stored at −80 °C. The experiments involving the handling of mice were non-blinded.
Tissue and blood collection, ipGTT, handling and sacrifice of mice were conducted by Cathleen Geißler, Martina Grohs, Christin Krause and Henriette Kirchner. Further information on ipGTT and insulin ELISA are accessible in (Geißler et al. 2022)

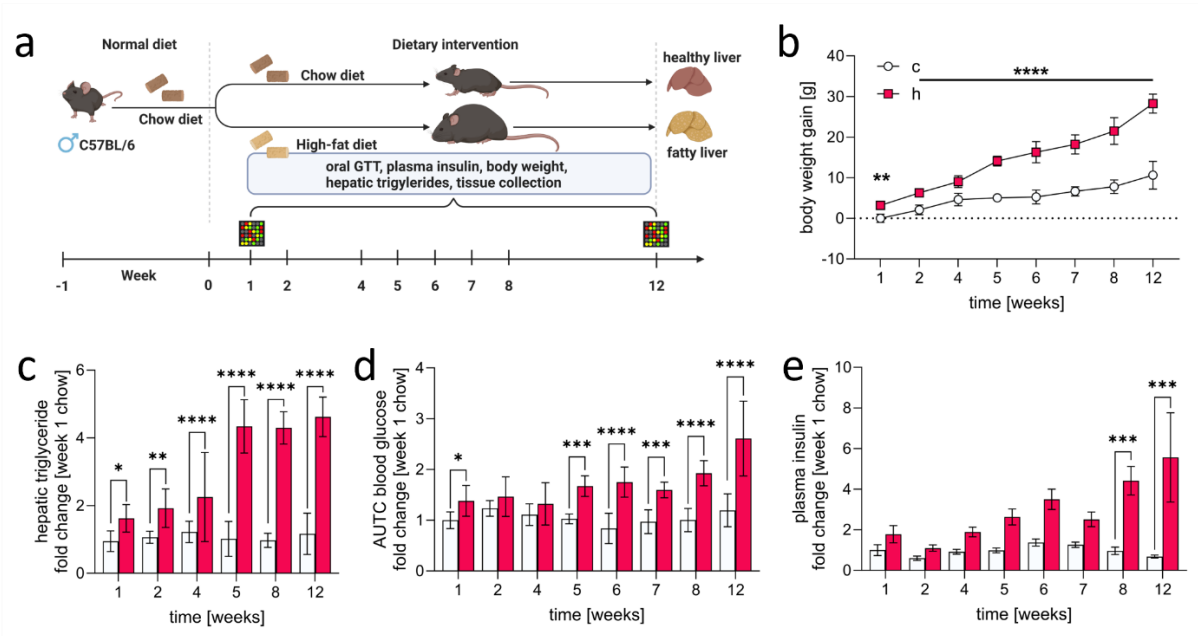

Figure 9: Overview of the longitudinal mouse model for DIO. a: Schematic feeding regime. Mice are either fed a standard chow-control or hfd over a period of 12 weeks, after a one week acclimatisation phase to the housing facility. At week 1, 2, 4, 5, 6, 7, 8, and 12, oral GTTs are performed and sub cohorts are sacraficed for tissue collection and subsequent downstream analysis. At week 1 and 12, gene arrays are performed from liver. b: Body weight gain [in grams] over the period for chow and hfd animals. c: Hepatic triglyceride content for week 1, 2, 4, 5, 8 and 12 normalized to chow week 1. Multiple, two-sided, unpaired t test is performed on the absolute, unnormalized hepatic triglyceride content (n = 8). d: Area under the curve (AUTC) from the oral GTT normalized to chow week 1 (n = 7 - 16). e: Plasma insulin levels normalized to week 1 (n = 5 - 8). Mean and standard deviation are shown. * = $p < 0.05$, ** = $p < 0.01$, *** = $p < 0.001$, **** = $p < 0.0001$.

4.2.2. Weight-loss intervention mouse models

The following experiments are conducted at the Helmholtz Zentrum München by Sonja C. Schriever and colleagues and are therefore briefly described. Permission to use the presented data in this work are kindly granted on request by Sonja C. Schriever.
30 C57BL/6J mice are purchased from Janvier Labs (Saint-Berthevin, FR) and are housed on a 12 h light-dark cycle with free access to water and standard chow diet (Altromin, #1314). Then, 24 animals are fed a high-fat diet (Research Diets, D12331) to promote diet-induced obesity for 22 weeks and 6 animals are maintained on the chow diet as control. Then, the hfd-fed animals underwent different weight-loss interventions for 10 days, either receiving exendin-4 treatment, caloric restriction or a diet-switch from hfd back to chow. A group of 6 animals are maintained on hfd ad libitum. Subsequently,

animals are sacrificed after an overnight fast and liver tissue is collected for miRNA and gene expression analysis in qPCR, for a miRNA microarray and quantification of hepatic triglyceride content Figure 13(Figure 10 & Figure 13).

4.2.3. Metformin reversal mouse study

Mouse handling and conception of the study design was conducted by Natalie Taege. IpGTT was performed by Natalie Taege, Martina Grohs and Jan Hendric Britsemmer. Mice sacrifice and tissue collection were done by Natalie Taege, Christin Krause, Henriette Kirchner and Jan Hendric Britsemmer. In brief, 5-weeks old male C57BL/6N mice are obtained from Charles River. Mice are housed on a 12-hour light/12-hour light/dark cycle. Mice had access to water and food ad libitum. After one week of acclimation, mice are randomized into two groups with similar body weight. Then, one group of animals received either a chow diet (= control group; Breeding Diet 1314 obtained from Altromin, DE) or 60 % high-fat diet (= treated group; HFD, D12492, Research Diets, US) for 12 weeks ad libitum. Subsequently, hfd-fed mice are randomized into two sub cohorts with similar body weights and for an additional 6 weeks, one of these hfd-fed sub cohort is treated with metformin at 250 mg/kgBW/day via the drinking water. Access to drinking water was ad libitum. Water intake is monitored on a daily base and the metformin doses are adjusted consequently. At the day of sacrifice, mice are anesthetized with isoflurane (IsoFlo®, Zoetis, Belgium) and killed by decapitation. Tissues are dissected and directly snap-frozen and stored at -80°C for further usage. All procedures were in accordance to the local animal welfare guidelines and the EU Directive 2010/63/EU on the protection of animals used for scientific purposes approved. All procedures were approved by the MELUR Schleswig–Holstein, Germany (V 242-59721/2016). For further information, this mouse model is published in (Geißler et al. 2022).

4.2.4. Vertical sleeve gastrectomy

Mouse handling and conception of the study design was conducted by Cathleen Geißler and Anne-Marie Neumann. Surgery procedure is performed as described in (Neumann et al. 2021) and mouse model is published in (Geißler et al. 2022).
In brief, male C57BL/6N mice are purchased from Charles River and are maintained on a 60 % hfd for 12 weeks (HFD, D12492, Research Diets, USA) on a constant 12-hour light/12-hour dark cycle at 22 ± 1°C. Mice had access to food and water ad libitum. Then, mice are separated and single-housed for two weeks prior to surgery. Three days prior to surgery, mice are prepared by feeding a liquid diet (Nutricia Fortimel, Nutricia, Germany) and one day before surgery, mice are randomized into a VSG and sham-surgery group. After overnight fasting, mice are anaesthetized with isoflurane in oxygen (5 % for induction, 1.5 % throughout the surgery) and subcutaneously injected with 1 mg/kg meloxicam and 8 mg/kg gentamicin in 1 ml 0.9 % NaCl. Subsequently, mice underwent the surgical procedure and about 80 % of the stomach are removed. For the sham-surgery, stomach size is not decreased in size. Animals received analgesia (Meloxicam, 1 mg/kg s.c.) for maximally five days post-surgically. Mice are fed liquid diet for two days exclusively. From three days after surgery, mice received hfd again. Nine and 35 days after surgery mice are sacrificed by cervical dislocation and liver tissue is dissected. Tissue is immediately frozen and stored at -80°C. All procedures are approved by the MELUR Schleswig–Holstein, Germany.

4.3. Cell culture experiments

4.3.1. HepG2 cell culture

For maintenance, HepG2 cells are cultivated in HepG2-maintenance medium in T75 flasks (Sarstedt AG, DE) at 37 °C and 5 % CO_2. When cells reach confluence, medium is discarded and cells are washed with 10 ml cell-culture grade PBS. Subsequently, cells are detached from the cell culture surface using 3 ml trypsine (Gibco, Thermo Fischer Scientific, US) for 10 to 15 min at 37 °C and 5 % CO_2. Trypsin reaction is stopped using 7 ml of HepG2-maintenance medium. Then HepG2 cells are either seeded into a new T75 flask in a ratio of 1:5 or seeded into plates for experiments.
Fresh medium is supplied every 2 to 3 days.

4.3.2. 3T3 cell culture

For maintenance, undifferentiated 3T3 preadipocytes are cultivated in 3T3-proliferation medium at 37 °C and 5 % CO_2 in a T75 flask (Sarstedt AG, DE). When cells reach 70 % confluence, medium is removed and cells are washed in 10 ml cell-culture grade PBS (Gibco, Thermo Fisher Scientific, US). Then, cells are detached from cell culture surface with 3 ml trypsin for 3 min at 37 °C and 5 % CO_2. Trypsin reaction is stopped using 7 ml of proliferation medium and are either seeded into a new T75 flask (Sarstedt AG, DE) or are seeded into plates for experiments.
Fresh proliferation medium is supplied every 2 to 3 days.

4.3.3. HEK293T cell culture

For maintenance, HEK293T cells are cultivated in HEK-maintenance medium at 37 °C and 5 % CO_2 in a T75 flask (Sarstedt AG, DE). At 70 % confluence, medium is removed and cells are washed in 10 ml cell-culture grade PBS (Thermo Fisher Scientific, US). Then, cells are detached from cell culture surface with 3 ml trypsin for 3 min at 37 °C and 5 % CO_2. Trypsin reaction is stopped using 7 ml of proliferation medium and are either seeded into a new T75 flask (Sarstedt AG, DE) or are seeded into plates for experiments.
Fresh proliferation medium is supplied every 2 to 3 days.

4.3.4. Metabolic stimulation of HepG2 cells

HepG2 cells are seeded into 6-well plates (Sarstedt AG, DE) and cultured in HepG2-maintenance medium for 24 h at 37 °C and 5 % CO_2 until 70 % confluence is reached. Then, the old medium is removed and replaced with fresh medium including either 0.5 mM palmitate/oleate (ratio 1:2), 50 mM fructose, 50 mM fructose and 25 mM glucose, or 50 µM myristic acid. For palmitate/oleate and myristic acid medium substituted with 7.5 % BSA is used as control and for fructose and glucose stimulation normal HepG2 maintenance medium. Cells are incubated for 24 h at 37 °C and 5 % CO_2 with the perspective treatment and are then harvested for RNA extraction. Experiments are performed in technical triplicates and at three different days and cell passages.

Metabolic stimulation of HepG2 cells with palmitate/oleate, glucose and glucose/fructose are conducted by Alison-Michelle Naujack.

4.3.5. Differentiation and palmitate/oleate treatment of 3T3 cells

$2x10^4$ of 3T3-preadipocytes are seeded in duplicates into 12-well cell culture plates for DNA and RNA extraction (Day -4) and are cultured in 3T3-proliferation medium for 4 days at 37 °C and 5 % CO_2 until confluence is reached. Then, proliferation medium is removed and replaced by 3T3-initiation medium (Day 0) and are either treated with 0.5 mM palmitate/oleate (ratio 1:1) or 7.5 % BSA for three days at 37 °C and 5 % CO_2. Afterwards, 3T3-initiation medium is replaced by 3T3-differentiation medium and 3T3 cells are treated again with 0.5 mM palmitate/oleate or 7.5 % BSA (Day 3). Cells are harvested at Day 5, Day 7, Day 10 and Day 14 post-initiation and repetitive palmitate/oleate treatment is conducted at Day 5, Day 7, Day 9 and Day 12 post-initiation. Harvest and extraction of DNA and RNA is performed as described in 4.4.7 and 4.4.9.

4.3.6. Preparation of MirVana miRNA mimic transfection reagent

The MirVana miRNA mimic transfection reagent is prepared directly before the transfection. Therefore, 2.5 µl of Lipofectamine® RNAiMAX is diluted in 250 µl of Opti-MEM™ medium per transfection reaction and incubated for 5 min at room temperature. Meanwhile, 2.5 µl of MirVana miRNA mimic is diluted in 250 µl of Opti-MEM™. After the 5 min incubation, Lipofectamine dilution and MirVana miRNA mimic dilution are mixed in a ratio 1:1 (250 µl Lipofectamine + 250 µl MirVana miRNA mimic) and are incubated for 20 min at room temperature resulting in 500 µl MirVana miRNA mimic transfection reagent for each transfection.
The MirVana miRNA mimic transfection reagent is directly used in the transfection.

4.3.7. Transfection of HepG2 cells with miRNAs

For miRNA-overexpression in HepG2 cells, MirVana™ miRNA Mimics are used and as a control transfection, MirVana™ miRNA Mimic, negative control #1 is used.
Therefore, approximately 2 x 10^5 cells/cm^2 of HepG2 cells are seeded into a 6-well plate (for RNA and metabolite extractions) with 2 ml HepG2-transfection medium or into a 96-well plate (for glucose uptake assay) in . Then, HepG2 cells are reversed transfected with 500 µl MirVana miRNA mimic transfection reagent (see Table 9 & 4.3.6) to reach a final MirVana miRNA mimic concentration of 10 nM of MirVana miRNA mimic per well. Cells are incubated for 48 h at 37 °C and 5 % CO_2. Then, supernatant is removed and subsequent extractions or glucose uptake assays are performed.

4.3.8. CpG-sensitive reporter gene assay in HEK293T cells

HEK293T cells are seeded into 96-well plate in triplicates using HEK293T transfection medium and are incubated for 24 h at 37 °C and 5 % CO_2 to reach 90 % confluence. Afterwards, HEK293T cells are co-transfected with either 100 ng methylated pCpGL-basic Slc2a4-inserted vector with 1 ng pRenilla

control vector or 100 ng unmethylated pCpGL-basic Slc2a4-inserted vector with 1 ng pRenilla control vector per well using 0.5 µl lipofectamine 2000. Then, cells are incubated for 24 h at 37 °C and 5 % CO_2. On the next day, old medium is discarded and cells are washed with PBS. Reporter gene assay is performed using the Dual-Glo® Luciferase Assay system (Promega, US) according to manufacturer instructions. In brief, 100 µl of Dual-Glo® Reagent are added to each well and plates are incubated for 10 min at room temperature and are agitated gently. Then, the lysate/Dual-Glo® solution is transferred into a 96-well ELISA-plate white High Bind (Sarstedt AG, DE) and Firefly luminescence signal is measured with a Microplate reader CLARIOstar Plus (BMG Labtech, DE). Afterwards, 100 µl of Dual-Glo® Stop & Glo® Reagent are added and mixed thoroughly and pRenilla luminescence signal is measured after a 10 min incubation at room temperature. The experiment is repeated three times at three different days and cell passages. For analysis, Firefly luminescence signal is normalized to pRenilla luminescence signal. Then, the mean and standard deviation is calculated of unmethylated and methylated pCpGL-basic Slc2a4-inserted signal. Fold change is calculated by normalizing the methylated signal to the unmethylated signal.

4.4. Molecular methods and extractions

4.4.1. Amplification and purification of *Slc4a2* region of interest

Prior to cloning the *Slc2a4* insert into the pCpGL-basic vector, the region of interest (ROI) is amplified from genomic murine DNA. Therefore, 250 ng of gDNA are diluted in water to a final volume of 7.5 µl and ROI is amplified using 2.5 µl of 10 µM forward and reverse Slc2a4-luci assay primer (see Table 14) and 12.5 µl of GoTaq® G2 Green Master Mix with the PCR-amplification protocol in Table 18.
The forward primer carries a 5'-overhang HindIII restriction enzyme site and the reverse primer a 5'-overhang NcoI restriction enzyme site, which is needed for the cloning and ligation into the pCpGL-basic vector.
The final length of the Slc2a4-insert is 159 nt long.

Table 18: PCR amplification protocol for Slc2a4 luciferase insert

Step	**Temperature [°C]**	**Time**	**Cycles**
Denaturation	95	2 min	1
	95	30 s	
Amplification	65	30 s	30
	72	1 min	
Termination	72	5 min	1
Hold	4	Hold	Hold

Then, amplified Slc2a4-insert is separated in a 1 % agarose gel electrophoresis at 140 V for 30 min and is purified with a Wizard® SV Gel and PCR Clean-Up System (Promega GmbH, US). In brief, Slc2a4-insert band is excised from the agarose gel under UV light and transferred into a pre-weighted 2 ml reaction tube. Reaction tube is weighted again and 10 µl of Membrane Binding Solution per 10 mg of agarose gel slice is added. Reaction tube is incubated at 65 °C until the agarose gel is completely dissolved. Then, the dissolved gel mixture is transferred onto a Minicolumn and incubated 1 min at room temperature. Minicolumn is centrifuged at 16000 g for 1 min at room temperature and flowthrough is discarded. Minicolumn is washed with 700 µl Membrane Wash Solution and centrifuged at 16000 g for 1 min at room temperature. Washing step is repeated with 500 µl Membrane Wash Solution, followed

by a membrane drying step at 16000 g for 1 min. Minicolumn is transferred onto a clean 1.5 ml reaction tube and Slc2a4-insert is eluted in 30 µl nuclease-free water. Insert concentration is measured using a NanoDrop™ One (Thermo Fisher Scientific, US) and stored at -20 °C for further experiments or directly used in the enzyme digestion.

4.4.2. HindIII and NcoI enzyme digestion of *Slc2a4*-insert and pCpG-basic plasmid

1 µg of pCpGL-basic plasmid and 500 ng of *Slc2a4*-insert are digested with 1 µl of NcoI-HF (20 units, NEB) and 1 µl of HindIII-HF (20 units, NEB), 5 µl 10x rCutSmart Buffer and to a final volume of 50 µl with nuclease-free water. Then, restriction is followed by incubation at 37 °C for 15 min and an inactivation step at 80 °C for 20 min. Afterwards, restricted plasmid and insert are separated in agarose gel electrophoresis (0.8 % for plasmid and 1 % for insert), followed by a purification using the Wizard® SV Gel and PCR Clean-Up System (Promega GmbH, US) as previously described.
50 ng of purified plasmid and 12.5 ng of insert are combined and diluted into a final volume of 20 µl with nuclease-free water. Then, 10 µl of 2x Quick Ligase Reaction Buffer and 1 µl of Quick Ligase (NEB) are added. Afterwards, ligation is performed for 10 min at room temperature.
Ligated pCpGL-basic Slc2a4-insert construct is stored at – 20 °C or directly used for transformation into OneShot E.coli bacteria. Vector map of the pCpGL-basic plasmid are shown in the supplementary information 9.8.1.

4.4.3. Transformation of OneShot E. coli with pCpG-basic Slc2a4-insert construct

One Shot™ competent E. coli bacteria (Thermo Fisher Scientific, US) are carefully thawed on ice for 20 min. After thawing, 2 µl of ligated pCpG-basic Slc2a4-insert construct is gently applied to the bacteria and 30 min incubated on ice. Then, bacteria are placed in a thermocycler at 42 °C for 45 sec to allow heat shock-induced transformation and are placed on ice again for 2 min. Afterwards, 250 µl of Invitrogen™ S.O.C. (Thermo Fisher Scientific, US) media are added to the bacteria and vial is placed in a shaking incubator at 37 °C for 60 min.
Subsequently, 50 µl of bacterial solution are plated on a zeocin-LB agar petri dish. The pCpG-basic vector carries a zeocin resistance, which only allows pCpG-basic vector positive bacteria to on the selective medium. The petri dish is incubated over night at 37 °C.
Afterwards, single colonies are picked from the plate with a pipette tip and transferred into 15 ml falcon tube containing 5 ml zeocin-LB growing medium and incubated in a shaking incubator at 37 °C for 12 hours, allowing the bacteria to amplify the pCpG-basic *Slc2a4*-inserted vector. Then, bacteria are centrifuged at 7000 g, 4 °C for 30 min. Supernatant is discarded and bacteria pellet is either stored at – 20 °C or directly processed in a Miniprep to extract pCpG-basic *Sl2a4*-inserted vector.

4.4.4. Miniprep from bacteria cells

To extract pCpG-basic Slc2a4-inserted vector from transformed One Shot™ E. coli bacteria, the QIAprep® Spin Miniprep Kit (QIAGEN) is used according to manufacturer instructions. In brief, pelleted bacterial cells are resuspended in 250 µl P1 buffer and transferred to a 1.5 ml reaction tube. Then, 250 µl of P2 buffer are added and mixed thoroughly by inverting the tube four to six times until solution is cleared. Subsequently, 350 µl of N3 buffer is added and mixed immediately and centrifuged at 17900 g

for 10 min at room temperature. 800 µl of the supernatant are transferred to a QIAprep 2.0 spin column. Afterwards, spin column is centrifuged at 17900 g for 1 min at room temperature, followed by a washing step with 500 µl of PB buffer. A second washing step with 750 µl of PE buffer is performed under same centrifugation conditions. Then, a drying centrifugation step is performed at 17900 g for 1 min at room temperature. Spin column is placed in a fresh 1.5 ml reaction tube and plasmid is eluted in 30 µl EB buffer. Plasmid concentration is measured using the Qubit 4 fluorometer (Thermo Fisher Scientific, US).
Plasmid is stored at – 20 °C until use.
100 ng of plasmid are sent to Eurofins Genomics for sequencing to check for the correct insertion of the *Slc2a4* fragment.

4.4.5. Methylation of purified pCpG-basic *Slc2a4*-insert construct

750 ng of pCpG-basic *Slc2a4*-inserted vector are in vitro methylated using 0.75 µl M.SssI CpG methyltransferase (New England Biolabs, US), 3 µl SAM (B9003S, New England Biolabs, US), 1.5 µl NEBuffer 2 (B7002S, New England Biolabs, US) and nuclease-free water to a final concentration of 15 µl. For unmethylated vector, M.SssI CpG methyltransferase is substituted with 0.75 µl nuclease-free water. Then, solution is incubated for 4 h at 37 °C, followed by an inactivation step at 65 °C for 20 min. Methylated and unmethylated vector are directly used in transfections or stored at – 20 °C until usage.

4.4.6. RNA extraction from tissue

The procedure of RNA extraction from adipose tissue or liver tissue is carried out in the same manner, but differ in the amount of weighted tissue. For RNA extractions from adipose tissue a total of 50 to 100 mg of snap frozen is weighted in. For RNA extractions from liver tissue approximately of 25 mg of snap-frozen tissue is weighted in. The tissue is transferred into 2 ml screw cap micro tubes (Sarstedt AG, DE), which are prepared with three Zirconium oxide beads (Precellys, FR) for tissue homogenization and are either stored at – 80 °C or are directly processed for RNA extraction using the miRNeasy Mini Kit (QIAGEN) according to manufacturers instructions.
In brief, tissue is homogenized in 700 µl QIAZOL using a Bead Ruptor 24 (s = 5 m/s, c = 2, t = 20 s). After a 2 minute incubation at room temperature, 140 µl of chloroform (Carl Roth, DE) are added and samples are mixed thoroughly and are incubated for 3 min at room temperature,. Then, samples are centrifuged at 12000 g, 4 °C for 15 minutes. Afterwards, approximately 300 µl of the upper phase are transferred into a new 1.5 ml reaction tube and RNA is precipitated by adding 525 µl of 100 % ethanol. Samples are mixed thoroughly and 700 µl of precipitated RNA solution is applied onto the mRNA spin column. Then, samples are centrifuged at 8000 g and room temperature for 1 min. Flow through is discarded and samples are washed with 700 µl of RWT buffer. Subsequently, an on-column gDNA digestion is performed by incubating the samples in 80 µl DNase solution (1:8, DNase : RDD Buffer) for 15 min at room temperature. Then, samples are washed with 700 ul of RWT buffer followed by two washing steps with 500 µl of RPE Buffer. Afterwards, spin columns are dried by a centrifugation step at 8000 g for 2 min at room temperature and RNA is eluted in 50 µl nuclease-free water into a new 1.5 ml reaction tube.
RNA is stored at – 80 °C for further experiments.

4.4.7. RNA extraction from cells

Supernatant of HepG2 or 3T3 cells is removed from the culture well and is replaced by 1 ml of ice-cold PBS (Thermo Fisher Scientific, US). PBS is removed and cells are washed once more in ice-cold PBS. Afterwards, cells are lysed in 700 µl QIAZOL and incubated for 5 min at room temperature. Then, cell suspension is transferred into a 1.5 ml reaction tube and are either stored at – 80 °C or directly processed for RNA extraction using the miRNeasy Mini Kit (QIAGEN) according to manufacturer instructions.
From here on, the RNA extraction follows the brief protocol described in 4.4.6.

4.4.8. DNA extraction from tissue

25 mg of snap-frozen liver or 50 mg of snap-frozen adipose tissue are weighted in and are transferred into a 2 ml screw cap micro tube (Sarstedt AG, DE), which are prepared with three Zirconium oxide beads (Precellys, FR). Tissue is homogenized in 265 µl of DNA-extraction Buffer using a Bead Ruptor 24 (s = 5 m/s, c = 3, t = 20 s) and DNA extraction is carried out with the QIAamp Fast DNA Tissue Kit (QIAGEN) according to manufacturers instructions.
In brief, homogenized tissue is incubated at 1000 rpm for 10 min at 56 °C. Then, 265 µl of MVL buffer is added to the lysate and mixed by pipetting. Afterwards, lysate is transferred onto a QIAmp Mini spin column and centrifuged at 8000 g and room temperature for 1 min. Flow-through is discarded and column is washed by adding 500 µl AW1 buffer. After centrifugation, flow-through is discarded and column is washed with 500 µl AW2 buffer. Column is centrifuged for 2 min to allow the membrane to dry. Spin column is transferred into a 1.5 ml reaction tube and DNA is eluted in 50 µl ATE buffer. DNA is stored at – 20 °C for further processing.

4.4.9. DNA extraction from cells

Supernatant of HepG2 or 3T3 cells is removed and replaced with 1 ml room temperature PBS. Afterwards, PBS is removed and fresh 1 ml PBS is added into the well. Cells are detached from the cell culture surface using a cell scraper (Sarstedt AG, DE). Cell-PBS solution is transferred into a 1.5 ml reaction tube and DNA is extracted using the QIAmp Fast DNA Tissue Kit (QIAGEN) according to manufacturers instructions.
The brief procedure is described in 4.4.8

4.4.10. Protein extraction from adipose tissue

50 mg of snap-frozen visceral adipose tissue of mice is weighted in on dry ice and transferred into a 2 ml screw cap micro tube (Sarstedt AG, DE). Then, three Zirconium oxide beads (Precellys, FR) are added to each tube with 300 µl of RIPA buffer (1:1000 proteinase inhibitors) and are homogenized using a Bead Ruptor 24 (s = 5 m/s, c = 1, t = 20 s). Afterwards, lysate is centrifuged at 18000 g for 20 min at 4 °C. Approximately 250 µl of the supernatant are transferred into a clean 1.5 ml reaction tube and a second centrifugation step with the same conditions is performed. Afterwards, approximately 200 µl of the supernatant is carefully transferred again into a clean 1.5 ml reaction tube to reduce fatty acid contamination. Therefore, the transfer from separated fatty acid layer is avoided. Then, protein concentrations are measured using the Pierce™ BCA Protein Assay Kit (Thermo Fisher Scientific, US)

according to manufacturer instructions.
In total 40 µg of total protein are aliquoted for western blot analysis. Therefore, 40 µg of total protein are diluted in RIPA buffer to a final volume of 16 µl and 7.2 µl of Blue Protein Loading Dye (New England Biolabs) and 0.8 µl of 30x reducing reagent (DTT) are added (in total 24 µl).
Aliquots are either stored at – 20 °C or directly processed in western blots.

4.4.11. Western blots of Glut4/Slc2a4 from adipose tissue

Prepared protein aliquots (see 4.4.10) are thawed on ice. When completely thawed, aliquots are incubated at 98 °C for 10 min and are cooled on ice again. Then, 24 µl of the aliquots are loaded onto 10 % Criterion™ Stain-Free™ Protein Gel (Bio-Rad), which is previously placed into a Criterion™ Cell (Bio-Rad) with running buffer. Proteins are separated at 300 V for 25 min. Then, proteins are transferred onto a Trans-Blot Turbo Midi 0.2 µm PVDF membrane (Bio-Rad) using the Trans-Blot Turbo Transfer System (Bio-Rad) with the predesigned turbo-transfer protocol for Midi membranes. Afterwards, PVDF membrane is blocked in 5 % milk powder dissolved in TBS for 1 h at room temperature. After the blocking step, PVDF membrane is incubated with anti-Glut4 antibody (1:1000 in 5 % milk powder/TBS) over night at 4 °C. Subsequently, the PVDF membrane is washed in TBS-T three times for 20 min at room temperature, followed by the incubation with the secondary antibody-horse raddish peroxidase (HRP) conjugate (1:5000 in 5 % milk powder/TBS) for one hour at room temperature. Then, membrane is washed three times with TBS-T at room temperature for 20 min each and membrane is rinsed with water. Afterwards, membrane is incubated in 2 ml Clarity Max Western ECL Substrate (1:1, luminol/enhancer solution : peroxide solution, Bio-Rad) for one min and the HRP-signal is measured using a ChemiDoc™ Touch imaging system (Bio-Rad).
For incubation with second primary antibody anti-Hsp90, PVDF membrane is washed for 5 min in TBS-T and is stripped with 5 ml RestorePLUS Western Blot Stripping buffer (Thermo Fisher Scientific, US) for 10 min at room temperature. Then, membrane is washed three times in TBST for 15 min each and blocked in 5 % milk powder/TBS. Subsequently, membrane is incubated with second primary antibody anti-Hsp90 (1:1000 in 5 % milk powder/TBST) over night at 4 °C. Washing, blocking and imaging steps are repeated as described for first primary antibody anti-Glut4.
The HRP-signals are analyzed with the Image Lab software 6.0.1 (Bio-Rad) and the background-corrected band volume is used for calculation of the Glut4/Hsp90 ratio. Then, the mean fold change of each group and standard deviation are calculated and normalized to the chow-control group mean at each week (see Equation 1). Statistics are calculated on the unnormalized Glut4/Hsp90 ratios.

Equation 1: Formula to calculate fold change of the western blot signals

$$Fold\ Change_{week\ X} = \frac{(\sum_{k=1}^{n} k = \frac{Glut4_{individual}}{Hsp90_{individual}}) \div n}{(\sum_{k=1}^{n} k = \frac{Glut4_{control}}{Hsp90_{control}}) \div n}$$

4.4.12. mRNA-cDNA synthesis

RNA concentration is measured using a NanoDrop One (Thermo Fisher Scientific, US). The following steps are carried out on ice or a cooling block. A total of 2 µg RNA is diluted in a final volume of 10 µl nuclease-free water (final concentration = 200 ng/µl).
RNA is transcribed using the High-Capacity cDNA Reverse Transcription Kit (Thermo Fisher Scientific,

US) according to manufacturers instructions. 10 µl of High-Capacity RT Master Mix are added to each well and RNA is transcribed to cDNA using the incubation protocol listed in Table 19. Afterwards, cDNA is diluted to a final concentration of 5 ng/µl for SYBR green RT-qPCR or 2.5 ng/µl for TaqMan or PrimeTime RT-qPCR.
cDNA is stored at – 20 °C.

Table 19: Incubation protocol for mRNA-cDNA synthesis using the High-Capacity cDNA Reverse Transcription Kit

Settings	**Step 1**	**Step 2**	**Step 3**	**Step 4**
Temperature	25 °C	37 °C	85 °C	4 °C
Time [min]	10	120	5	Hold

4.4.13. miRNA-cDNA synthesis

For miRNA-cDNA synthesis, the TaqMan™ Advanced miRNA cDNA Synthesis Kit (Thermo Fisher Scientific, US) is used. First, 2 µg of extracted RNA from cells or liver tissue is diluted to a final concentration 5 ng/µl. For miRNA-cDNA synthesis, 10 ng of total RNA (2 µl of 5 ng/ µl dilution) is transcribed into cDNA.
10 ng of RNA are incubated with 3 µl of miRNA-polyadenylation Master Mix (see Table 19) with the incubation protocol in Table 20. Afterwards, 10 µl of Adaptor Ligation Master Mix are added (see Table 19) to each well of polyadenylated miRNA and are incubated with the incubation protocol in Table 21. Then, adaptor-ligated and polyadenylated miRNA are reverse transcribed into cDNA using the miRNA Reverse Transcription Master Mix with the incubation protocol in Table 22.
After the reverse transcription step, miRNA-cDNA is stored for up to 1 month at – 20 °C before amplification step or directly processed in the miR-amplification step (miR-Amp reaction).
For the miR-Amp reaction, 5 µl of miRNA-cDNA is transferred into a fresh reaction tube and 45 µl of miR-Amp Reaction Master mix are added and are incubated with the incubation protocol in Table 23. After miR-Amp reaction, amplified miRNA-cDNA is diluted in a ratio 1:10 with nuclease-free water for TaqMan-miRNA RT-qPCR or stored at – 20 °C.

Table 20: Polyadenylation incubation protocol for miRNA-cDNA synthesis

Step	**Temperature [°C]**	**Time [min]**
Polyadenylation	37	45
Stop reaction	65	10
Hold	4	Hold

Table 21: Ligation incubation protocol for miRNA-cDNA synthesis

Step	**Temperature [°C]**	**Time [min]**
Ligation	16	60
Hold	4	Hold

Table 22: Reverse Transcription incubation protocol for miRNA-cDNA synthesis

Step	**Temperature [°C]**	**Time [min]**
Reverse Transcription	42	15
Stop reaction	85	5
Hold	4	Hold

Table 23: miR-Amp incubation protocol for miRNA-cDNA synthesis

Step	Temperature [°C]	Time	Cycles
Enzyme activation	95	5 min	1
Denature	95	3 s	14
Anneal/Extend	60	30 s	
Stop reaction	90	10 min	1
Hold	4	Hold	Hold

All steps are carried out on ice or a cooling block.

4.4.14. DNA bisulfite conversion

For bisulfite conversion of genomic DNA (gDNA) the EpiTect Bisulfite Kit (QIAGEN) is used according to manufacturers instructions. Therefore, a total of 1 µg gDNA is diluted to 50 ng/µl in a final volume of 20 µl nuclease-free water. Then, 85 µl of Bisulfite Mix and 35 µl of DNA Protect Buffer are added to each reaction (DNAbis solution). Afterwards, the DNAbis solution is incubated with the following incubation protocol in Table 24.
Subsequently, a clean up procedure of bisulfite converted DNA (bisDNA) is performed. For this, bisDNA is transferred into a 1.5 ml reaction tube and bisDNA is precipitated with 250 µl 100 % ethanol. Samples are mixed thoroughly and 390 µl are transferred onto a EpiTect spin column. EpiTect spin columns are centrifuged at 5800 g and room temperature for 1 min and flowthrough is discarded. EpiTect spin columns are washed with 500 µl BW Buffer and centrifuged at 18000 g, room temperature for 1 min and flowthrough is discarded. Then, EpiTect spin columns are incubated with 500 µl BD Buffer to allow desulfonation. Flowthrough is discarded after a centrifugation step at 18000 g, room temperature for 1 min. Afterwards, EpiTect spin columns are washed two times with 500 µl BW Buffer, followed by a washing step with 250 µl 100 % ethanol and placed on a preheated thermos cycler at 60 °C for 5 min to allow evaporation of residual ethanol. Then, EpiTect spin columns are placed on a clean 1.5 ml reaction tube for elution. bisDNA is eluted in 50 µl EB Buffer to adjust for a final bisDNA concentration of 20 ng/µl, which is used in the following bisPCRs.
Eluted bisDNA is stored at – 20 °C until use in bisPCR.

Table 24: gDNA bisulfite conversion protocol

Step	Temperature [°C]	Time [min]
Denaturation	95	5
Incubation	60	30
Denaturation	95	5
Incubation	60	20
Hold	20	hold

4.4.15. *Slc2a4*-bisulfite PCR and pyrosequencing

Bisulfite-converted DNA from visceral adipose tissue is amplified in a bisPCR using the PyroMark PCR Kit (Qiagen, US) according to manufacturer instructions. Therefore, 20 ng of bisDNA (1 µl) form murine or human VAT is amplified in 24 µl of bis-PCR Master Mix (see Table 9) using the bis-PCR amplification

protocol (see Table 25). Afterwards, 4 µl of PCR product are loaded on a 1 % agarose gel and separated in an electrophoresis for quality control. The remaining PCR product either directly processed in pyrosequencing or stored over night at 4 °C.
For human and murine bis-PCR the same amplification protocol is used. Primer used in bis-PCR are listed in Table 16.

Table 25: bis-PCR amplification protocol used for *Slc2a4* ROI amplification

Step	Temperature [°C]	Time [min:sec]	Cycles
Initial PCR activation step	95	15:00	1
Denaturation	94	00:30	
Annealing	53.6	00:30	40
Extension	72	00:30	
Final extension	72	10:00	1
Hold	10	Hold	Hold

4.4.16. Triglyceride assay from liver tissue

Approximately 50 mg of snap-frozen liver tissue is weighted in and individual weights are noted. Then, tissue is transferred into a 2.5 ml homogenization tube with 3 ceramic beads. Subsequently, 250 µl of NP40 buffer (supplied with the TG colorimetric assay Kit, Cayman chemical, US) and 2.5 µl of cOmplete™ proteinase inhibitor cocktail (Roche Applied Science, DE) are added to each sample, followed by a homogenization using a Bead Ruptor 24 (s = 5 m/s, c = 1, t = 20 s). Afterwards, homogenate is incubated at 90 °C for 3 min and cooled to room temperature. This process is performed twice. Then, homogenate is centrifuged at 10000 g and 4 °C for 10 min. Supernatant, including the fat pat, is transferred into a clean 1.5 reaction tube and either directly processed in the triglyceride assay or stored at – 80 °C until further processing.
To perform the triglyceride assay (TG assay), extracts are diluted 1:5 in NP40 buffer and 10 µl of diluted extracts is used per reaction in duplicates in a 96-well plate (Sarstedt AG, DE) for the TG assay. Then, 10 µl of each standard is added to the 96-well plate. Subsequently 150 µl of diluted Enzyme Mixture solution (supplied with the TG colorimetric assay Kit) are added to each well. The plate is covered and reagents are carefully mixed, followed by an incubation at 37 °C for 30 min. Then, absorbance is measured at 540 nm using the CLARIOstar Plus (BMG Labtech, DE). Standard absorbance is corrected by blank measurement and triglyceride concentrations of samples are calculated based on a linear fit of the corrected standard values. Afterwards, concentrations are normalized to the weighted tissue. Mean and standard deviation for each group are calculated and are either shown as absolute values or normalized to control group in the graphs. For statistical tests, the absolute triglyceride concentrations normalized to tissue weight are used.

4.4.17. Glucose uptake assay in HepG2 cells after miR-21-5p and miR-149-5p overexpression

HepG2 cells are seeded into 6-well plates in triplicates and are reverse transfected with miR-21-5p, miR-149-5p or mimic control as described in 4.3.7. Then, cells are incubated for 24 h at 37 °C and 5 % CO_2. On the next day, cells are either stimulated with 500 mM insulin for 15 min or remained unstimulated. Subsequently, a Glucose Uptake-Glo™ Assay (Promega GmbH, US) is performed according to manufacturer instructions. In brief, medium is removed and cells are washed with PBS.

Then, 1 ml of 1 mM 2DG compound solved in PBS is added to each well, mixed and incubated for 10 min at room temperature. Subsequently, 500 µl of Stop Buffer are added, mixed and 75 µl of the suspension are transferred into a white 96-well ELISA plate in triplicates. Then, 25 µl of neutralization Buffer are added, followed by 100 µl of 2DG6P and incubated for 30 min on a shaking platform. Subsequently, luminescence signal is measured in a CLARIOstar Plus (BMG Labtech, DE) microplate reader.
For analysis, luminescence signal of miRNA-transfected cells is normalized to luminescence signal of mimic control transfected cells. The experiment is repeated three times at three different days and the mean and standard deviation of all experiments is calculated. For statistical analysis, the fold change is used in an unpaired, two sided students t test.

4.4.18. Bulk-mRNA sequencing and library preparation

Bulk-mRNA sequencing from HepG2 cells was performed by Kristian Händler and Nathalie Kruse at the institute of human genetics, Lübeck. For library preparation, the QuantSeq 3'mRNA Seq V2 Library Prep Kit (Lexogen Inc., US) is used according to manufacturer instructions with an add on PCR included. Quality control of the library preparation was assessed with the Qubit 1X dsDNA HS Assay Kit with a Qubit® fluorometer 2.0 according to manufacturer's instructions. Additionally, a quality control step was performed with the 2100 Bioanalyzer Instrument. For quantification of the library the NEBNext® Library Quant Kit for Illumina® is used according to manufacturer instructions and qPCR performed with the 7300 Real Time PCR System. The final calculation are performed with the NEBioCalculator®. The sequencing is performed with the NextSeq 2000 System. The data from the RNA sequencing is processed as described in 4.4.20.

4.4.19. Analysis of bulk-mRNA sequencing and differentially expressed genes analysis

Preprocessing of RNA sequencing data includes mapping of the sequence reads, poly-A and trimming of adaptor sequencing, quality assessment and gene calling and couting of reads. Preprocessing was performed by Christin Krause. Therefore, sequence reads are mapped using the spliced transcript alignment to a reference (STAR) procedure as described by (Dobin et al. 2013). For poly-A tails and trimming of adaptor sequences cutadapt v3.4 is used and for quality assessment fastQC v0.11.9. Counting of reads to genomic features and gene calling is performed with featureCounts for Ubuntu. To identify differentially expressed genes, the preprocessed data is used for DESeq2 v1.44.0 and low-counts genes with a count-sum < 30 are excluded from analysis. A DEG is defined by an adjusted P-value < 0.05 using a FDR of 0.05. Principal component analysis is performed from preprocessed data after exclusion of low-count genes. DEGs are used in further computational analysis such as gene ontology or REACTOME (see 4.5).

4.4.20. Gene array analysis

Hepatic array-based gene expression profile is reanalyzed from DIO mice at week 1 (chow n=7; HFD n=8) and week 12 (chow n=7; HFD n=8) using Clariom D microarrays for mice (Thermo Fisher Scientific, US) according to the manufacturer instructions. Therefore, total-RNA isolated from snap-frozen liver is used as described in 4.4.6. The data is analyzed with the Transcriptome Analysis Console software (version 4.0.2.15) using the analysis type 'Expression (Gene + Exon)'. For summarization, the 'Gene +

Exon - SST-RMA' method and as ANOVA method 'ebayes' were used. A probe set is considered expressed if at least 50 % of the detection above background (DABG) values are below the DABG threshold. A gene is considered differentially expressed with an FDR P-value < 0.05. Data are published previously (Geißler et al. 2022)

4.4.21. Hepatic microRNA microarray from DIO and VSG mice

To determine high-throughput hepatic miRNA expression from DIO mice (22 weeks on hfd) or VSG mice, a Affymetrix GeneChip™ miRNA 4.0 array (Thermo Fisher Scientific, US) is performed according to manufacturer instructions from total RNA extracted as described in 4.4.6. Subsequently, to identify differentially expressed miRNA the Transcriptome Analysis Console software (version 4.0.2.15) is used. A miRNA is considered differentially expressed with a linear fold change of < - 1.5 or > 1.5 and an FDR P-value < 0.05. Preparing the samples for microarray analysis of the VSG mice was conducted Cathleen Geißler and the DIO mice by Sonja Schriever and colleagues.

4.4.22. Real-time qPCR using TaqMan, PrimeTime or SYBR green

For mRNA-gene expression analysis, three different RT-qPCR protocols are used, namely TaqMan, PrimeTime and SYBR green. The first two protocols include probe-based approaches with predesigned assays, which allow a RT-qPCR protocol without a melting curve. The latter includes a conventional SYBR green approach with forward and reverse primer. Assay IDs are listed in Table 13 and Table 15 and SYBR green primer sequences are listed in Table 14.

TaqMan RT-qPCR 4 µl of 2.5 ng/µl mRNA-cDNA stocks are used in each reaction (total cDNA = 10 ng) or 4 µl of miRNA-cDNA stock and are added into a 96-well RT-qPCR reaction plate (Sarstedt AG, DE). Then, 6 µl of PrimeTime RT-qPCR Master Mix (see Table 9) are supplied to each reaction and RT-qPCR reaction plate is sealed with a optical clear cover foil. RT-qPCR plate is centrifuged at 300 g at room temperature for 2 min and placed afterwards in a QuantStudio 5 machine. Then the plate is incubated with the following protocol in Table 26.

Table 26: mRNA RT-qPCR TaqMan reaction protocol

Step	Temperature [°C]	Time	Cycle
Initiation	95	10 min	1
Amplification	95	15 s	40
	60	1 min	

PrimeTime RT-qPCR 4 µl of 2.5 ng/µl mRNA-cDNA stocks are used in each reaction (total cDNA = 10 ng) and are added into a 96-well RT-qPCR reaction plate (Sarstedt AG, DE). Then, 6 µl of PrimeTime RT-qPCR Master Mix (see Table 9) are supplied to each reaction and RT-qPCR reaction plate is sealed with a optical clear cover foil. RT-qPCR plate is centrifuged at 300 g at room temperature for 2 min and placed afterwards in a QuantStudio 5 machine. Then the plate is incubated with the following protocol in Table 27

Table 27: PrimeTime RT-qPCR reaction protocol

Step	Temperature [°C]	Time	Cycle
Initiation	95	10 min	1
Amplification	95	15 s	40
	60	1 min	

SYBR® green RT-qPCR 4 µl of 5 ng/µl mRNA-cDNA stocks are used in each reaction (total cDNA = 20 ng) and are added into a 96-well RT-qPCR reaction plate (Sarstedt AG, DE). Then, 6 µl of SYBR green RT-qPCR Master Mix (see Table 9) are supplied to each reaction and RT-qPCR reaction plate is sealed with a optical clear cover foil. RT-qPCR plate is centrifuged at 300 g at room temperature for 2 min and placed afterwards in a QuantStudio 5 machine. Then the plate is incubated with the following protocol in Table 28.

Table 28: SYBR green RT-qPCR reaction protocol

Stage	Step	Temperature [°C]	Time	Cycle
Hold Stage	Initiation	50	2 min	1
	Denaturation	95	10	1
PCR Stage	Denaturation	95	15 s	40
	Amplification	60	1 min	
Melt Curve Stage	Denaturation	95	15 s	
	Annealing	60	1 min	
	Dissociation	95	1 s	

Gene expression of each gene of interest is normalized to the housekeeping gene *HPRT* across all conditions and species, since *HPRT* proved to be the most stable gene. Stability analysis is performed in NormFinder (Andersen, Jensen, and Ørntoft 2004). Relative gene expression is calculated using the Pfaffl method (Pfaffl 2001). If not stated otherwise, gene expression is displayed in mean ± standard deviation. For statistical analysis the dCt value and for correlation analysis the -dCt value is used.

4.5. Computational methods

A variety of R-packages are used for computational analysis of transcriptomic or metabolomic data (Table 29Table 1).

Table 29: List of used R-packages

name	version	function
gprofiler2	0.2.3	REACTOME analysis
ggplot2	3.5.1	visualisation
dplyr	1.1.4	basic R-functions
pheatmap	1.0.12	clustered heatmap plots
org.Hs.eg.db	3.19.1	genome wide annotations for human
stringi	1.8.4	basic R-functions
Bioconductor	3.19	bioinformatic analysis
stringr	1.5.1	basic R-functions
stats	0.1.0	statistical analysis
tidyr	1.3.1	basic R-functions

tidyverse	1.3.0	basic R-functions
KEGGREST	1.44.0	access to Kyoto Encyclopedia of Genes and Genomes

4.5.1. Gene ontology analysis of DEGs with DAVID

DEGs (padj. < 0.05) from either RNA sequencing of HepG2 cells overexpressing miR-149-5p or from hepatic gene array data of DIO mice are used in gene ontology (GO) analysis with the webtool DAVID (D. W. Huang, Sherman, and Lempicki 2009). Therefore, the list of official gene symbol names of DEG is converted to ENSEMBL IDs with the integrated DAVID function and the perspective reference genome is selected as background. Then, results of GO analysis are implemented into R and ggplot2 v3.5.1 is used for individual visualization. GO analysis is adjusted by FDR = 0.05 and terms with a padj. < 0.05 are considered significant and are displayed in the individual graphs.

4.5.2. REACTOME analysis of significant-downregulated miR-149-5p target genes with gprofiler2

Significantly downregulated genes from RNA sequencing analysis after miR-149-5p overexpression in HepG2 cells are filtered first for conserved, predicted miR-149-5p target genes obtained from miRNA Nvis seed sequence prediction by simple list comparison. Then, the remaining significantly downregulated and conserved target genes are filtered for genes expressed in human liver based on the annotations from protein atlas (Fagerberg et al. 2014) to avoid false pathway enrichment for non-liver specific pathways. Afterwards, genes are ranked by their log2 fold change and used as input for the integrated gprofiler2 function that performs GO, KEGG pathway and REACTOME analysis in parallel. The output graph is visualized in a Manhattan plot (see Figure 22g) and pvalue is adjusted by FDR < 0.05.

4.5.3. Metabolite set enrichment analysis (MSEA) and retrieving metabolite/gene annotations from KEGG resources

Differentially enriched metabolite (p < 0.05) names are converted to compound IDs first using the human metabolome database website (Wishart et al. 2007). Then, an unranked list of differentially enriched metabolite compound IDs is used as an input for the metabolite set enrichment analysis using the integrated webtool from MetaboAnalyst v6.0 (Xia et al. 2009) with feature type set to metabolites. As background, the human metabolome is selected. Results from the MSEA are exported as an excel file and are imported to R for visualization with ggplot2.
To retrieve metabolite/gene annotations for correlation analysis of involved metabolites in the metabolic pathways with mmu-miR-149-5p expression from murine liver, the KEGGREST v1.44.0 R-package is utilized to obtain a genome-wide annotation list. Then, the list is filtered for the genes of interest involved in the metabolism pathways and associated metabolites measured in metabolomics are correlated with mmu-miR-149-5p expression Figure 24c & Figure 25c & d).

4.5.4. Transcription factor binding prediction to *GPC1* gene and selection of transcription factors

To find transcription factor that regulate *GPC1* and miR-149-5p expression, the *GPC1* promoter sequence (1500 bp upstream of GPC1 gene) is retrieved from the UCSC browser (hg19). Then, the sequence information is imported to CiiiDER (Gearing et al. 2019) and a transcription factor binding prediction is performed using the JASPAR 2018 vertebrate database (Rauluseviciute et al. 2023). Afterwards, results are imported into R and predicted transcription factors are filtered for differentially expressed transcription factors utilizing the hepatic gene array data from DIO mice at week 12 and the list of all known human transcription factors (Lambert et al. 2018). Subsequently, differentially expressed and predicted transcription factors are correlated with *GPC1* gene expression and transcription factors are manually selected from significant correlations ($p < 0.05$, see Figure 26f).

4.6. General statistics

In general, for gene expression data generated in RT-qPCR, normalized counts from bulk-mRNA sequencing or normalized gene array signals, the mean and standard deviation or standard error of the mean are shown, which is also noted in the figure caption. RT-qPCR statistics are performed with the delta Ct value and normalization for relative gene expression is performed according to the Pfaffl method (Pfaffl 2001). Outlier testing is performed in GraphPad Prism v10.2.3 using the Grubb's test with alpha = 0.05. For comparing of two groups, a standard two-tailed, unpaired students t test is performed. Comparison of three groups or more for a single time point, a Tukey's multiple comparison (one-way ANOVA) is calculated and p-values are adjusted for multiple testing. For comparison of longitudinal data of two groups, a two-way ANOVA is performed. For gene expression data of bulk-mRNA sequencing or gene array, the adjusted p-values by DESeq2 or the Transcriptome Analysis Console software are shown.
DNA methylation data is shown as mean with standard deviation. If not stated otherwise, a two-way ANOVA is performed to test for statistical significance.
For correlation with RT-qPCR data, the negative delta Ct value is used and all correlations shown use the Pearson correlation method.
In general, prior to each statistical analysis, data are tested for normal distribution.

5. Results

The result section of this thesis is separated into three chapters according to the main hypothesis questions. The first chapter deals with the search of one master regulator miRNA, which significantly contribute to the progression of MASLD by regulating the expression of the local controlling genes (LCGs).
Since there are many unknown epigenetic mechanisms that contribute to MASLD progression or development of insulin resistance, the aim of the second project is to find a master regulator miRNA of metabolic pathways in the liver independent of the LCGs. To find this master regulator, transcriptomic and metabolomic data from cell culture, DIO mouse and intervention models are combined. Additionally, the human transcriptome of an obese human liver cohort categorized into subjects with high and low HbA1c levels and a public available liver cohort (SteatoSITE) is employed to validate the findings in human.
In the third project, DNA methylation in the insulin-dependent glucose transporter Slc2a4 in the VAT of DIO mice and obese humans with or without type 2 diabetes is investigated.

5.1. The master regulator for local controlling genes

5.1.1. miR-21a-5p and miR-149-5p target the local controlling genes *Inhbe*, *Ddx3x* and *Smim13*

The initial hypothesis is, that the gene expression of the previously described ;*local controlling genes'*, or short LCGs, is disrupted during the development of MASLD. Thus, this disruption also contributes to the progression. MicroRNAs are invovled in disease development and progression likewise. Therefore, it is logical to assume a connection between disrupted miRNA expression and LCG expression. The optimal outcome would be one miRNA with the potential of regulating all investigated LCGs, a so called master regulator miRNA. Additionally, the hypothesis involves the development and progression into MASLD rather than rescuing later stages of MASLD, such as MASH or HCC, it is applicable to choose a model of diet-induced obesity (DIO). Hence for the following experiments a DIO mouse model is used, where the high-fat diet (hfd) fed group was exposed to 22 weeks of high-fat diet and the hepatic gene expression of LCGs is measured. Afterwards, LCG expression is correlated with hepatic miRNA expression from micro array data of the same mice in combination with a seed sequence prediction between differentially expressed miRNAs with differentially expressed LCGs.
After a time period of 22 weeks on hfd, the LCGs *Arhgap24* (0.591 ± 0.234, p = 0.0136, q = 0.0172), *Cd82* (0.530 ± 0.253, p = 0.0355, padj = 0.0373), *Cobll1* (0.578 ± 0.065, p = 0.0008, padj = 0.0013), *Ddx3x* (0.489 ± 0.02, p = 0.0002, padj = 0.0006) and *Smim13* (0.455 0.134, p = 0.0003, padj = 0.0006) are significantly downregulated and *Inhbe* (2.829 ± 0.963, p = 0.0001, padj = 0.0006) signficantly upregualted (Figure 10a). Since LCGs are repressed and induced, the original hypothesis of one master regulator miRNA needs to be adjusted. A negative correlation of the miRNA/mRNA pairs is necessary, as miRNAs regulate target gene expression through mRNA degradation (see 1.2.1.1), which decreases the probability that miRNA and target gene are induced simultaneously. Instead of one master regulator, two master regulators are required – an induced miRNA for the downregulated genes and a repressed miRNA for the upregulated genes.
To cover the miRNA expression pattern of the hfd-fed mice, a microRNA micro array is performed. Principal component analysis (PCA) reveals a separation of three populations. Allthough, chow and hfd

animals clearly separate from each other, two hfd animals are segrated from the residual hfd

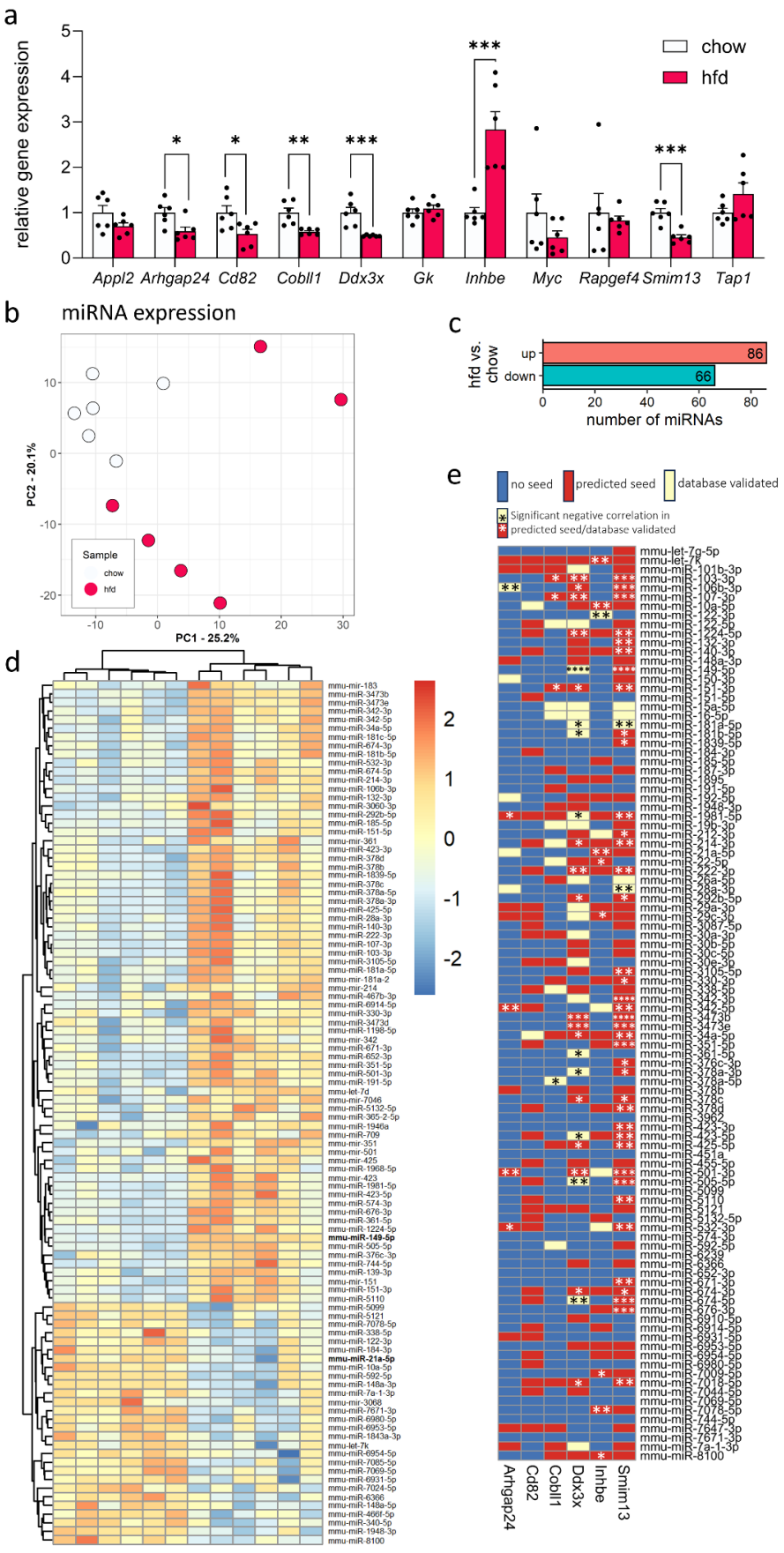

Figure 10: Identification of potential master regulator miRNAs by combining LCG gene expression data with microRNA microarray data from mice fed a chow or hfd for 22 weeks. a: Relative gene expression data measured in RT-qPCR of LCG genes in liver of chow and hfd mice (n = 6). A multiple, unpaired and two-sided student's t test is performed with * = padj. < 0.05, ** = padj. < 0.01, *** = padj. < 0.001, **** = padj. < 0.0001. b: Principal component analysis of hepatic microRNA microarray data from chow and hfd-fed animals (n = 6). c: Number of significantly (padj. < 0.05) up- and downregulated mature miRNAs. d: Seed sequence prediction and correlation analysis of differentially expressed LCGs with 100 differentially expressed miRNAs. Blue boxes indicate no predicted seed sequence, red boxes indicate a predicted seed sequence and yellow boxes indicate a validated seed sequence within a database. Asterisk indicates significant negative correlation between perspective LCG and miRNA with *= p < 0.05, ** = p < 0.01, *** = p < 0.001, **** = p < 0.0001.

population (Figure 10b). In total 152 miRNAs are differentially expressed in the hfd group when compared to the chow group, of which 86 miRNAs are upregulated and 66 downregulated (Figure 10c, p < 0.05). Nevertheless, euclidean-hierarchical clustering of the top 100 differentially expressed miRNAs, selected by magnitude of significance, shows an explicit categorization of two groups into chow and hfd animals (Figure 10d). Subsequently, a correlation and seed-sequence prediction analysis of differentially expressed LCGs (*Arhgap24*, *Cd82*, *Cobll1*, *Ddx3x*, *Inhbe* and *Smim13,* Figure 10a) with the top 100 differentially expressed miRNAs (Figure 10d) is performed. The seed sequence prediction function of the microRNA network visualizer (miRNA NVis) was used (Krause et al. 2023). The analysis is shown in an unclustered heatmap, with blue squares indicating no predicted or validated seed between a miRNA and a LCG, red squares indicating a predicted seed and yellow squares indicating a validated database entry for a miRNA and a LCG. Asterisk highlights only significant negative correlations of miRNA/mRNA pairs, when a predicted or validated seed has been observed (negative correlation with * = p < 0.05, ** = p < 0.01, *** = p < 0.001, **** = p < 0.0001, Figure 10e). In total 52 miRNAs show a predicted/validated seed and a signicant negative correlation with at least one LCGs.

For selecting the potential miRNA master regulator candidates, only those 52 miRNAs are considered. To evaluate the effect size, by which the 52 miRNAs are affected in the hfd group, the miRNAs are ordered ascending by their log2 fold change (Figure 11a). *Mmu-miR-21a-5p* displays the highest decrease in miRNA expression (Figure 11b), whereas *mmu-miR-149-5*p displays the highest increase in miRNA expression (Figure 11c). Mmu-miR-21a-5p targets the *Inhbe* gene and mmu-miR-149-5p the *Ddx3x* and *Smim13*. Therefore *mmu-miR-21-5p* and *mmu-miR-149-5p* are selected for further investigations and only the connected LCGs are further investigated. The expression data of the remaining LCGs are shown in the appendix data for the VSG and metformin mouse model (Supplementary Figure 1), or dietary intervention models (Supplementary Figure 2), but are beyond the scope of this work.

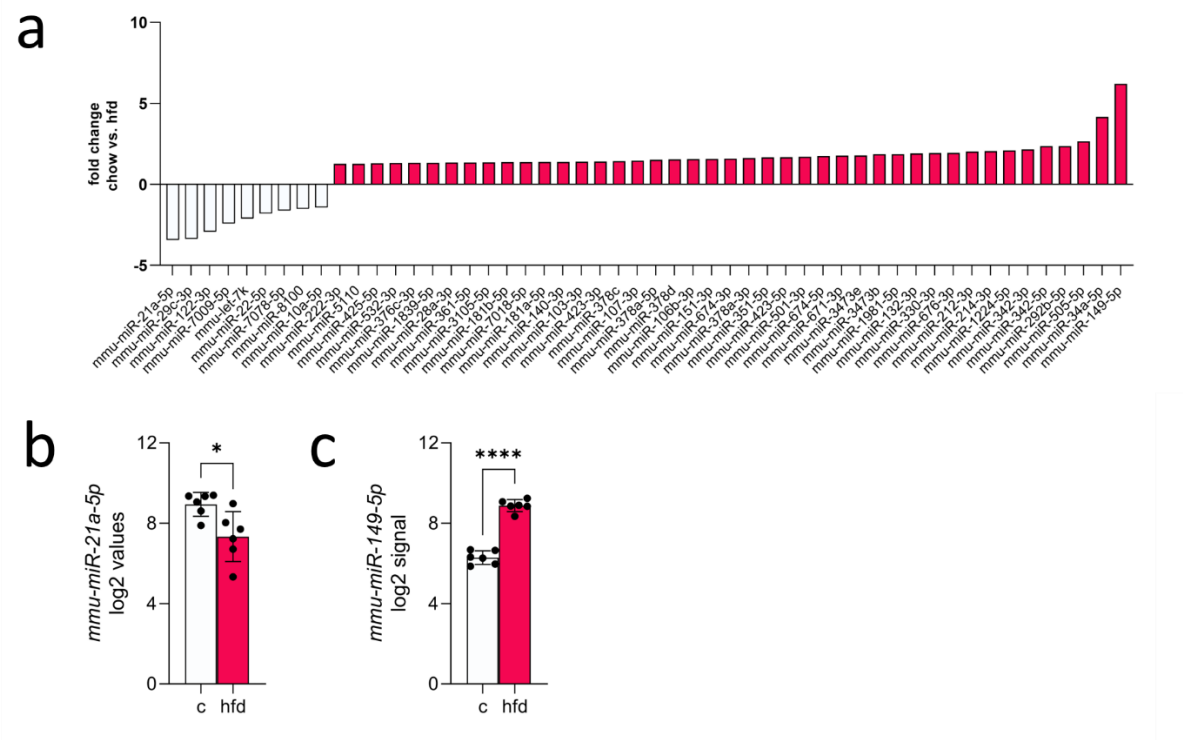

Figure 11: Mmu-miR-21a-5p and mmu-miR-149-5p show the greatest degree of dysregulation. a: Hepatic microRNA microarray data of differentially expressed miRNAs with predicted seed sequence for at least one LCG ranked ascending by log2 fold change (hfd vs. chow). b & c: Absolut array signals for *mmu-miR-21a-5p* and *mmu-miR-149-5p* (n = 6). * = $p < 0.05$, **** = $p < 0.0001$.

5.1.2. miR-21a-5p and miR-149-5p are causative in MASLD progression

Since *mmu-miR-21a-5p* and *mmu-miR-149-5p* are identified as potential master regulator miRNAs and their expression is disrupted in the DIO mouse models, it is crucial to differentiate if the disruption is a consequence to the hfd feeding or is also causative to the development of MASLD. To distinguish between cause and consequence, it is beneficial to determine the time point of the disrupted miRNA expression. Therefore, *mmu-miR-21a-5p* and *mmu-miR-149-5p* expression together with their corresponding target LRGs are measured in a longitudinal mouse model for DIO (see4.2.1). Also, miRNA expression is correlated with metabolic parameters, such as blood glucose and hepatic triglyceride content to gain further information for potential factors affected by the miRNAs or potentially are involved in miRNA regulation.

After a slight, non-significant increase at week one and two (week 1: 1.18 ± 0.07, p = 0.0641; week 2: 1.14 ± 0.06, p = 0.1023), *mmu-miR-21a-5p* expression starts to decrease at week four (0.77 ± 0.02, p = 0.0007) and remains significantly downregulated until week twelve (0.67 ± 0.05, p = 0.01,Figure 12 a). Its target LCG *Inhbe* is significantly increased from week 1 (2.37 ± 0.37, $p < 0.0001$) on and remains upregulated for the throughout the investigated time period of twelve weeks (3.15 ± 0.18, $p < 0.0001$; Figure 12b). Mmu-miR-21a-5p and *Inhbe* expression display a significant, negative correlation (r = - 0.3504, $p < 0.0001$; Figure 12c). During acute hfd-feeding (week one and two), mmu-miR-21a-5p displays a positive correlation with plasma insulin (r = 0.6217, p = 0.0233) and hepatic triglyceride levels (r = 0.6195, p = 0.0105). However, during chronic conditions under hfd, mmu-miR-21a-5p correlates negatively with body weight (week 12: r = - 0.5255, p = 0.0379), blood glucose (r = - 0.6646, p = 0.0050).

and hepatic triglyceride levels (r = - 0.5677, p = 0.0218; data for correlation with body weight, blood glucose, plasma insulin and hepatic triglyceride levels are shown in Figure 9b to e, partial correlations shown in Figure 12d). Mmu-miR-149-5p expression shows no response to acute hfd-feeding, but is significantly induced with chronic conditions from week six (1.56 ± 0.15, p = 0.0021) to week twelve (3.81 ± 0.35, p < 0.0001; Figure 12e). In contrast, the predicted target LCGs *Ddx3x* and *Smim13* are significantly downregulated in hfd-fed mice from week eight on (*Ddx3x*: 0.87 ± 0.03, p < 0.0001; *Smim13*: 0.65 ± 0.04, p = 0.0089; Figure 12f and g), following the previously upregulation of mmu-miR-149-5p. Both predicted target LCG expressions correlate negatively with mmu-miR-149-5p expression (*Ddx3x*: r = - 0.5372, p < 0.0001; *Smim13*: r = - 0.6612, p < 0.0001; Figure 12h and i). Partial correlations for each week reveal a positive correlation of mmu-miR-149-5p expression with blood glucose (r = 0.3502, p = 0.0494), body weight (r = 0.5527, p = 0.0010), plasma insulin (r = 0.6214, p = 0.0005) and hepatic triglyceride levels (r = 0.5328, p = 0.0017) at week four. This association between mmu-miR-149-5p expression and the measured metabolic parameters reached its climax at week eight (blood glucose: r = 0.8237, p < 0.0001; body weight: r = 0.8893, p < 0.0001; plasma insulin: r = 0.6938, p < 0.0001; hepatic triglyceride: r = 0.8652, p < 0.0001; Figure 12j).

The early onset in disrupted mmu-miR-21a-5p and mmu-miR-149-5p expression imply a causative role in MASLD progression, rather than being a consequence of high-fat diet feeding. Additionally, the negative correlation between miRNA expression with their corresponding target LCGs manifests a regulatory role.

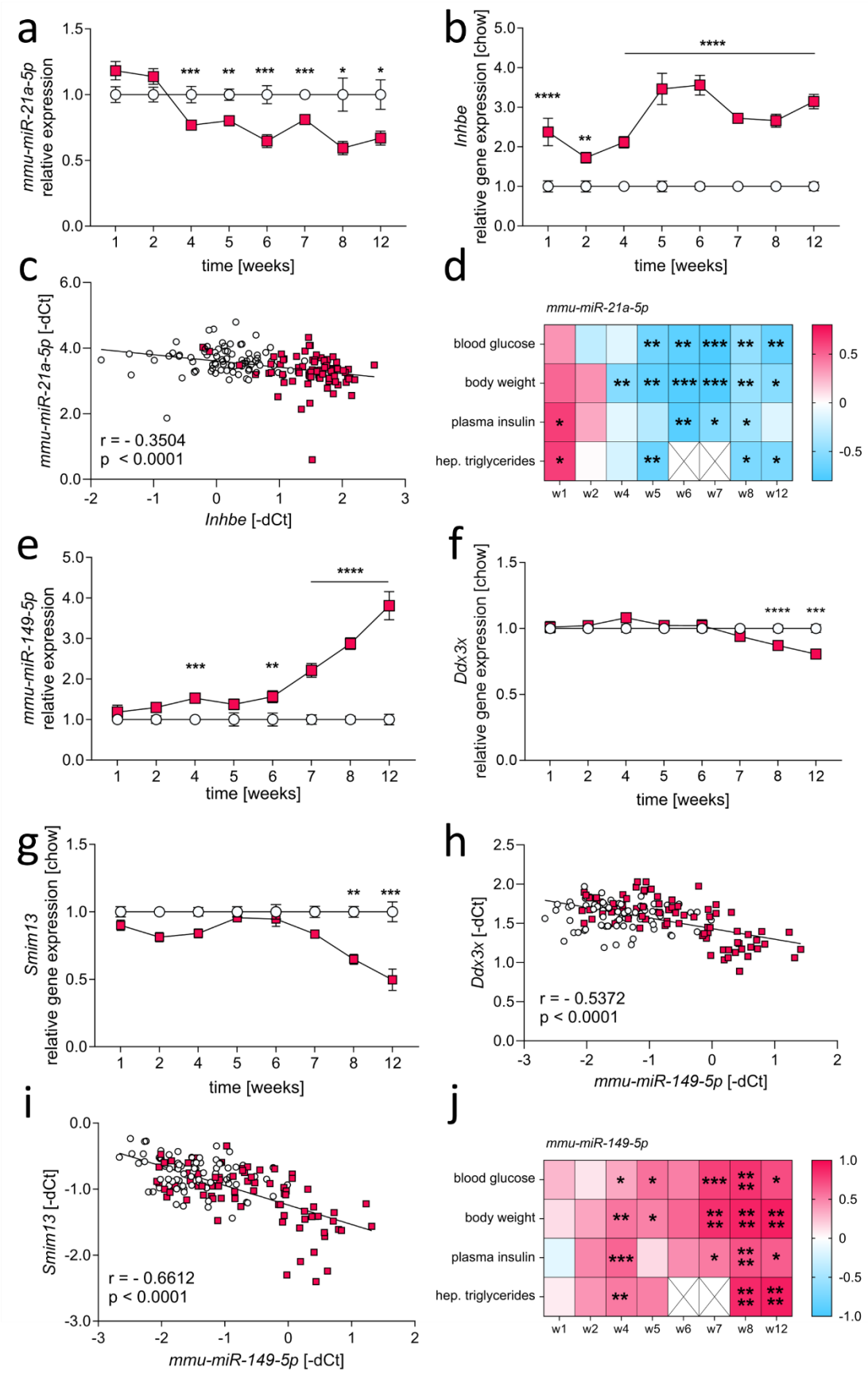
a
mmu-miR-21a-5p
relative expression
time [weeks]
b
Inhbe
relative gene expression [chow]
time [weeks]
c
mmu-miR-21a-5p [-dCt]
r = - 0.3504
p < 0.0001
Inhbe [-dCt]
d
mmu-miR-21a-5p
blood glucose
body weight
plasma insulin
hep. triglycerides
w1
w2
w4
w5
w6
w7
w8
w12
e
mmu-miR-149-5p
relative expression
time [weeks]
f
Ddx3x
relative gene expression [chow]
time [weeks]
g
Smim13
relative gene expression [chow]
time [weeks]
h
Ddx3x [-dCt]
r = - 0.5372
p < 0.0001
mmu-miR-149-5p [-dCt]
i
Smim13 [-dCt]
r = - 0.6612
p < 0.0001
mmu-miR-149-5p [-dCt]
j
mmu-miR-149-5p
blood glucose
body weight
plasma insulin
hep. triglycerides
w1
w2
w4
w5
w6
w7
w8
w12

Figure 12: Longitudinal hepatic expression of mmu-miR-21a-5p and mmu-miR-149-5p and predicted target LCG expression in mouse model for DIO. a & b: Relative mmu-miR-21a-5p and *Inbhe* expression (chow: n = 8 – 16, hfd: n = 7 - 16). c: Pearson correlation of mmu-miR-21a-5p expression and Inhbe gene expression across all time points (n = 159). d: Partial, weekly Pearson correlation of mmu-miR-21a-5p expression with blood glucose, body weight, plasma insulin and hepatic triglyceride content. e – g: Relative mmu-miR-149-5p, *Ddx3x* and *Smim13* expression (chow: n = 8 – 16, hfd: n = 7 - 16). h & i: Pearson correlation of mmu-miR-149-5p expression with *Ddx3x* and *Smim13* gene expression across all time points (n = 159). j: Partial, weekly Pearson correlation of mmu-miR-149-5p expression with blood glucose, body weight, plasma insulin and hepatic triglyceride content. RT-qPCR data is shown as mean with standard deviation and for statistical analysis a two-way ANOVA is performed. * = p < 0.05, ** = p < 0.01, *** = p < 0.001, **** = p < 0.0001.

5.1.3. miR-21a-5p and miR-149-5p expression is rescued by weight-loss interventions

The longitudinal data from DIO mice suggest a causative role of *mmu-miR-21a-5p* and *mmu-miR-149-5p* in the development of MASLD by also regulating the LCG gene expression of *Inhbe*, *Ddx3x* and *Smim13*, since the onset of dysregulation occurs early during hfd-feeding. Weight-loss interventions are associated with a remission of obesity and MASLD. If *mmu-miR-21a-5p* and *mmu-miR-149-5p* have a causative role in MASFLD progression, the miRNA expression should be rescued according to the remission of hepatic injury and reduction in hepatic triglyceride content. MiRNA expression is interpreted as rescued, when no significant changes in expression between the intervention group and the control chow-fed group or when significant changes in miRNA expression between the hfd-exposed group and an intervention group tending towards the control chow-fed group is detected. Several different weight-loss intervention were investigated, comprehending moderate weight-loss intervention, such as a caloric-restriction (cr), an exendin-4 treatment (ex-4) and a dietary intervention (h<c) model (see 4.2.2). The moderate weight-loss intervention models were conducted at the Helmholtz Zentrum Munich by Schriever and colleagues according to previous publications and mice are exposed to the intervention treatment for 10 days (Harrison, Pfuhlmann, et al. 2019; Harrison, Schriever, et al. 2019).

Interestingly, mice reduce body weight between 10 to 20 % over an investigated time period of 10 days depending on the intervention method. Exendin-4 treatment thereby is most efficient in reducing the body weight of up to 20 % (Figure 13a). Hepatic triglyceride levels are significantly increased after high-fat diet feeding (2.11 ± 0.16, p = 0.0002), but show no significant reduction after the interventions when compared to the continuous hfd-fed animals. However, trends of reduced hepatic triglyceride content after interventions is detected (Figure 13b). *Mmu-miR-21a-5p* is significantly downregulated after hfd-feeding (0.66 ± 0.04, p = 0.0022) and caloric restriction, when compared to the control chow-fed animals (0.63 ± 0.03, p = 0.0006; Figure 13c). No significant changes in *mmu-miR-21a-5p* expression between the chow-fed control group and dietary switch (h<c: 0.78 ± 0.06, p = 0.1147) or exendin-4 treated (ex-4: 0.79 ± 0.07, p = 0.1174), as well as no significant changes between the hfd-fed group and any intervention group are detected (Figure 13c). *Inhbe* gene expression is significantly increased in the hfd-fed group when compared to chow-fed control (2.83 ± 0.39, p = 0.0006). However, there are no significant differences in *Inhbe* gene expression between the chow-fed control and the intervention groups (h<c: 1.89 ± 0.37, p = 0.0901; cr: 1.49 ± 0.19, p = 0.4279; ex-4: 1.17 ± 0.15, p = 0.9662). *Inhbe* expression is significantly downregulated in the cr intervention (p = 0.0384) and ex-4 treated group (p = 0.0028, Figure 13c). *Mmu-miR-21a-5p* expression correlates negatively with hepatic triglyceride content (r = - 0.5367, p = 0.0022) and *Inhbe* gene expression across all cohorts (r = - 0.4962, p = 0.0053; Figure 13d).
Mmu-miR-149-5p expression is significantly upregulated in the hfd-fed group (4.39 ± 0.34, p < 0.0001), as well as in all intervention groups (h<c: 3.68 ± 0.27, p < 0.0001; cr: 3.36 ± 0.17, p < 0.0001; ex-4: 4.68 ± 0.44, p < 0.0001) when compared to the chow-fed control group, but caloric restricted animals show tendency of reduced *mmu-miR-149-5p* expression levels before p value adjustment (Figure 13e). *Ddx3x* expression is significantly reduced in animals exposed to high-fat diet (hfd: 0.49 ± 0.02, p = 0.0191) or

caloric restriction (cr: 0.31 ± 0.14, p < 0.0001) when compared to the standard chow diet control. Interestingly, caloric restriction seems to reduce *Ddx3x* expression to a greater extent than high-fat diet feeding. Diet switched from high-fat to chow diet (h<c: 0.62 ± 0.25, p = 0.1078) and exendin-4 treatment (ex-4: 0.70 ± 0.23, p = 0.3973) rescues *Ddx3x* expression when compared to standard chow diet control, since there are no significant differences detected. However, diet switch (#/p = 0.0146) and exending-4 treatment (#/p = 0.0022) significantly upregulates *Ddx3x* expression when compared to caloric restriction, the condition with the greatest impact on *Ddx3x* repression (Figure 13e). The second target LCG of *mmu-miR-149-5p* is *Smim13*. *Smim13* gene expression is significantly reduced after high-fat diet (hfd: 0.45 ± 0.13, p = 0.0010), but shows no significant differences after diet switch (h<c: 0.66 ± 0.27, p = 0.0863), caloric restriction (cr: 1.03 ± 0.23, p = 0.9995) and exendin-4 (0.85 ± 0.29, p = 0.8254) treatment when compared to standard chow diet control. However, when compared to the hfd group, caloric restriction (p = 0.0006) and exendin-4 treatment significantly increase *Smim13* expression (p = 0.0130, Figure 13e). Over all interventions, *mmu-miR-149-5p* expression correlates positively with hepatic triglyceride content (r = 0.6198, p = 0.0003) and negatively with *Ddx3x* expression (r = -0.4476, p = 0.0131, Figure 13f). However, *Smim13* expression shows no significant correlation with mmu-miR-149-5p expression over all cohorts (r = -0.3596, p = 0.0510, Figure 13f). Performing group-wise correlations, a dominant negative correlation between *mmu-miR-149-5p* and *Smim13* expression within the high-fat diet and standard chow diet group is observed (r = -0.8356, p = 0.0007, Supplementary Figure 3a). This negative correlation is annulled in the intervention cohorts (h<c: r = -0.5494, p = 0.0643; cr: r = 0.0747, p = 0.8175; ex-4: r = 0.3038, p = 0.3370; Supplementary Figure 3b – d). This observation suggests that *mmu-miR-149-5p* is sufficient or responsible of downregulating *Smim13* expression during high-fat diet feeding, but the reversibility of *Smim13* in the intervention models is regulated by a different mechanism aside of *mmu-miR-149-5p*.
Astonishingly, those intervention models have a reduction in body weight in common, without displaying magnificent changes in hepatic triglyceride content.

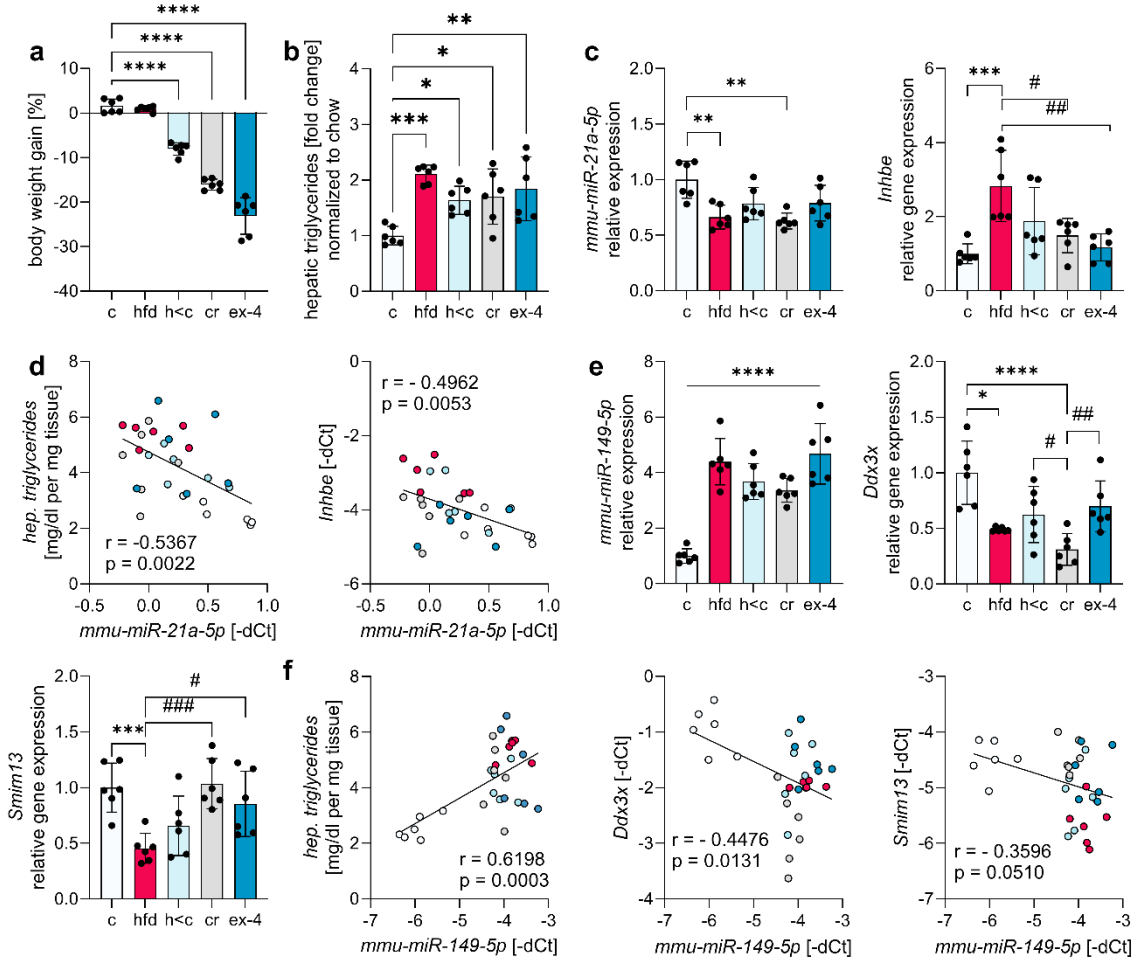

Figure 13: Body weight gain, hepatic triglyceride content, gene expression data and correlation analysis in moderate weight-loss interventions**.** a: Body weight gain after 10 days of intervention b: Fold change in hepatic triglyceride content normalized to standard chow-control (c). c*: mmu-miR-21-5p* and target LCG *Inhbe* expression (n = 6 per group). d: Pearson's correlation of *mmu-miR-21-5p* with hepatic triglyceride content [mg/dl per mg tissue] and *Inhbe* gene expression. e: *mmu-miR-149-5p* and target LCG *Ddx3x* and *Smim13* expression (n = 6 per group). f: Pearson's correlation of *mmu-miR-149-5p* with hepatic triglycerides, *Ddx3x* and *Smim13* expression. If not stated otherwise, data are shown as mean ± standard deviation. Gene expression data is measured in RT-qPCR and the single signal fold changes are normalized to the chow mean. For statistical testing, a One Way ANOVA on the dCt values is performed with * indicating significant differences to the chow control and # between hfd and metformin treated animals. * = p < 0.05, ** = p < 0.01, *** = p < 0.001, **** = p < 0.0001, # = p < 0.05, ## = p < 0.01 and ns = not significant.

5.1.4. mmu-miR-21a-5p is acutely reversed and mmu-miR-149-5p is persistently reduced after vertical sleeve gastrectomy

In the previous experiment, the effect of moderate-weight loss interventions on the miRNAs *mmu-miR-21a-5p* and *mmu-miR-149-5p* are investigated without significant effects on the hepatic triglyceride content. Before the great improvements in medical therapies using incretin-analogues, such as semaglutide or tirzapetide, the most efficient approach in reducing body weight was bariatric surgeries (Carlsson et al. 2020; Jastreboff et al. 2022; T. D. Müller et al. 2022). To study the effect of bariatric surgery on the expression of *mmu-miR-21a-5p* and *mmu-miR-149-5p*, a mouse model of vertical sleeve gastrectomy was used (4.2.4). In brief, mice were fed a high-fat diet for twelve weeks (n = 33) and are then divided into two groups. One group (n = 16) underwent a sham surgery, whereas the other group

underwent a vertical-sleeve gastrectomy (n = 17). At day 9 post-surgery (sham: n = 8, vsg: n = 8) and at the end point of 35 days post-surgery (sham: n = 8, vsg: n = 9), mice were sacrificed and hepatic triglyceride levels were measured at both time points post-surgery. *Mmu-miR-21a-5*p and *mmu-miR-149-5p* expression is assessed in six animals of each group on a miRNA micro array (d9: sham/vsg: n = 6, d35: sham/vsg: n = 6). Body weight was measured before surgery and tracked until sacrifice. The complete study cohort of day 35 post-surgery is published previously (Geißler et al. 2022).

5.1.4.1. Acute and persistent weight-loss in VSG and sham mice

The differentiation into a recovery and maintenance phase is crucial to avoid confounding effects of the surgery in the recovery phase, which is also present in the sham control group (Garibay and Cummings 2017). In the recovery phase post-surgery, both groups start to lose weight within the first four days post-surgery (Figure 14a & b), which might be due to recovery after the surgery. However, sham mice regain body weight faster than vsg mice and almost reach their pre-surgery body weight again after nine days and display a body weight gain of roughly 0.41 % ± 2.69 or in total 0.18 grams ± 1.17. Vsg mice showed a reduction of -20.58 % ± 4.31 or in total -9.07 grams ± 2.04 nine days post-surgery. The reduction in body-weight between sham and vsg mice is significant ($p < 0.0001$).
After day nine, both groups start to gain weight persistently. Nevertheless, sham mice increase their body weight on the average by 7.43 grams ± 1.53 or 20.17 % ± 3.10, which is a significant increase in body weight when compared to pre-surgery ($p < 0.0001$), whereas vsg mice reduced their body weight by -2.23 grams ± 2.23 or -5.41 % ± 10.07. The reduction in body weight of vsg mice is significant compared to their pre-surgery body weight ($p = 0.0087$) but also compared to sham mice ($p < 0.0001$).

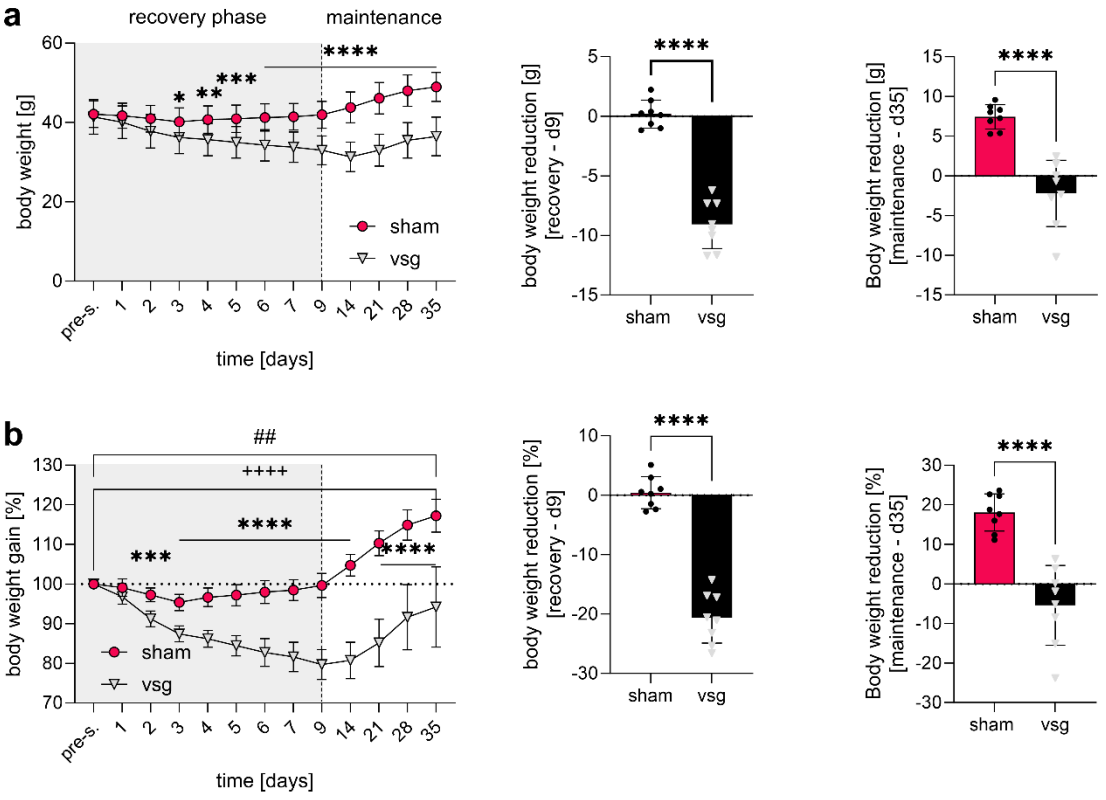

Figure 14: Body weight changes post-surgery. a: Body weight progression in absolute grams (sham: n = 8 – 16, vsg: n = 8 – 17) and absolute body weight changes at nine days (sham: n = 8, vsg: n = 8) and 35 days post-surgery (sham: n = 8, vsg: n = 9). b:

Body weight gain in percentages of body weight pre-surgery (sham: n = 8 – 16, vsg: n = 8 – 17) and body weight reduction in percentages at nine days (sham: n = 8, vsg: n = 8) and 35 days post-surgery (sham: n = 8, vsg: n = 9). For comparison and statistical testing of body weight changes in a and b, a two-way ANOVA was performed, whereas for comparison at nine days and 35 days post-surgery a two-tailed stundent's t-Test. * comparison between sham and vsg group with * = $p < 0.05$, ** = $p < 0.01$, *** = $p < 0.001$ and **** = $p < 0.0001$. + comparison between pre-surgery and post-surgery weight within the sham group with ++++ = $p < 0.0001$ and # comparison between pre-surgery and post-surgery weight within the vsg group with ## = $p < 0.01$.

5.1.4.2. mmu-miR-21a-5p expression is reversed in recovery phase after VSG and correlates with body weight

In the recovery phase, hepatic triglyceride content is significantly lower in vsg mice (62.97 % ± 27.47, p = 0.0407) when compared to the sham control group (Figure 15a) and is accompanied by a significant increase in *mmu-miR-21a-5p* expression (Δlog2: 0.877, $p < 0.0001$) and a non-significant tendency of reduced target LCG expression *Inhbe* (0.65 ± 0.24, p = 0.2558, Figure 15b). Mmu-miR-149-5p is not-significantly reduced nine days post-surgery in the vsg mice (Δlog2: -0.458, p = 0.4967). Both target LCGs, Ddx3x (1.24 ± 0.13, p = 0.0063) and Smim13 (1.20 ± 0.18, p = 0.0178), are significantly increased in vsg mice when compared to control sham mice (Figure 15c). In the recovery phase, mmu-miR-21a-5p expression correlates negatively with body weight loss (r = -0.84, p = and target gene *Inhbe* expression (r = -0.65, p =). Interestingly, mmu-miR-149-5p correlates positively with hepatic triglyceride content (r = 0.74, p =) and body weight loss (r = 0.72, p =), suggesting a higher mmu-miR-149-5p expression with increasing hepatic triglyceride content. A negative correlation between mmu-miR-149-5p and target LCG Ddx3x expression is observed (r = - 0.89, $p < 0.0001$), but not with *Smim13*

(r = - 0.53, p = , Figure 15d).

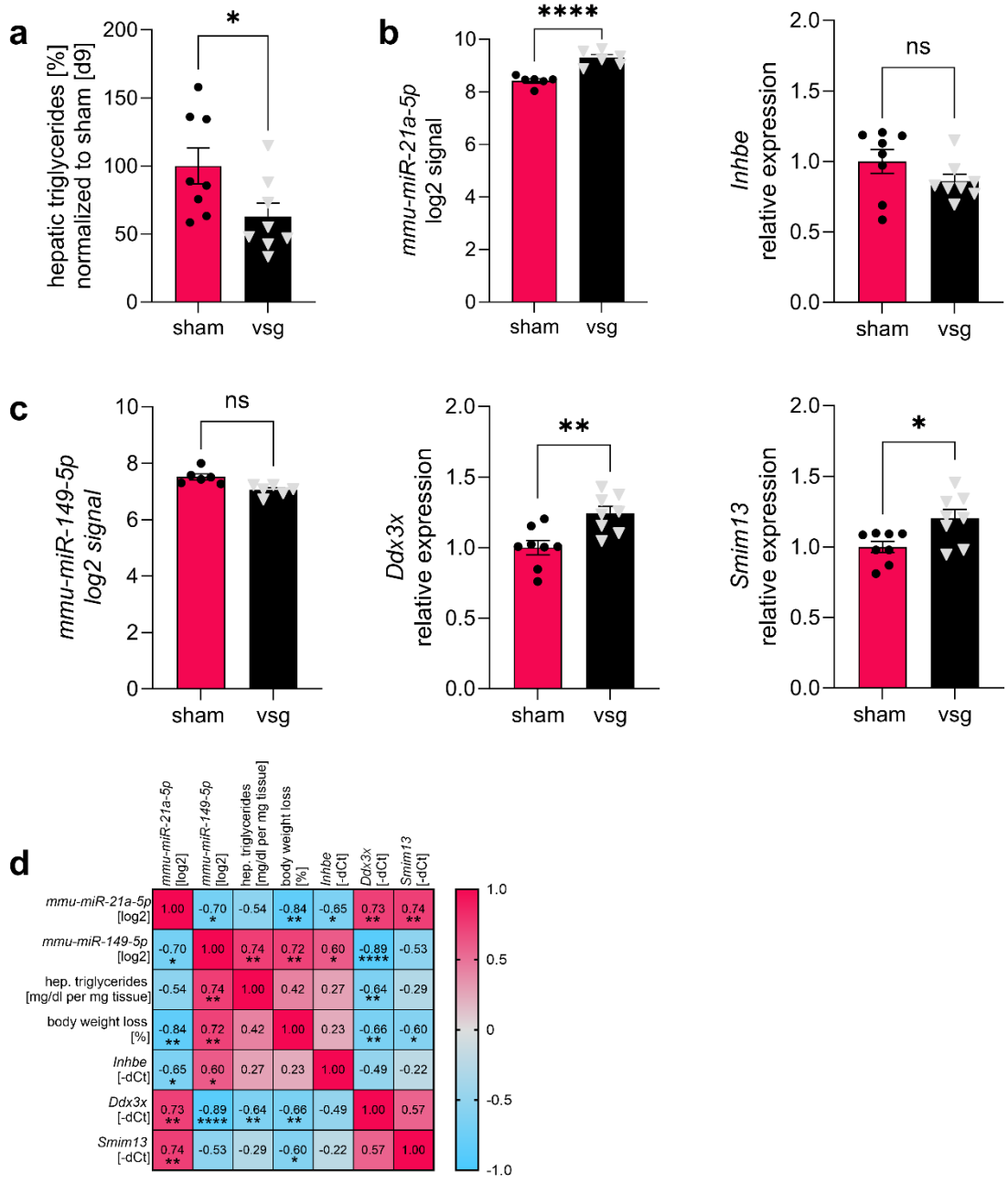

Figure 15: Hepatic triglyceride levels and gene expression in recovery phase nine days post-surgery. a: Hepatic triglyceride content normalized to sham control group (sham: n = 8, vsg: n = 8). b: MiRNA micro array expression of mmu-miR-21a-5p (log2 values, sham: n = 6, vsg: n = 6) and *Inhbe* gene expression measured in RT-qPCR (sham: n = 8, vsg: n = 8). c: MiRNA micro array expression of mmu-miR-149-5p (log2 values, sham: n = 6, vsg: n = 6) and *Ddx3x* and *Smim13* gene expression measured in RT-qPCR (sham: n = 8, vsg: n = 8). d: Pearson's correlation matrix of gene expression with hepatic triglycerides (hep. triglycerides) and body weight loss. The color label is according to Pearson's r correlation coefficient ranging from -1 (blue) to 1 (red). Statistical testing of hepatic triglyceride content using a student's two tailed t-Test on the not normalized [mg/dl per mg of tissue] data was performed. For statistical testing of RT-qPCR expression a student's two-tailed t-Test on the dCt values was performed. * = $p < 0.05$, ** = $p < 0.01$, *** = $p < 0.001$, **** = $p < 0.0001$ and ns = non-significant.

5.1.4.3. mmu-miR-149-5p is reversed in maintenance phase after VSG and correlates with hepatic triglyceride content

After 35 days post-surgery, vsg mice display 24.98 % ± 27.33 ($p = 0.0002$) of the hepatic triglyceride content when compared to control sham mice (Figure 16a). Interestingly, the increase in *mmu-miR-21a-5p* expression, which could be observed previously in the recovery phase, is abrogated in the maintenance phase, but *Inhbe* gene expression remains downregulated (0.6542 ± 0.24, $p = 0.0264$, Figure 16b). The tendency in reduced mmu-miR-149-5p expression during the recovery phase achieves significant downregulation in the maintenance phase (Δlog2: -1.51, $p = 0.0030$), which is accompanied by a moderate increase in *Ddx3x* (1.18 ± 0.17, $p = 0.08$) and significant upregulation of *Smim13* (1.47 ± 0.30, $p = 0.0014$) expression (Figure 16c). *Mmu-miR-21a-5p* expression correlates neither with hepatic triglycerides, body weight loss, nor *Inhbe* gene expression in the maintenance phase. In contrast, *mmu-miR-149-5p* expression correlates positively with hepatic triglycerides ($r = 0.84$, $p = 0.0001$) and body weight loss ($r = 0.64$, $p = 0.0360$), but negatively with target LCG expression *Ddx3x* ($r = -0.58$, $p = 0.0480$) and *Smim13* ($r = -0.67$, $p = 0.0170$, Figure 16d).
Overall, the reversed expression of *mmu-miR-21a-5p* in the recovery phase could be an indicator, that inflammation process are responsible for *mmu-miR-21a-5p* regulation, which are induced acutely after the surgery and are more dominant in vsg compared to sham surgery, rather than hepatic triglyceride or body weight changes. Contrary to regulation of *mmu-miR-149-5p*. The maintenance correlation with hepatic triglyceride content in the recovery and maintenance phase indicates either a triglyceride-dependent regulation of *mmu-miR-149-5p* or a role of *mmu-miR-149-5p* in balancing hepatic triglyceride content. Additionally, an interesting finding is that hepatic triglyceride content shows no correlation with body weight loss (Figure 15d & Figure 16d), which means that improvements in hepatic function and MASLD progression could be achieved independently of weight loss, since fat accumulation in hepatocytes is the major diagnostic marker of MASLD.

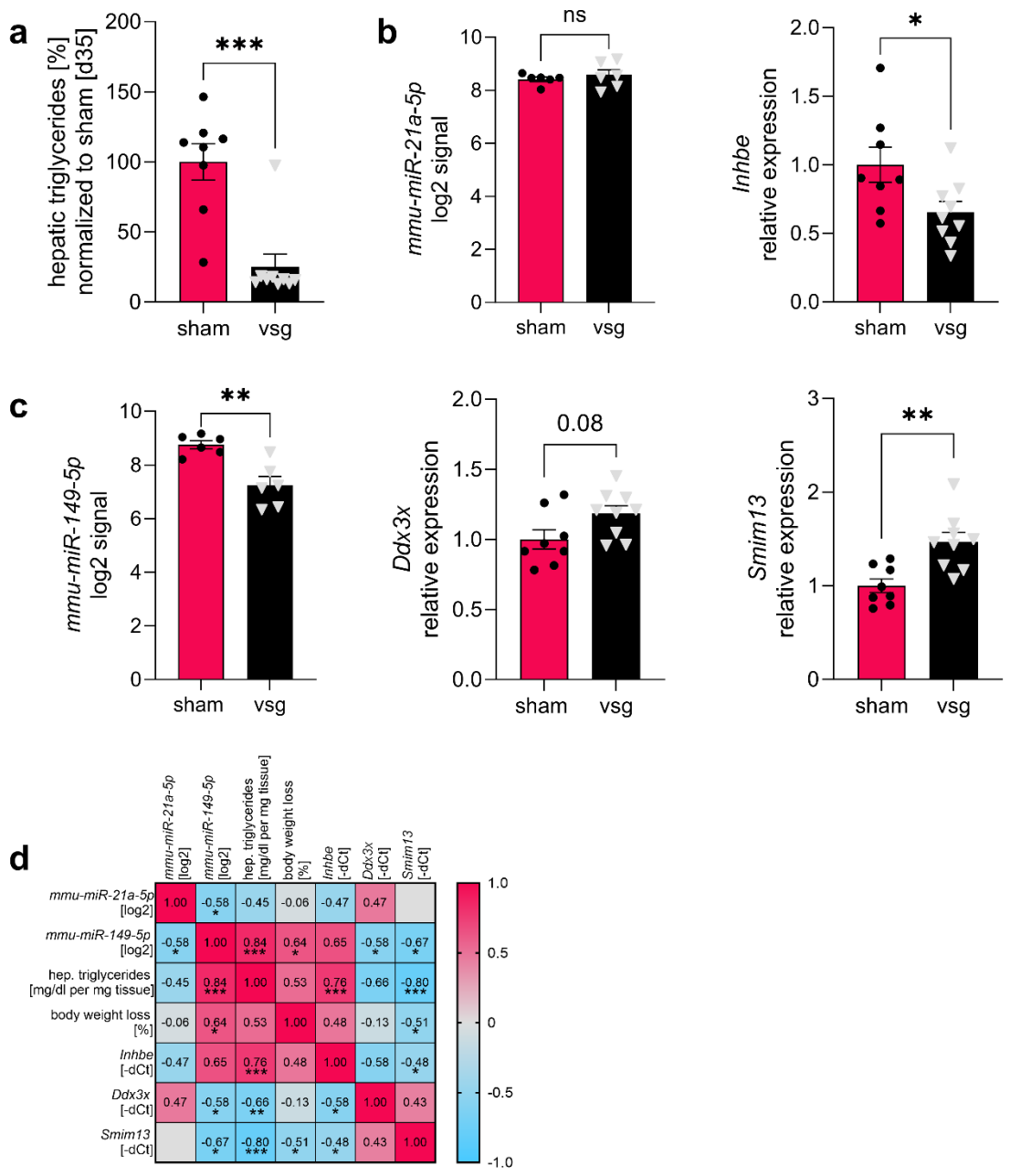

Figure 16: Hepatic triglyceride levels and gene expression in maintenance phase 35 days post-surgery. a: Hepatic triglyceride content normalized to sham control group (sham: n = 8, vsg: n = 9). b: MiRNA micro array expression of mmu-miR-21a-5p (log2 values, sham: n = 6, vsg: n = 6) and *Inhbe* gene expression measured in RT-qPCR (sham: n = 8, vsg: n = 9). c: MiRNA micro array expression of mmu-miR-149-5p (log2 values, sham: n = 6, vsg: n = 6) and *Ddx3x* and *Smim13* gene expression measured in RT-qPCR (sham: n = 8, vsg: n = 9). d: Pearson's correlation matrix of gene expression with hepatic triglycerides (hep. triglycerides) and body weight loss. The color label is according to Pearson's r correlation coefficient ranging from -1 (blue) to 1 (red). Statistical testing of hepatic triglyceride content using a student's two tailed t-Test on the not normalized [mg/dl per mg of tissue] data was performed. For statistical testing of RT-qPCR expression a student's two-tailed t-Test on the dCt values was performed. * = $p < 0.05$, ** = $p < 0.01$, *** = $p < 0.001$, **** = $p < 0.0001$ and ns = non-significant.

5.1.5. Metformin treatment depletes hepatic fat content and is associated with reversed *Inhbe* gene expression

The treatment of diet-induced obese mice with metformin is a weight-loss independent intervention model. Mice are fed for twelve weeks with a high-fat diet (hfd: n = 20) or standard control chow diet (chow: n = 10). After twelve weeks, a subgroup of the hfd cohort (met: n = 10) mice received 250 mg/kgBW/day of metformin via the drinking water for six weeks and the remaining mice continued on a hfd (hfd: n = 10). The body weight and hepatic triglyceride content have been published previously (Geißler et al. 2022).

The six week metformin treatment did not alter the body weight of hfd mice, but significantly reduced the hepatic triglyceride content (Figure 17a & b). On average, metformin treated hfd mice had 4.46 ± 2.89 fold increased hepatic triglyceride levels ($p = 0.0247$), whereas hfd mice showed 8.84 ± 3.65 fold increase ($p < 0.0001$) when compared to standard chow control mice (Figure 17b). In contrast, metformin treatment reduced hepatic triglyceride content by approximately 50 % (hfd vs. met: $p = 0.0042$). Interestingly, *mmu-miR-21a-5p* displayed no significant differences, neither after 18 weeks of hfd nor after the metformin treatment (Figure 17c). In contrast, mmu-miR-21a-5p target LCG *Inhbe* expression is significantly reduced after metformin treatment when compared to hfd mice (ΔFold change: -0.662, $p = 0.0251$, Figure 17c). *Mmu-miR-149-5p* expression shows no significant differences in expression after metformin treatment, but is induced in hfd and metformin treated mice when compared to standard chow diet control mice ($p < 0.0001$, Figure 17d). This is pattern is reflected in the two target LCGs *Ddx3x* and *Smim13*, which are significantly reduced in hfd and metformin mice. Pearson correlation of mmu-miR-21a-5p expression reveals a significant negative correlation with hepatic triglyceride content ($r = -0.41$, $p = 0.024$), but no other correlations are detected. Whereas mmu-miR-149-5p expression shows positive correlations with hepatic triglycerides (r 0 0.67, $p < 0.0001$) and body weight ($r = 0.90$, $p < 0.0001$). *Ddx3x* ($r = -0.87$, $p < 0001$) and *Smim13* ($r = -0.69$, $p < 0.0001$) show significant negative correlations with *mmu-miR-149-5p* expression (Figure 17e).

In summary, *mmu-miR-149-5p* shows a consistent association with hepatic triglyceride content, where higher levels of *mmu-miR-149-5p* correlate with higher hepatic triglyceride content over all intervention models. Additionally, higher *mmu-miR-149-5p* expression is associated with lower target LCG *Ddx3* and *Smim13* expression. An exception are the weight-loss intervention, which show no effect on the hepatic triglyceride content (diet switch, caloric restriction and exendin-4 treatment)., where *mmu-miR-149-5p* expression is not negatively correlated with *Smim13* expression. Still, those findings suggest a regulation of *Ddx3x* and *Smim13* by *mmu-miR-149-5p*, which might be driven by hepatic triglyceride content. Interestingly, *mmu-miR-21a-5p* shows no consistent pattern with any of the measured parameters. Surprisingly, *mmu-miR-21a-5p* expression is not significantly downregulated after 18 weeks of consistent high-fat diet (metformin intervention model), but is significantly reduced after 12 weeks (longitudinal mouse model) and 22 weeks in hfd-mice (diet switch, caloric restriction and exendin-4 treatment).

The results of the intervention models raise the questions, what is responsible for the change in *mmu-miR-149-5p* and *mmu-miR-21a-5p* expression.

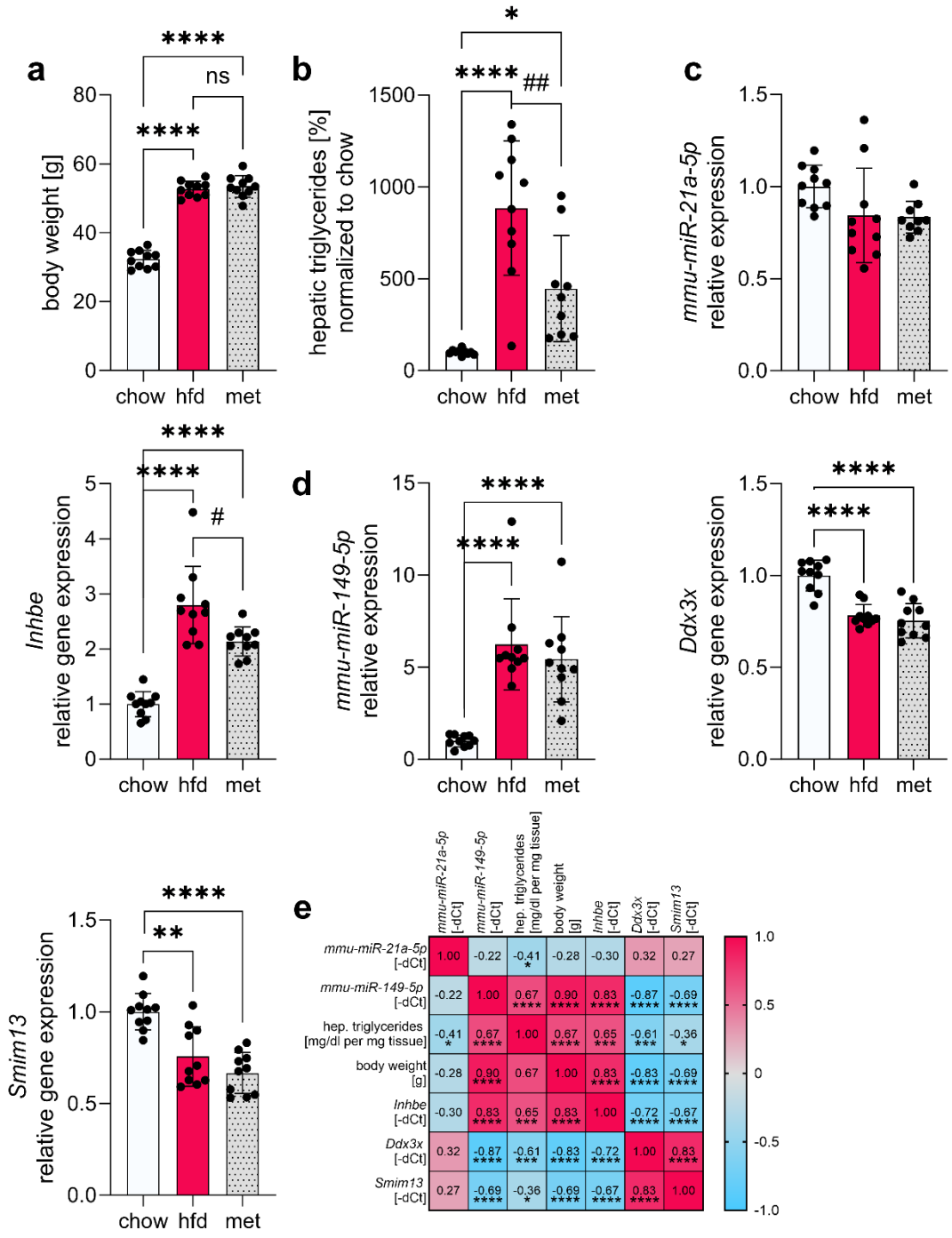

Figure 17: Body weight, hepatic triglyceride levels and miRNA/gene expression in the liver of metformin treated mice. a: Absolute body weight [g] of standard chow control diet-fed, hfd-fed and hfd-fed plus 6 weeks of metformin treated animals (n = 10). b: Hepatic triglyceride content [%] normalized to the chow control animals (chow/hfd: n = 10, met: n = 9). c: *mmu-miR-21a-5p* (chow/hfd: n = 10, met: n = 9) and target LCG *Inhbe* (n = 10) expression. d: mmu-miR-149-5p and target LCG Ddx3x and Smim13 expression (n = 10). e: Pearson's correlation matrix with numeric values indicating the Pearson correlation coefficient r. If not stated otherwise, data are shown as mean ± standard deviation. Gene expression data is measured in RT-qPCR and the single signal fold changes are normalized to the chow mean. For statistical testing, a One Way ANOVA on the dCt values is performed with * indicating significant differences to the chow control and # between hfd and metformin treated animals. * = p < 0.05, ** = p < 0.01, *** = p < 0.001, **** = p < 0.0001, # = p < 0.05, ## = p < 0.01 and ns = not significant.

5.1.6. Solving the cavities of interspecies miRNA-interactions with the miRNA Nvis tool

In the previous experiments, murine samples and models are used to investigate *mmu-miR-21a-5p* and *mmu-miR-149-5p*. With the transition into human in vitro models, such as HepG2 cells, it is important to ensure, if the miRNA sequence is conserved between both species or if there is no conserved equivalent in human. Sequence comparison between *mmu-miR-21a-5p* and its human equivalent *hsa-miR-21-5p* reveals a 100 % conserved sequence between both species as well as for *mmu-miR-149-5p* and its human counterpart *hsa-miR-149-5p* (Supplementary Table 2). However, validating the conservation of a miRNA sequence is not sufficient, since mRNA sequences may alter between mouse and human. It is crucial to perform a new seed sequence prediction in human. To solve this issue, the seed sequence prediction function of the miRNA Nvis tool was adapted from the murine to the human genome to study conserved miRNA/mRNA interactions. Therefor, the working procedure of the miRNA Nvis tool is explained.

MiRNAs interact mainly with the 3'-end untranslated region (3'UTR) of mRNAs by partial-complementary base pairing of the miRNA seed sequence and the miRNA-response element within the 3'UTR. This allows the prediction of miRNA-mRNA interactions based on simple seed matching (Krützfeldt et al. 2005). Though, there are many web-tool based databases, such as miRTarBase, TarBase or TargetScan (Lewis, Burge, and Bartel 2005) (Chou et al. 2018; Karagkouni et al. 2018), with deposited miRNA-mRNA interactions, it is complicated to integrate those information in a high-throughput manner and integration of real world expression data is infeasible. Therefore, I contributed to the development of the miRNA Nvis tool under the supervision of Christin Krause.

The miRNA Nvis tool contains a seed sequence prediction function, which allows the user to predict miRNA-mRNA interactions based on either a customized miRNA and mRNA gene list or own sequence information. Interactions between miRNAs with a subset of genes or the complete genome can be predicted for mouse and human with predefined sequence meta files. To fulfill this task, the seed sequence prediction function retrieves the miRNA sequence of interest information from Mirbase (Kozomara, Birgaoanu, and Griffiths-Jones 2019) and the 3'UTR-mRNA sequences of interest information from Ensembl version 110 (F. J. Martin et al. 2023). Both can optionally also be retrieved by biomaRt (Durinck et al. 2009) though the provided sequence meta files allow an offline usage for stable high throughput prediction. Subsequently, the function selects the longest 3'UTR-mRNA sequence of each gene of interest and performs a seed matching and calculates additional conditions of binding. In the output data, the binding position relative to the start of the 3'UTR, binding mode (8mer, 7mer etc), AU content 30 nt up and downstream of the seed pairing, additional base pairing within the miRNA backbone and binding energy are saved in a data frame. The miRNA/mRNA-pairs are added to an asymmetrical adjacency matrix with columns representing genes and rows representing miRNAs. Interactions in the adjacency matrix are coded 0 for no interaction and 1 for an interaction. Subsequently, this adjacency matrix is extended with the interactions deposited in the miRTarBas and TarBase databases. Predictions and validated database entries are encoded differently to discriminate between predictions and validated interactions. Afterwards, gene expression and miRNA expression data from RT-qPCR, bulk-mRNA sequencing or micro array are integrated and simple pearsons correlation analysis between miRNA/mRNA-pairs based on the generated adjacency matrix are performed. The correlation analysis is used to generate the network, where blue edges indicate a negative correlation of validated miRNA/mRNA pairs from the databases, red edges pairs from the seed sequence prediction and negative correlation, and grey edges show positive correlations with predicted or database validated miRNA/mRNA interactions. Alternatively, the network can also be generated without implementation of gene expression data and is solely drawn from the adjacency matrix (Figure 18**Error! Reference source not found.**).

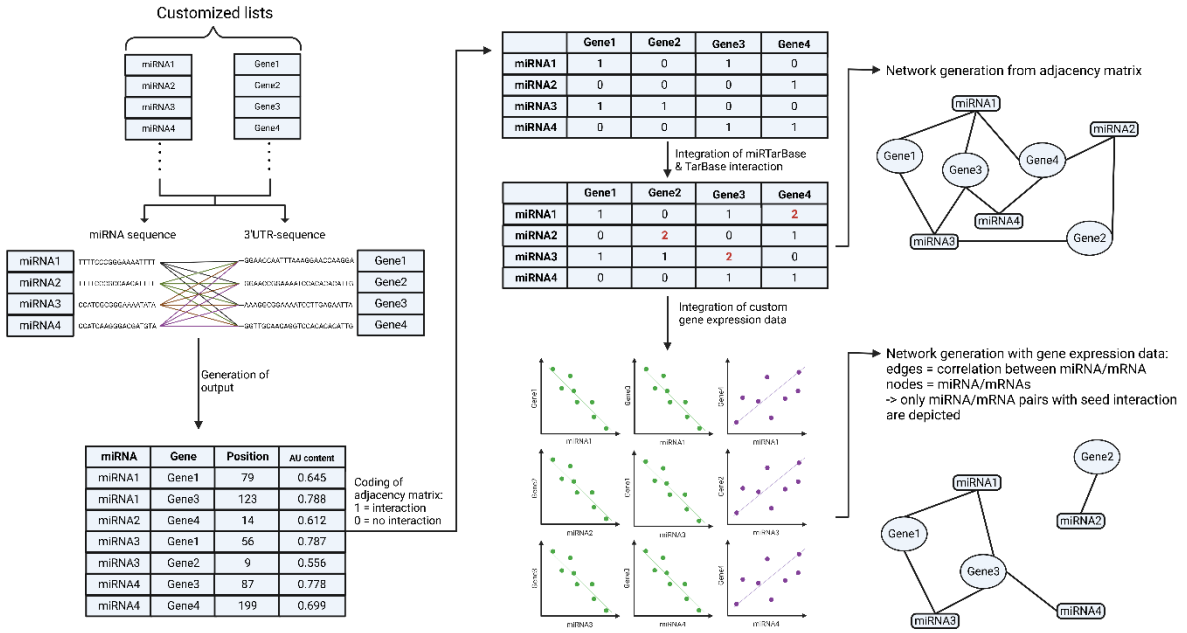

miRNA	Gene	Position	AU content
miRNA1	Gene1	79	0.645
miRNA1	Gene3	123	0.788
miRNA2	Gene4	14	0.612
miRNA3	Gene1	56	0.787
miRNA3	Gene2	9	0.556
miRNA4	Gene3	87	0.778
miRNA4	Gene4	199	0.699

	Gene1	Gene2	Gene3	Gene4
miRNA1	1	0	1	0
miRNA2	0	0	0	1
miRNA3	1	1	0	0
miRNA4	0	0	1	1

	Gene1	Gene2	Gene3	Gene4
miRNA1	1	0	1	2
miRNA2	0	2	0	1
miRNA3	1	1	2	0
miRNA4	0	0	1	1

Figure 18: Schematic procedure of the miRNA nVis tool. First, a customized gene and miRNA list or miRNA-sequence is submitted. Then, the seed sequence prediction function of the miRNA nVis tool performs a simple seed matching based on the longest 3'UTR of the gene list. The results are saved in a data frame object and based on miRNA/mRNA-interactions an asymmetric adjacency matrix is generated, where interactions are coded as 1 and no interactions with 0. Additionally, deposited miRNA/mRNA interactions are integrated from data bases, where validated interactions are coded as 2. Based on the miRNA/mRNA-interactions coded within the asymmetrical adjacency matrix pearsons correlation is performed from gene expression data and a network is generated.

This computational approach is very helpful in finding predicted miRNA target genes and the implementation of gene expression data serve as a further filter criteria, since miRNA binding can induce mRNA degradation and testing for negative correlations improves the quality of identifying target genes. The tool allows the integration of any target gene data, therefore protein measurements from proteomics or Western Blot could also be used in case of ribosomal drop off. From the drawn networks or output data, miRNA/mRNA pairs can be selected manually for further mechanistical investigations and identification of potential master regulators.

Investigating miRNA/mRNA interactions between species is challenging, since miRNA sequences and 3'UTR-mRNA sequences are frequently not conserved between the murine and human genome (Krause et al. 2023). This can lead to observations in mice, which might not be transferable into humans and vice versa. The miRNAvis therefore is a great tool to avoid transfer issues from mice into human studies, since networks or miRNA/mRNA prediction can be performed and compared for both species and subsequent selection of only conserved miRNA/mRNA interactions.

The miRNAvis tool receives updates consistently and functions to predict miRNA-exosome secretion or miRNA/mRNA binding prediction within exon and introns are in progress. Additionally, the integration of metabolomics data into the network is planned.

5.1.7. In vitro investigations in HepG2 cells and in obese human liver cohort to study mmu-miR-21a-5p and mmu-miR-149-5p expression

The collected data from the different mouse models raised the question, which factor is responsible for regulating the miRNA expression and is the expression levels in the liver of obese human. To investigate this question, hsa-miR-149-5p and hsa-miR-21-5p expression and their target LCGs are measured in the liver of obese human subjects (obese: n = 19) and obese subjects with type 2 diabetes (obese w/T2D: n = 21). This human cohort was stratified based on the *American Diabetes Association* (ADA) criteria, where subjects with an HbA1c level (in %) below 5.7 % are considered as non-diabetic and above or equal 6.5 % as diabetic (Committee 2021). The cohort parameters are listed in Table 30. Additionally, a variety of stimulations of HepG2 cells are tested, which are commonly used to induce or model MASLD *in vitro*. Widely distributed models are the treatment with fatty acids, such as palmitate/oleate solutions in different ratios, fructose or fructose/glucose treatments (F. A. Müller and Sturla 2019). Recently, myristic acid has been found to be upregulated in serum of type 2 diabetic subjects and shows a positive association with MASLD (Jiang and Sun 2022). Hence, HepG2 cells were treated with 0.5 mM palmitate/oleate solution in a ratio of 1:2, 50 mM fructose, 50 mM fructose with 25 mM glucose and 50 µM myristic acid.
The seed sequence prediction in human reveals a predicted binding between *DDX3X* (Figure 19a) and *INHBE* Figure 19b) with *hsa-miR-149-5p* and *DDX3X* and *SMIM13* with *hsa-miR-21-5p* (Figure 19c).

Table 30: Cohort parameters of the obese human liver cohort

	ob (n = 19)		T2D (n = 21)		
	Mean	SD	Mean	SD	p value
HbA1c [%]	5.24	0.41	8.17	1.51	**0.0000**
NASH Score	1.74	1.91	4.13	2.03	**0.0011**
Sex [m/f]	3/16		12/10		**0.0147**
BMI	51.88	9.35	49.17	8.48	0.3421
Age	37.05	9.28	52.14	11.16	**0.0000**
Glucose	95.05	9.29	170.14	79.60	**0.0002**
Triglyceride	161.56	88.33	258.20	128.57	**0.0113**

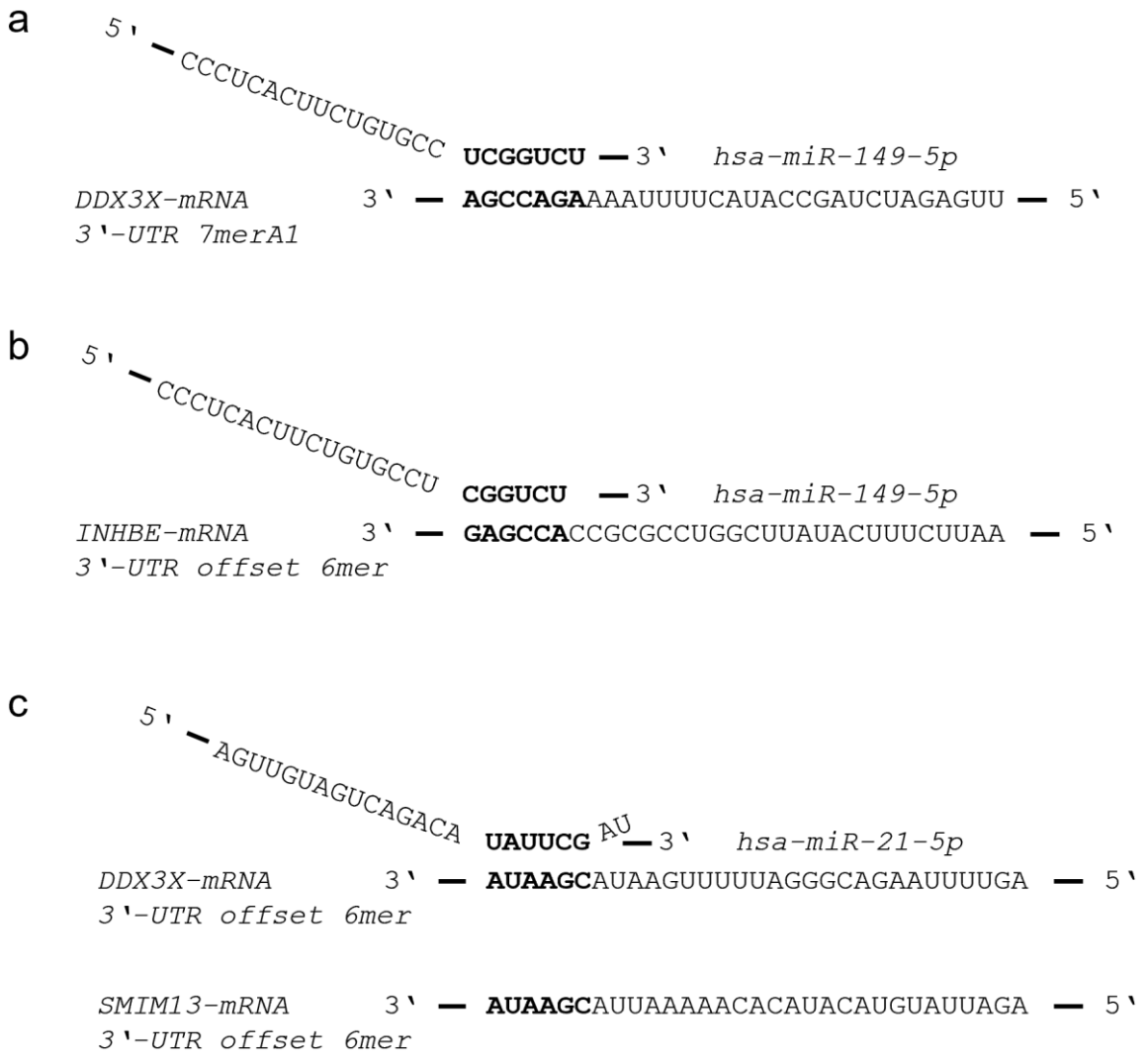

Figure 19: Target gene prediction of *hsa-miR-149-5p* and *hsa-miR-21-5p* with the LCGs *INHBE*, *DDX3X* and *SMIM13*. a: 7mer-A1 binding between the hsa-miR-149-5p seed-sequence with the DDX3X-3'UTR mRNA. b: Offset 6mer binding between the *hsa-miR-149-5p* seed-sequence with the *INHBE*-3'UTR mRNA. c: Offset 6mer binding between the *hsa-miR-21-5p* and *DDX3X*-3'UTR and *SMIM13*-3'UTR mRNA. The complementary binding between miRNA seed-sequence and the mRNA is highlighted in bold letters.

5.1.7.1. Hepatic hsa-miR-149-5p expression is upregulated and hsa-miR-21-5p shows tendency in obese subjects with type 2 diabetes

In the murine mouse model for DIO, *mmu-miR-21a-5p* is downregulated and *mmu-miR-149-5p* is upregulated in the liver after 12 weeks of hfd-feeding. Additionally, *mmu-miR-21a-5p* target LCG *Inhbe* is upregulated, whereas *mmu-miR-149-5p* target LCGs *Ddx3x* and *Smim13* are downregulated. This dysregulation of miRNA/LCG-pairs is partially reversed after interventions. However, murine mouse models may differ in disease progression and seed sequence prediction for the human genome reveals a target gene switch. In human, *hsa-miR-149-5p* targets the LCG *INHBE* and *DDX3X* and *hsa-miR-21-5p* the *DDX3X* and *SMIM13*. To validate that miRNA/LCG-interactions are also conserved in human, miR-21-5p and miR-149-5p are overexpressed in HepG2 cells using mirVana mimics. Additionally, hepatic miRNA and LCG expression is measured in an obese human liver cohort stratified into subjects with

high and low HbA1c levels. Also to characterize a role of *miR-21-5p* and *miR-149-5p*, a glucose uptake assay in HepG2 cells after overexpression is performed, since in the murine models both miRNAs correlate with blood glucose levels.

Interestingly, after overexpression of *miR-149-5p* in HepG2 cells, the target LCG *INHBE* is significantly downregulated, whereas *DDX3X* expression remains unaltered (Figure 20a). Overexpression of *miR-21-5p* shows no significant effect on the gene expression of target LCGs *DDX3X* and *SMIM13 (*Figure 20b).

In the liver of obese subjects with type 2 diabetes, hsa-miR-21-5p shows a tendency to be 1.27 ± 0.48 fold upregulated when compared to obese subjects without type 2 diabetes (p = 0.1316), whereas hsa-miR-149-5p is significantly upregulated by 1.42 ± 0.50 fold (p = 0.0001). Interestingly, only *INHBE* gene expression, a predicted target LCG of the *hsa-miR-149-5p* in human, is significantly upregulated in obese subjects with type 2 diabetes (1.47 ± 0.74, p = 0.0242), but *DDX3X* and *SMIM13* show no significant differences (Figure 20c). Hsa-miR-21-5p shows no significant correlation with metabolic parameters, such as fasting glucose levels or serum triglycerides. However, hsa-miR-149-5p expression correlates positively with *INHBE* expression (r = 0.48, p = 0.002), *SMIM13* expression (r = 033, p = 0.038), HbA1c levels (r = 0.41, p = 0.008) and age (r = 0.35, p = 0.025). Additionally, higher expression levels of hsa-miR-149-5p are associated with higher fasting glucose (r = 0.29, p = 0.067) or serum triglyceride levels (r = 0.31, p = 0.057, Figure 20d). The positive correlation between hsa-miR-149-5p and its predicted target LCG *INHBE* indicates no regulatory function of *hsa-miR-149-5p* by RNA-interference in the human liver, even though miR-149-5p overexpression in HepG2 cells results in significant reduction of *INHBE* gene expression.
Hsa-miR-21-5p tends to be upregulated in obese subjects with type 2 diabetes and *hsa-miR-149-5p* is significantly upregulated. This assumes a role in regulating the glucose uptake in the liver, most likely independent of the investigated local controlling genes. To test this hypothesis, a glucose uptake assay in HepG2 cells was performed after overexpression of either *hsa-miR-21-5p* or *hsa-miR-149-5p* for 24 hours. Additionally, to differentiate between insulin-independent and insulin-dependent glucose uptake, the experiment was conducted without insulin stimulation (w/o insulin) and insulin stimulation (insulin) for 15 minutes prior to the assay. Interestingly, overexpression of *hsa-miR-21-5p* enhances insulin-independent glucose uptake (1.27 ± 0.14, p = 0.0056) when compared to the mock transfection, whereas *hsa-miR-149-5p* overexpression decreases insulin-dependent glucose uptake (0.75 ± 0.05, p = 0.0037, Figure 20e).
In summary, the human data suggest a role of *hsa-miR-21-5p* and *hsa-miR-149-5p* in obesity-associated MASLD and a role in regulating hepatic glucose metabolism. However, this seems to be independent of the local controlling genes *INHBE*, *DDX3X* and *SMIM13*.

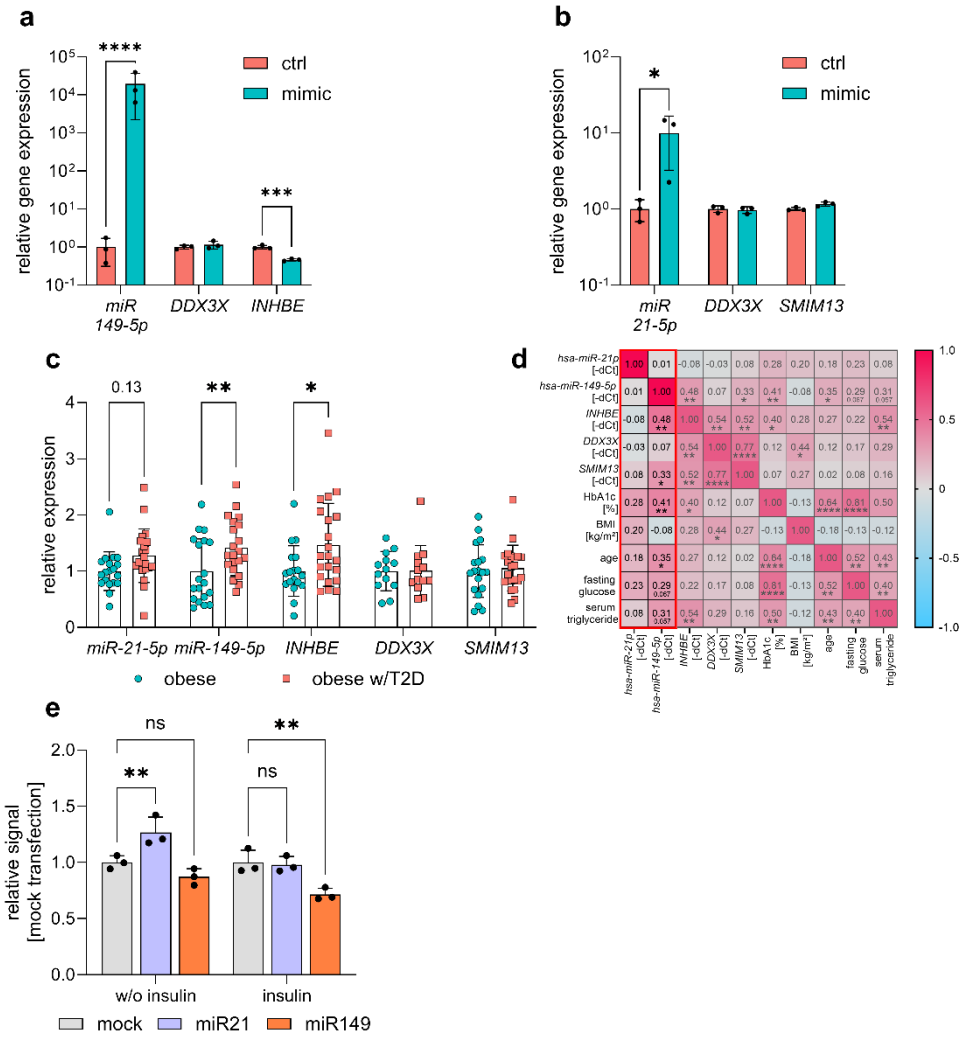

Figure 20: MiRNA and target LCG expression after miR-149-5p and miR-21-5p overexpression in HepG2 cells and in obese human liver cohort. a: *Hsa-miR-149-5p* and target LCG DDX3X & INHBE gene expression in miR-149-5p overexpressing HepG2 cells. b: Hsa-*miR-21-5p* and target LCG *DDX3X* & *SMIM13* gene expression in miR-21-5p overexpressing HepG2 cells. c: Hepatic *hsa-miR-21-5p*, *hsa-miR-149-5p*, *INHBE*, *DDX3X* and *SMIM13* gene expression (obese: n = 19, obese w/T2D: n = 21) measured in RT-qPCR. For statistical testing a multiple student's T-test is performed with the dCt values. P-values are adjusted according to FDR = 0.05 with *** = padj. < 0.001, * = padj. < 0.05 and numeric = padj. d: Pearson correlation matrix of miRNA and LCG expression with HbA1c, BMI, age, fasting glucose and serum triglyceride levels. The most relevant correlations are highlighted in the red box. Numeric values indicate the Pearson correlation coefficient r and * = $p < 0.05$, ** = $p < 0.01$, *** = $p < 0.001$ and **** = $p < 0.0001$. e: Relative luciferase signal of the glucose uptake assay in HepG2 cells after hsa-miR-21-5p or hsa-miR149-5p overexpression. Cells are either unstimulated (w/o insulin) or stimulated with insulin (insulin) 15 min. prior to performing the assay. Signals are normalized to the mock transfection with a scrambled control mirVana mimic. The experiment is repeated on three different days and cell passages (n = 3) in technical triplicates. Each point resembles the mean of the technical triplicates of each individual n. For statistical analysis, a One-Way ANOVA is performed with ns = not significant and ** = $p < 0.01$.

5.1.7.2. Metabolic challenge of HepG2 cells shows no effect on hsa-miR-21-5p and hsa-miR-149-5p expression

Since *hsa-miR-149-5p* is significantly upregulated and *hsa-miR-21-5p* shows tendencies for upregulation in the liver of obese subjects with high HbA1c levels, several metabolic stimulations of HepG2 cells are tested to investigate the cause of miRNA induction. The different metabolic stimulations are selected based on commonly used in vitro models for MASLD, such as high fructose treatment (Swapna Sasi, Sindhu, and Raghu 2020) or based on the correlation analysis of human miRNA expression with blood parameters. Hsa-miR-149-5p correlates positively with HbA1c levels and also miR-149-5p overexpression reduces insulin-stimulated glucose uptake. Therefore, glucose might play a role in miR-149-5p regulation. Also, a weak correlation with serum triglycerides with miR-149-5p is observed and therefore HepG2 cells are treated with the most common fatty acids palmitate and oleate, which are needed for triglyceride synthesis as mentioned previously (Ogawa et al. 2018). Additionally, myristic acid, an long-chain saturated fatty acid, was chosen, since it is reported to be positively associated with MASLD-risk (Jiang and Sun 2022).
Interestingly, with no metabolic stimulation of HepG2 cells an induction in miR-21-5p or miR-149-5p expression is achieved (

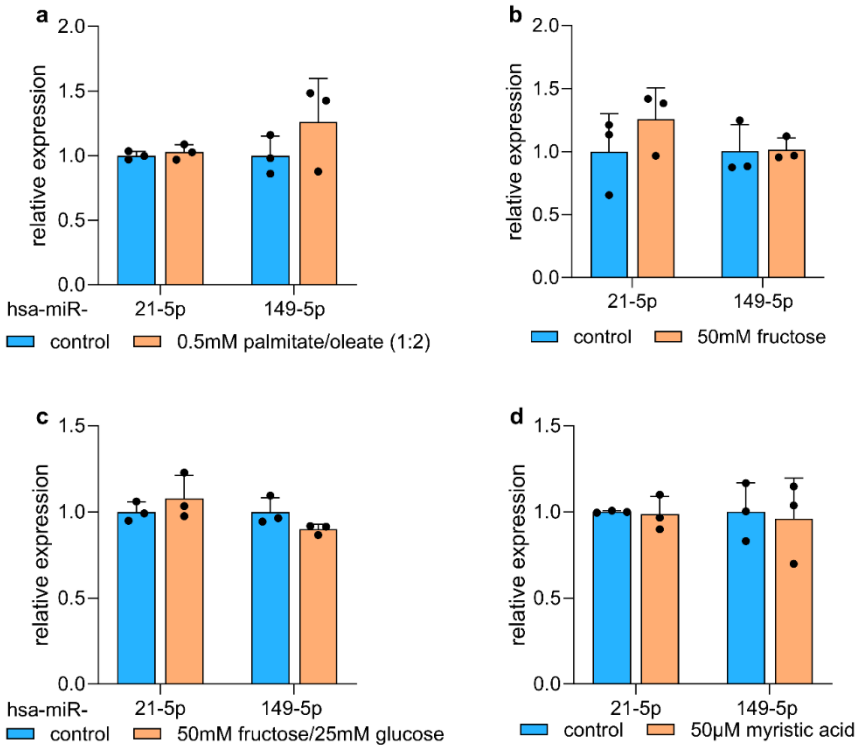

Figure 21). Only a minor, non-significant increase in miR-149-5p expression to

Figure 21: miRNA expression after treatment of HepG2 cells with palmitate/oleate, fructose, fructose and glucose or myristic acid. Experiments are repeated at three different days with three different cell passages (n = 3) in either technical duplicates or triplicates. Points represent the mean of each n. For statistical analysis a student's t-test with the dCt values is performed.

1.26 ± 0.33 fold is observed (p = 0.28) after treatment of HepG2 cells with palmitate/oleate (

Figure 21a). Also, hsa-miR-21-5p expression slightly increases to 1.26 ± 0.25 fold (p = 0.32) after the treatment of HepG2 cells with 50 mM fructose (

Figure 21b)

In summary, there are no significant changes in miRNA expression after metabolic challenging of HepG2 cells.

5.2. Hsa-miR-149-5p is a central regulator of metabolic pathways in MASLD

Since the hypothesis of *miR-21-5p* and *miR-149-5p* contributing to MASLD by regulating the local controlling genes *INHBE*, *DDX3X* and *SMIM13* could not be proven, but miR-149-5p shows great potential as regulator in the disease progression, the second aim was to evaluate novel target genes and pathways, which are not the previously described LCGs and therefore contribute to MASLD progression. Because the interspecies transfer between mouse and human displays great difficulties in miRNA research, right from the beginning the focus is on finding conserved target genes between both species.

5.2.1. Conserved and predicted target genes of hsa-miR-149-5p are enriched in metabolic pathways

MiR-149-5p displays a great potential to be involved in MASLD progression based on the findings from DIO mouse models and obese human subjects with Type 2 diabetes, where miR-149-5p expression is elevated in the liver. Thus, this investigation tries to identify novel miR-149-5p target genes, which are conserved between the murine and human genome that play a role in MASLD progression independent from the LCGs. To find those novel target genes, hsa-miR-149-5p was artificially overexpressed in HepG2 cells using RNAiMAX transfection of mirVana mimics combined with subsequent bulk-mRNA sequencing.
After overexpression of *hsa-miR-149-5p* (Figure 22a, $p < 0.0001$), bulk-mRNA sequencing is performed. Principal component analysis (PCA) from the raw gene count reveals two separated and clearly distinguishable populations, one carrying the hsa-miR-149-5p mirVana mimic and the second carrying a mirVana mimic control, where the first principal component explains 37.4 % and the second principal component 26.4 % of the variance (Figure 22b). In total, 931 genes are down and 813 genes are significantly upregulated (padj < 0.05) in HepG2 cells transfected with the hsa-miR-149-5p mimic, which is also depicted in hierarchical-heatmap clustering (Figure 22c & d). Gene ontology analysis of differentially expressed genes (DEGs) shows enrichment for pathways involved predominantly in liver-related terms, such as liver cirrhosis, liver carcinoma and liver fibrosis, aside from non-liver specific cancer pathways (Figure 22e). However, to discriminate between direct and indirect *hsa-miR-149-5p* effects, a whole miR-149-5p targetome prediction with subsequent pathway analysis considering only conserved, predicted and significantly downregulated *hsa-miR-149-5p* target genes is performed. In mouse a total of 9078 target genes are predicted, whereas in human 11005 are predicted. The intersection of 6071 target genes between both species is characterized as conserved targetome (Figure 22f, bar plot). In general 46.56 % of the conserved targetome is expressed in human liver tissue (Figure 22f, upper pie chart), of which in turn 81.17 % are expressed in HepG2 cells (Figure 22f, lower pie chart). Since the majority of the conserved targetome is also expressed in HepG2 cells, the cell line is a suitable model to investigate the function of *hsa-miR-149-5p*. Subsequent pathway analysis of conserved, significantly downregulated *hsa-miR-149-5p* target genes using the gprofiler2 R-package are enriched in the reactome pathway ‚GABA synthesis, release, reuptake and degradation' (padj = 0.026, Figure 22g), of which the involved genes *ABAT* (log2 FC: -1.53 ± 0.22, padj. < 0.0001), *SLC6A12* (log2 FC: -2.49 ± 0.66, padj. < 0.0001) and *ALDH5A1* (log2 FC: -1.54 ± 0.23, padj. < 0.0001) are significantly downregulated (Supplementary Figure 4). Interestingly, those genes are part of the citrate

cycle-(TCA) salvage pathway called GABA shunt, in which GABA is degraded to retrieve succinate (Geisler et al. 2021).The GABA/betaine transporter BGT1 (*SLC6A12* gene), links the metabolic pathways GABA shunt and TCA to the methionine/folate (one carbon metabolism) and urea cycle, since betaine serves as precursor for methionine synthesis (Figure 22h). Further investigations of those connected metabolic pathways reveal a significant downregulation of the TCA-related genes *IDH1* (log2 FC: -1.35 ± 0.24, padj. < 0.0001), *IDH2* (log2 FC: -1.29 ± 0.21, padj. < 0.0001), *ACLY* (log2 FC: -0.86 ± 0.0.17, padj. < 0.0001) and *AGXT* (log2 FC: -1.26 ± 0.43, padj. = 0.0292). Additionally, methionine and folate cycle-related genes *MAT1A* (log2 FC:-1.19 ± 0.18, padj. < 0.0001), *DHFR* (log2 FC: -1.13 ± 0.27, padj. = 0.0007) and *SHMT2* (log2 FC: -2.63 ± 0.21, padj. < 0.0001) are significantly down and *MTAP* (log2 FC: 1.77 ± 0.34, p < 0.0001) significantly upregulated. Further, The urea cycle gene *CBS* is significantly downregulated (log2 FC: -0.61 ± 0.22, padj. = 0.0426, Figure 22i). In total, 11 genes involved in the metabolic pathways are downregulated and 2 upregulated (Figure 22j). It is noteworthy that the *ARG1* and *OTC* gene are not detected in the bulk-mRNA sequencing. All genes involved in the metabolic pathways and if they are conserved, human or mouse predicted miR-149-5p targets is summarized in Table 31.

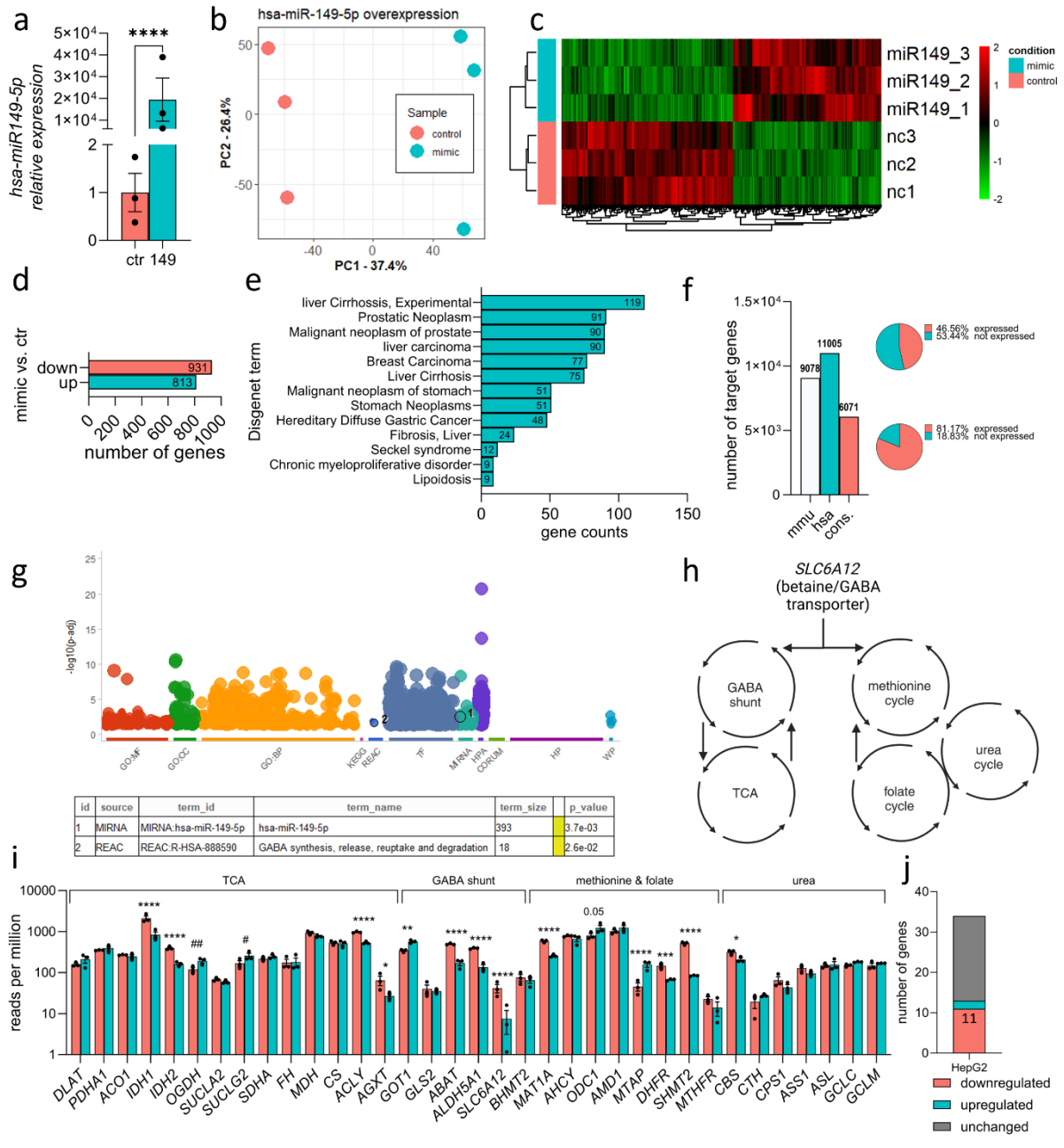

Figure 22: miR-149-5p target genes are enriched in metabolic pathways. a: Overexpression of miR-149-5p in HepG2 cells using mirVana mimics. b: Principal component analysis of bulk-mRNA sequencing after miR-149-5p overexpression. c: Disgenet term gene ontology analysis of differentially expressed genes (DEGs) using DAVID. d: Number of DEGs. e: Number of genes predicted as miR-149-5p target gene in mouse (mmu, mmu-targetome), human (hsa, hsa-targetome) and conserved (cons., conserved-targetome). Pie diagrams display the percentage expression of miR-149-5p conserved targetome in human liver (upper pie-diagram) and percentage expression of miR-149-5p conserved targetome in human liver and HepG2 cells (lower pie-diagram). f: Gene ontology an REACTOME enrichment for significantly downregulated, predicted, conserved targetome after miR-149-5p overexpression. g: Schematic overview that highlights the connection between amino acid cycles by the SLC6A12 gene. h: Heatmap displaying gene expression profile of genes involved in TCA, GABA shunt, methionine & folate cycle and urea cycle after miR-149-5p overexpression. i: Single reads per million of genes involved in TCA, GABA shunt, methionine & folate cycle and urea cycle from bulk-mRNA sequencing after miR-149-5p overexpression. j) Absolute number of genes downregulated, upregulated or unchanged from TCA, GABA shunt, methionine & folate cycle, and urea cycle. For statistical testing of bulk-mRNA sequencing the Wald test (integrated in DESeq2) was used with * = padj < 0.05, ** = padj < 0.01, *** = padj < 0.001, **** = padj < 0.0001, # = p < 0.05, ## = p < 0.01.

Table 31: Overview of detected miR-149-5p target genes by seed-sequence prediction to the 3'UTR-mRNA in mouse and human

Gene	Pathway	conserved	human	mouse
AGXT	TCA	yes	yes	yes
DLAT	TCA	no	no	no
PDHA1	TCA	yes	yes	yes
ACLY	TCA	yes	yes	yes
CS	TCA	no	no	no
ACO1	TCA	yes	yes	yes
IDH1	TCA	no	yes	no
IDH2	TCA	no	yes	no
OGDH	TCA	yes	yes	yes
SUCLA2	TCA	no	yes	no
SUCLG2	TCA	no	no	no
SDHA	TCA	no	no	yes
FH1	TCA	no	no	no
MDH1	TCA	no	no	no
GOT1	GABA	no	yes	no
GLS2	GABA	yes	yes	yes
ABAT	GABA	yes	yes	yes
ALDH5A1	GABA	yes	yes	yes
SLC6A12	GABA	yes	yes	yes
BHMT	methionine	no	yes	no
MAT1A	methionine	yes	yes	yes
AHCY	methionine	no	yes	no
ODC1	methionine	no	no	no
AMD1/AMD2	methionine	no	no	no
MTAP	methionine	yes	yes	yes
DHFR	folate	yes	yes	yes
SHMT2	folate	yes	yes	yes
MTHFR	folate	yes	yes	yes
CBS	urea	no	no	yes
CTH	urea	no	no	no
CPS1	urea	no	yes	no
OTC	urea	yes	yes	yes
ASS1	urea	no	no	no
ASL	urea	no	yes	no
ARG1	urea	no	no	no
GCLC	urea	yes	yes	yes
GCLM	urea	no	yes	no

5.2.2. Overexpression of hsa-miR-149-5p alters intracellular and extracellular metabolome of HepG2 cells

The bulk-mRNA sequencing analysis after *hsa-miR-149-5p* overexpression from HepG2 cells implies a crucial role of *hsa-miR-149-5p* in the regulation of the previously described metabolic pathways.

However, differences in mRNA expression have to be interpreted with caution in regards to an actual cellular response, since not all transcriptional changes are translated onto the protein levels. Even though protein levels are another layer of investigating miRNA-mRNA interactions, another final cellular response are changes on metabolite levels, which reflect the metabolic state of a cell (Martins-de-Souza 2014).

To evaluate further effects of *hsa-miR-149-5p* and potential mechanism contributing to MASLD progression, metabolite levels are measured in HepG2 cells (cellular) and in the supernatant medium, in which the cells are cultured (extracellular), after overexpression of *hsa-miR-149-5p* using the same procedure as for the bulk-mRNA sequencing. Metabolomics are performed 48 hours after incubation of the cells with *hsa-miR-149-5p* mirVana mimic (Figure 23a). Subsequent principal component analysis of the normalized relative abundance of the metabolites shows two distinguishable populations of hsa-*miR-149-5p* overexpressing cells (mimic) and mirVana mimic control expressing cells for the cellular fraction (control), where the first principal component explains 46.6 % and the second principal component 26.1 % of the variance. PCA from metabolomics of the extracellular fraction reveals that the first principal component explains 45.5 % and the second 22.6 % of the variance. One control mimic transfection and one miRNA-mimic transfection cluster together (Figure 23b). In total, two metabolites are significantly reduced, whereas 28 metabolites are significantly enriched in the cellular fraction ($log2 < | > 0$, $p < 0.05$, Supplementary Table 10), which are shown in the hierarchical-heatmap clustering (Figure 23c). From the metabolites involved in the metabolic pathways, citrulline, urea, ornithine and serine are significantly enriched (Figure 23c, bar plot). Additionally, in the extracellular fraction also differences in metabolite levels are detected. Although PCA of the normalized relative abundance shows no clear separation (Figure 23b), in total 10 metabolites are significantly reduced and three significantly enriched in the extracellular fraction (Supplementary Table 11, Figure 23d). Metabolites associated with the methionine/folate cycle 5-Methylthioadenosine (MTA) and folate are significantly reduced and choline is significantly increased. Also, malate involved in the TCA is significantly reduced and putrescine of the urea cycle is significantly increased (Figure 23d, bar plot). Interestingly, metabolite set enrichment analysis (MSEA) of differentially enriched metabolites (DEMs) show significant enrichment for metabolites involved in the urea cycle ($p < 0.0211$) and beta-alanine metabolism (0.0354) for the cellular fraction (Figure 23f, left plot) and significant enrichment for methionine metabolism ($p = 0.0067$), spermidine and spermine biosynthesis ($p = 0.0126$), and purine metabolism (0.0307) for the extracellular fraction (Figure 23f, right plot).

Especially the enrichment for the urea cycle and methionine metabolism align with the results previously described after bulk-mRNA sequencing, further emphasizing the capability of hsa-miR-149-5p altering not exclusively the gene expression of metabolic pathway-related genes, but also the metabolite levels of those pathways.

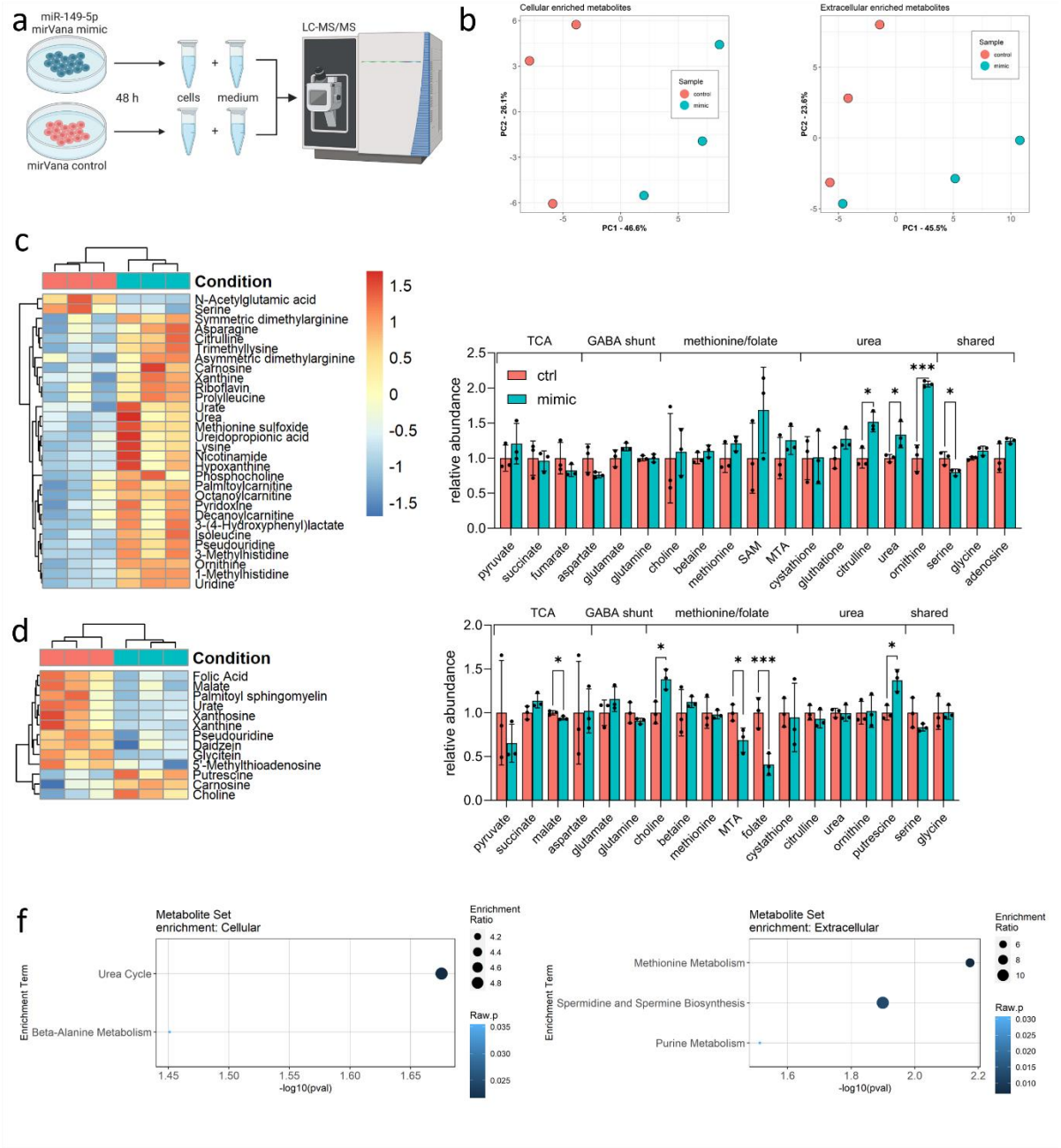

Figure 23: Overexpression of hsa-miR-149-5p alters intracellular and extracellular metabolome of HepG2 cells. a: Hsa-miR-149-5p was overexpressed in HepG2 cells for 48 hours using miRvana mimics and subsequently metabolomic measurements were performed from cells (cellular) and medium (extracellular). b: Principal component analysis of metabolites measured from cells (cellular) and medium (extracellular). c: Hierarchical clustering of differentially enriched metabolites in cellular fraction and measured metabolites involved in metabolic pathways. d: Hierarchical clustering of differentially enriched metabolites in extracellular fraction and measured metabolites involved in metabolic pathways. f: Metabolite set enrichment analysis plots performed with MetaboAnalyst for cellular (left) and extracellular (right) fraction. Differentially enriched metabolites were defined by $p < 0.05$ and log2 fold change < or > 0. The experiment was repeated at three different days (n = 3).

5.2.3. Conserved miR-149-5p target genes are downregulated in DIO mice and are associated with differences in the metabolome

The *in vitro* experiments in HepG2 cells, but also the previously described data from different mouse models (see 5.1) strengthen the role of *miR-149-5p* in MASLD progression by regulating metabolic pathways (TCA, GABA shunt, methionine/folate cycle, urea cycle) within the liver. However, the situation and gene expression patterns of these metabolic pathways during MASLD in this context has not been elucidated yet. Therefore, again the endpoint of twelve weeks of hfd-feeding of the longitudinal DIO mouse model (see 4.2.1) is investigated and combined with hepatic metabolomics from the same mice. Hepatic gene expression data from microarrays are reanalyzed that have been previously published (Geißler et al. 2022). PCA of hepatic gene expression and hepatic metabolomics show two separated populations, one displaying the standard chow control mice group (chow) and the other the high-fat diet fed group (hfd, Figure 24a). In total, 1482 genes are significantly up and 1083 significantly downregulated (padj. < 0.05), whereas three metabolites are significantly enriched and 54 significantly reduced in the hfd mice ($p < 0.05$, Figure 24b). Afterwards, genes are annotated to their perspective KEGG reaction ids to retrieve the information of the involved metabolites in those reactions, which are catalyzed by the gene. This allows to separate between DEGs and DEGs with DEMs. From the total of 2320 DEGs and 342 genes with DEMs, an overlap of 67 genes are differentially expressed and are associated with differentially enriched metabolites (Figure 24c). Hierarchical heatmap clustering of DEGs, DEMs and DEGs with DEMs reveal that the genes *Cbs* (log2 FC = - 1.46, padj. = 0.0414) , *Agxt* (log2 FC = - 1.93, padj. = 0.0010), *Cth* (log2 FC = - 1.79, padj. < 0.0001) and *Gls2* (log2 FC = - 2.00, padj. = 0.0009), which are involved in the metabolic pathways, are downregulated after twelve weeks of hfd-feeding and display also dysregulated levels of associated metabolites (Figure 24d). Additionally, the urea cycle gene Arg1 is significantly downregulated, which was not expressed in HepG2 cells (log2 FC = - 1.36, padj. = 0.0421). Functional gene ontology analysis of DEGs shows significant enrichment of genes involved in the urea cycle (padj. < 0.0228), beside the more dominant pathways involved in fatty acid metabolism. DEMs are significantly enriched in pathways of ammonia recycling ($p = 0.0005$), methionine ($p = 0.0028$) and betaine metabolism ($p = 0.0054$) and urea cycle ($p = 0.0155$, Figure 24e).

This analysis focuses on only differentially expressed genes with differentially enriched metabolites associated with the metabolic pathways, but it is very likely that target genes of *miR-149-5p* are differentially expressed without significant changes on the metabolite levels. Additionally, non-significant changes of metabolites can also be attributed to effects of *miR-149-5p*. Therefore, the expression of the remaining genes and metabolites associated with the metabolic pathways are shown and correlated with *miR-149-5p* expression.

Interestingly, there are no significant differences in the TCA cycle after hfd-feeding after adjustment of the p value by FRD, except for the *Agxt* (log2 FC = - 1.93, padj. = 0.0002) gene (*Dlat*: log2 FC = - 1.19, $p = 0.0356$, padj. = 0.2771; *Pdha1*: log2 FC = 1.30, $p = 0.0049$, padj. = 0.0977; *Suclg2*: log2 FC = 1.21, $p = 0.0068$, padj. = 0.1178; *Fh1*: log2 FC = - 1.16, $p = 0.0439$, padj. = 0.3042). On the other hand, the GABA shunt is consistently downregulated, which was also shown for the genes *ABAT*, *ALDH5A1* and *SLC6A12* in the in vitro experiments after *miR-149-5p* overexpression (*Got1*: log2 FC = - 1.70, $p = 0.0017$, padj. = 0.0531; *Gls2*: log2 FC = -2.00, padj. = 0.0009; *Abat*: log2 FC = - 1.15, padj = 0.005; *Aldh5a1*: log2 FC = - 1.05, padj. = 0.041; *Slc6a12*: log2 FC = - 1.13, padj. = 0.011; Figure 25a). Noteworthy, the *Got1* gene encodes the *aspartate aminotransferase* AST, which is commonly elevated in the serum of MASLD patients and is a marker for disease progression. It may seem counterintuitive giving the transcriptional downregulation in the liver after hfd-feeding.

Additionally, genes involved in the urea cycle are dominantly downregulated after hfd-feeding, aside the previously named *Cbs* gene (*Cth*: log2 FC = - 1.79, padj. = 0.0015; *Cps1*: log2 FC = -1.55, $p = 0.0003$;

Otc: -1.22, p = 0.0264, padj. = 0.2377; *Ass1*: log2 FC = -1.51, padj. = 0.0066; *Asl*: log2 FC = -1.62, padj. = 0.0226; *Arg1*: log2 FC = -1.36, padj. = 0.0421). However, after twelve weeks of hfd-feeding, there are minor changes in the methionine & folate cycle (*Bhmt*: 1.21, p = 0.0139, padj. = 0.1693; *Ahcy*: -1.19, p = 0.0040, padj. = 0.0882; *Odc1*: log2 FC: = 1.24, p = 0.0114, padj. = 0.1553; Figure 25a).
The majority of the downregulated genes correlate negatively with *mmu-miR-149-5p* expression (*Agxt, Got1, Gls2, Abat, Aldh5a1, Slc6a12, Cbs, Cth, Cps1, Otc, Ass1, Asl, Arg1* and *Ahcy). Odc1* correlates positively with *mmu-miR-149-5p* expression (Figure 25b, for correlation values see Supplementary Table 3). The downregulation of metabolic pathway-associated genes is also manifested in significant changes in metabolite involved in the pathways. Pyruvate from the TCA cycle is significantly reduced (log2 FC: - 0.5927, padj. = 0.0070). Metabolites involved in the GABA Shunt, only glutamine shows a tendency to be reduced in the liver of hfd-fed animals (log2 FC = -0.43744, p = 0.0207, padj. = 0.05167). Surprisingly, despite only slight changes in gene expression of methionine/folate cycle-associated genes are detected, metabolites from the pathways display reduction in betaine (log2 FC = - 1.4867, padj. = 0.0019), methionine (log2 FC = -0.5149, p = 0.0207, padj. = 0.0516), S-adenosylmethionine (log2 FC = -0.5832, padj. = 0.1257), and S-adenosylhomocysteine (log2 FC = -1.38, padj. = 0.0012) levels. Citrulline, a metabolite from the urea cycle, shows decreased tendency in the liver of hfd-fed animals likewise (log2 FC = -0.8987,p = 0.02812, padj. = 0.0675, Figure 25c). Shared metabolites, which are associated with at least two of the metabolic pathways, such as serine (log2 FC = -1.0826, p = 0.0069, padj. = 0.02543), glycine (log2 FC = -1.1914, p = 0.0003, padj. = 0.0019) and adenosine (log2 FC = -0.6710, p = 0.0006, padj. = 0.0032), are significantly reduced in the liver of hfd animals (Figure 25c).

Further, *mmu-miR-149-5p* expression correlates negatively with the abundance of pyruvate (r = -0.6600, p = 0.0054), betaine (r = - 0.6063, p= 0.0128), methionine (r = - 0.6485, p = 0.0065), S-adenosylhomocysteine (r = -0.7958, p = 0.0002), citrulline (r = - 0.5609, p = 0.0238), ornithine (r = -0.6276, p = 0.0092), serine (log2 FC: - 1.08, padj. = 0.0254), glycine (log2 FC = - 1.19, padj. = 0.0019), adenosine monophosphate (r = - 0.5669, p = 0.0215), and adenosine (r = -0.6603, p = 0.0054, Figure 25d).
Metabolite ratios provide further information about the metabolic state of a cell and the direction of a reaction catalyzed by an enzyme, since many reactions in the metabolic pathways are bidirectional. Interestingly, the SAM/SAH ratio, also called methylation index, is significantly increased in the liver of hfd animals, which indicate higher levels of SAM compared to SAH. The methylation index positively correlates with *mmu-miR-149-5p* expression (r = 0.7160, p = 0.0018, Figure 25e). The GSG index (glutamate/(serine * glycine) increases within the liver of hfd animals, when compared to standard chow-control mice and significantly correlates with mmu-miR-149-5p expression (r = 0.5821, p = 0.0180, Figure 25f).
Over all investigated metabolic pathways, a total of 15 metabolic pathway-associated genes are significantly downregulated and two genes upregulated (Figure 25g). Based on the correlation analysis of differentially expressed genes combined with differentially enrichment of metabolites with *mmu-miR-149-5p* expression, it is conceivable that *miR-149-5p* affects the metabolome by regulating genes involved in those pathways and therefore contributing to the MASLD progression.
However, the question which factor causes the induction of miR-149-5p expression during the development and progression of MASLD and how miR-149-5p is regulated in the liver remains elusive.

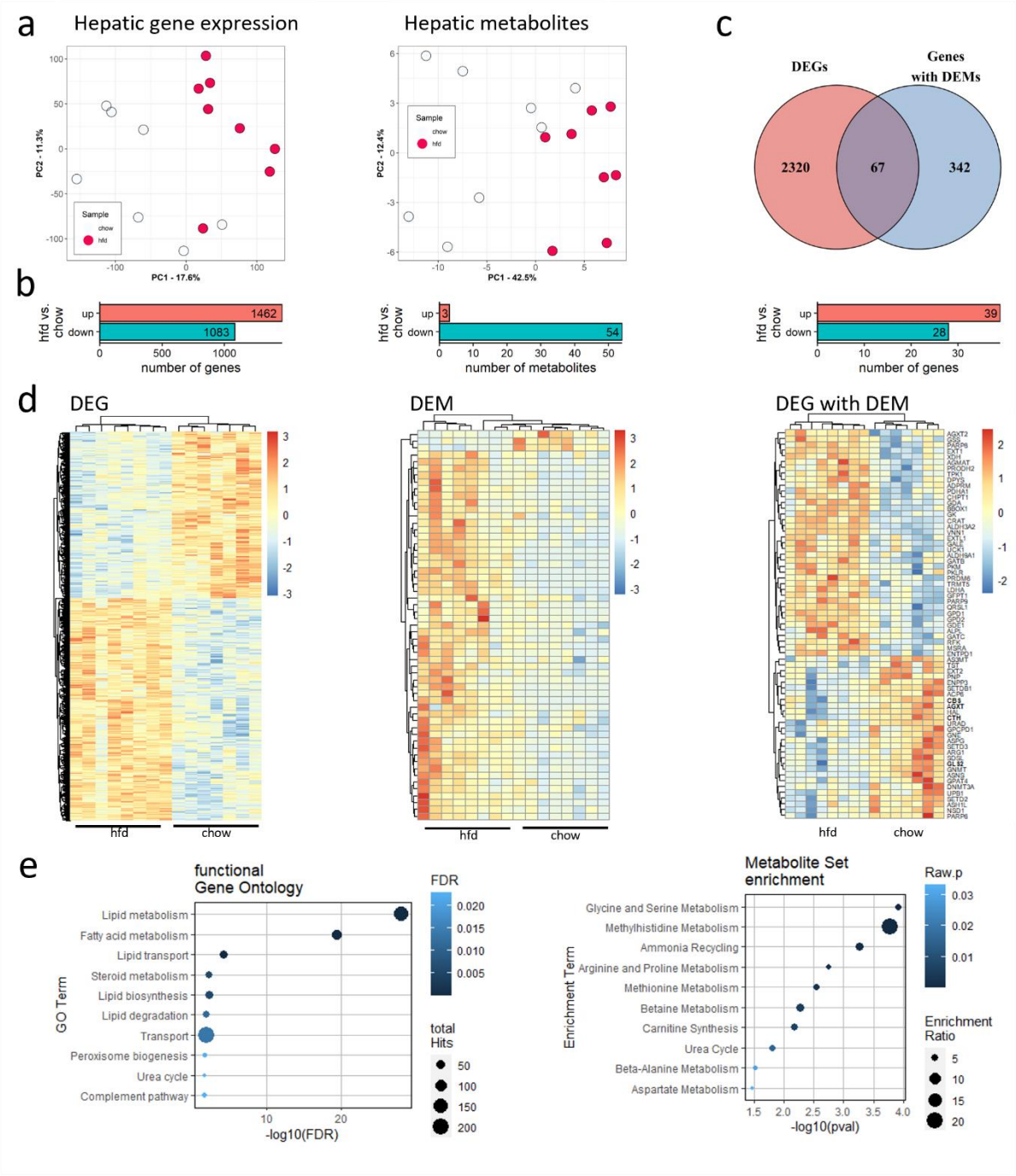

Figure 24: Changes in hepatic metabolome of DIO are associated with conserved miR-149-5p target genes. a: Principal component analysis of hepatic gene expression assessed with gene array and of hepatic metabolomics assessed with LM-MS/MS (gene array: hfd: n = 8, chow: n = 7, metabolomics: hfd: n = 8, chow: n = 8). b: Venn-diagram displaying differentially expressed genes (DEGs = 2387) and genes invovled in metabolism of differentially enriched metabolites (DEMs) based on KEGG resources (Genes with DEMs). The overlap of 67 genes indicates DEGs with DEMs. c: The proportion of DEGs, DEMs and DEGs with DEMs. d: Hierarchical clustering of DEGs, DEMs and DEGs with DEM. e: Functional gene ontology analysis performed with DAVID of differentially expressed genes and metabolite set enrichment analysis of differentially enriched metabolites performed with MetaboAnalyst.

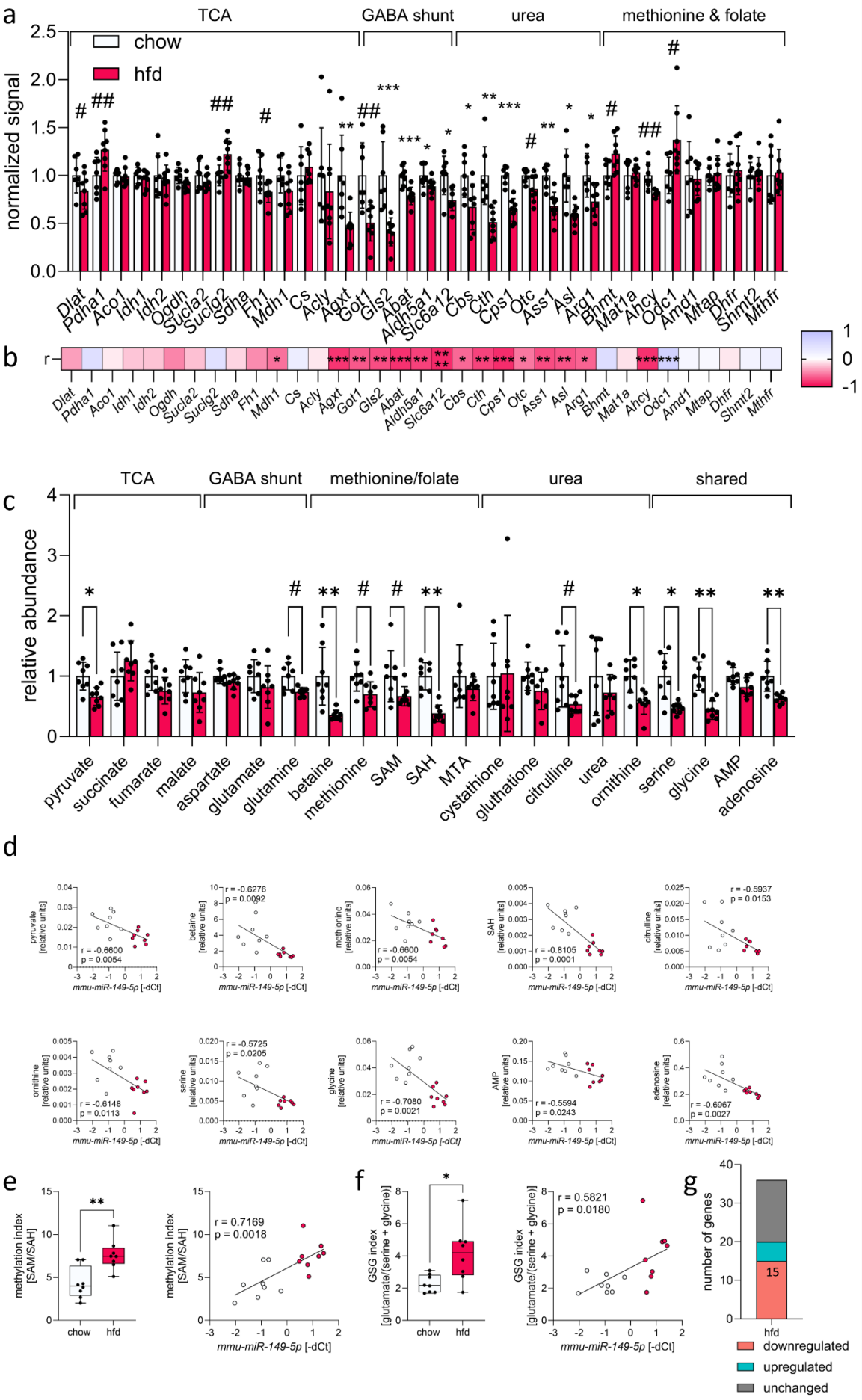
a
TCA
GABA shunt
urea
methionine & folate
chow
hfd
normalized signal
Dlat Pdha1 Aco1 Idh1 Idh2 Ogdh Suclg2 Suclg1 Sdha Fh1 Mdh1 Cs Acly Agxt Got1 Gls2 Abat Aldh5a1 Slc6a12 Cbs Cth Cps1 Otc Ass1 Asl Arg1 Bhmt Mat1a Ahcy Odc1 Amd1 Mtap Dhfr Shmt2 Mthfr
b
r
c
TCA
GABA shunt
methionine/folate
urea
shared
relative abundance
pyruvate succinate fumarate malate aspartate glutamate glutamine betaine methionine SAM SAH MTA cystathione gluthatione citrulline urea ornithine serine glycine AMP adenosine
d
pyruvate [relative units] r = -0.6600 p = 0.0054
betaine [relative units] r = -0.6276 p = 0.0092
methionine [relative units] r = -0.6600 p = 0.0054
SAH [relative units] r = -0.8105 p = 0.0001
citrulline [relative units] r = -0.5937 p = 0.0153
ornithine [relative units] r = -0.6148 p = 0.0113
serine [relative units] r = -0.5725 p = 0.0205
glycine [relative units] r = -0.7080 p = 0.0021
AMP [relative units] r = -0.5594 p = 0.0243
adenosine [relative units] r = -0.6967 p = 0.0027
mmu-miR-149-5p [-dCt]
e
methylation index [SAM/SAH]
chow
hfd
r = 0.7169
p = 0.0018
f
GSG index [glutamate/(serine + glycine)]
r = 0.5821
p = 0.0180
g
number of genes
15
hfd
downregulated
upregulated
unchanged

Figure 25: miR-149-5p expression correlates negatively with conserved target genes and differentially enriched metabolites. a: Gene array expression of genes invovled in TCA, GABA shunt, urea cycle and methionine/folate cycle (chow: n = 7, hfd: n = 8). b: Heatmap plot of Pearson r of mmu-miR-149-5p with depicted genes. c: Pearson correlations of metabolites with mmu-miR-149-5p expression of associated with genes depicted in b. e: Median methylation index in chow and DIO animals and Pearson correlation of methylation index with mmu-miR-149-5p expression. f: Median GSG index in chow and DIO animals and Pearson correlation with mmu-miR-149-5p expression. g: Number of genes involved in metabolic pathways that are downregualted, upregulated or unchanged in liver of DIO mice. * = padj < 0.05, ** = padj < 0.01, *** = padj < 0.001, **** = padj < 0.0001, # = p < 0.05, ## = p < 0.01.

5.2.4. Mmu-miR-149-5p expression is regulated by Pparγ-activity in DIO mice

Since miR-149-5p is upregulated in the liver of hfd-fed animals, which is accompanied by a dysregulation of metabolic pathway-associated genes and metabolites, the underlying cause of miR-149-5p induction is investigated. Therefore, the genomic context coding for the mmu-miR-149-5p gene is analyzed and the mmu-miR-149-5p expression is correlated with metabolic parameters, such as blood glucose or hepatic triglyceride levels. In the following experiments some of the depicted results has been shown previously (longitudinal *mmu-miR-149-5p* expression and weekly correlations, see Figure 12e and j), but are presented again in this chapter (Figure 26b and c) to increase reading comfortability. Additionally, parts of the VSG and caloric restriction model are described previously as well (see 5.1.3 and 5.1.4.3). For the VSG experiment, only the animals, which are measured on the miRNA-microarray, are analyzed (vsg: n = 6, sham: n = 6).

The miR-149-5p is an intronic encoded miRNA, which is located in the first intron of its host gene *Gpc1* – in mouse and human. From this the idea rose that miR-149-5p expression depends on its host gene expression and is driven by *Gpc1*-promoter activity (Figure 26a). As previously described, mmu-miR-149-5p expression increases with hfd-feeding and correlates with metabolic parameters (Figure 26b & c). The maximum of mmu-miR-149-5p expression is reached after twelve weeks on hfd, which is associated with an induction of *Gpc1* expression (log2 FC: 2.81, padj. < 0.0001, Figure 26d). *Gpc1* and mmu-miR-149-5p expression show a positive correlation, which underlines a possible causality (r = 0.9105, p < 0.0001, Figure 26d).

To find transcriptional regulators that induce *Gpc1* gene expression and therefore mmu-miR-149-5p, all differentially expressed transcription factors are retrieved from the gene array data set after 12 weeks on hfd using the data of all categorized transcription factors (Lambert et al. 2018). In total, 200 transcription factors are up and 268 downregulated in the hfd-fed animals (Figure 26e). Subsequently, a transcription factor binding motif prediction of the *Gpc1* promoter is performed with CiiiDER (Gearing et al. 2019) utilizing the JASPAR open-access database for vertebrates (Rauluseviciute et al. 2023). Afterwards, the expression of all differentially expressed transcription factors, which additionally harbor a binding motif within the *Gpc1* promoter region are correlated with the *Gpc1* gene expression to evaluate potential transcription factors regulating the *Gpc1* expression. Among the significant correlations, *peroxisome proliferator-activated receptor gamma* (Pparγ), *sterol regulatory element-binding protein 1* (*Srebf1*) and the *nuclear receptor 4A2* (*Nr4a2*) appear (Figure 26f). *Pparγ* is involved in MASLD progression and is described as the ‚lipid-storage' transcription factor of the adipose tissue, but serves similar functions in the liver by increasing *de novo* lipogenesis (Colca and Scherer 2022; Skat-Rørdam et al. 2019). *Srebf1* is involved in regulating lipid homeostasis (Moslehi and Hamidi-Zad 2018). There are ambiguous data about the *Nr4a2* transcription factor in MASLD, where on the one side *Nr4a2* activity seems to be protective of liver fibrosis (P. Chen et al. 2015), but on the other side *Nr4a2* activity is also linked to steatosis-to-NASH progression (B. Li et al. 2023).Due to the ambiguous data, *Nr4a2* is excluded from further analysis.

To verify if *Pparγ* and *Srebf1* binding has been observed previously to the Gpc1 promoter, publicly available chromatin immunoprecipitation sequencing (ChIP-seq) data from ENCODE are integrated and

merged with histone markers for promoter (H3K4me3) and enhancer regions (H3K4me1) to visualize chromatin accessibility. The ChIP-seq experiments are carried out in HepG2 cells (Supplementary Table 4). Interestingly, *Ppargγ*-ChIP seq. data show a dominant signal for the GPC1 promoter, whereas for *Srebf1*-ChIP seq. data a signal is assumed, but is accompanied with a strong background signal (Figure 26g).

Now that *Pparγ* binding is established and *Pparγ* is activated by fatty acid uptake within the hepatocyte, *mmu-miR-149-5p* expression should be rescued by interventions that reduce hepatic triglyceride levels (Grygiel-Górniak 2014). Therefore, the vertical sleeve gastrectomy model and caloric restriction model are revisited again. Both models show significant reduction in bodyweight, but the surgical intervention is more effective in reducing hepatic triglyceride accumulation. On average, vsg reduced bodyweight by 8.94 % ± 9.02 ($p < 0.0001$) compared to the sham control group, whereas caloric restriction reduced body-weight by 16.10 % ± 1.21 ($p < 0.0001$) compared to the starting point. 10 days continuous hfd-feeding or chow-diet did not significantly increased body-weight (Figure 26h).

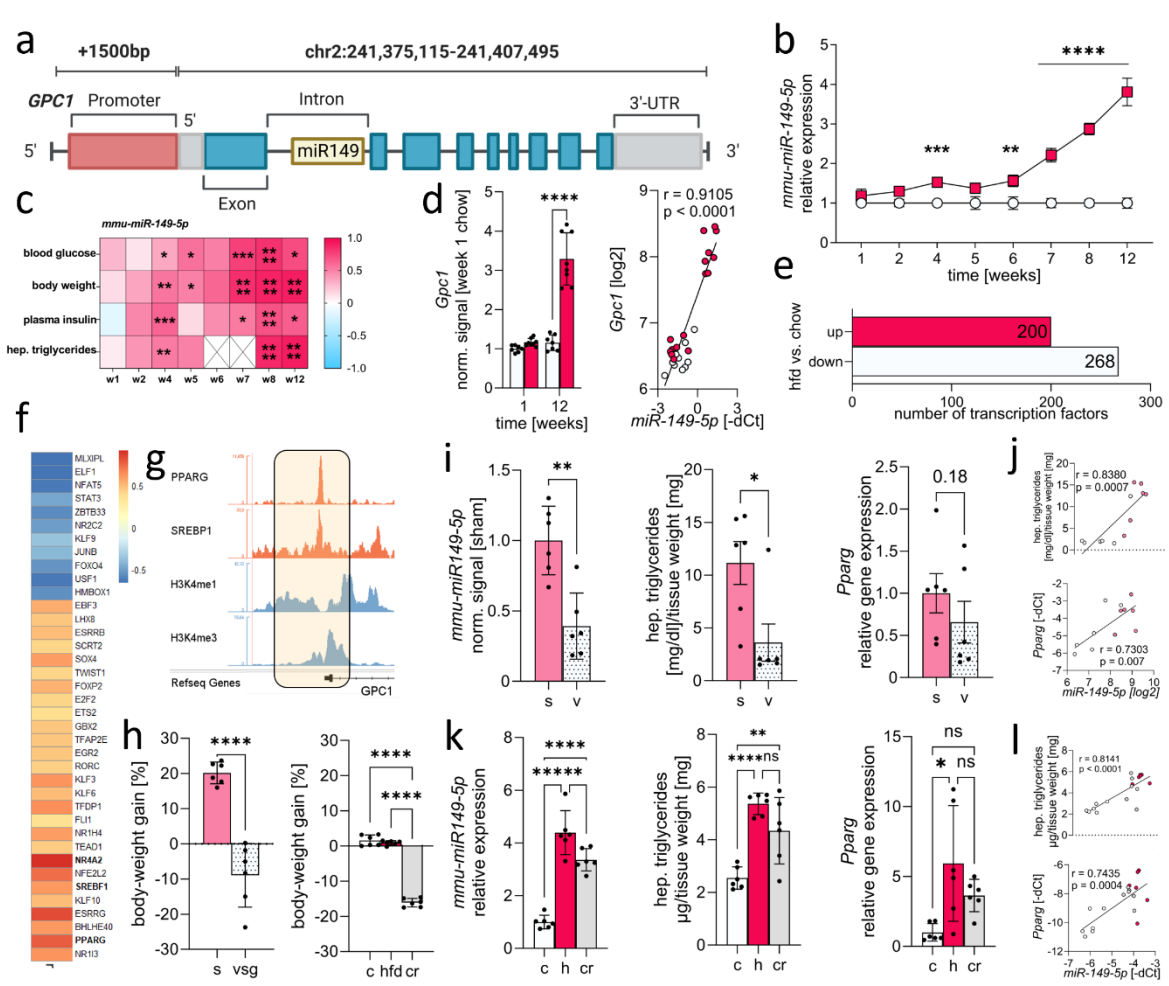

Figure 26: miR-149-5p is regulated by hepatic Pparγ-activity in DIO mice and intervention models. a: miR-149-5p coding region within first intron of GPC1 host gene and Gpc1 promoter region used for transcription factor binding prediction. b: Longitudinal expression of miR-149-5p in hfd and chow diet, normalized to each respective chow week (chow: n = 8 – 16, hfd: n = 7 – 16). c: Week-specific Pearsson correlation matrix of miR-149-5p expression with blood glucose, body weight, plasma insulin, and hepatic triglycerides (hep. triglycerides). d: Gpc1 array expression (signals normalized to week 1, chow: n = 8, hfd: n = 8) and Pearsson correlation of miR-149-5p expression with Gpc1 expression. e: Differentially expressed transcription factors (DETF) in mice fed a high-fat diet after 12 weeks. f: Heatmap plot of Pearsson-r of Gpc1 expression correlated with significantly DETF, which are predicted to bind Gpc1 promoter. g: Publicly available SREBF1 and PPARγ ChIP-seq. data from HepG2 cells merged with marker for enhancer (H3K4me1) and promoter (H3K4me3) region. h: miR-149-5p expression and hepatic triglyceride content after vertical sleeve gastrectomy (v: n = 6) compared to sham surgery (s: n = 6). i: Pearsson correlation of miR-149-5p expression with hep.triglycerides content and Pparγ gene expression in vsg cohort. j: miR-149-5p expression and hep. triglyceride content after caloric restriction (cr: n = 6) and hfd (n = 6) compared to chow diet (c: n = 6). k:

Pearsson correlation of miR-149-5p expression with hep.triglycerides content with hep. triglycerides and Pparγ gene expression. For statistical testing of b a Two-way ANOVA was performed. For h student's t-Test was performed and j a One-Way ANOVA. * = p < 0.05, ** = p < 0.01, *** = p < 0.001, **** = p < 0.0001, ns = not significant.

After normalizing the mmu-miR-149-5p count signal from miRNA microarray data set, mmu-miR-149-5p expression is significantly reduced to 0.39 ± 0.23-fold (p = 0.0030). Hepatic triglyceride content is reduced to 3.61 ± 4.32 mg/dl per mg of tissue weight after vsg, compared to 11.15 ± 4.99 in the control cham mice (p = 0.0189). Interestingly, *Pparγ* and *Gpc1* gene expression tends to be reduced, without reaching statistical significance (Figure 26i & Supplementary Figure 5a), whereas for the *Srebf1* gene expression no tendencies are observed (Supplementary Figure 5a). It is noteworthy that mmu-miR-149-5p, hepatic triglyceride levels, *Pparγ* and *Gpc1* gene expression show a similar pattern after vertical sleeve gastrectomy, suggesting a close connection between these parameters. This connection is additionally reflected in the positive correlation between hep. triglyceride content (r = 0.8380, p = 0.0007), *Pparγ* (r = 0.7303, p = 0.007) and *Gpc1* (r = 0.8308, p = 0.0008) gene expression with *mmu-miR-149-5p* expression (Figure 26j & Supplementary Figure 5a). *Srebf1* gene expression shows no significant correlation with mmu-miR-149-5p expression (Supplementary Figure 5a).
This connection between *mmu-miR-149-5p* expression, hep. triglycerides, *Pparγ* and *Gpc1* gene expression is also observed after caloric restriction, since *mmu-miR-149-5p* (Δcr/hfd = - 0.715, p = 0.0151) expression is reversed, which is associated with a tendency of reduction in hep. triglycerides (Δcr/hfd = - 1.027, p = 0.1017), *Pparγ* (Δcr/hfd = - 2.297, p = 0.2811) and *Gpc1* (Δcr/hfd = - 2.983, p = 0.8845) expression (Figure 26k & Supplementary Figure 5b). All parameters show a positive correlation with *mmu-miR-149-5p* expression (hep. triglycerides: r = 0.8141, p < 0.0001; *Pparγ*: r = 0.7435, p = 0.0004; *Gpc1*: r = 0.9084, p < 0.0001, Figure 26l & Supplementary Figure 5b). Also after caloric restriction, there is no effect on the Srebf1 expression detected or correlation with mmu-miR-149-5p expression (Supplementary Figure 5b).

In summary, these experiments show that *mmu-miR-149-5p* might be regulated by *Pparγ* transcription factor binding to a PPAR response element within the Gpc1 promoter. *Pparγ* are activated by fatty acids, which are imported into the hepatocytes. Thereby a logical conclusion is that during MASLD, which is characterized by an accumulation of fatty acids within the hepatocytes, these fatty acids induce miR-149-5p expression in a *Pparγ*-dependent manner and subsequently induced miR-149-5p expression leads to downregulation of metabolic pathway-associated genes. This cascade accelerates or promotes MASLD progression.

5.2.5. Hsa-miR-149-5p upregulation correlates with conserved target genes in the liver of obese human subjects with type 2 diabetes

The previous experiments showed the great potential of miR-149-5p promoting MASLD progression by downregulation of metabolic pathway-associated genes. Due to the higher relevance of human compared to exclusively murine data, especially with potential as a treatment therapy, the previously described metabolic pathway genes (see Table 31) are measured in bulk-mRNA sequencing from the liver of the already mentioned human obese liver cohort (see Table 30). *Hsa-miR-149-5p* expression is shown previously (see Figure 20a), but is viewed again in the following paragraph to increase reading comfort. P-values might vary between both section due to adjustment of multiple testing.
Hepatic hsa-miR-149-5p expression is increased in obese subjects with type 2 diabetes when compared with obese subjects without (see Figure 20a & Figure 27a) and correlates positively with HbA1c levels (r = 0.4137, p = 0.008), NAS score (r = r = 0.3952, p = 0.0188) and AST levels (r = 0.3929, p = 0.0133; see Figure 20b & Figure 27b). Bulk-mRNA sequencing reveals a tendency of increased GPC1 expression in the subjects with type 2 diabetes (log2 FC = 0.20 ± 0.10, p = 0.0515, padj. = 0.2211, Supplementary

Figure 6b), confirming and further validating the data explored in mice. PCA analysis of bulk-mRNA sequencing shows no clear separation of the type 2 diabetic subjects from the non-type 2 diabetics (Supplementary Figure 6c). An explanation might be the underlying obese condition in both groups, which allows only for minor transcriptomic differences. However, hierarchical clustering of metabolic pathway-related genes improves the separation between type 2 diabetics and non-type 2 diabetics (obese, Figure 27c), assuming that individuals within each group share similarities in gene expression of the metabolic pathway-related genes. Subsequently, the metabolic pathway-related genes measured in bulk-mRNA sequencing are correlated with *hsa-miR-149-5p* expression and are plotted in a network-dandelion plot (Figure 27d), which is performed in the previously mentioned miRNA network visualizer utilizing the seed-sequence prediction and drawPlot function. Blue colored edges represent target genes, which are validated in at least one data base for miRNA/mRNA interactions (miRTarBase and TarBase; (Chou et al. 2018; Karagkouni et al. 2018)) and show a negative association with *hsa-miR-149-5p* expression. Red colored edges represent target genes, which are predicted target genes from the miRNA NVis seed-sequence prediction function and show a negative association with *hsa-miR-149-5p* expression, but are not validated in the mentioned data bases. Grey edges represent either a validated or predicted target, but with a positive association with hsa-miR-149-5p expression (Figure 27d). The integration of validated target genes from data bases results in two additional target genes in the metabolic pathways, which are not detected by the seed-sequence prediction, namely *CTH* and *CBS*. Therefore, *CTH* and *CBS* are not labeled as predicted target gene previously (see Table 31). Interestingly, the majority of predicted and validated target genes involved in the metabolic pathways show significant negative correlation or negative associations with hsa-miR-149-5p expression. The single correlations are shown in Supplementary Figure 7.

However, a great limitation of the obese human liver cohort is the small sample size (obese: n = 19, T2D: n = 21) and the lack of a lean, normal-weighted control group. To overcome this issue, publicly available bulk-mRNA sequencing data from the SteatoSITE are integrated into the analysis (https://shiny.igc.ed.ac.uk/SteatoSITE_gene_explorer/). This cohort comprises a total of 632 sequenced individuals. The individual NAS score is assessed and the individuals are grouped by their fibrosis stage (ranging from F0 to F4) based on the NASH-Clinical Research Network (NASH-CRN) score. The individuals of F0 and F1 group are comprised into a F01 group. Additionally, this cohort includes a normal-weighted control group (nw: n = 32, (Kendall et al. 2023)).

The extracted bulk-mRNA sequencing data from the SteatoSITE website shows a significant downregulation of 30 genes involved in the metabolic pathways in late stage fibrosis (F4) when compared to normal-weighted individuals. Three genes are significantly upregulated, whereas one gene remains unaffected (Figure 27e & f). Impressingly, 23 of the 30 significantly downregulated genes are also *hsa-miR-149-5p* target genes in human (see Table 31 and *CTH* and *CBS*). The comparison between the normal-weight and F4 group resembles two extremes of non-fibrotic and late stage fibrosis. However, including the intermediate stages F01 to F3 into the analysis reveals a stepwise downregulation of the genes *AGXT*, *ACO1*, *IDH1*, *SUCLG2*, *SDHA*, *FH*, *ABAT*, *ALDH5A1*, *BHMT*, *MAT1A*, *AHCY*, *SHMT2*, *CTH*, *CPS1*, *ASL* and *GCLC* with increasing fibrosis stage (Supplementary Figure 8). This implies a causative role of those genes in the progression of MASLD rather than a consequence to it. Assuming that *hsa-miR-149-5p* expression might increase with fibrosis stages, based on the positive correlation with NAS score (Figure 27b), *hsa-miR-149-5p* could contribute to the stepwise downregulation.

Similarity comparison between all conducted experiments from in vitro cell culture (HepG2), murine model for DIO (murineLiver) and human liver data (humanLiver: SteatoSITE nw/F4 and obese human liver cohort) reveal that five *miR-149-5p* target genes are consistently downregulated in all conditions and across species (*AGXT*, *ABAT*, *ALDH5A1*, *SLC6A12* and *CBS*). Further five human target genes (*IDH1*, *IDH2*, *MAT1A*, *DHFR* and *SHMT2*) are downregulated in the in vitro experiments and human liver. Additionally, six genes (*GLS2*, *CTH*, *CPS1*, *ASS1*, *ASL* and *ARG1*) are significantly downregulated in the

murine model for DIO and human liver (Figure 27g).

In summary, these analysis imply a causative role of *hsa-miR-149-5p* in the progression of MASLD also in human. Similarities across species in *miR-149-5p* and target gene expression are detected, assuming that *hsa-miR-149-5p* serves a similar function in the murine and human liver. This allows for further intensive animal studies, since the increased relevance in human. To study interspecific similarities in the context of miRNAs remains challenging.

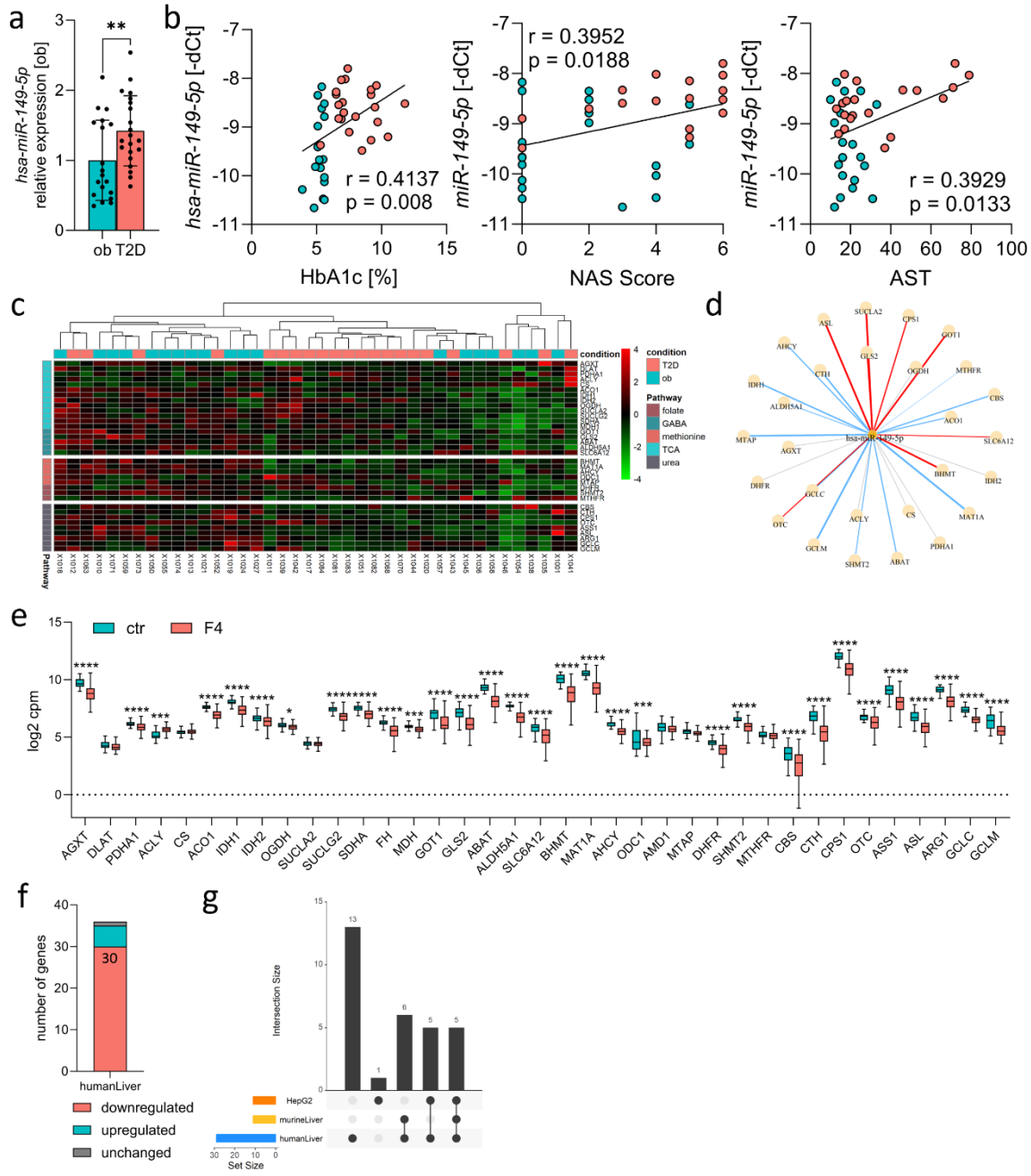

Figure 27: Conserved miR-149-5p target genes are downregulated in obese human with type 2 diabetes and fibrosis. a: miR-149-5p expression in obese type 2 diabetic (T2D: n = 21) vs. obese non-diabetic (ob: n = 19) measured in RT-qPCR. b:Pearsson correlation of miR-149-5p expression with HbA1c, NAS-Score, and AST serum levels. c: Heatmap expression plot from bulk-mRNA sequencing of genes involved in amino acids metabolism. d: Dandelion plot of miR-149-5p target genes with predicted seed sequence and negative correlation (red), seed validated in data base with negative correlation (blue) and predicted/validated seed with no or positive correlation (grey). e: Log2 counts per million (cpm) data from public available SteatoSITE hepatic bulk-mRNA sequencing comparing normal-weight individuals (ctr: n = 31) with individuals of a NASH-CRN Score of 4 (F4: n = 115). f: Absolute number of genes downregulated, upregulated or unchanged from TCA, GABA shunt, methionine & folate cycle, and urea cycle in human TD2 and SteatoSITE cohort. g: UpSet Plot comparing similarities in

downregulated genes between HepG2 cells, murine liver (murineLiver) and human liver (humanLiver = SteatoSITE + T2D cohort). * = padj < 0.05, ** = padj < 0.01, *** = padj < 0.001, **** = padj < 0.0001, # = p < 0.05, number = specific p-value. P-value were adjusted to multiple testing using a false discovery rate of 0.05.

5.3. Fatty acid induced hypermethylation in the *SLC2A4* gene in visceral adipose tissue is associated to insulin-resistance and obesity

The results of the following project are already published (Britsemmer et al. 2023). Displayed figures are published and are adapted with minor changes or without any changes.
The underlying hypothesis in this project is that during obesity, the expression of the insulin-dependent glucose transporter *solute carrier family 2 member 4* (*SLC2A4*), also referred to as GLUT4 protein, decreases in the visceral adipose tissue and thus promotes the development of insulin resistance. However, the molecular mechanism behind it remains elusive. Therefore, the hypothesis is that maybe DNA methylation is causative for the downregulation by interfering with the binding of transcription factors to a binding motif in a regulatory element of the *SLC2A4* gene. The *SLC2A4*-mediated insulin-dependent glucose uptake into the adipocyte is crucial in regulating adipose tissue de novo lipogenesis (DNL) via the glucose sensor *carbohydrate-responsive element binding protein* (ChREBP or *MLXIPL* gene), which regulates the DNL-related genes *fatty acid synthase* (*FASN*) and *acetyl-CoA carboxylase alpha* (*ACACA*).
DNL-capacity decreases in obesity, which further promotes systemic insulin resistance, since metabolites generated in DNL serve insulin sensitizing function.

5.3.1. Enhancer-associated SLC2A4 DNA methylation is increased in visceral adipose tissue of morbidly obese subjects with high HbA1c

To find a molecular mechanism that could be causative for decreased *SLC2A4* expression in the visceral adipose tissue (VAT) during obesity, DNA methylation in an enhancer region (GeneCards Enhancer ID: GH17J007279) that contains SP1 and SREBP-1c binding motifs is investigated by bisulfite pyrosequencing in obese mice and human. SP1 has been shown to be DNA methylation sensitive (Douet, Heller, and Le Saux 2007). Therefore, the focus is set to the chromosomal area chr17:7282504-7282531 (ENST00000317370.13, UCSC) containing four CpG sites (Figure 28a, region of interest (ROI), reference genome hg38) which is located in intron 1 of *SLC2A4* and in the shore of an CpG island. SP1 binding in this region is previously observed by ChIP-Sequencing in HepG2 cells (Supplementary Table 4)(Project 2012). The cohort consisting of 101 individuals is stratified into subjects with a BMI > 35 and low HbA1c (≤ 6.5%, n = 65) or high HbA1c (> 6.5%, n = 36) (Figure 28b). *SLC2A4* gene expression is significantly decreased (FC = 0.52 ± 0.64, p = 0.0035) in obese subjects with high HbA1c compared to obese subjects with low HbA1c. FASN and MLXIPL gene expression is similarly decreased (*FASN*: FC = 0.58 ± 0.33, p = 0.0130; *MLXIPL*:FC = 0.80 ± 0.42, p = 0.0335) in the high HbA1c group, whereas *ACACA* gene expression is non-significantly decreased (Figure 28c).
Furthermore, the expression of DNL-related genes *FASN* and *MLXIPL* correlates positively with *SLC2A4* gene expression (*FASN*: r = 0.3958, p = 0.0004; *MLXIPL*: r = 0.3261, p = 0.0017; Figure 28d). Though the group-wise difference of *ACACA* expression is not significant, a significant positive correlation with *SLC2A4* gene expression is observed (*ACACA*: r = 0.3818, p = 0.0002; Figure 28d).
The decreased *SLC2A4* gene expression is associated with an increased DNA methylation at all four CpGs in the obese subjects with high HbA1c, with the first CpG (CpG1) not reaching significant differences ($\Delta CpG1_{median}$ = 2.23 %, p = 0.0504; $\Delta CpG2_{median}$ = 1.97 %, p = 0.0416; $\Delta CpG3_{median}$ = 2.96 %,

p = 0.0231; $\Delta CpG3_{median}$ = 4.02 %, p = 0.0028; Figure 28e) .

To evaluate potential factors that influence DNA methylation and *SLC2A4* gene expression, a Pearson's correlation analysis with blood parameters, BMI and age is performed (Figure 28f, red box). *SLC2A4* gene expression correlates negatively with age (r = -0.263, p = 0.01, n = 101), HbA1c (r = -0.221, p = 0.032, n = 94), fasting glucose (r = - 0.215, p = 0.04, n = 90), fasting insulin (r = -0268, p = 0.01, n = 87), HOMA index (r = -0251, p = 0.02, n = 83), serum C-peptide levels (r = -0219, p = 0.039, n = 89), and serum triglyceride levels (r = -0.248, p = 0.02, n = 94) (Figure 28f). Interestingly, SLC2A4 expression shows no correlation with fasting blood glucose levels.

Although, no direct correlation of *SLC2A4* DNA methylation with *SLC2A4* gene expression in the entire cohort is observed, putatively relevant correlations in sub-cohorts that are stratified by medical indication to analyze possible effects of the medication on DNA methylation and gene expression, are identified (Supplementary Figure 9). Whereas metformin or insulin medication shows no significant effect on *SLC2A4* gene expression or DNA methylation (Supplementary Figure 9a & b), CpG4 DNA methylation negatively correlates with *SLC2A4* gene expression (Figure S3c, r = -0.595, p = 0.041) and insulin levels (Figure S3d , CpG1: r = -0.649, p = 0.042; CpG3: r = -0.689, p = 0.027; CpG4: r = -0.732, p = 0.016) in obese subjects with metformin treatment (Supplementary Figure 9c & d). Moreover, a negative correlation between DNA methylation with glucose levels in individuals receiving insulin is detected (CpG1: r = -0.719, p = 0.013; CpG2: r = -0.633, p = 0.036, Supplementary Figure 9e).

Since DNA methylation shows no direct correlation with *SLC2A4* expression over all individuals, a stepwise regression model is calculated to evaluate the influence of DNA methylation on the prediction of *SLC2A4* gene expression. Inclusion of *SLC2A4* DNA methylation as a predictor into the regression improves the accuracy for modelling the *SLC2A4* gene expression (R^2 = 0.347; Adjusted R^2 = 0.211; p = 0.00324; Figure 28g, Table S1) compared to the stepwise-regression model excluding DNA methylation (R2 = 0.0691; Adjusted R^2 = 0.059, p = 0.0105, Figure S4, Supplementary Table 13), when compared to a stepwise regression model, where DNA methylation is excluded as a predictor (R^2 = 0.0691; Adjusted R^2 = 0.059, p = 0.0105, Supplementary Figure 10)

In summary, *SLC2A4* gene expression is reduced in the VAT of obese individuals with high HbA1c and this is associated with a hypermethylation at multiple SP1 binding motifs. Since *SLC2A4* gene expression correlates with serum triglyceride levels, but not with fasted glucose levels, *SLC2A4* might be regulated by fatty acid induced DNA methylation. Again, the limitation of the human cohort is the lack of a normal-weighted, lean control group. However, based on the hypermethylation in the high HbA1c group and the positive correlation of CpG1 with BMI, it is suggested that DNA methylation increases during obesity and therefore the DNA methylation levels of lean individuals is supposed to be lower than of obese individuals.

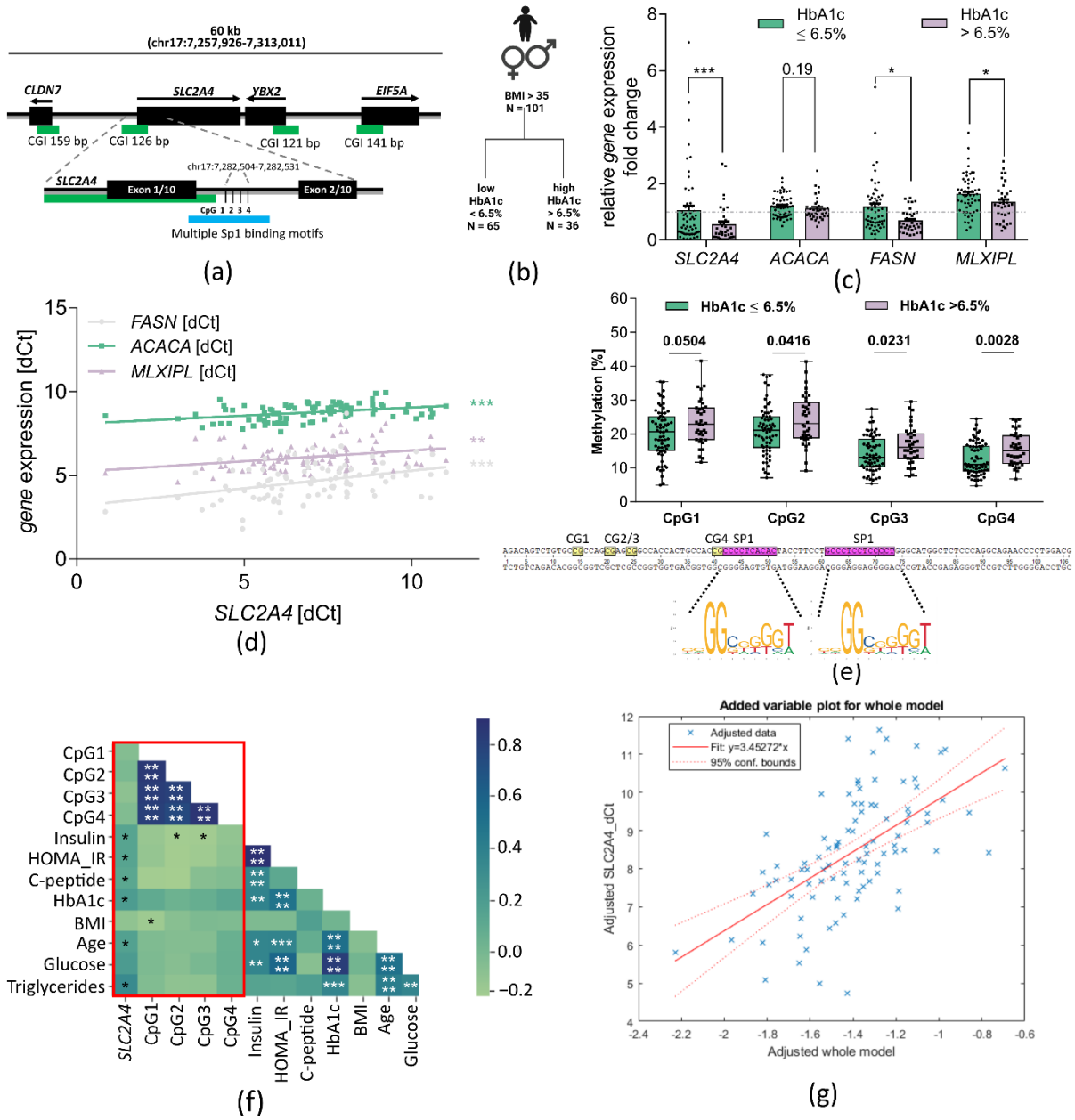

Figure 28: *SLC2A4* gene expression and DNA methylation in humans. (a) Overview of the SLC2A4 gene and the CpG sites that were analyzed for DNA methylation. The ROI is downstream of the first exon and includes four CpG sites in the proximity of multiple Sp1 binding motifs. Green bars indicate CpG islands, black bars indicate genes or exons; (b) Overview of the human cohort used for analysis of DNA methylation and gene expression in VAT; (c) Relative gene expression of SLC2A4 (l-HbA1c = 58; h-HbA1c = 35), ACACA (l-HbA1c = 57; h-HbA1c = 35), FASN (l-HbA1c = 58; h-HbA1c = 35) and MLXIPL (l-HbA1c = 56; h-HbA1c = 35) in VAT of morbidly obese individuals. Gene expression was measured with RT-qPCR. Fold change to obese individuals with low HbA1c is shown as mean ± SEM. Mann-Whitney test was performed after testing for normal distribution using the D'Agistino&Pearson normality tests. (d) Pearson correlation of SLC2A4, ACACA, FASN and MLXIPL gene expression; (e) Methylation in ROI in VAT of morbidly obese subjects with low (n=65) and high HbA1c (n=36). Methylation was measured by bisulfite-pyrosequencing. Median ± Min./Max. is shown. Mann-Whitney test was performed after testing for normal distribution using D'Agistino&Pearson normality tets; (f) Correlation matrix of clinical parameters with SLC2A4 gene expression and methylation in VAT. Blue squares indicate positive correlation coefficients and green squares negative ones. * = $p < 0.05$, ** = $p < 0.01$, *** = $p < 0.001$, **** = $p < 0.0001$. Pearson correlation was performed. Correlation analysis with SLC2A4 gene expression was conducted using –dCt values; (g) Adjusted stepwise regression model for SLC2A4 gene expression prediction. Figure taken from Britsemmer et al. 2023.

5.3.2. *Slc2a4* gene is hypermethylated in the VAT of diet-induced obese mice

To study if DNA methylation of the *SLC2A4* gene and the associated mRNA downregulation of *SLC2A4* and DNL-related genes can be induced by life style factors such as a westernized diet rich in fat (HFD), DNA methylation in the ROI and gene expression in the VAT of the previously introduced longitudinal mouse model for diet-induced obese (DIO) is measured (Figure 29a. see 4.2.1). This model allows for a differentiation between a causal or consequential effect of *Slc2a4* DNA methylation and DNL, since the gene expression and DNA methylation is tracked over a time period of twelve weeks.
Since in human *SLC2A4* gene expression and DNA methylation is assessed in obese subjects with or without insulin resistance, the HFD group of the longitudinal mouse cohort is classified in week one to week four as lean, week five to week seven as obese and week eight and twelve as obese with insulin resistance (Figure 29a). The classification is defined by significant changes in plasma glucose levels at week five and significant increase in plasma insulin levels from week eight on. Additionally, the HOMA-IR is assessed to further validate the insulin resistance in the HFD animals from week eight on. The HOMA-IR in the HFD animals at week eight is 3.17 ± 2.16 ($p < 0.0001$) and 3.85 ± 4.17 ($p < 0.0001$) at week twelve (Figure 29b).
The adipose tissue expresses an additional insulin-independent glucose transporter, namely the *solute carrier family 2 member 1* (*Slc2a1* or GLUT1 protein). To exclude that the observed differences in DNL-related genes are attributed to a dysregulated *Slc2a1* gene expression, the expression is also measured in RT-qPCR.
After an acute increase in *Slc2a1* gene expression to 2.31 (± 0.47) fold in the HFD fed mice at week one, gene expression normalizes to the chow level over the time of HFD-feeding, except of a short decrease at week 8 to 0.43 (±0.08) fold (Figure 29b). In contrast, *Slc2a4* gene expression decreases over the investigated time period. The gene expression is significantly reduced to 0.55 (± 0.06, $p < 0.05$) fold at week four and further decreases to 0.14 (± 0.03, $p < 0.0001$) fold at week twelve (Figure 29c). Interestingly, DNL-related genes and *Mlxipl* gene expression seem to follow the *Slc2a4* expression pattern. After an acute increase at week one, *Acc1*, *Fasn* (DNL) and *Mlxipl* (glucose signaling) gene expressions are significantly decreased at week four in HFD mice ((*Acc1*: 0.29 (± 0.06; $p < 0.0001$, Figure 29d), *Fasn*: 0.42 (± 0.11; $p < 0.05$, Figure 29e), *Mlxipl*: 0.44 (± 0.06; $p < 0.001$, Figure 29f)).
However, even though Slc2a4 gene expression significantly decreases during HFD-feeding, the protein levels of Glut4 tend to decrease without reaching significantly differences (Supplementary Figure 11a & b). It is likely that fat contamination during the protein extraction from the adipose tissue, which interfere with the protein quantification, causes this issue. This is indicated by the varying Hsp90 band intensities, to which Glut4 protein levels are normalized.
Since *SLC2A4* DNA methylation increases in VAT of obese human with high HbA1c levels, which is accompanied by decreased *SLC2A4* gene expression and Slc2a4 gene expression decreases in mice fed a HFD, DNA methylation in the equivalent region in the murine genome is measured. Therefore, the equivalent region in the murine genome is identified by a LiftOver analysis using the UCSC genome browser. The region is conserved between the human and murine genome including the Sp1 binding motif (Figure 29h, reference genome = mm39). Both regions only differ in their number of CpG sites. The murine ROI exhibits two CpG sites at position chr11:69838231 (CpG1) and at position chr11:69838257 (CpG2), whereas the human region harbors four CpGs.
DNA methylation of the two CpG sites in the VAT of HFD and chow-fed animals is measured over the period of twelve weeks using bisulfite-pyrosequencing. Interestingly, DNA methylation gradually increases in the VAT of HFD-fed mice. The onset of increased DNA methylation at CpG1 occurs at week one and is prior to the decrease in Slc2a4 gene expression (ΔCpG1 = 4.004%, $p = 0.0124$, Figure 29i). The difference in DNA methylation between HFD mice and chow mice increases to a final difference of ΔCpG1 = 18.01% ($p < 0.0001$) at week twelve (Figure 29i). DNA methylation at CpG2 is significantly

increased at week two (ΔCpG2 = 5.36%, $p < 0.01$) and gradually increases to a final difference of ΔCpG2 = 14.38% ($p < 0.0001$) at week 12 (Figure 29j).
DNA methylation at both positions demonstrates a strong negative correlation with *Slc2a4* gene expression (CpG1: r = -0.5454, $p < 0.0001$; CpG2: r = -0.4942, $p < 0.0001$; Figure 29k). Additionally, DNA methylation shows a positive correlation with body weight, insulin, blood glucose, and hepatic triglyceride content (Figure 29k). This indicates that higher DNA methylation in the region of interest (ROI) of the *Slc2a4* gene is associated with obesity-related parameters such as increased body weight, plasma insulin levels, and blood glucose levels. Moreover, *Slc2a4* gene expression correlates positively with genes involved in de novo lipogenesis (DNL) (*Fasn*, *Acc1*) and glucose signaling (*Mlxipl*).

The findings observed in humans are reproducible in the longitudinal diet-induced obesity (DIO) mouse model, where increased DNA methylation in the ROI is associated with lower expression of the *Slc2a4* gene. But the factor inducing the changes in DNA methylation and consequently in Slc2a4 gene expression is unsolved. However, the data suggest a potential role of fatty acids, since SLC2A4 gene expression correlates in human with plasma triglyceride levels and DNA methylation and Slc2a4 gene expression in the mouse model correlate with hepatic triglyceride levels.

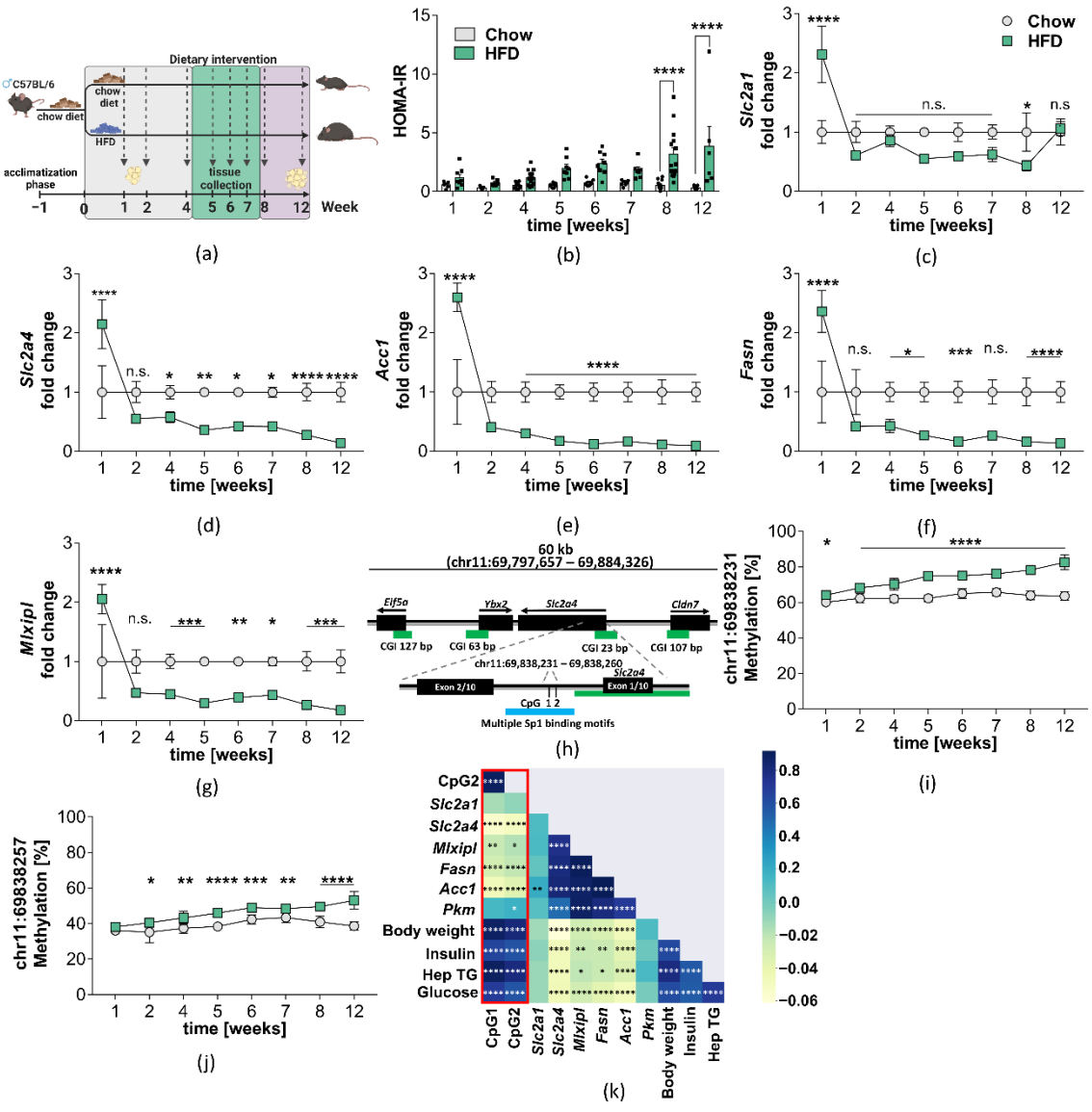

Figure 29: Gene expression and DNA methylation of the Slc2a4 gene in VAT of DIO mice fed a high-fat diet. (a) Feeding regime of high-fat mice over a period of 12 weeks. Time points of sacrifices are indicated in weeks. Colored background demonstrates stages of obesity and insulin resistance in HFD mice, with grey = lean; green = obese; purple = obese and insulin-resistant; (b) to (f) Expression of genes involved in glucose uptake (Slc2a1, Slc2a4), glucose signaling (Mlxipl) and de novo lipogenesis (Acc1, Fasn) in VAT. Mean ± SEM of fold change between HFD (n = 7 -16) and chow (n = 8-16) is shown, after normalizing expression to Hprt. A Two-Way ANOVA was performed with n.s. = non significant, * = $p < 0.05$, ** = $p < 0.01$, *** = $p < 0.001$, **** = $p < 0.0001$; (g) Schematic overview of region of interest in mouse genome. The ROI is downstream of the first exon and includes two CpG sites in the proximity of multiple Sp1 binding motifs. Green bars indicate CpG islands and black bars genes/exons in this area; (h) and (i) Methylation in VAT at CpGs in the ROI. The chromosomal coordinates of the CpGs are chr11:69838231 (CpG1) and chr11:69838257 (CpG2). Mean ± SD of HFD (n = 7-16) and chow (n = 8-16) is shown. A Two-Way ANOVA using the Sidak correction for multiple testing was performed with n.s. = non significant, * = $p < 0.05$, ** = $p < 0.01$, *** = $p < 0.001$, **** = $p < 0.0001$; (j) Pearson Correlation matrix of Slc2a4 DNA methylation with metabolic parameters and gene expression. Blue indicates positive correlation and yellow negative. Figure taken from Britsemmer et al. 2023.

5.3.3. DNA methylation in Slc2a4 ROI is sensitive to palmitate/oleate treatment in differentiating 3T3-derived adipocytes

In order to examine the possibility that FFA could elevate *Slc2a4* DNA methylation and consequently contribute to the reduction in *Slc2a4* gene expression, 3T3 preadipocytes were subjected to palmitate/oleate (PO) treatment during differentiation for 14 days following induction (Figure 29a). Throughout the PO treatment period, Slc2a4 gene expression initially increases to 1.85 (±0.23) fold at day 5 after induction, which appears to be a compensatory response. Despite continued PO treatment and differentiation, *Slc2a4* gene expression remains elevated compared to the BSA control, albeit with a decreasing discrepancy between the BSA control and PO treatment, with PO-treated cells showing only a 1.29 (±0.14) fold increase over the BSA control at D14 (Figure 30b). Notably, from D10 onward, the difference between PO and BSA treatment becomes statistically insignificant. The decline in *Slc2a4* expression at day 10 relative to D5 is accompanied by a relative decrease in the downstream genes *Mlxipl* and *Fasn*, but not *Acc1* (Figure 30c - e).

These findings align with the observations in the visceral adipose tissue (VAT) of high-fat diet (hfd) mice, where DNA methylation and *Slc2a4* gene expression exhibit an inverse correlation. The greatest disparity in DNA methylation is observed at day 10 in CpG2 (ΔCpG2 = 8.4%) and at day 14 in CpG1 (ΔCpG1 = 5.17%, Figure 30f & g). As treatment progresses, *Slc2a4* gene expression and DNA methylation return to normal levels, showing no significant differences compared to the BSA control. Furthermore, to confirm that methylation in the region of interest (ROI) near a Sp1 binding motif affects gene expression, a methylation-sensitive reporter gene assay is conducted (Figure 30h). The ROI is inserted into a CpG-free luciferase vector, and the luciferase signal is measured in both unmethylated (0% methylated) and fully methylated states (100% methylated). In the fully methylated state, the luciferase signal decreases to 77.53% (± 16.71%, $p = 0.039$, Figure 30i).

This outcome corresponds with previous findings in mice, humans, and differentiating 3T3 preadipocytes, where higher levels of DNA methylation are associated with reduced Slc2a4 gene expression and the regulatory role of the DNA methylation is finally proven by the methylation sensitive reporter gene assay.

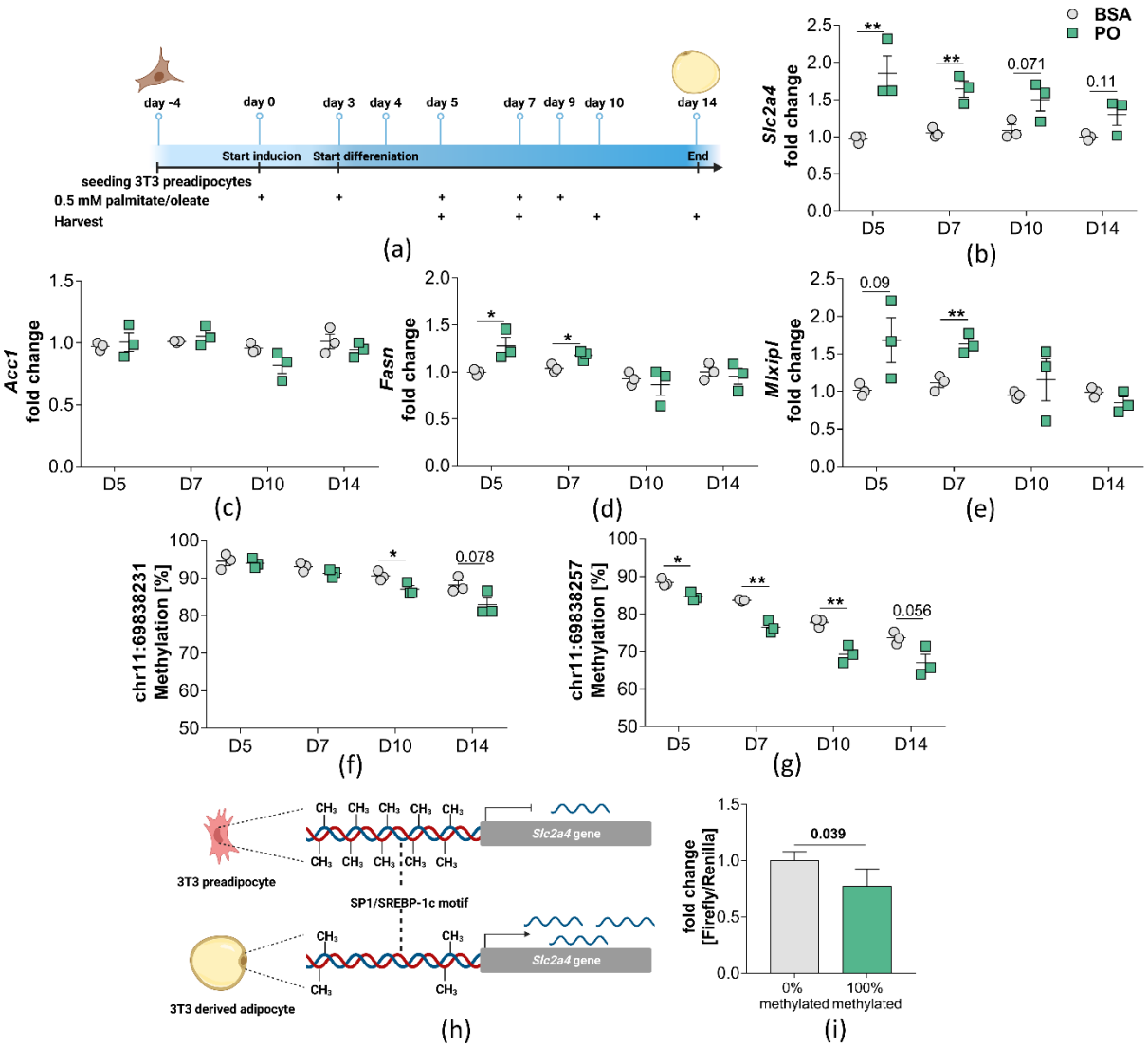

Figure 30: Gene expression and DNA methylation in 3T3 cells after treatment with palmitate/oleate. (a) Treatment regime of 3T3 cells during differentiation with either 0.5 mM palmitate/oleate (P/O, ratio 1:1) or 0.75% BSA (vehicle). 3T3 cells were seeded at D-4, start of induction of differentiation was performed at D0 and start of differentiation at D3. Crosses indicate time points of treatment. Cells were harvested at D4, D5, D7 and D10 for DNA and RNA extraction. (b) to (e) expression of genes involved in glucose uptake (Slc2a1, Slc2a4), glucose signalling (Mlxipl) and de novo lipogenesis (Acc1, Fasn). Mean ± SEM of fold change between P/O treatment (n = 3) and BSA treatment (n = 3) is shown, after normalizing expression to Hprt. A Two-Way ANOVA was performed with n.s. = non significant, * = $p < 0.05$, ** = $p < 0.01$, *** = $p < 0.001$, **** = $p < 0.0001$; (f) and (g) DNA methylation in the ROI under palmitate/oleate treatment or vehicle. Mean ± SD A Two-Way ANOVA was performed with n.s. = non significant, * = $p < 0.05$, ** = $p < 0.01$, *** = $p < 0.001$, **** = $p < 0.0001$. h) Scheme on how DNA methylation may impair transcription factor binding and influences gene expression; (i) Methylation sensitive reporter gene assay. ROI was amplified from genomic murine DNA and cloned into a CpG-free reporter gene vector. Afterwards ROI was methylated using a DNA methyltransferase and the vector was transfected into HEK293T cells. Displayed is mean ± SD after normalizing to 0% methylated as control. For statistical analysis unpaired, two-sided students t-test was performed. Figure taken from Britsemmer et al. 2023.

6. Discussion

The global pandemic of metabolic diseases, such as obesity, insulin resistance or MASLD, burdens health care systems and displays a drastic threat to the lives of many people world wid. Unraveling novel epigenetic mechanisms, which are involved in the progression and establishment of those diseases by altering the gene expression of disease-related genes, might facilitate the development of new treatment strategies. Therefore, I investigated the regulatory role of miRNAs in the context of liver-specific local controlling genes, which are previously described as a subset of genes with an essential role in regulating liver metabolism. Contrary to the hypothesis, a single master regulator miRNA that regulates all LCGs could not be identified, since the investigated epigenetic mechanism is not conserved between the murine animal model and human. However, the identified miR-149-5p shows a great potential as MASLD-driver independent from the LCGs by regulating key enzymes and transporters in metabolic hepatic pathways across both species.
Additionally, the VAT plays a crucial role in the development of insulin resistance in obesity, which is also linked to obesity-mediated downregulation of the *SLC2A4* gene, encoding for the main insulin-dependent glucose transporter of the adipose tissue. Glucose uptake by *SLC2A4* into the adipocyte is connected to de novo lipogenesis, which in turn generates insulin-sensitizing metabolites. The molecular mechanism behind the decreasing *SLC2A4* gene expression are incompletely understood. I hypothesized that alterations in DNA methylation of the *SLC2A4* gene could contribute to this phenotype. I could confirm the hypothesis by investigating the DNA methylation in the VAT of an obese human cohort and in a longitudinal mouse model for diet-induced obesity. Additionally, an in vitro cell culture model supports the findings and regulatory role of DNA methylation on *SLC2A4* expression.

The discussion will be subdivided into three major sections in which the results of each hypothesis will be discussed separately. This will be followed by a combined proposed model and a summary with outlook for the future and the importance of the studies.

6.1. The miRNA master regulator/LCG hypothesis – why finding the master regulator miRNA for LCGs failed

Local controlling genes of the liver has been identified to be involved in regulating hepatic metabolism. During MASLD, expression of the LCGs is disrupted. Identification of one comprehensive regulatory mechanism for all LCGs, which rescues the disruption in gene expression, might harbor great potential as a therapeutic target. Since miRNAs are capable of regulating many genes, the aim was to identify a single miRNA, the master regulator, that regulates all LCGs.
Therefore, the hepatic expression from miRNA microarray of chow-fed or hfd-fed mice after 22 weeks of diet-regime are analyzed and correlated with RT-qPCR expression of published LCGs (*Appl2, Arhgap24, Cd82, Cobll1, Ddx3x, Gk, Inhbe, Myc, Rapgef4, Smim13* and *Tap1*). From the eleven LCGs, *Arhgap24*, *Cd82*, *Cobbl1*, *Ddx3x* and *Smim13* are significantly downregulated in the liver of hfd-animals, whereas *Inhbe* is significantly upregulated. The gene expression of LCGs immediately changed the original hypothesis, since LCGs are up- or downregulated. Therefore, a single master regulator miRNA regulating all LCGs is impossible and the hypothesis was adapted. Consequently, two master regulator miRNAs are needed. One miRNA targeting the upregulated LCGs (*Inhbe*) that itself is downregulated, and one miRNA targeting the downregulated LCGs (*Arhgap24*, *Cd82*, *Cobll1*, *Ddx3x* and *Smim13*) that itself is upregulated. Correlation analysis of the 152 significantly differentially expressed miRNAs from micro array data coupled with seed-sequence prediction reveals 52 miRNAs that potentially regulate the LCGs and show at least a negative correlation with at least one of the LCGs.
However, no miRNA is found that show a predicted or validated binding to all downregulated LCGs simultaneously. An explanation might be that the downregulated LCGs posses distinct cellular functions and are involved in different gene networks. Research on evolutionary functionality of miRNAs suggest that the impact of miRNAs is attributed to weakly repression of many target genes within a gene regulatory network (GRN) rather than a strong repression of a few target genes within the same GRN. This also assumes that the likelihood increases for one miRNA regulating many genes within one GRN rather than many GRNs of distinct function (Zhao et al. 2017). A very broad regulation of unconnected GRNs increases the possibility of counteracting forces and therefore a miRNA might annul its effect (Y. Chen et al. 2017). Additionally, *Arhgap24* (Rho-GTPase-activating protein) for instance is involved in GTPase signaling (Yang et al. 2022), whereas the ATP-dependent RNA helicase *Ddx3x* is involved in RNA processing (Gadek, Sherr, and Floor 2023). The membrane protein Tspan-27, also known as *Cd82*, distributes membrane proteins across the cell membrane and its repression is associated with increased metastasis and tumor progression (Tonoli and Barrett 2005). Further, the cordon-blue protein-like 1 (*Cobll1*) is responsible for actin remodeling in the SAT and the non-coding variant rs6712203 in the *Cobbl1* gene is associated with impaired actin remodeling in differentiating SAT and metabolically obese normal weight (MONW) phenotype (Glunk et al. 2023). But those associations seem to be SAT specific and similar findings for liver or MASLD are not reported. The function of the small integral membrane protein 13 (*Smim13*) is not reported in the literature, but it is positively correlated with hepatic TAG content in overweighted humans (Klaus et al. 2021). The distinct molecular function of the downregulated LCGs decreases the possibility to be regulated by the same miRNA.

Nevertheless, the seed sequence and correlation analysis found a miRNA regulating the Smim13 and Ddx3x in mice – namely the mmu-miR-149-5p, which also displays the highest increase in expression in hfd-fed mice. For the upregulated *Inhbe* LCG, the *mmu-miR-21-5p* is identified, which also displays the greatest decrease in expression. The *Inhbe* gene encodes the *inhibin subunit beta E*, which is also considered a hepatokine. Hepatokines are proteins specifically secreted from the liver that involved in regulating lipid and glucose metabolism (Stefan and Häring 2013). Just recent studies discovered independently two loss of function variants in the *INHBE* gene in humans, which are associated with

obesity and type 2 diabetes development. The first variant is protective against obesity (Deaton et al. 2022) and the second variant is protective against liver damage, since it rebalances dysregulated fat distribution in obesity (Akbari et al. 2022). Both groups suggest *INHBE* as a potential therapeutic target and reducing INHBE levels in obesity or MASLD are desired.

6.1.1. Inconsistencies in miRNA and LCG expression patterns across intervention mouse models, but not in mouse model for DIO

To find ways to revert the expression of *mmu-miR-21a-5p* and *mmu-miR-149-5p* to physiological levels, 5 intervention models are tested, two dietary models (diet-switch and caloric restriction), one surgical (vsg) and two pharmacological treatments with anti-diabetic drugs (exendin-4 and metformin.)

In the longitudinal mouse model for DIO, *mmu-miR-21a-5p* expression is significantly decreased at week 4 and *mmu-miR-149-5p* expression persistently increases at week 6 in the hfd-fed animals. Due to their early onset in dysregulation, both miRNAs are potentially causative for MASLD development and progression rather than consequential effects of the hfd. In the DIO mouse model, the onset of dysregulation of the LCG target genes follow their perspective regulator miRNA in an inverse manner and a negative correlation between target LCG and regulator miRNA is observed. This criteria is essential for a regulating role of a miRNA on its target gene, since RNA-interference induces mRNA degradation (Y.-P. Wang and Li 2009). Therefore, it is plausible that repression of mmu-miR-21a-5p leads to an induction of *Inhbe* expression and induced mmu-miR-149-5p represses *Ddx3x* and *Smim13* expression in the DIO mouse model.
However, this relationship is not consistent throughout all intervention models. For instance, *Smim13* expression is rescued after exendin-4 treatment and caloric restriction, but *mmu-miR-149-5p* expression remains induced in those conditions. This implies that regulation of Smim13 gene expression is independent of mmu-miR-149-5p or the epigenetic regulation gets disrupted. Unfortunately, the data on Smim13 gene regulation is scarce and therefore the interpretation of the these results remains speculative. Studies in HepG2 cells cotreated with oleate and exendin-4 show an induction of autophagy pathways (H.-H. Yu et al. 2022). Autophagy is associated with intense membrane remodeling and the redistribution of membrane proteins (L. Li et al. 2021). During this process, integral membrane proteins play an essential role and become activated to initiate autophagy (Namkoong et al. 2015). Since *Smim13* is a small integral membrane protein, it might be that it becomes activated and probably even induced in gene expression upon exendin-4 treatment, which would uncouple the regulatory effect of *mmu-miR-149-5p*. This uncoupling is also seen in the correlation analysis of the individual sub cohorts, where negative correlation of *mmu-miR-149-5p* and *Smim13* expression is observed when only chow and hfd-fed animals are correlated but diminishes in chow-fed and exendin-4 treated animals (Supplementary Figure 3a & d). Interestingly, also caloric restriction is reported to induce autophagy (Shabkhizan et al. 2023). It is possible that induced autophagy is the common mechanism in caloric restriction and exendin-4 treatment, which results in the rescue of *Smim13* gene expression and Smim13 is no direct target of *mmu-miR-149-5p* in these conditions. This phenomenon of a miRNA changing its regulatory function or also its targetome in different conditions is also defined by the term targetome-degeneration or degeneracy (Bhajun, Guyon, and Gidrol 2016). A shift of a miRNA-targetome has been observed for the miR-124-3p in age-related macular degeneration (AMD). Even though miR-124-3p displays no significant differences in gene expression between a healthy and an AMD retina, the subset of targeted mRNAs is different between both conditions (Chu-Tan et al. 2021). r
Mmu-miR-21a-5p expression is reversed after dietary switch and exendin-4 treatment and *Inhbe* expression after dietary switch, caloric restriction and exendin-4. *Mmu-miR-21a-5p* and *Inhbe*

expression correlate negatively across all interventions. Therefore it is likely, that *mmu-miR-21a-5p* regulates *Inhbe* gene expression in these conditions and *mmu-miR-21a-5p*-mediated *Inhbe* regulation contributes to remission of MASLD in mice, since loss-of-function SNPs in the *INHBE* gene are associated with increased hepatic fat content and systemic fat distribution in human.

6.1.2. Acute and chronic response of miR-21-5p and miR-149-5p in surgical weight-loss induction (VSG)

Before the development of incretin-analogues, bariatric surgery was the most efficient strategy to achieve long term body weight loss. Therefore, vertical sleeve gastrectomy in diet-induced obese mice is expected to show the greatest effect on the reversal of miRNA and LCG expression. Bariatric surgery has previously shown to reduce hepatic-specific miRNA expression in the serum of obese human subjects, but direct liver miRNA expression has not been assessed before (Sangiao-Alvarellos et al. 2020).

The VSG cohort is divided into a recovery/weight-loss phase (9 days post-surgery) and maintenance/body weight regain phase-cohort (35 days post-surgery). Since surgeries expose the organism to a variety of stress stimuli, this discrimination is made to differentiate between effects on miRNA and LCG expression due to post-surgery stress, such as increase in inflammatory processes, and long-term effects on body weight reduction. Even though inflammatory markers for liver, such as interleukin-6 (IL-6), are not measured, it is reported that vsg surgery induces a stronger inflammatory response in the liver when compared to mice underwent a sham surgery (Ahn et al. 2021).
Interestingly, mmu-miR-21a-5p expression increases in the liver of vsg mice in the recovery phase, but is normalized to sham levels in the maintenance phase (Figure 31). Mmu-miR-21a-5p shows no correlation with hepatic triglyceride content in recovery or maintenance phase, but correlates negatively with body weight in recovery phase. This indicates that mmu-miR-21a-5p expression is independent of liver fat content. However, inflammation processes are induced in the recovery phase. This suggests that mmu-miR21a-5p might be induced by liver inflammation or that its origin resides not within the hepatocyte itself. MASLD progression is associated with proinflammatory processes promoting the establishment of MASH. This process goes along with infiltration of macrophages but also thrombocytes (Dalbeni et al. 2022). Interestingly, miR-21 is also characterized as a profibrotic miRNA derived from megakaryocytes, a progenitor cell for thrombocytes in red marrow (Barwari et al. 2018). The authors could show that miR-21-mediated downregulation of the Wiskott-Aldrich syndrome protein (WASp) increases TGF-β1 secretion from thrombocytes and thereby promotes fibrosis within tissues (Barwari et al. 2018). Similar findings are reported that miR-21 is induced by inflammation in tumorigenic tissues and is supposed serve as a ‚key switch' in inflammatory response (Kumarswamy, Volkmann, and Thum 2011; Sheedy 2015). When inflammation processes decrease after surgery recovery, miR-21a-5p expression therefore relevels. A hallmark of MASH compared to MASLD are induction of inflammation and fibrosis (Loomba, Friedman, and Shulman 2021) and miR-21 is found to be upregulated in obese subjects with higher degree of liver inflammation and fibrosis when compared to obese subjects with lower degree (Rodrigues et al. 2023). This might also explain, why *miR-21a-5p* is downregulated in the longitudinal mouse model for DIO. Since this model represents the early spectrum of MASLD development rather than MASH, *miR-21-5p* might be suppressed in the early onset by an unknown mechanism, but is induced once inflammation processes start in the liver and the MASLD liver transitions into MASH. Counterintuitively, miR-21a knock out mice show reduced degree of liver fibrosis and reduced portal inflammation (Kennedy et al. 2016). This finding is in contrast to my data showing decreased miR-21-5p levels in MASLD. However, it is noteworthy that the miR-21a knock

out abolishes the complete *miR-21a* gene and thus both mature miRNAs, miR-21a-3p and miR-21a-5p are removed. Additionally, this knock out model is not a liver-specific one. Therefore, comparison and effects of the mmu-miR-21a-5p in after vsg with the complete miR-21a knock out mice is vague. The *mmu-miR-21a-5p* target LCG tends to decrease in the recovery phase post-surgery and is significantly downregulated in the maintenance phase and correlates negatively with mmu-mIR-21a-5p expression in the recovery phase. This suggests that mmu-miR-21a-5p might mediate the downregulation of *Inhbe* in that phase, but the prolonged effect of Inhbe downregulation in the maintenance phase is mmu-miR-21a-5p independent.

Interestingly, *mmu-miR-149-5p* expression tends to decrease in recovery and is significantly reduced in the maintenance phase after vsg when compared to sham control mice. The expression pattern of *mmu-miR-149-5p* is highly connected with the degree of reduction in hepatic triglyceride content (Figure 31) and correlates positively with hepatic triglyceride content. Mmu-miR-149-5p target LCG *Ddx3x* expression significantly increases in the liver of vsg mice in the recovery phase and tends to remain upregulated in the maintenance phase. *Smim13* expression is upregulated in both phases. Both LCGs correlate negatively with mmu-miR-149-5p expression, which suggests a regulatory role of mmu-miR-149-5p on LCG expression. These results emphasize a possible role of the hepatic triglyceride content on *mmu-miR-149-5p* expression followed by a mmu-miR-149-5p mediated downregulation of LCGs. Hepatic triglyceride content decreases after vsg due to reduced food intake, body weight reduction and increased capacity of adipose tissue to store fatty acids again (Al-Najim, Docherty, and le Roux 2018).
Overall, the results from the DIO model, intervention models and vsg suggest a role of mmu-miR-21a-5p in response to inflammation, which would explain the downregulation during hfd-feeding. Micro gene array data from week 12 of DIO model show no significant changes in hepatic inflammation marker on gene expression level (Supplementary Figure 12). Probably with ongoing MASLD progression and increase in inflammation, miR-21a-5p becomes activated but remains suppressed in the absence of inflammation like in the DIO model. However, miR-149-5p expression seems to be closely connected with hepatic fat content, which links miR-149-5p to the primary MASLD characteristic.

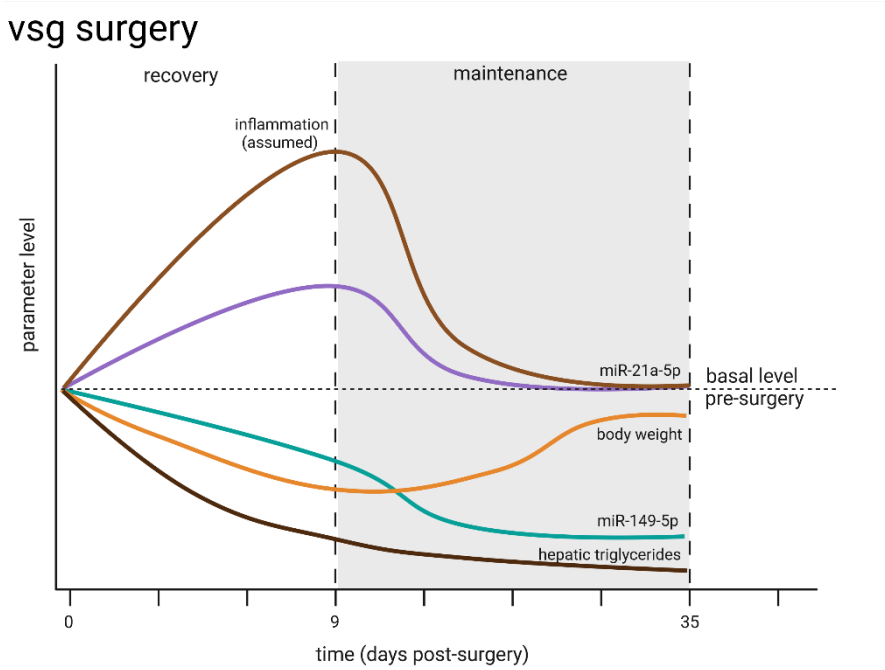

Figure 31: Schematic overview of events post-vsg surgery. The vsg cohort is separated into a sub cohort, which are sacrificed 9 days post-surgery, and a maintenance sub cohort, which are sacrificed 35 days post-vsg. Mmu-miR-21a-5p is significantly downregulated in DIO mice, but is significantly increased in expression in the recovery phase, which normalizes in the maintenance phase. Since hepatic triglyceride content keeps decreasing, it might be another factor influencing mmu-miR-21a-5p expression. This factor might be inflammation. Mmu-miR-149-5p expression starts to decrease in the recovery phase, and is significantly downregulated in the maintenance phase. It follows a similar pattern to the hepatic triglyceride content.

6.1.3. Weight-loss independent reversal of miR-21a-5p and miR-149-5p: pharmacological treatment with metformin

Metformin is an oral anti-diabetic drug, which is primarily metabolized within the liver and preliminary research also show an effect on depletion of hepatic fat content and improvement of liver fibrosis, which were investigated in MASH mouse models using a methionine-choline deficient (MCD) diet or a fat, fructose and cholesterol rich diet (Brandt et al. 2019; KATSURA et al. 2015). Interestingly, metformin treatment of MASH-induced MCD-diet fed animals shows a distinct miRNA-profile, when compared to MCD-diet fed animals that did not receive metformin. Those data show the potential of metformin treatment in MASH on altering miRNA expression, but the effect of metformin on hepatic miRNAs in a hfd-mouse model for diet-induced obesity are not tested. Therefore, in this study, the effect of metformin treatment on DIO-induced miR-21-5p and miR-149-5p dysregulation is assessed.
In comparison with the previously discussed intervention models, metformin treatment displays significant reduction in hepatic triglyceride content independent from body weight changes. Whereas caloric restriction, diet switch or exendin-4 treatment reduces body weight without altering hepatic triglyceride content and vsg reduces body weight and hepatic triglyceride content. Therefore, tendencies in gene expression after metformin treatment are regarded as hepatic triglyceride-driven rather than body weight-driven. Mice are fed either a hfd or chow control diet for twelve weeks and are subsequently treated with metformin for six weeks. A sub cohort are continuously fed with a hfd without metformin treatment and chow control mice received chow diet throughout the time period. Metformin treatment surprisingly has no effect on body weight of the mice, but significantly reduced hepatic triglyceride content. Furthermore, glucose tolerance is significantly improved validating that metformin worked properly in the mice (data not shown). Mmu-miR-21a-5p expression is unaffected

by the metformin treatment, whereas *mmu-miR-149-5p* expression tends to decrease without reaching significant differences. Interestingly, *Inhbe* expression is significantly reduced after metformin treatment when compared to continuous hfd-feeding, which suggests that rescue of *Inhbe* expression is mmu-miR-21a-5p independent.
Metformin-mediated hepatic fat content depletion after five weeks of hfd-feeding is reported in rats, where metformin treatment significantly decreases hepatic DAG content, total ceramide levels, plasma free fatty acids (FFAs) and increase in hepatic insulin sensitivity (Zabielski et al. 2018). Interestingly, metformin treatment results in the decrease of hepatocyte-fatty acid transporters Cd36 and Fatp2 and additional repression of hepatic DNL by activation of AMPK through phosphorylation. Therefore, the authors hypothesize that the reduction in hepatic fat content after metformin treatment is achieved by reduced fatty acid uptake and reduced DNL. Those mechanism might be preserved in mice likewise. The tendencies in *mmu-miR-149-5p* might be a consequence to the reduced hepatic fat content rather than causing the decrease in liver fat, which aligns with the previous results. Mmu-miR-149-5p target LCGs remain significantly downregulated after metformin treatment and correlate negatively with mmu-miR-149-5p expression. Similar to the longitudinal DIO mouse model, *mmu-miR-149-5p* seems to mediate *Ddx3x* and *Smim13* downregulation and keeps *Ddx3x* and *Smim13* repressed after metformin treatment.
In summary, metformin seems to be efficient in reducing liver fat content in mice and might prevent MASLD progression by rescuing *Inhbe* expression independent of mmu-miR-21a-5p.

6.1.4. Translation of murine mouse models into an obese human liver cohort: Are the target LCGs of miR-21-5p & miR-149-5p conserved?

To translate the findings from mice to humans, hsa-miR-21-5p and hsa-miR-149-5p and their corresponding target LCG-expression is studied in a obese human liver cohort, which is stratified into subject with high HbA1c (> 6.5 %) and low HbA1c levels (< 5.7 %) based on the ADA criteria for diagnostics of type 2 diabetes. In the mouse models, hfd-feeding represses *mmu-miR-21a-5p* and induces *mmu-miR-149-5p* expression when compared to chow control diet fed animals. The expression of LCG target genes show consistent negative correlations exclusively in chow and hfd groups, but not throughout all intervention models. This suggests a role of mmu-miR-21a-5p and mmu-miR-149-5p in MASLD by regulating LCGs, but reversibility through interventions might uncouple miRNA/mRNA interactions and LCGs are regulated differently in interventions. Therefore, miRNA and LCG expression is measured in the liver of obese subjects stratified into low (< 6.5 %, n = 19) and high (≥ 6.5 %, n = 21) HbA1c levels, a common diagnostic marker for type 2 diabetes (T2D). T2D and insulin resistance are common risk factors for MASLD and vice versa. The switch of organism from mouse to human is challenging, since miRNA sequences or 3'UTR sequences of the mRNAs might not be conserved. However, *mmu-miR-21a-5p* sequence is completely conserved and its human ortholog is the *hsa-miR-21-5p*. The same accounts for the *mmu-miR-149-5p*, whose human ortholog is the *hsa-miR-149-5p* with completely conserved sequence. 3'UTR-mRNA sequences of INHBE, DDX3X and SMIM13 on the other hand are not completely conserved and repeated seed-sequence prediction between candidate miRNAs and LCGs reveal a target switch. Therefore in human *INHBE* and *DDX3X* are targeted by the hsa-miR-149-5p and *SMIM13* by the hsa-miR-21-5p. This is a well known challenge when performing interspecies studies of miRNAs (Xiaowei Wang and El Naqa 2008).
Hsa-miR-21-5p tends to increase in subjects with high HbA1c levels and *SMIM13* levels remain unaltered. No correlation between SMIM13 and *hsa-miR-21-5p* is observed as well as no correlation of *hsa-miR-21-5p* with other metabolic parameters, such as BMI, HbA1c levels, serum insulin or triglyceride levels. Therefore, it is very unlikely that in human SMIM13 is a direct target of hsa-miR-21-5p. Noteworthily, hsa-miR-21-5p tends to increase. Previously in mouse, mmu-miR-21a-5p is

downregulated after hfd-feeding, but increases in expression in the recovery phase after vsg, where inflammation is assumed to be high. A vague speculation could be that *hsa-miR-21-5p* starts to increase with further progressing liver damage or hepatic inflammation. Additionally, the human cohort contains male and female subjects, which might explain some differences in miR-21-5p expression across the species, since the mouse models contain solely male mice. Sexual dimorphism in miRNA expression is commonly observed and even opposing miRNA expression levels in the same disease between both genders has been reported (Guo et al. 2017). However, no differences in hsa-miR-21-5p expression is detected between male obese subjects with high HbA1c levels when compared to obese male obese with low HbA1c. Similar when compared for female subjects (data not shown). But it is noteworthy that sub cohort analysis by sex drastically reduces cohort size and therefore statistical power.
Interestingly, *hsa-miR-149-5p* is significantly upregulated in obese subjects with high HbA1c levels when compared to low HbA1c and correlates positively with HbA1c levels, NAS score, and shows a non-significant correlation with serum triglyceride levels ($p = 0.057$). This aligns with the results observed in the mouse model. But the target LCG *INHBE* is upregulated likewise, which conflicts with the hypothesis that *INHBE* expression is regulated by *hsa-miR-149-5p*. Since loss of function variants for INHBE are reported that are protective for liver damage, it is plausible that INHBE contributes to MASLD and its progression independently of hsa-miR-149-5p. Nonetheless, a great limitation of the human obese liver cohort is the deficit of a normal-weight, healthy control group. Therefore, only assumption about the expression changes from lean to obese can be made.

In summary, the miRNA master regulator theory for LCG genes in MASLD failed with transfer into human. Nonetheless, LCGs might play a role in human MASLD progression as well as hsa-miR-21-5p and hsa-miR-149-5p, but independently from each other. Still, hsa-miR-149-5p shows great potential since its upregulation in human obese type 2 diabetic livers and its correlation with metabolic parameters. Also its reversibility through interventions, such as vsg, shows its great potential and therefore, hsa-miR-149-5p became the foundation of the following studies.

6.2. Hsa-miR-149-5p as central regulator of liver metabolic pathways

This paragraph will be separated into individual discussions of each metabolic pathway (TCA and GABA shunt, methionine and folate cycle (one carbon metabolism), and urea cycle) across all conditions (in vitro HepG2 experiments, DIO mouse model, and obese human liver cohorts). Followed by a combined discussion to integrate all findings into the overall context of MASLD. In summary, overexpression of miR-149-5p in HepG2 cells decreases the gene expression of key enzymes involved in the metabolic pathways and metabolome analysis of significantly differentially enriched metabolites from the intracellular and extracellular fraction of HepG2 cells overexpressing miR-149-5p results in significant enrichment of metabolites involved in methionine and urea cycles. Further, those results are reproducible in a mouse model for diet-induced obesity, where mmu-miR-149-5p is upregulated in the liver of hfd-fed animals, which is accompanied by downregulation of genes and metabolites of the metabolic pathways. Those findings are conserved in the liver of an obese human cohort and in a public available human cohort with normal-weight controls (SteatoSITE).
Additionally, a short discussion on miR-149-5p regulation on the glucose uptake in HepG2 will be conducted as first. Since the bulk-mRNA sequencing reveals insights on the mechanism, which might lead to the reduced insulin-stimulated glucose uptake in HepG2 cells after hsa-miR-149-5p overexpression.

6.2.1. Hsa-miR-149-5p overexpression reduces insulin-stimulated glucose uptake in HepG2 cells – the role of *SLC2A4* expression

Since hsa-miR-149-5p is upregulated in the liver of DIO mice and in the liver of obese human subjects with high HbA1c levels when compared to subjects with low HbA1c levels and further correlates positively with HbA1c levels, it is assumed that hsa-miR-149-5p might play also a role in regulating blood glucose levels and hepatic insulin resistance. To investigate this question, hsa-miR-149-5p is overexpressed in HepG2 cells using mirVana mimics and subsequently, HepG2 cells are stimulated for 10 min with insulin or remain unstimulated prior to performing a glucose uptake assay. Interestingly, hsa-miR-149-5p reduces insulin-stimulated glucose uptake, but unstimulated glucose uptake is unaltered.

HepG2 cells display a distinct glucose metabolism compared to primary hepatocytes culture or liver tissue (Molinaro, Becattini, and Solinas 2020). HepG2 cells are a hepatoma-derived cell line and generally cancer cells depend more on glycolysis for energy production than on oxidative phosphorylation (Fadaka et al. 2017). Also, HepG2 cells express the insulin-dependent glucose transporter GLUT4 (*SCL2A4* gene) (B. Chen et al. 2021), which is not expressed in primary hepatocytes or the liver tissue. Hepatocytes rely on GLUT1, GLUT2, GLUT5, GLUT8 and GLUT9 glucose transporters (Chadt and Al-Hasani 2020a). Interestingly, overexpression of miR-149-5p decreases *SLC2A4* gene expression and *SLC2A4* is a conserved, predicted miR-149-5p target gene (Supplementary Figure 13: SLC2A4 expression from bulk-mRNA sequencing after hsa-miR-149-5p overexpression. a: Relative reads per million normalized to control-mimic transfection. b: Seed prediction and match pairing of miR-149-5p to human (*SLC2A4*) and murine (*Slc2a4*) 3'UTR.Supplementary Figure 13a & b). Thereby hsa-miR-149-5p might contribute to the reduction in insulin-stimulated glucose uptake in HepG2 cells by downregulating the GLUT4 transporter, which is an interesting finding for tissues where GLUT4 and hsa-miR-149-5p are co-expressed, such as the adipose tissue, but might be irrelevant in the context of liver. Further research exploring the role of miR-149-5p and SLC2A4 within the adipose tissue should be conducted to elucidate the miR-149-5p function in regulating glucose uptake.

6.2.2. Hsa-miR-149-5p in regulating the TCA and GABA shunt in MASLD – consequences for MASLD progression

Overexpression of miR-149-5p in HepG2 results in significant downregulation of the TCA genes *IDH1*, *IDH2*, *ACLY* and *AGXT*. Additionally, the TCA genes *OGDH* and *SUCLG2* tend to be increased. Genes involved in the GABA shunt, a TCA recycling pathway for succinate from GABA, are downregulated, such as *ABAT*, *ALDH5A*1 and *SLC6A12*, and *GOT1* is significantly upregulated. *GOT1* encodes for the AST enzyme, whose serum levels are elevated in patients with MASLD and is a commonly used diagnostic marker for liver damage (Hadizadeh, Faghihimani, and Adibi 2017; Hossain et al. 2009).
Unfortunately, the majority of metabolites involved in the TCA and GABA shunt are not detected in the metabolomics to validate the effects measured on transcriptome level (Figure 32). Additionally, the amino acids glutamate and glutamine, which are derivates in the GABA shunt and are products/educts of many reactions in metabolic pathways, remain unchanged after miR-149-5p overexpression in HepG2 cells. A plausible explanation for this phenomenon might be the composition of the cell culture medium. HepG2 cells are cultured in GlutaMAX DMEM medium with pyruvate supplementation. Cell culture media have the property to supply the cultured cells with nutrients and amino acids to maintain cellular function, which in vivo are provided by the diet (Arora 2013; Yao and Asayama 2017).According to manufacturers instructions (Thermo Fisher Scientific, US), GlutaMAX is a glutamine substitute

designed to reduce ammonia production in cell cultures and DMEM medium contains a 4-fold increased amino acid concentration compared to other commonly used media. Therefore, HepG2 cells might compensate for the loss of enzymes by increased glutamine uptake from the media. Nevertheless, glutamine levels are significantly reduced in DIO mouse liver, which is accompanied by a significant downregulation of the *Gls2* enzyme. *Gls2* catalyzes the reaction from glutamine into glutamate and is a predicted conserved target of miR-149-5p. Further, *GLS2* is significantly decreased in late-stage MASLD (SteatoSITE cohort) and *GLS2* expression displays a negative association with induced hsa-miR-149-5p expression levels in the liver of the obese human cohort. Decreasing serum glutamine levels are reported for patients with MASLD (Simón, Martínez-Chantar, and Delgado 2021). Even though it is unclear if decreasing serum glutamine levels are derived from the liver, it is possible that downregulation of *GLS2* by *hsa-miR-149-5p* contributes to the phenotype. Interestingly, glutamine supplementation in hfd-fed mice lowers serum triglyceride levels and shows protective effects on hfd-induced liver damage, when supplemented simultaneously with the start of hfd-feeding regime (Y. Zhang et al. 2024). Besides reduced serum glutamine levels in MASLD, also abnormally high concentrations of glutamine are associated with acute and chronic liver failure (Helling et al. 2016). This suggests that both abnormalities in glutamine levels are unfavorable in MASLD and emphasizes that there is no general ‚good' or ‚bad' metabolite levels in regard of glutamine. Probably a balanced, normal level of glutamine is desired, which might be disturbed by abnormal hsa-miR-149-5p expression.

The key enzyme for GABA degradation throughout all tissues is the ABAT enzyme, which degrades GABA into succinate semialdehyde (Vogel et al. 2018). Neither GABA nor succinate semialdehyde could be measured in the metabolomics of HepG2 cells or liver from DIO mice. Nevertheless, *ABAT* gene expression is significantly reduced in HepG2 cells after miR-149-5p overexpression, in DIO mouse liver, where it shows a negative correlation with induced mmu-miR-149-5p expression, and in the SteatoSITE human cohort. Also, ABAT tends to decrease in the human obese liver cohort and ABAT expression shows a negative association with hsa-miR-149-5p expression. Pharmacological inhibition of ABAT lead to GABA accumulation within the liver (Qume and Fowler 1996). Recently, hepatic GABA accumulation by impaired *Abat* function has been associated with insulin resistance and reducing hepatic GABA levels improves insulin sensitivity in hfd-fed animals by increasing glucose clearance by the muscle tissue (Geisler et al. 2021). Furthermore, low *ABAT* expression in hepatocellular carcinoma (HCC), the end stage of MASLD progression, is associated with a poor prognosis of HCC (Gao et al. 2022). Similar findings are reported by Hui Han et al. The authors suggested a regulatory role of induced miR-183-5p in HCC on low levels of *ABAT* expression (H. Han et al. 2021). Those results also support the hypothesis of a potential epigenetic regulation of *ABAT* mediated by a miRNA. Based on the reported findings on HCC-related low *ABAT* expression and the fact that pharmacological inhibition of *ABAT* lead to increased GABA accumulation, it can be assumed that miR-149-5p-mediated *ABAT* repression could cause a similar phenotype in MASLD and therefore promotes MASLD progression in mice and in human.

Another important reaction is catalyzed by the *AGXT* enzyme, which is involved in glyoxylate detoxification (Wanders and Waterham 2006). *AGXT* degrades glyoxylate and serine into pyruvate and glycine (KEGG enzyme ID: EC 2.6.1.45). Deficiency of the *AGXT* gene is causative for a disorder called Primary Hyperoxaluria Type 1 (PH1), due to accumulation of glyoxylate and oxylate. Currently, there are 146 mutations in the *AGXT* gene associated with PH1 (Williams et al. 2009). Patients suffering from PH1 have recurrent kidney stones, nephrocalcinosis (accumulation of calcium oxalate/phosphate in the nephron) up to kidney failure (Groothoff et al. 2023). Even though PH1 disorder affects the kidneys, the root of the disease lies within the liver, since glyoxylate detoxification by *AGXT* is a liver-specific reaction and the only available treatment is liver or kidney transplantation (X.-Y. Wang et al. 2023). Recently, hypermethylation of the *AGXT* gene is identified as one cause of *AGXT* downregulation in MASLD

patients or DIO mice, which emphasizes an epigenetic regulation of *AGXT* in the progression of this disease (Gianmoena et al. 2021). *AGXT* is a conserved, predicted target of miR-149-5p and *AGXT* expression is significantly decreased after hsa-miR-149-5p overexpression in HepG2 cells, decreases in liver of DIO mice and correlates negatively with mmu-miR-149-5p expression. Furthermore, it tends to decrease in the live of obese human subjects with high HbA1c levels and is significantly reduced in late stage MASLD (SteatoSITE cohort). Intracellular serine levels, one of the substrates of AGXT-mediated glyoxylate degradation, are significantly reduced in HepG2 cells after overexpression of miR-149-5p as well as in the liver of DIO mice and negatively correlate with mmu-miR-149-5p expression. Additionally, glycine and pyruvate levels are significantly decreased in liver of DIO mice and correlate negatively with mmu-miR-149-5p expression (Figure 32). Unfortunately, glyoxylate is not measured in the metabolomics, but supported by the reported findings, it is plausible that miR-149-5p-mediated AGXT downregulation in MASLD leads to impaired glyoxylate detoxification and accumulation. Though serine, glycine and pyruvate are not exclusively synthesized or degraded by *AGXT*, it is reasonable that AGXT-downregulation contributes to the decreased levels. However, pyruvate and glycine are not differentially enriched in HepG2 cells after miR-149-5p overexpression. A possible reason again might be the pyruvate supplementation and the high glycine concentration of the cell culture medium.

GOT1 encodes the aspartate aminotransferase AST, which is a commonly used bio- and diagnostic marker for general liver health. AST levels are elevated in the circulation of MASLD patients (Hadizadeh, Faghihimani, and Adibi 2017). Interestingly, *GOT1* gene expression is upregulated in HepG2 cells after miR-149-5p overexpression and is no predicted target gene of miR-149-5p, which suggests that *GOT1* is compensatory upregulated or induced indirectly by some elevated metabolite. In the human obese liver cohort, serum AST level positively correlate with *hsa-miR-149-5p* expression, despite the *GOT1* gene itself is significantly downregulated in the liver of obese subjects with high HbA1c levels and gene expression negatively correlates with hsa-miR-149-5p expression. Therefore, either the transcriptomic changes of GOT1 expression are not reflected on a protein level, or elevated AST in the circulation might not be exclusively derived from the liver. Other sources for increased AST in the circulation might be skeletal muscle damage, which has also been reported in MASLD (J.-H. Han et al. 2022; T. Zhou et al. 2023).

DIO mice display a higher GSG index (glutamate to serine and glycine ratio) in their livers compared to standard chow-control animals. GSG index positively correlates with mmu-miR-149-5p expression. Recent studies suggest an increased GSG index in the plasma as potential biomarker for MASLD and study subjects with MASLD display a higher GSG index when compared to the non-MASLD control group (Leonetti et al. 2020). However, it is not solved if the origin of increased GSG index in plasma lies within the liver. Nevertheless, Melania Gaggini and colleagues found increased GSG index in plasma of MASLD patients directly correlated with liver enzyme expression (Gaggini et al. 2018). Further, the authors claim to discriminate based on the GSG index in plasma between low fibrosis state (F0 to 2) and high fibrosis state (F3 and 4). This might play an important role in MASH diagnostic and prediction, since for MASH diagnosis a biopsy is required (Sheka et al. 2020).

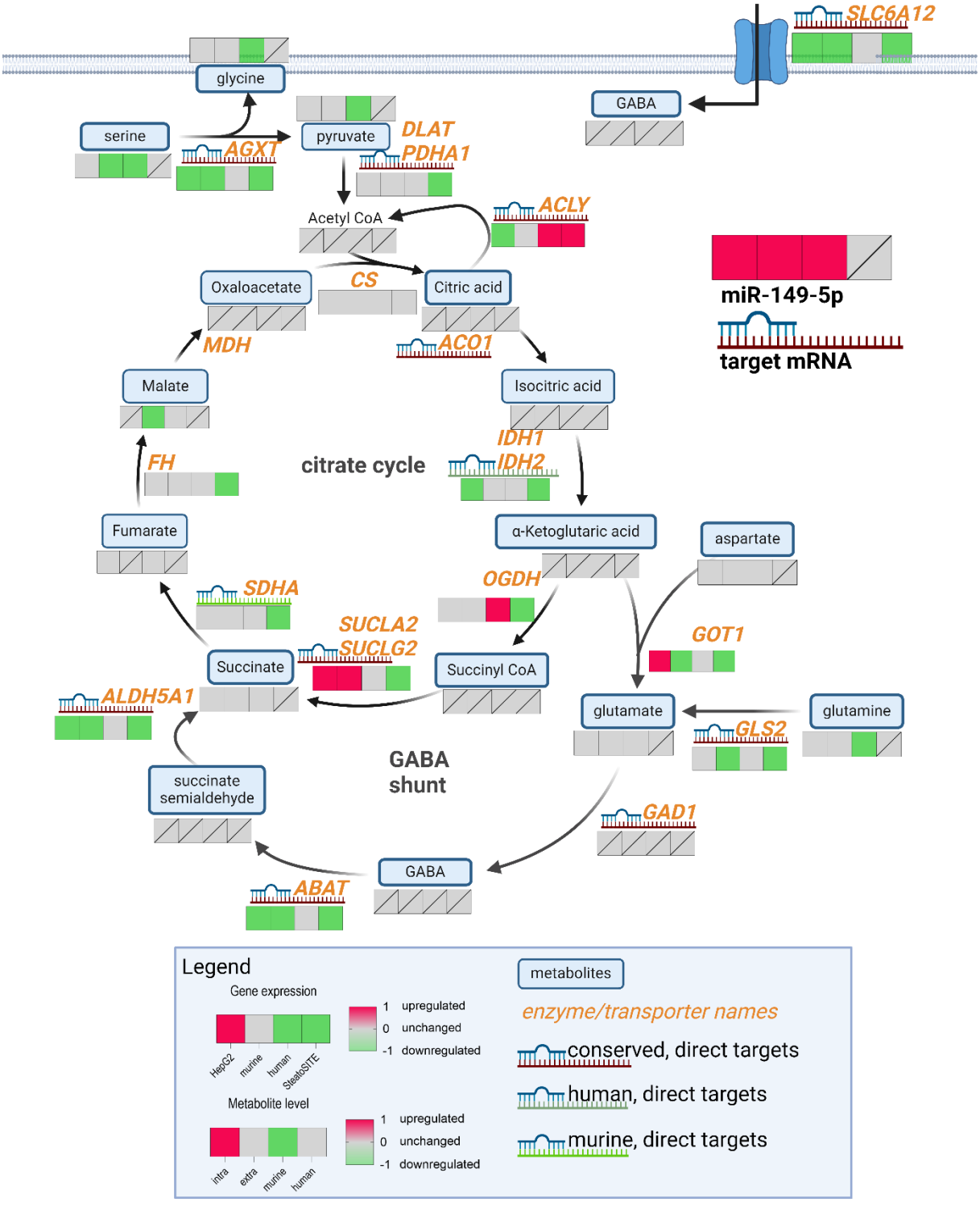

Figure 32: Summary figure of transcriptomic and metabolomic data from HepG2 cells after miR-149-5p overexpression, from liver of DIO mice, obese human liver cohort and SteatoSITE cohort for the TCA cycle and GABA shunt. For gene expression and metabolites, red boxes indicate upregulation, grey unchanged and green downregulation. Grey box with line indicates not measured/expressed. First to fourth box from left to right for gene expression: Data collected from HepG2 cells after miR-149-5p overexpression, murine liver data from DIO mice, human obese liver cohort or SteatoSITE cohort. First to fourth box from left to right for metabolite levels: Data collected from the intracellular fraction of HepG2 cells after miR-149-5p overexpression, data collected from the extracellular fraction of HepG2 cells after miR-149-5p overexpression, murine liver data from DIO mice, and human metabolomics data are not measured.

6.2.3. miR-149-5p in regulating the one-carbon metabolism and urea cycle in MASLD

The one-carbon metabolism summarizes the nested reactions of the methionine and folate cycle (Ducker and Rabinowitz 2017). Both cycles are essential for liver health and some dietary MASH models involve methionine-deficient, methionine/choline-deficient or folate deficient diets to induce fibrosis and steatosis in the liver (Stephenson et al. 2018). Therefore, low levels of those metabolites are considered harmful in the context of MASLD progression. Important metabolites, such as SAM, the main methyl donor in eucaryotic cells (Chiang et al. 1996) necessary for DNA methylation, and SAH are generated in the methionine cycle (Wen Shen et al. 2020). Besides the import of methionine into the liver, hepatocytes synthesize methionine by the conversion of betaine and homocysteine catalyzed by the BHMT enzyme (Feng et al. 2011).
Betaine is either imported through BGT-1 (*SLC6A12* gene) or is generated by the conversion of choline (Y. Zhou et al. 2012). *SLC6A12* is the transporter linking the TCA/GABA shunt with the one carbon metabolism, since it serves as a GABA/betaine transporter. *SLC6A12* is a conserved, predicted target gene of miR-149-5p and is significantly downregulated after miR-149-5p overexpression in HepG2 cells, significantly decreases in the liver of DIO mice and shows a negative correlation with mmu-miR-149-5p expression. Further, *SLC6A12* tends to decrease in the liver of obese subjects with high HbA1c levels and shows a negative association with induced hsa-miR-149-5p expression. Finally, it is significantly reduced in late stage MASLD subjects, when compared to normal-weight controls (SteatoSITE). Betaine levels are reduced in liver of DIO mice and negatively correlate with mmu-miR-149-5p expression, but betaine is unaltered in HepG2 cells, whereas choline is significantly increased in the extracellular supernatant (Figure 33). For findings in DIO mice, it is reasonable that mmu-miR-149-5p-mediated downregulation of *Slc6a12* reduces the betaine uptake in therefore results in lower levels of betaine. Interestingly, Yanlin Li and colleagues report that betaine treatment via drinking water reduces hepatic lipid accumulation in hfd-fed mice (Y. Li et al. 2022). But direct betaine levels in the liver and *Slc6a12* expression are not measured in the reported study. Nonetheless, normalizing betaine levels in MASLD is commonly considered as beneficial for liver health. As mentioned previously, hepatocytes generate betaine by conversion of choline. Increased choline levels in the extracellular medium of HepG2 cells suggest a reduced uptake by HepG2 cells, which is unaffected in liver of DIO mice. This is supported by the fact that the choline transporter CTL4 (*SLC44A4* gene) (Hedtke and Bakovic 2019) is significantly downregulated in HepG2 cells after miR-149-5p overexpression, but is unaltered in mice (Supplementary Figure 14a & b). However, *SLC44A4* is no predicted target for miR-149-5p in neither of the both species. The mechanism behind the downregulation in HepG2 cells remains speculative. Probably, miR-149-5p targets a transcription factor in human, which induces *SLC44A4* expression and contributes to *SLC44A4* downregulation by degrading this transcription factor. Therefore *SLC44A4* might be regulated indirectly by miR-149-5p. Additionally, one has to be aware that the effects observed in HepG2 cells are derived exclusively from miR-149-5p overexpression. In the liver of DIO mice the predominant effect comes from the diet. This may explain further differences observed in HepG2 cells and DIO mice aside the species and in vitro versus in vivo effect.

BHMT is significantly downregulated in obese human with high HbA1c levels, correlates negatively with *hsa-miR-149-5p* expression and is downregulated in late stage MASLD (SteatoSITE). It is a predicted target for miR-149-5p in human, but not in mice. However, *BHMT* remains unchanged in HepG2 and even tends to be upregulated in the liver of DIO mice (Figure 33). The discrepancy between HepG2 cells and human liver might be explained by a different mode of regulation of miR-149-5p. This study focuses on the transcriptome changes after miR-149-5p overexpression, given that miRNA regulate gene expression by mRNA-degradation. However, miRNAs are capable of inhibiting the translation of mRNA into protein by ribosomal blocking. Probably, *BHMT* is reduced on protein level in HepG2 cells.

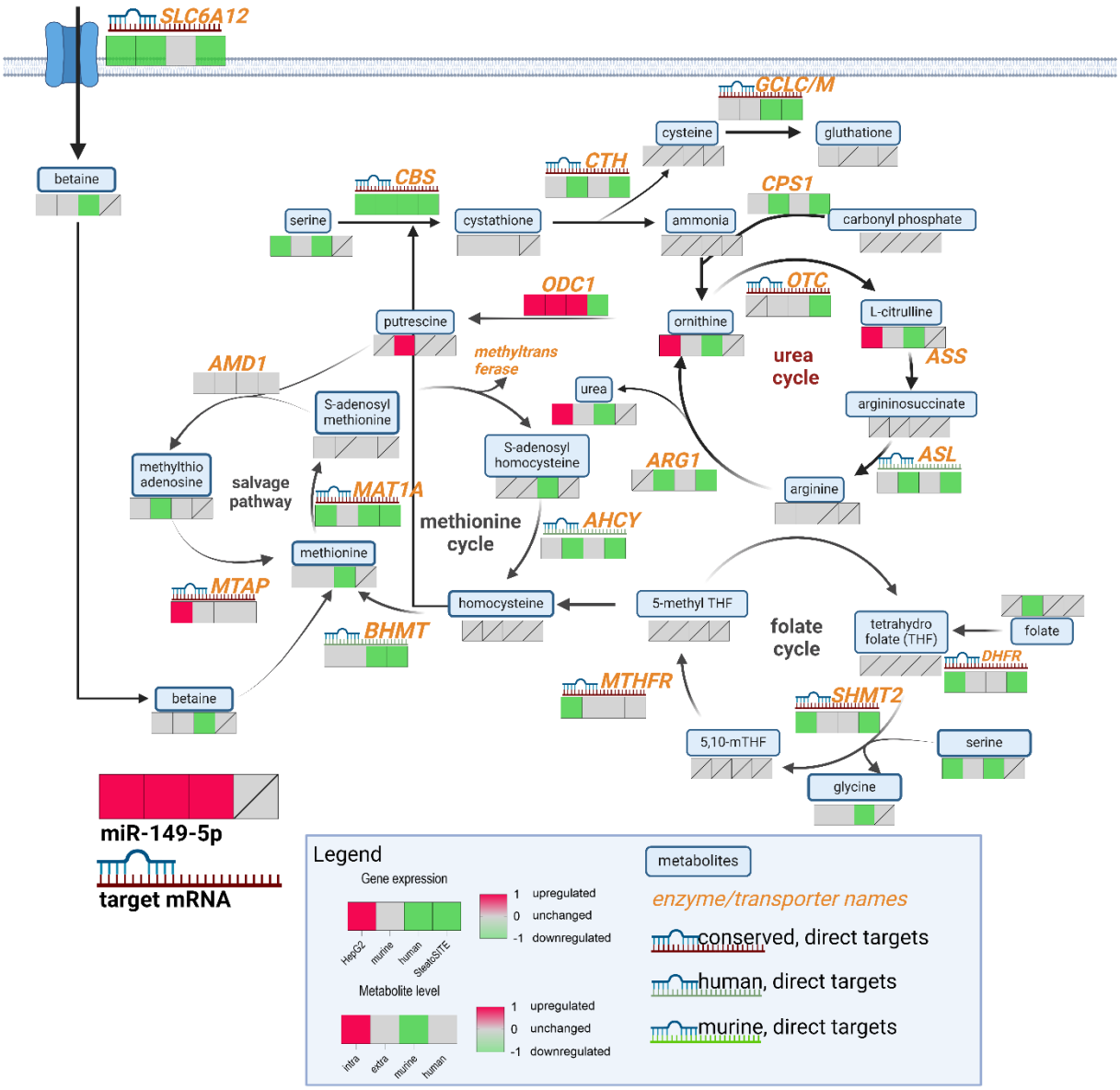

Figure 33: Summary figure of transcriptomic and metabolomic data from HepG2 cells after miR-149-5p overexpression, from liver of DIO mice, obese human liver cohort and SteatoSITE cohort for the one-carbon metabolism (methionine/folate cycle) and urea cycle. For gene expression and metabolites, red boxes indicate upregulation, grey unchanged and green downregulation. Grey box with line indicates not measured/expressed. First to fourth box from left to right for gene expression: Data collected from HepG2 cells after miR-149-5p overexpression, murine liver data from DIO mice, human obese liver cohort or SteatoSITE cohort. First to fourth box from left to right for metabolite levels: Data collected from the intracellular fraction of HepG2 cells after miR-149-5p overexpression, data collected from the extracellular fraction of HepG2 cells after miR-149-5p overexpression, murine liver data from DIO mice, and human metabolomics data are not measured.

After conversion of homocysteine into methionine by *BHMT*, adenosyl from ATP is transferred to methionine to generate SAM by the *MAT1A* enzyme. *MAT1A* is a conserved, predicted target of miR-149-5p and decreases in HepG2 cells after miR-149-5p overexpression, is significantly reduced in obese human with high HbA1c levels and correlates negatively with induced *hsa-miR-149-5p* expression. Further, *MAT1A* is downregulated in late stage MASLD (SteatoSITE) (Figure 33). However, *Mat1a* is unchanged in the liver of DIO mice, but methionine levels are significantly reduced and correlate with mmu-miR-149-5p expression, which indicates an impaired methionine metabolism. Probably in mice *Mat1a* is regulated by miR-149-5p through ribosomal blocking rather than degradation of its mRNA, which results in stable mRNA levels, but protein levels and *Mat1a* activity is reduced. *MAT1A* is an

essential key enzyme in the methionine cycle and serves as main enzyme for SAM synthesis from methionine (TORRES et al. 2000). SAM is crucial for maintaining DNA methylation, due to its role as substrate for DNMTs and methyl donor. However, SAM levels are not significantly changed, but tend to be reduced in the liver of DIO mice (log2FC: - 0.58, p = 0.065, padj. = 0.13), which further indicates a dysregulated methionine cycle in DIO mice. Genetic deficiency of the *MAT1A* gene causes a condition called hypermethioninemia, which describes elevated methionine levels in the blood circulation (Schweinberger and Wyse 2016) and is linked to decreasing SAM and glutathione levels in the liver (Lu et al. 2001). This leads to liver injury and steatosis in mice lacking the *Mat1a* gene by production of ROS. Additionally, *Mat1a* liver-specific knock out (KO) mice show increased VLDL particle secretion, but display lower triglyceride content per particle. The authors suggest that the reduced triglyceride secretion further promotes lipid accumulation in the liver of *Mat1a* KO mice (Cano et al. 2011). MiR-149-5p-mediated downregulation might therefore promote MASLD progression through two different ways: 1) dysregulation in methionine cycle causing ROS and 2) increased lipid accumulation by reduced lipid secretion.

SAM is demethylated by DNMTs into SAH and SAH is further converted to homocysteine by the enzyme *AHCY*. SAH levels are significantly lower in liver of DIO mice when compared to standard chow-fed animals and correlate negatively with *mmu-miR-149-5p* expression. *AHCY* is a predicted target in human for miR-149-5p and tends to be downregulated in the liver of DIO mice, where it negatively correlates with miR-149-5p expression. Further, *AHCY* is significant downregulated in late stage MASLD (SteatoSITE). In mice, no binding to the 3'UTR of *Ahcy* by mmu-miR-149-5p is predicted Figure 33. However, the strong negative correlation between *mmu-miR-149-5p* with *Ahcy* expression and SAH levels indicate a potential role of miR-149-5p-mediated regulation. While miRNA/mRNA interactions in the 3'UTR are well established, also binding of miRNAs outside the 3'UTR has been reported (von Brandenstein et al. 2018; H. C. Martin et al. 2014). Possibly, miR-149-5p regulates *Ahcy*-mRNA by non-canonical binding outside the 3'UTR, which is not detected by the miRNAvis seed sequence prediction function, hence it performs simple seed matching within a given 3'UTR sequence and extended sequence context is not considered yet.
Furthermore, DIO mice show a higher methylation index in the liver compared to the control chow-diet animals, which is positively correlated with mmu-miR-149-5p expression in DIO mice. The methylation index is the ratio between SAM and SAH and a higher methylation index indicates lower levels of SAH compared to SAM. SAH itself is a DNMT-inhibitor and DNMTs exert higher affinity towards the inhibitory SAH than to their substrate SAM (Isakovic et al. 2009; W. J. Lee and Zhu 2006). Thereby it can be assumed that higher methylation index promotes a favorable environment for DNA methylation, due to an increased DNMT activity, since less DNMT inhibitor is abundant and thus may also lead to genome-wide hypermethylation within the liver. Interestingly, *AHCY* overexpression is reported to increase genome-wide DNA methylation by erasing intracellular SAH levels and based on enhanced DNMT1 activity. Interestingly, the same authors could also show, that *AHCY* and DNMT1 colocalize and even physically interact to facility DNMT-catalyzed DNA methylation (Ponnaluri et al. 2018). Therefore, an impact on whole-genome DNA methylation by miR-149-5p mediated SAH levels seems plausible. However it is noteworthy that the studies of Ponnaluri and colleagues are not conducted in the context of MASLD or liver disease and further research needs to elucidate if those processes are essential in MASLD progression and thus mmu-miR-149-5p plays a role within it. But it can be assumed that *miR-149-5p*-mediated downregulation of Mat1a and Ahcy might contribute to aberrant DNA methylation in MASLD by altering the methylation index.

Homocysteine from the methionine cycle can enter the transsulfuration pathway, where the enzyme *CBS* generates cystathionine under consumption of homocysteine and serine (Sbodio, Snyder, and Paul 2019). *CBS* serves as rate limiting enzyme of the transsulfuration pathway. Though it is upregulated in many diseases, such as cancer, its role in MASLD remains ambiguous (Sarna, Siow, and O 2015). For

instance, *CBS* KO mice display increased lipid accumulation in the liver and increased plasma homocysteine levels (Watanabe et al. 1995). A similar phenotype is observed in MASH patients, where increased plasma homocysteine can be ascribed to a downregulation of *CBS* and *BHMT* in the liver of those patients (García-Tevijano et al. 2001). On the other hand, also lower homocysteine plasma levels in the context of increased hepatic *CBS* expression are reported in patients with MASLD (Polyzos et al. 2012). Despite the opposing data in the literature, in general a dysregulated CBS/homocysteine system is believed to be harmful (Sarna, Siow, and O 2015). *CBS* expression is significantly downregulated across all conditions and correlates negatively with miR-149-5p expression. *CBS* is a conserved target gene based on seed sequence prediction and integration of database validated interactions. Therefore, it is plausible that miR-149-5p contributes to dysregulation of the transsulfuration pathway in MASLD.

Cystathionine is catalyzed by *CTH* to generate cysteine. In this reaction, ammonia is released, which in turn enters the urea cycle. The urea cycle is restricted to the liver (Keshet et al. 2018). Urea cycle disorders (UCDs) show deficiency for a majority of genes involved in the urea cycle, such as *ARG1*, *CPS1* and *CTH* (Matsumoto et al. 2019). Patients suffering from UCDs and MASLD or MASH share some characteristics(De Chiara et al. 2018). For instance, hyperammonemia in MASH patients is reported, which is attributed to a decreased *CPS1* and *CTH* expression (De Chiara et al. 2018). The increase in ammonia in the blood circulation is caused by the dysregulation of the urea cycle by impaired metabolism of ammonia into urea (Auron and Brophy 2012). However, the urea cycle displays the greatest discrepancy on metabolite and transcriptome level between DIO mice and overexpression of miR-149-5p in HepG2 cells. Whereas in DIO mice it seems like the urea cycle is completely downregulated on a transcriptome and metabolome level and miR-149-5p target genes plus associated metabolites (ornithine and citrulline) correlate negatively with miR-149-5p expression, in HepG2 cells the urea cycle remains largely unaltered on the transcriptome level (except for *CBS*). This suggests that miR-149-5p target genes are probably regulated by translation inhibition in HepG2 cells, since metabolite levels of the urea cycle are significantly increased, such as ornithine, citrulline and urea (Figure 33). Interestingly, HepG2 cells are deficient for the liver-specific *ARG1* enzyme. *ARG1* catalyzes urea production from arginine under the production of ornithine. *ARG1* correlates negatively with miR-149-5p expression in the obese human liver cohort and in the mouse model. HepG2 might generate urea by a compensatory enzyme, such as *ARG2*, which is natively expressed in the human kidneys and HepG2 cells but not in liver (Z. Li et al. 2022). Additionally, HepG2 cells do not express the urea transporters *SLC14A2* and the ornithine transporter *SLC25A15*. Therefore, urea and ornithine might accumulate within HepG2 cells rather than being secreted (Makris et al. 2024).

In summary, miR-149-5p shows a great potential in human and in DIO mouse model in regulating a variety of metabolic pathways and metabolite levels in MASLD, which on the one side promote the development of MASLD by increasing lipid accumulation and on the other side further enhance MASLD progression into MASH.

6.2.4. Regulation of miR-149-5p by PPARG activity at the *GPC1* promoter

MiR-149-5p is encoded in the first intron of its host gene *GPC1* in mice and in human and therefore might rely on the *GPC1* promoter activity. *GPC1* is a glypican and is reported to be upregulated in HCC with poor prognosis. Also, *Gpc1* gene expression increases in the liver of DIO mice and correlates positively with *mmu-miR-149-5p* expression. Transcription factor binding prediction for Gpc1 promoter reveals a binding motif of PPARG and subsequent Pearson correlation analysis show a positive correlation of PPARG expression with Gpc1 and mmu-miR-149-5p expression in the liver of DIO mice. Integration of publicly available ChIP-seq data from HepG2 cells verify PPARG binding to the *GPC1*

promoter. This relationship of *Pparg*, *Gpc1* and *mmu-miR-149-5p* is also seen in intervention mouse models, where *Pparg*, *Gpc1* and mmu-*miR-149-5p* expression are reversed, which seems to be driven by hepatic triglyceride content.

The data in this work highlight a possible mechanism how fatty acids may regulate the miR-149-5p expression by activating PPARG in hepatocytes. Fatty acids are shown to induce PPARG activity (Varga, Czimmerer, and Nagy 2011). However, treatment of HepG2 cells with palmitate/oleate for 24 hours failed to induce miR-149-5p expression, but a tendency of a slight upregulation is noticeable. Probably a longer treatment time with palmitate/oleate or a higher concentration might lead to a greater induction. Additionally, a pharmacological treatment activating PPARG directly with a PPAR-agonist, such as pioglitazone or rosiglitazone, could answer the question of PPARG-mediated miR-149-5p induction and verify the hypothesis. PPAR-agonists are commonly used in obesity-related type 2 diabetes and show improvement in insulin sensitivity and have also shown to reduce hepatic lipid accumulation (Hsiao et al. 2017; Ma et al. 2018). In the first place, it would seem counterintuitive that PPARG activation may lead to a harmful hepatic phenotype by inducing miR-149-5p. But PPARG is a lipogenic transcription factor that regulates DNL in adipose and liver tissue (Witte et al. 2015). Interestingly PPARG activity declines in adipose tissue (AT) in obesity and MASLD, which contributes to the lipolytic shift in AT, but increases in MASLD liver and therefore enhances hepatic DNL (Skat-Rørdam et al. 2019; Torres et al. 2022; S. Yu et al. 2003). Despite their positive effect on hepatic lipid accumulation, it is assumed that the hepatic lipid accumulation reduces with PPAR-agonists, because their primarily target tissue is the AT. By PPARG-activation in the AT, adipocyte function improves and the capacity to store fatty acids, which in turn leads to reduced lipid accumulation in the hepatocytes (Skat-Rørdam et al. 2019). PPARG agonism within in the liver might cause liver damage, which has been also reported for the first developed PPARG-agonist troglitazone (Jaeschke 2007). Just recently, researchers reported induced reactive oxygen species (ROS) production in HepG2 cells following pioglitazone treatment (G. Huang et al. 2024). ROS contribute to MASLD progression by inducing oxidative stress and liver damage (Delli Bovi et al. 2021). They arise from impaired mitochondrial function and lipotoxicity. ROS also attract immune cells in the liver, such as macrophages, which in turn induce stellate cell-mediated collagen production in the liver and fibrosis (Wiering, Subramanian, and Hammerich 2023). Since miR-149-5p dysregulates genes and ROS-protective pathways, such as *CBS* and cystathionine synthesis, the induced ROS-production after pioglitazone treatment in HepG2 cells might be partially attributed to induced miR-149-5p levels.

Regulating transcription factor for miR-149-5p are identified by binding prediction to the Gpc1 promoter and correlation analysis with gene expression. Though, induced or repressed expression of a transcription factor may not always reflect an induced or repressed activity. Therefore, other transcription factors, which show no differential expression in the liver of DIO mice might contribute to miR-149-5p expression likewise.

6.3. Limitations of the miR-149-5p studies

In summary, this work suggests a great importance of miR-149-5p in regulating metabolic pathways in MASLD by using in vitro overexpression coupled with an in silico approach to identify miR-149-5p target genes. Even though the provided data and the consistency of miR-149-5p correlation with metabolites and predicted target genes throughout all conditions show strong evidence, but in the end a predicted target gene remains a predicted target unless a proof of physical interaction is shown. Further, HepG2 cells might be a suitable model for identifying target genes for miR-149-5p, since over 80 % of miR-149-5p predicted targets are expressed, their role as cell culture model for MASLD or other metabolic

diseases is debatable. The in vitro metabolomics studies need to be interpreted with caution, despite the astonishing effect of miR-149-5p on the metabolome of HepG2 cells regarding a short incubation time (48 h) and the fact that only a single miRNA is overexpressed. In an intact liver organ, many cell types interact with each other and metabolite clearance or secretion into the circulation play a major role in an organism. Those processes can not be reproduced in cell culture, but need to be taken into account. Additionally, the composition of the cell culture medium may have great impact on the metabolome, since the induced loss-of-function by miR-149-5p-mediated downregulation of target genes can be compensated by the import or availability of amino acids within the medium.
A second limitation of the human obese liver cohort of patients with high and low HbA1c is the lack of a lean control group. This makes interpretations from the mouse model into human challenging. In the mouse model, lean mice are compared to mice with ongoing fatty liver disease, whereas in human obesity is already the underlying metabolic disease. This drawback is compensated by using publicly available transcriptomic data of a human cohort comparing different steatosis states with normal weight controls (SteatoSITE). HbA1c is a diagnostic marker for type 2 diabetes and type 2 diabetes with insulin resistance is a major risk factor for MASLD and vice versa. However, T2D is by no means equivalent to MASLD. Stratification by NAS score is avoided, since the NAS score is not known for all subjects, which would reduce the statistical power of the RNA-seq data. Additionally, the metabolome for the human obese liver cohort is missing. Therefore, it remains elusive if the metabolome changes observed in liver of DIO mice are reflected in human MASLD livers. Comparison with references in the literature are challenging, since predominantly plasma or circulating metabolites but not liver metabolites are measured in human. How well plasma metabolites reflect the liver metabolites remain elusive.
Also, the transcriptome and metabolome changes after reversal of mmu-miR-149-5p expression from caloric restriction or vertical sleeve gastrectomy would be great indicator, if the dysregulation of the metabolic pathways is abolished when mmu-miR-149-5p expression is normalized.

6.4. Hypermethylation of the SLC2A4 gene in VAT of obese subjects

Expression of the glucose transporter GLUT4, encoded by the *SLC4A2* gene, is reduced in the adipose tissue during obesity but the under-lying mechanism is incompletely understood. To investigate a potential epigenetic mechanism, DNA methylation in the an enhancer region of the SLC2A4 gene combined with gene expression of *SLC2A4* and downstream DNL genes is measured in the VAT of obese humans with impaired glycemic control (high HbA1c). The region of interest (ROI) contains multiple binding motifs for SP1, a transcription factors previously described to regulate *SLC2A4* gene expression (Im et al. 2006). Since epigenetic changes are induced by environmental factors, such as diet and diet composition, palmitate/oleate treatment of 3T3-derived adipocytes during differentiation is conducted to find a possible inducing factor for DNA methylation. Consequently, the downregulation of *SLC2A4* may be linked to a reduced DNL capacity of adipose tissue in obesity (Eissing et al. 2013; Sievert, Krause, Geiβler, et al. 2021; Z. Song, Xiaoli, and Yang 2018b). A reduced DNL in adipose tissue leads to impaired inter-organ crosstalk and is associated with increase in insulin resistance through altered secretion adipose tissue derived lipokines (H. Cao et al. 2008b). This promotes the development of insulin resistances in obese individuals. The data are previously published (Britsemmer et al. 2023)

SLC2A4 gene expression is downregulated in the VAT of obese subjects with high HbA1c levels when compared to obese subjects with low HbA1c. *SLC2A4* gene expression correlates positively with DNL gene expression, negatively with serum triglycerides and insulin levels, and is accompanied by a hypermethylation in the ROI. Interestingly, *SLC2A4* gene expression shows no correlation with fasted

glucose levels. This observation lead to the conclusion that *SLC2A4* gene expression might rather be regulated by triglyceride levels than by glucose levels, even though it is an glucose transporter. Interestingly, the AT contributes less to post-prandial glucose uptake, when compared to the liver or muscle, where glucose is primarily stored in form of glycogen (Chadt and Al-Hasani 2020b), since the AT rather stores fatty acids. However, the Ats primarily role is in regulating the glucose uptake of other organs via *SLC2A4* (Abel et al. 2001). The increased methylation in the proximity of SP1 binding motifs might impair SP1 binding, which consequently reduces *SLC2A4* gene expression. Impaired SP1 binding mediated by DNA methylation has previously been shown to play a role in the same human cohort, where hypermethylation in a SP1 binding motif decreases *FASN* gene expression, one of the DNL-associated genes (Dantas Machado et al. 2015; Sievert, Krause, Geißler, et al. 2021). This observation supports the hypothesis that genes involved in glucose and lipid homeostais are regulated by DNA methylation in the VAT.
Surprisingly, DNA methylation did not correlate directly with *SLC2A4* gene expression, but a stepwise-linear regression model including DNA methylation as predictor for *SLC2A4* expression increases the accuracy of the model, when compared to a model excluding DNA methylation as a predictor. This suggests a regulatory role of DNA methylation on *SLC2A4* gene expression. The absent direct correlation might be explained by anti-diabetic medication of the cohort subjects. It is known that anti-diabetic medication, for instance metformin, can alter DNA methylation (Cuyàs et al. 2018). On the other hand, insulin stimulates DNL gene expression and insulin-signaling induces translocation of GLUT4 protein into the membrane. (Santoro, McGraw, and Kahn 2021). Obese subjects of this cohort partially receive insulin or metformin medication. This might interfere with the ‚native' regulation of *SLC2A4* by DNA methylation. This assumption is supported by the sub-cohort correlation analysis, where DNA methylation and SLC2A4 gene expression is correlated within a sub-cohort of study subjects receiving metformin medication and in a sub-cohort correlation analysis of subjects receiving insulin. Interestingly, in the metformin medicated sub-cohort, DNA methylation correlates negatively with SLC2A4 gene expression. The correlation is abolished in the insulin-receiver sub-cohort. This indicates that insulin medication may uncouple the epigenetic regulation of *SLC2A4* by DNA methylation. Interestingly, it has been reported that insulin induces *Slc2a4* gene expression independently of SP1 (Moraes et al. 2014). Nonetheless, it is noteworthy that the sub-cohort analysis should be interpreted with caution as the sample size is low.

6.4.1. Hypermethylation in VAT in longitudinal mouse model for DIO

In VAT of DIO mice, Slc2a4 gene expression decreases at week 4 and DNA methylation starts to increase at both CpG-sites of the ROI in mouse genome at week 2. Additionally, DNL-associated genes (Mlxipl, Fas, Acaca) display the same expression pattern as the Slc2a4 gene. DNL-genes correlate positively with S*lc2a4* gene expression, which in turn correlates negatively with *Slc2a4* DNA methylation. *Slc2a4* gene expression and DNA methylation show a strong association with metabolic parameters. Plasma glucose, insulin and hepatic triglyceride levels correlate positively with DNA methylation, whereas correlation with Slc2a4 gene expression are negatively.
Those findings in general are reproducible with the findings from human subjects, which emphasizes a comprehensive mechanism across both species.
The longitudinal data from the DIO mouse model provide information about the onset of changes in DNA methylation and *Slc2a4* gene expression. This helps to unriddle the puzzle of cause and consequence. Interestingly, the changes in DNA methylation already occur in a very early state after hfd-feeding. DNA methylation was significantly increased at week 2 at both CpG sites in the mouse genome. The decrease in *Slc2a4* gene expression follows at week 4. Therefore it can be assumed that the prior changes in DNA methylation are causative for the downregulation of gene expression rather

than being a consequence to hfd-feeding. Longitudinal data are scarce in the literature for mice, but especially for human and are warranted, since endpoint studies might overestimate the strength of association between observed DNA methylation and gene expression (F. He et al. 2019). Therefore, the longitudinal mouse model for DIO is a great model to decipher the development of obesity.
Interestingly, DNL-genes follow the expression of *Slc2a4* in VAT of DIO mice. This confirms further the crucial role of Slc2a4 on DNL.
Additionally, *SLC2A4* gene expression correlates with serum triglyceride levels in obese human and with hepatic triglyceride levels in the DIO mouse model. This emphasizes the important role of fatty acids to regulate the glucose homeostasis of adipose tissue in obesity. Supporting to this observation, similar effects of fatty acids on *Slc2a4* gene expression in adipose tissue are reported in mice, where treatment with atorvastatin, a drug applied for hypercholesterolemia, rescues *Slc2a4* gene expression by lowering serum cholesterol and triglycerides (Poletto et al. 2015).

6.4.2. DNA methylation and Slc2a4 gene expression in 3T3-derived adipocytes

The human studies and the longitudinal mouse model of DIO mice suggested a possible link between fatty acids and DNA methylation. It is plausible that fatty acids may cause the hypermethylation observed in the SLC2A4 gene in murine and human VAT. Therefore, 3T3 cells are treated with palmitate/oleate (PO) during differentiation.
Interestingly, PO treatment induces Slc2a4 gene expression in the early time points, which normalizes with the treatment regime over 14 days. This induction in the beginning is accompanied by an induced expression of DNL-genes. The induction of Slc2a4 gene expression goes in hand with a reduction in DNA methylation in the PO treated cells when compared to BSA control treated cells. DNA methylation levels normalize with gene expression towards the end of the treatment period.
Those results may appear counterintuitive on the first sight, since DNA methylation increases in obese subjects and mice, whereas *SLC2A4* gene expression decrease. This might be explained by differentiation process of 3T3 into adipocytes, which seems to be accelerated by PO treatment. Fatty acids play a crucial role in adipogenesis and the epigenetic changes, including DNA methylation, attributed to it (Azain 2004). Nevertheless, the PO treatment of 3T3 cells confirm that the CpGs in the ROI are sensitive to the treatment and are modulated by it. Additionally, the regulatory function of the CpGs remain integer, since lower levels of DNA methylation are associated with higher levels of Slc2a4 gene expression, similar to the findings from human and murine VAT. Probably a longer treatment or a treatment of mature 3T3 adipocytes would show the expected effect, where fatty acids start to induce the Slc2a4 hypermethylation. This is supported by reports, where fatty acid treatment reduces insulin-dependent glucose uptake of differentiated 3T3 cells, which is accompanied by an increased global DNA methylation and hypermethylation of adipogenic gene promoters, such as *Pparg*, *Adipoq* and also *Slc2a4*. The hypermethylation is there while accompanied by a downregulation of gene expression (Małodobra-Mazur et al. 2021).
The repressive regulatory role of the investigated CpGs in the ROI is finally confirmed by the methylation-sensitive reporter gene from HEK293T cells, where the methylated vector decreases the luciferase signal. Despite HEK293T are commonly used as cell culture model to investigate gene enhancer or gene regulatory functions with luciferase assay and also massively parallel reporter assays (MPRAs), they may express distinct transcription factors to adipocytes. This still needs to be taken into consideration when interpreting the data. Also, primary adipocytes may display an alternative model for the 3T3-derived adipocytes. Additionally, SP1 binding is previously confirmed in HepG2 ChIP-Seq data. If SP1 physically interacts with the binding motifs in the ROI and if the DNA methylation indeed impairs with the binding of SP1 remains elusive.

6.4.3. Summary of the *SLC2A4* investigations

The results indicate a possible epigenetic regulation of the *SLC2A4* gene in the VAT of obese human and mice by DNA methylation. The increase in DNA methylation contributes to the downregulation of *SLC2A4* expression and thereby regulates systemic insulin-sensitivity, due to an impaired DNL capacity of the VAT. Further, those changes might be triggered by increased fatty acid uptake in adipocytes, which is commonly seen in obesity. The study improves the understanding how insulin resistance establishes in obesity and emphasizes the role of dietary fatty acids and adipose tissue in type 2 diabetes.

6.5. Proposed model: Interorgan crosstalk between VAT and liver

Since *Slc2a4* gene expression decreases and *Slc2a4*-DNA methylation increases very early in the longitudinal mouse model for DIO and seems to be induced by fatty acids, it can be possible that the dysregulation in the VAT contributes to the induction of miR-149-5p in the liver. Interorgan crosstalk in the progression of obesity and its comorbidities plays a crucial role. To test this hypothesis, *Slc2a4* expression and DNA methylation from VAT are correlated with the mmu-miR-149-5p expression in the liver from the same mice. Interestingly, a significant negative correlation between *Slc2a4* expression in the VAT and mmu-miR-149-5p expression in the liver is observed (Supplementary Figure 15a). Additionally, fatty acid induced DNA hypermethylation in the Slc2a4 gene displays a significant positive correlation (Supplementary Figure 15b). This emphasizes that both, *Slc2a4* DNA methylation and miR-149-5p might be induced by the same metabolite – namely fatty acids. Further it introduces a possible link between the changes going on in the VAT and in the liver. A potential model of the link between both epigenetic mechanisms and how they might act synergistically in the progression of obesity and MASLD is proposed in the following paragraph, which aligns with the evidence reported in literature and the results of this study.

Based on the longitudinal mouse model for DIO, it is known that the DNA methylation increases early in week 1 (CpG1) or week 2 (CpG2) in the VAT of hfd-fed mice. Subsequently, Slc2a4 gene expression decreases, followed by decreased GLUT4 transporters. This decreases the sensitivity for insulin-dependent glucose uptake, which results in a decreased activation of the ChREBP. Therefore, DNL genes (Fasn & Acaca) decrease and the VAT undergoes a transition into a more lipolytic tissue. The VAT starts to secrete more fatty acids, which are transported by the portal vein into the liver (portal vein hypothesis). As mentioned previously, approximately 69 % of the accumulated triglycerides in MASLD are derived from increased lipolytic adipose tissue. This increase in fatty acid uptake activates the PPARG transcription factor in hepatocytes, whose expression increases in MASLD patients likewise. PPARG induces the expression of the GPC1 gene and consequently miR-149-5p is induced. The upregulation of miR-149-5p results in the dysregulation of metabolic pathways and the disbalance in metabolite levels, either accumulation of toxic or depletion of protective ones, induces the production of reactive oxygen species, insulin resistance, liver damage and fibrosis. Ultimately, the MASLD liver progresses into its more severe state MASH (Figure 34).

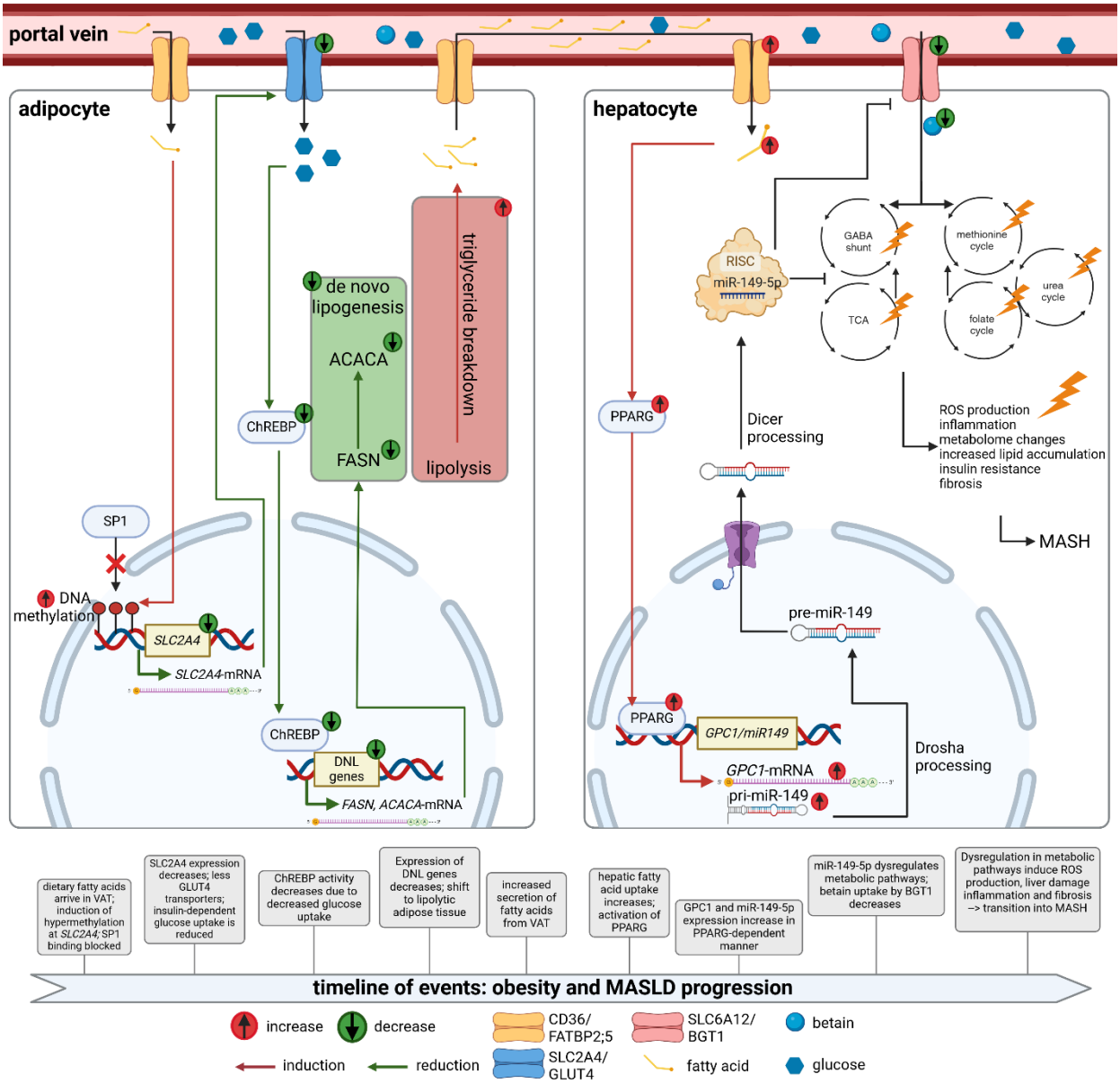

Figure 34: A proposed model for interorgan-crosstalk between the adipose tissue and liver during obesity, based on the data from the longitudinal DIO-mouse model. The first changes observed are occurring in the VAT, where hfd-feeding of mice is accompanied by and increased DNA methylation of the *Slc2a4* gene. Consequently, SP1 binding is impaired and *Slc2a4* gene expression decreases. This results in reduced GLUT4 transporters in the membrane of the VAT and glucose signaling via ChREBP (Mlxipl gene) causes a downregulation of DNL. Subsequently, lipolysis increases in the VAT and the VAT secrets fatty acids. This seems to happen around four to five weeks on hfd-feeding. The secreted fatty acids are transported through the portal vein to the liver, where the increased fatty acid uptake induces Pparg. Pparg acts upon the *Gpc1* promoter and induces *Gpc1* and *miR-149-5p* expression. miR-149-5p starts to dysregulate the metabolic pathways, which in turn promotes the progression of MASLD and may contribute to the transition into MASH.

7. Conclusion and outlook

In conclusion, both DNA methylation of SLC2A4 in VAT and miR-149-5p expression in the liver contribute to the complex progression of obesity and its comorbidities. It shows a revolutionary role of miR-149-5p with the property of regulating a variety of metabolic pathways in the liver that ultimately contribute to the progression of MASLD. Comparable findings are not reported in the literature so far. This also indicates miR-149-5p as a suitable therapeutic target, since induced miR-149-5p expression in the liver results in the dysregulation of the here presented metabolic pathways. Inhibiting miR-149-5p expression might stop the progression of MASLD.

To validate this hypothesis, modulating miR-149-5p expression in vivo in the liver of mice might decipher that role. For instance, it could be studied if overexpression of miR-149-5p in chow-diet fed animal induces some degree of steatosis and combination of transcriptomic and metabolomic analysis could show, which genes involved in the metabolomic pathways are consequently downregulated and what are the resulting changes in the metabolome. On the other hand, inhibiting miR-149-5p expression with antagomirs in animals fed a hfd might have a protective effect on progression of MASLD by preventing the dysregulation of the metabolic pathways.

The vsg mouse model represses miR-149-5p expression. In accordance to the hypothesis, this should lead to a normalization of miR-149-5p-mediated dysregulation of the metabolic pathways. This can be proven or further supported by transcriptomic and metabolomic investigations in the liver of those mice.

Since HepG2 cells are a suitable model to investigate miRNA/mRNA-interactions, their role as physiological model are debatable. Alternatively to HepG2 cells, the experiments could be conducted in cell culture models that are metabolically closer to primary hepatocytes. A good example would be induced pluripotent stem cell (iPSC)-derived hepatocytes or human hepatocyte organoids (Hendriks et al. 2023).

Overall I identified two epigenetic mechanisms that contribute to the better understanding of the molecular mechanisms of T2D and MASLD pathogenesis and that could be exploited as drug targets in the future.

8. References

Abdelmalek, Manal F et al. 2001. “Betaine, a Promising New Agent for Patients with Nonalcoholic Steatohepatitis: Results of a Pilot Study.” *The American Journal of Gastroenterology* 96(9): 2711–17. https://www.sciencedirect.com/science/article/pii/S0002927001026910.

Abel, E. Dale et al. 2001. “Adipose-Selective Targeting of the GLUT4 Gene Impairs Insulin Action in Muscle and Liver.” *Nature* 409(6821): 729–33. https://www.nature.com/articles/35055575.

Ahmed, Bulbul, Rifat Sultana, and Michael W. Greene. 2021. “Adipose Tissue and Insulin Resistance in Obese.” *Biomedicine & Pharmacotherapy* 137: 111315. https://linkinghub.elsevier.com/retrieve/pii/S0753332221001001.

Ahn, Chang Ho et al. 2021. “Vertical Sleeve Gastrectomy Induces Distinctive Transcriptomic Responses in Liver, Fat and Muscle.” *Scientific Reports* 11(1): 2310. https://www.nature.com/articles/s41598-021-81866-5.

Ahrens, Markus et al. 2013. “DNA Methylation Analysis in Nonalcoholic Fatty Liver Disease Suggests Distinct Disease-Specific and Remodeling Signatures after Bariatric Surgery.” *Cell Metabolism* 18(2): 296–302. https://linkinghub.elsevier.com/retrieve/pii/S1550413113002933.

Akbari, Parsa et al. 2022. “Multiancestry Exome Sequencing Reveals INHBE Mutations Associated with Favorable Fat Distribution and Protection from Diabetes.” *Nature Communications* 13(1): 4844. https://www.nature.com/articles/s41467-022-32398-7.

Al-Najim, Werd, Neil G. Docherty, and Carel W. le Roux. 2018. “Food Intake and Eating Behavior After Bariatric Surgery.” *Physiological Reviews* 98(3): 1113–41. https://www.physiology.org/doi/10.1152/physrev.00021.2017.

Alegría-Torres, Jorge Alejandro, Andrea Baccarelli, and Valentina Bollati. 2011. “Epigenetics and Lifestyle.” *Epigenomics* 3(3): 267–77. https://pubmed.ncbi.nlm.nih.gov/22122337.

Alles, Julia et al. 2019. “An Estimate of the Total Number of True Human MiRNAs.” *Nucleic Acids Research* 47(7): 3353–64. https://doi.org/10.1093/nar/gkz097.

Allis, C. David, and Thomas Jenuwein. 2016. “The Molecular Hallmarks of Epigenetic Control.” *Nature Reviews Genetics* 17(8): 487–500. http://dx.doi.org/10.1038/nrg.2016.59.

Andersen, Claus Lindbjerg, Jens Ledet Jensen, and Torben Falck Ørntoft. 2004. “Normalization of Real-Time Quantitative Reverse Transcription-PCR Data: A Model-Based Variance Estimation Approach to Identify Genes Suited for Normalization, Applied to Bladder and Colon Cancer Data Sets.” *Cancer research* 64(15): 5245–50.

Anstee, Quentin M, Giovanni Targher, and Christopher P Day. 2013. “Progression of NAFLD to Diabetes Mellitus, Cardiovascular Disease or Cirrhosis.” *Nature Reviews Gastroenterology & Hepatology* 10(6): 330–44. https://doi.org/10.1038/nrgastro.2013.41.

Apsley, Abner T. et al. 2023. “Biological Stability of DNA Methylation Measurements over Varying Intervals of Time and in the Presence of Acute Stress.” *Epigenetics* 18(1). https://www.tandfonline.com/doi/full/10.1080/15592294.2023.2230686.

Ardekani, Ali M, and Mozhgan Moslemi Naeini. 2010. “The Role of MicroRNAs in Human Diseases.” *Avicenna journal of medical biotechnology* 2(4): 161–79.

Arimbasseri, Aneeshkumar G, and Richard J Maraia. 2016. “RNA Polymerase III Advances: Structural and TRNA Functional Views.” *Trends in biochemical sciences* 41(6): 546–59.

Arora, Meenakshi. 2013. “Cell Culture Media: A Review.” *Materials and Methods* 3.

http://www.labome.com/method/Cell-Culture-Media-A-Review.html.

Auinger, A. et al. 2010. “A Promoter Polymorphism in the Liver-Specific Fatty Acid Transport Protein 5 Is Associated with Features of the Metabolic Syndrome and Steatosis.” *Hormone and Metabolic Research* 42(12): 854–59. http://www.thieme-connect.de/DOI/DOI?10.1055/s-0030-1267186.

Auron, Ari, and Patrick D. Brophy. 2012. “Hyperammonemia in Review: Pathophysiology, Diagnosis, and Treatment.” *Pediatric Nephrology* 27(2): 207–22. http://link.springer.com/10.1007/s00467-011-1838-5.

Austin, Gregory O., and Alejandra Tomas. 2023. “Variation in Responses to Incretin Therapy: Modifiable and Non-Modifiable Factors.” *Frontiers in Molecular Biosciences* 10. https://www.frontiersin.org/articles/10.3389/fmolb.2023.1170181/full.

Azain, M. J. 2004. “Role of Fatty Acids in Adipocyte Growth and Development1,2.” *Journal of Animal Science* 82(3): 916–24. https://academic.oup.com/jas/article/82/3/916/4835330.

Azuri, Joseph et al. 2023. “Liraglutide versus Semaglutide for Weight Reduction—a Cost Needed to Treat Analysis.” *Obesity* 31(6): 1510–13. https://onlinelibrary.wiley.com/doi/10.1002/oby.23752.

Baca, Paulina et al. 2022. “DNA Methylation and Gene Expression Analysis in Adipose Tissue to Identify New Loci Associated with T2D Development in Obesity.” *Nutrition & Diabetes* 12(1): 50. https://www.nature.com/articles/s41387-022-00228-w.

Ball, Madeleine P. et al. 2009. “Targeted and Genome-Scale Strategies Reveal Gene-Body Methylation Signatures in Human Cells.” *Nature Biotechnology* 27(4): 361–68.

Bannister, Andrew J. et al. 2001. “Selective Recognition of Methylated Lysine 9 on Histone H3 by the HP1 Chromo Domain.” *Nature* 410(6824): 120–24. https://www.nature.com/articles/35065138.

Bannister, Andrew J, and Tony Kouzarides. 2011. “Regulation of Chromatin by Histone Modifications.” *Cell Research* 21(3): 381–95. https://doi.org/10.1038/cr.2011.22.

Barwari, Temo et al. 2018. “Inhibition of Profibrotic MicroRNA-21 Affects Platelets and Their Releasate.” *JCI Insight* 3(21). https://insight.jci.org/articles/view/123335.

BasuRay, Soumik et al. 2019. “Accumulation of PNPLA3 on Lipid Droplets Is the Basis of Associated Hepatic Steatosis.” *Proceedings of the National Academy of Sciences* 116(19): 9521–26. https://pnas.org/doi/full/10.1073/pnas.1901974116.

Bell, R M, and R A Coleman. 1980. “Enzymes of Glycerolipid Synthesis in Eukaryotes.” *Annual Review of Biochemistry* 49(1): 459–87. https://www.annualreviews.org/doi/10.1146/annurev.bi.49.070180.002331.

Ben-Hamo, Rotem, and Sol Efroni. 2015. “MicroRNA Regulation of Molecular Pathways as a Generic Mechanism and as a Core Disease Phenotype.” *Oncotarget* 6(3): 1594–1604.

Berezikov, Eugene et al. 2007. “Mammalian Mirtron Genes.” *Molecular Cell* 28(2): 328–36. https://linkinghub.elsevier.com/retrieve/pii/S1097276507006697.

Besse, Arnaud et al. 2015. “The GABA Transaminase, ABAT, Is Essential for Mitochondrial Nucleoside Metabolism.” *Cell Metabolism* 21(3): 417–27. https://www.sciencedirect.com/science/article/pii/S1550413115000601.

Bhajun, Ricky, Laurent Guyon, and Xavier Gidrol. 2016. “MicroRNA Degeneracy and Pluripotentiality within a Lavallière-Tie Architecture Confers Robustness to Gene Expression Networks.” *Cellular and molecular life sciences : CMLS* 73(15): 2821–27.

Bikeyeva, Viktoriya et al. 2022. “Nonalcoholic Fatty Liver Disease and Hypothyroidism: What You

Need to Know." *Cureus*. https://www.cureus.com/articles/101051-nonalcoholic-fatty-liver-disease-and-hypothyroidism-what-you-need-to-know.

Bjørndal, Bodil et al. 2011. "Different Adipose Depots: Their Role in the Development of Metabolic Syndrome and Mitochondrial Response to Hypolipidemic Agents." *Journal of Obesity* 2011: 1–15. http://www.hindawi.com/journals/jobe/2011/490650/.

Blüher, Matthias. 2019. "Obesity: Global Epidemiology and Pathogenesis." *Nature Reviews Endocrinology* 15(5): 288–98. https://doi.org/10.1038/s41574-019-0176-8.

Bofill-De Ros, Xavier et al. 2019. "Structural Differences between Pri-MiRNA Paralogs Promote Alternative Drosha Cleavage and Expand Target Repertoires." *Cell Reports* 26(2): 447-459.e4. https://www.sciencedirect.com/science/article/pii/S2211124718319843.

von Brandenstein, Melanie et al. 2018. "Beyond the 3'UTR Binding-MicroRNA-Induced Protein Truncation via DNA Binding." *Oncotarget* 9(67): 32855–67. https://www.oncotarget.com/lookup/doi/10.18632/oncotarget.26023.

Brandt, Annette et al. 2019. "Metformin Attenuates the Onset of Non-Alcoholic Fatty Liver Disease and Affects Intestinal Microbiota and Barrier in Small Intestine." *Scientific Reports* 9(1): 6668. https://www.nature.com/articles/s41598-019-43228-0.

Brenet, Fabienne et al. 2011. "DNA Methylation of the First Exon Is Tightly Linked to Transcriptional Silencing" ed. Nina Papavasiliou. *PLoS ONE* 6(1): e14524. https://dx.plos.org/10.1371/journal.pone.0014524.

Britsemmer, Jan H et al. 2023. "Fatty Acid Induced Hypermethylation in the Slc2a4 Gene in Visceral Adipose Tissue Is Associated to Insulin-Resistance and Obesity." *International Journal of Molecular Sciences* 24(7).

Broderick, Joan B., William E. Broderick, and Brian M. Hoffman. 2023. "Radical SAM Enzymes: Nature's Choice for Radical Reactions." *FEBS Letters* 597(1): 92–101. https://febs.onlinelibrary.wiley.com/doi/10.1002/1873-3468.14519.

Burke, James M., Demetra P. Kelenis, Rodney P. Kincaid, and Christopher S. Sullivan. 2014. "A Central Role for the Primary MicroRNA Stem in Guiding the Position and Efficiency of Drosha Processing of a Viral Pri-MiRNA." *RNA* 20(7): 1068–77. http://rnajournal.cshlp.org/lookup/doi/10.1261/rna.044537.114.

Cano, Ainara et al. 2011. "Methionine Adenosyltransferase 1A Gene Deletion Disrupts Hepatic Very Low-Density Lipoprotein Assembly in Mice." *Hepatology* 54(6): 1975–86. https://onlinelibrary.wiley.com/doi/10.1002/hep.24607.

Cao, Haiming et al. 2008a. "Identification of a Lipokine, a Lipid Hormone Linking Adipose Tissue to Systemic Metabolism." *Cell* 134(6): 933–44. https://www.sciencedirect.com/science/article/pii/S0092867408010143.

———. 2008b. "Identification of a Lipokine, a Lipid Hormone Linking Adipose Tissue to Systemic Metabolism." *Cell* 134(6): 933–44. https://linkinghub.elsevier.com/retrieve/pii/S0092867408010143.

Cao, Man-Qing et al. 2018. "MiR-182-5p Promotes Hepatocellular Carcinoma Progression by Repressing FOXO3a." *Journal of Hematology & Oncology* 11(1): 12. https://jhoonline.biomedcentral.com/articles/10.1186/s13045-018-0555-y.

Carlsson, Lena M S et al. 2020. "Life Expectancy after Bariatric Surgery in the Swedish Obese Subjects Study." *New England Journal of Medicine* 383(16): 1535–43. https://doi.org/10.1056/NEJMoa2002449.

Carman, George M., and Gil-Soo Han. 2009. “Phosphatidic Acid Phosphatase, a Key Enzyme in the Regulation of Lipid Synthesis.” *Journal of Biological Chemistry* 284(5): 2593–97. https://linkinghub.elsevier.com/retrieve/pii/S0021925819818227.

Carvalho, Eugenia, Ko Kotani, Odile D. Peroni, and Barbara B. Kahn. 2005. “Adipose-Specific Overexpression of GLUT4 Reverses Insulin Resistance and Diabetes in Mice Lacking GLUT4 Selectively in Muscle.” *American Journal of Physiology - Endocrinology and Metabolism* 289(4 52-4).

Chadt, Alexandra, and Hadi Al-Hasani. 2020a. “Glucose Transporters in Adipose Tissue, Liver, and Skeletal Muscle in Metabolic Health and Disease.” *Pflügers Archiv - European Journal of Physiology* 472(9): 1273–98. https://link.springer.com/10.1007/s00424-020-02417-x.

———. 2020b. “Glucose Transporters in Adipose Tissue, Liver, and Skeletal Muscle in Metabolic Health and Disease.” *Pflugers Archiv European Journal of Physiology* 472(9): 1273–98.

Champagne, Karen, and Tatiana Kutateladze. 2009. “Structural Insight Into Histone Recognition by the ING PHD Fingers.” *Current Drug Targets* 10(5): 432–41. http://www.eurekaselect.com/openurl/content.php?genre=article&issn=1389-4501&volume=10&issue=5&spage=432.

Cheloufi, Sihem, Camila O. Dos Santos, Mark M. W. Chong, and Gregory J. Hannon. 2010. “A Dicer-Independent MiRNA Biogenesis Pathway That Requires Ago Catalysis.” *Nature* 465(7298): 584–89. https://www.nature.com/articles/nature09092.

Chen, Bingting et al. 2021. “Taurine Ameliorates Oxidative Stress by Regulating PI3K/Akt/GLUT4 Pathway in HepG2 Cells and Diabetic Rats.” *Journal of Functional Foods* 85: 104629. https://linkinghub.elsevier.com/retrieve/pii/S1756464621002784.

Chen, Hong et al. 1996. “Evidence That the Diabetes Gene Encodes the Leptin Receptor: Identification of a Mutation in the Leptin Receptor Gene in Db/Db Mice.” *Cell* 84(3): 491–95. https://linkinghub.elsevier.com/retrieve/pii/S0092867400812945.

Chen, Pengguo et al. 2015. “Orphan Nuclear Receptor NR4A2 Inhibits Hepatic Stellate Cell Proliferation through MAPK Pathway in Liver Fibrosis.” *PeerJ* 3: e1518.

Chen, Shenghui et al. 2020. “Uric Acid Induced Hepatocytes Lipid Accumulation through Regulation of MiR-149-5p/FGF21 Axis.” *BMC gastroenterology* 20(1): 39.

Chen, Yuxin, Yang Shen, Stefano Allesina, and Chung-I Wu. 2017. “From Foodwebs to Gene Regulatory Networks (GRNs) - Weak Repressions by MicroRNAs Confer System Stability.” *bioRxiv*: 176701. http://biorxiv.org/content/early/2017/08/16/176701.abstract.

Cheng, Yuan et al. 2019. “Targeting Epigenetic Regulators for Cancer Therapy: Mechanisms and Advances in Clinical Trials.” *Signal Transduction and Targeted Therapy* 4(1): 62. https://doi.org/10.1038/s41392-019-0095-0.

Chiang, P K et al. 1996. “S-Adenosylmethionine and Methylation.” *FASEB journal : official publication of the Federation of American Societies for Experimental Biology* 10(4): 471–80.

De Chiara, Francesco et al. 2018. “Urea Cycle Dysregulation in Non-Alcoholic Fatty Liver Disease.” *Journal of hepatology* 69(4): 905–15.

Choi, Sung Hee, and Henry N Ginsberg. 2011. “Increased Very Low Density Lipoprotein (VLDL) Secretion, Hepatic Steatosis, and Insulin Resistance.” *Trends in Endocrinology & Metabolism* 22(9): 353–63. https://linkinghub.elsevier.com/retrieve/pii/S1043276011000725.

Chou, Chih-Hung et al. 2018. “MiRTarBase Update 2018: A Resource for Experimentally Validated MicroRNA-Target Interactions.” *Nucleic Acids Research* 46(D1): D296–302.

https://doi.org/10.1093/nar/gkx1067.

Chu-Tan, Joshua A. et al. 2021. “Functional MicroRNA Targetome Undergoes Degeneration-Induced Shift in the Retina.” *Molecular Neurodegeneration* 16(1): 60. https://molecularneurodegeneration.biomedcentral.com/articles/10.1186/s13024-021-00478-9.

Chypre, Melanie, Nousheen Zaidi, and Karine Smans. 2012. “ATP-Citrate Lyase: A Mini-Review.” *Biochemical and Biophysical Research Communications* 422(1): 1–4. https://linkinghub.elsevier.com/retrieve/pii/S0006291X12008339.

Cifuentes, Daniel et al. 2010. “A Novel MiRNA Processing Pathway Independent of Dicer Requires Argonaute2 Catalytic Activity.” *Science* 328(5986): 1694–98. https://www.science.org/doi/10.1126/science.1190809.

Clouaire, T., and I. Stancheva. 2008. “Methyl-CpG Binding Proteins: Specialized Transcriptional Repressors or Structural Components of Chromatin?” *Cellular and Molecular Life Sciences* 65(10): 1509–22. http://link.springer.com/10.1007/s00018-008-7324-y.

Colca, Jerry R., and Philipp E. Scherer. 2022. “The Metabolic Syndrome, Thiazolidinediones, and Implications for Intersection of Chronic and Inflammatory Disease.” *Molecular Metabolism* 55: 101409. https://linkinghub.elsevier.com/retrieve/pii/S2212877821002672.

Committee, American Diabetes Association Professional Practice. 2021. “2. Classification and Diagnosis of Diabetes: Standards of Medical Care in Diabetes—2022.” *Diabetes Care* 45(Supplement_1): S17–38. https://doi.org/10.2337/dc22-S002.

Cortellino, Salvatore et al. 2011. “Thymine DNA Glycosylase Is Essential for Active DNA Demethylation by Linked Deamination-Base Excision Repair.” *Cell* 146(1): 67–79. https://linkinghub.elsevier.com/retrieve/pii/S0092867411006623.

Crujeiras, A.B. et al. 2016. “Genome-Wide DNA Methylation Pattern in Visceral Adipose Tissue Differentiates Insulin-Resistant from Insulin-Sensitive Obese Subjects.” *Translational Research* 178: 13-24.e5. https://linkinghub.elsevier.com/retrieve/pii/S1931524416301074.

Cuyàs, E. et al. 2018. “Metformin Regulates Global DNA Methylation via Mitochondrial One-Carbon Metabolism.” *Oncogene* 37(7): 963–70.

Dai, Xiaofeng, and Li Shen. 2022. “Advances and Trends in Omics Technology Development.” *Frontiers in Medicine* 9. https://www.frontiersin.org/articles/10.3389/fmed.2022.911861/full.

Dalbeni, Andrea et al. 2022. “Platelets in Non-Alcoholic Fatty Liver Disease.” *Frontiers in Pharmacology* 13. https://www.frontiersin.org/articles/10.3389/fphar.2022.842636/full.

Dantas Machado, Ana Carolina et al. 2015. “Evolving Insights on How Cytosine Methylation Affects Protein-DNA Binding.” *Briefings in functional genomics* 14(1): 61–73.

Deaton, Aimee M. et al. 2022. “Rare Loss of Function Variants in the Hepatokine Gene INHBE Protect from Abdominal Obesity.” *Nature Communications* 13(1): 4319. https://www.nature.com/articles/s41467-022-31757-8.

Defour, Merel et al. 2020. “Transcriptomic Signature of Fasting in Human Adipose Tissue.” *Physiological Genomics* 52(10): 451–67. https://journals.physiology.org/doi/10.1152/physiolgenomics.00083.2020.

Delli Bovi, Anna Pia et al. 2021. “Oxidative Stress in Non-Alcoholic Fatty Liver Disease. An Updated Mini Review.” *Frontiers in Medicine* 8. https://www.frontiersin.org/articles/10.3389/fmed.2021.595371/full.

Dixon, Laura J. et al. 2013. “Kupffer Cells in the Liver.” In *Comprehensive Physiology*, Wiley, 785–97. https://onlinelibrary.wiley.com/doi/10.1002/cphy.c120026.

Dobin, Alexander et al. 2013. “STAR: Ultrafast Universal RNA-Seq Aligner.” *Bioinformatics (Oxford, England)* 29(1): 15–21.

Doege, Holger et al. 2006. “Targeted Deletion of FATP5 Reveals Multiple Functions in Liver Metabolism: Alterations in Hepatic Lipid Homeostasis.” *Gastroenterology* 130(4): 1245–58. https://linkinghub.elsevier.com/retrieve/pii/S0016508506002642.

Dong, A. 2001. “Structure of Human DNMT2, an Enigmatic DNA Methyltransferase Homolog That Displays Denaturant-Resistant Binding to DNA.” *Nucleic Acids Research* 29(2): 439–48. https://academic.oup.com/nar/article-lookup/doi/10.1093/nar/29.2.439.

Donnelly, Kerry L et al. 2005. “Sources of Fatty Acids Stored in Liver and Secreted via Lipoproteins in Patients with Nonalcoholic Fatty Liver Disease.” *The Journal of clinical investigation* 115(5): 1343–51.

Douard, Veronique, and Ronaldo P. Ferraris. 2013. “The Role of Fructose Transporters in Diseases Linked to Excessive Fructose Intake.” *The Journal of Physiology* 591(2): 401–14. https://physoc.onlinelibrary.wiley.com/doi/10.1113/jphysiol.2011.215731.

Douet, Vanessa, Matthew B Heller, and Olivier Le Saux. 2007. “DNA Methylation and Sp1 Binding Determine the Tissue-Specific Transcriptional Activity of the Mouse Abcc6 Promoter.” *Biochemical and biophysical research communications* 354(1): 66–71. https://pubmed.ncbi.nlm.nih.gov/17214963.

Ducker, Gregory S, and Joshua D Rabinowitz. 2017. “One-Carbon Metabolism in Health and Disease.” *Cell metabolism* 25(1): 27–42.

Durinck, Steffen, Paul T Spellman, Ewan Birney, and Wolfgang Huber. 2009. “Mapping Identifiers for the Integration of Genomic Datasets with the R/Bioconductor Package BiomaRt.” *Nature Protocols* 4(8): 1184–91. https://www.nature.com/articles/nprot.2009.97.

Eissing, Leah et al. 2013. “De Novo Lipogenesis in Human Fat and Liver Is Linked to ChREBP-β and Metabolic Health.” *Nature Communications* 4.

Ejigu, Bedilu Alamirie, and Fentanesh Nibret Tiruneh. 2023. “The Link between Overweight/Obesity and Noncommunicable Diseases in Ethiopia: Evidences from Nationwide WHO STEPS Survey 2015” ed. Tomohiro Katsuya. *International Journal of Hypertension* 2023: 1–11. https://www.hindawi.com/journals/ijhy/2023/2199853/.

Esau, Christine et al. 2006. “MiR-122 Regulation of Lipid Metabolism Revealed by in Vivo Antisense Targeting.” *Cell Metabolism* 3(2): 87–98. https://linkinghub.elsevier.com/retrieve/pii/S1550413106000295.

Fadaka, Adewale et al. 2017. “Biology of Glucose Metabolization in Cancer Cells.” *Journal of Oncological Sciences* 3(2): 45–51. https://linkinghub.elsevier.com/retrieve/pii/S2452336417300420.

FÆRGEMAN, Nils Joakim, and Jens KNUDSEN. 1997. “Role of Long-Chain Fatty Acyl-CoA Esters in the Regulation of Metabolism and in Cell Signalling.” *Biochemical Journal* 323(1): 1–12. https://portlandpress.com/biochemj/article/323/1/1/33577/Role-of-long-chain-fatty-acyl-CoA-esters-in-the.

Fagerberg, Linn et al. 2014. “Analysis of the Human Tissue-Specific Expression by Genome-Wide Integration of Transcriptomics and Antibody-Based Proteomics.” *Molecular & Cellular Proteomics* 13(2): 397–406. https://linkinghub.elsevier.com/retrieve/pii/S1535947620346338.

Falcon, Alaric et al. 2010. “FATP2 Is a Hepatic Fatty Acid Transporter and Peroxisomal Very Long-Chain Acyl-CoA Synthetase.” *American Journal of Physiology-Endocrinology and Metabolism* 299(3): E384–93. https://www.physiology.org/doi/10.1152/ajpendo.00226.2010.

Fedorenko, Andriy, Polina V. Lishko, and Yuriy Kirichok. 2012. “Mechanism of Fatty-Acid-Dependent UCP1 Uncoupling in Brown Fat Mitochondria.” *Cell* 151(2): 400–413. https://linkinghub.elsevier.com/retrieve/pii/S0092867412011130.

Felipo, Vicente et al. 2012. “Contribution of Hyperammonemia and Inflammatory Factors to Cognitive Impairment in Minimal Hepatic Encephalopathy.” *Metabolic Brain Disease* 27(1): 51–58. https://doi.org/10.1007/s11011-011-9269-3.

Felsenfeld, Gary. 2014. “A Brief History of Epigenetics.” *Cold Spring Harbor perspectives in biology* 6(1).

Feng, Qiping et al. 2011. “Betaine-Homocysteine Methyltransferase: Human Liver Genotype–Phenotype Correlation.” *Molecular Genetics and Metabolism* 102(2): 126–33. https://linkinghub.elsevier.com/retrieve/pii/S1096719210003690.

Filipovic, Branka et al. 2021. “The New Therapeutic Approaches in the Treatment of Non-Alcoholic Fatty Liver Disease.” *International journal of molecular sciences* 22(24).

Filippatos, Theodosios D., Thalia V. Panagiotopoulou, and Moses S. Elisaf. 2014. “Adverse Effects of GLP-1 Receptor Agonists.” *The Review of Diabetic Studies* 11(3–4): 202–30. http://www.soc-bdr.org/content/e4/e887/volRdsVolumes14222/issRdsIssues14231/chpRdsChapters14232/strRdsArticles14678/?preview=preview.

Fitz-James, Maximilian H, and Giacomo Cavalli. 2022. “Molecular Mechanisms of Transgenerational Epigenetic Inheritance.” *Nature Reviews Genetics* 23(6): 325–41. https://doi.org/10.1038/s41576-021-00438-5.

Flessa, Christina-Maria et al. 2022. “Genetic and Diet-Induced Animal Models for Non-Alcoholic Fatty Liver Disease (NAFLD) Research.” *International journal of molecular sciences* 23(24).

Fontaine, Kevin R et al. 2003. “Years of Life Lost Due to Obesity.” *JAMA* 289(2): 187–93.

Frühbeck, Gema. 2008. “Overview of Adipose Tissue and Its Role in Obesity and Metabolic Disorders.” In , 1–22. http://link.springer.com/10.1007/978-1-59745-245-8_1.

Gadek, Margaret, Elliott H. Sherr, and Stephen N. Floor. 2023. “The Variant Landscape and Function of DDX3X in Cancer and Neurodevelopmental Disorders.” *Trends in Molecular Medicine* 29(9): 726–39. https://linkinghub.elsevier.com/retrieve/pii/S1471491423001387.

Gaggini, Melania et al. 2018. “Altered Amino Acid Concentrations in NAFLD: Impact of Obesity and Insulin Resistance.” *Hepatology* 67(1): 145–58. https://journals.lww.com/01515467-201801000-00018.

Gao, Xiaoqiang et al. 2022. “Regulation of Gamma-Aminobutyric Acid Transaminase Expression and Its Clinical Significance in Hepatocellular Carcinoma.” *Frontiers in Oncology* 12. https://www.frontiersin.org/articles/10.3389/fonc.2022.879810/full.

García-Tevijano, Elena Ruiz et al. 2001. “Hyperhomocysteinemia in Liver Cirrhosis.” *Hypertension* 38(5): 1217–21. https://www.ahajournals.org/doi/10.1161/hy1101.099499.

Garibay, Darline, and Bethany P Cummings. 2017. “A Murine Model of Vertical Sleeve Gastrectomy.” *Journal of visualized experiments : JoVE* (130).

Gearing, Linden J et al. 2019. “CiiiDER: A Tool for Predicting and Analysing Transcription Factor Binding Sites.” *PLOS ONE* 14(9): 1–12. https://doi.org/10.1371/journal.pone.0215495.

Geisler, Caroline E et al. 2021. “A Critical Role of Hepatic GABA in the Metabolic Dysfunction and Hyperphagia of Obesity.” *Cell Reports* 35(13): 109301. https://www.sciencedirect.com/science/article/pii/S221112472100677X.

Geisler, Caroline E, and Benjamin J Renquist. 2017. “Hepatic Lipid Accumulation: Cause and Consequence of Dysregulated Glucoregulatory Hormones.” *Journal of Endocrinology* 234(1): R1–21. https://joe.bioscientifica.com/view/journals/joe/234/1/R1.xml.

Geißler, Cathleen et al. 2022. “Dietary Induction of Obesity and Insulin Resistance Is Associated with Changes in Fgf21 DNA Methylation in Liver of Mice.” *The Journal of Nutritional Biochemistry* 100: 108907. https://www.sciencedirect.com/science/article/pii/S0955286321003272.

van Gerwen, Julian, Amber S. Shun-Shion, and Daniel J. Fazakerley. 2023. “Insulin Signalling and GLUT4 Trafficking in Insulin Resistance.” *Biochemical Society Transactions* 51(3): 1057–69. https://portlandpress.com/biochemsoctrans/article/51/3/1057/233101/Insulin-signalling-and-GLUT4-trafficking-in.

Ghafouri-Fard, Soudeh et al. 2021. “A Review on the Role of MiR-149-5p in the Carcinogenesis.” *International journal of molecular sciences* 23(1).

Gianmoena, Kathrin et al. 2021. “Epigenomic and Transcriptional Profiling Identifies Impaired Glyoxylate Detoxification in NAFLD as a Risk Factor for Hyperoxaluria.” *Cell reports* 36(8): 109526.

Glunk, Viktoria et al. 2023. “A Non-Coding Variant Linked to Metabolic Obesity with Normal Weight Affects Actin Remodelling in Subcutaneous Adipocytes.” *Nature Metabolism* 5(5): 861–79. https://www.nature.com/articles/s42255-023-00807-w.

Groothoff, Jaap W. et al. 2023. “Clinical Practice Recommendations for Primary Hyperoxaluria: An Expert Consensus Statement from ERKNet and OxalEurope.” *Nature Reviews Nephrology* 19(3): 194–211. https://www.nature.com/articles/s41581-022-00661-1.

Grove, Jane I. et al. 2023. “Identification and Characterisation of a Rare MTTP Variant Underlying Hereditary Non-Alcoholic Fatty Liver Disease.” *JHEP Reports* 5(8): 100764. https://linkinghub.elsevier.com/retrieve/pii/S2589555923000952.

Gruzdeva, Olga et al. 2019. “Leptin Resistance: Underlying Mechanisms and Diagnosis.” *Diabetes, Metabolic Syndrome and Obesity: Targets and Therapy* Volume 12: 191–98. https://www.dovepress.com/leptin-resistance-underlying-mechanisms-and-diagnosis-peer-reviewed-article-DMSO.

Grygiel-Górniak, Bogna. 2014. “Peroxisome Proliferator-Activated Receptors and Their Ligands: Nutritional and Clinical Implications--a Review.” *Nutrition journal* 13: 17.

Guo, Li et al. 2017. “MiRNA and MRNA Expression Analysis Reveals Potential Sex-Biased MiRNA Expression.” *Scientific Reports* 7(1): 39812. https://www.nature.com/articles/srep39812.

Hadizadeh, Fatemeh, Elham Faghihimani, and Peyman Adibi. 2017. “Nonalcoholic Fatty Liver Disease: Diagnostic Biomarkers.” *World Journal of Gastrointestinal Pathophysiology* 8(2): 11. http://www.wjgnet.com/2150-5330/full/v8/i2/11.htm.

Han, Hui et al. 2021. “ABAT Targeted by MiR-183-5p Regulates Cell Functions in Liver Cancer.” *The International Journal of Biochemistry & Cell Biology* 141: 106116. https://linkinghub.elsevier.com/retrieve/pii/S1357272521001977.

Han, Ji-Hee et al. 2022. “Markedly Elevated Aspartate Aminotransferase from Non-Hepatic Causes.” *Journal of Clinical Medicine* 12(1): 310. https://www.mdpi.com/2077-0383/12/1/310.

Han, Jinju et al. 2006. “Molecular Basis for the Recognition of Primary MicroRNAs by the Drosha-

DGCR8 Complex." *Cell* 125(5): 887–901. https://linkinghub.elsevier.com/retrieve/pii/S0092867406005162.

Harrison, Luke, Sonja C Schriever, et al. 2019. "Fluorescent Blood–Brain Barrier Tracing Shows Intact Leptin Transport in Obese Mice." *International Journal of Obesity* 43(6): 1305–18. https://doi.org/10.1038/s41366-018-0221-z.

Harrison, Luke, Katrin Pfuhlmann, Sonja C Schriever, and Paul T Pfluger. 2019. "Profound Weight Loss Induces Reactive Astrogliosis in the Arcuate Nucleus of Obese Mice." *Molecular metabolism* 24: 149–55.

Hassa, Paul O., Sandra S. Haenni, Michael Elser, and Michael O. Hottiger. 2006. "Nuclear ADP-Ribosylation Reactions in Mammalian Cells: Where Are We Today and Where Are We Going?" *Microbiology and Molecular Biology Reviews* 70(3): 789–829. https://journals.asm.org/doi/10.1128/MMBR.00040-05.

Havens, Mallory A., Ashley A. Reich, Dominik M. Duelli, and Michelle L. Hastings. 2012. "Biogenesis of Mammalian MicroRNAs by a Non-Canonical Processing Pathway." *Nucleic Acids Research* 40(10): 4626–40. https://academic.oup.com/nar/article-lookup/doi/10.1093/nar/gks026.

He, Fan et al. 2019. "Association between DNA Methylation in Obesity-Related Genes and Body Mass Index Percentile in Adolescents." *Scientific Reports* 9(1): 2079. https://www.nature.com/articles/s41598-019-38587-7.

He, Linfeng et al. 2024. "Changing from NAFLD to MASLD: The New Definition Can More Accurately Identify Individuals at Higher Risk for Diabetes." *Journal of Hepatology* 80(2): e85–87. https://linkinghub.elsevier.com/retrieve/pii/S0168827823051644.

Hedtke, Vera, and Marica Bakovic. 2019. "Choline Transport for Phospholipid Synthesis: An Emerging Role of Choline Transporter-like Protein 1." *Experimental Biology and Medicine* 244(8): 655–62. http://journals.sagepub.com/doi/10.1177/1535370219830997.

Heebøll, Sara et al. 2022. "Impaired Glucagon-Mediated Suppression of VLDL-Triglyceride Secretion in Individuals With Metabolic Dysfunction–Associated Fatty Liver Disease (MAFLD)." *Diabetes* 71(11): 2402–11. https://diabetesjournals.org/diabetes/article/71/11/2402/147515/Impaired-Glucagon-Mediated-Suppression-of-VLDL.

Helling, Gunnel et al. 2016. "Plasma Glutamine Concentrations in Liver Failure" ed. Sheng-Nan Lu. *PLOS ONE* 11(3): e0150440. https://dx.plos.org/10.1371/journal.pone.0150440.

Hendriks, Delilah et al. 2023. "Engineered Human Hepatocyte Organoids Enable CRISPR-Based Target Discovery and Drug Screening for Steatosis." *Nature Biotechnology* 41(11): 1567–81. https://www.nature.com/articles/s41587-023-01680-4.

Herman, Mark A. et al. 2012. "A Novel ChREBP Isoform in Adipose Tissue Regulates Systemic Glucose Metabolism." *Nature* 484(7394): 333–38.

Hildreth, Andrew D. et al. 2021. "Single-Cell Sequencing of Human White Adipose Tissue Identifies New Cell States in Health and Obesity." *Nature Immunology* 22(5): 639–53. https://www.nature.com/articles/s41590-021-00922-4.

Hochreuter, Mette Yde, Morten Dall, Jonas T. Treebak, and Romain Barrès. 2022. "MicroRNAs in Non-Alcoholic Fatty Liver Disease: Progress and Perspectives." *Molecular Metabolism* 65: 101581. https://linkinghub.elsevier.com/retrieve/pii/S2212877822001508.

Holliday, R., and G.W. Grigg. 1993. "DNA Methylation and Mutation." *Mutation Research/Fundamental and Molecular Mechanisms of Mutagenesis* 285(1): 61–67. https://linkinghub.elsevier.com/retrieve/pii/002751079390052H.

Horwitz, Avital, and Ruth Birk. 2023. “Adipose Tissue Hyperplasia and Hypertrophy in Common and Syndromic Obesity—The Case of BBS Obesity.” *Nutrients* 15(15): 3445. https://www.mdpi.com/2072-6643/15/15/3445.

Hossain, Noreen et al. 2009. “Independent Predictors of Fibrosis in Patients With Nonalcoholic Fatty Liver Disease.” *Clinical Gastroenterology and Hepatology* 7(11): 1224-1229.e2. https://linkinghub.elsevier.com/retrieve/pii/S1542356509005795.

Houten, Sander M., Sara Violante, Fatima V. Ventura, and Ronald J.A. Wanders. 2016a. “The Biochemistry and Physiology of Mitochondrial Fatty Acid β-Oxidation and Its Genetic Disorders.” *Annual Review of Physiology* 78(1): 23–44. https://www.annualreviews.org/doi/10.1146/annurev-physiol-021115-105045.

Houten, Sander M, Sara Violante, Fatima V Ventura, and Ronald J A Wanders. 2016b. “The Biochemistry and Physiology of Mitochondrial Fatty Acid β-Oxidation and Its Genetic Disorders.” *Annual review of physiology* 78: 23–44.

Hsiao, Pi-Jung et al. 2017. “Pioglitazone Enhances Cytosolic Lipolysis, β-Oxidation and Autophagy to Ameliorate Hepatic Steatosis.” *Scientific Reports* 7(1): 9030. https://www.nature.com/articles/s41598-017-09702-3.

Hsu, Cynthia L., and Rohit Loomba. 2024. “From NAFLD to MASLD: Implications of the New Nomenclature for Preclinical and Clinical Research.” *Nature Metabolism* 6(4): 600–602. https://www.nature.com/articles/s42255-024-00985-1.

Hsu, Shu-hao et al. 2012. “Essential Metabolic, Anti-Inflammatory, and Anti-Tumorigenic Functions of MiR-122 in Liver.” *Journal of Clinical Investigation* 122(8): 2871–83. http://www.jci.org/articles/view/63539.

Huang, Da Wei, Brad T Sherman, and Richard A Lempicki. 2009. “Systematic and Integrative Analysis of Large Gene Lists Using DAVID Bioinformatics Resources.” *Nature Protocols* 4(1): 44–57. https://www.nature.com/articles/nprot.2008.211.

Huang, Guohao et al. 2024. “Pioglitazone, a Peroxisome Proliferator-activated Receptor γ Agonist, Induces Cell Death and Inhibits the Proliferation of Hypoxic HepG2 Cells by Promoting Excessive Production of Reactive Oxygen Species.” *Oncology Letters* 27(4): 160. http://www.spandidos-publications.com/10.3892/ol.2024.14294.

Im, Seung-Soon et al. 2006. “Regulation of GLUT4 Gene Expression by SREBP-1c in Adipocytes.” *Biochemical Journal* 399(1): 131–39. https://doi.org/10.1042/BJ20060696.

Ipsen, David Højland, Jens Lykkesfeldt, and Pernille Tveden-Nyborg. 2018. “Molecular Mechanisms of Hepatic Lipid Accumulation in Non-Alcoholic Fatty Liver Disease.” *Cellular and Molecular Life Sciences* 75(18): 3313–27. http://link.springer.com/10.1007/s00018-018-2860-6.

Isakovic, Ljubomir et al. 2009. “Constrained (l-)-S-Adenosyl-l-Homocysteine (SAH) Analogues as DNA Methyltransferase Inhibitors.” *Bioorganic & Medicinal Chemistry Letters* 19(10): 2742–46. https://linkinghub.elsevier.com/retrieve/pii/S0960894X09004387.

Iwakawa, Hiro-oki, and Yukihide Tomari. 2022. “Life of RISC: Formation, Action, and Degradation of RNA-Induced Silencing Complex.” *Molecular Cell* 82(1): 30–43. https://linkinghub.elsevier.com/retrieve/pii/S1097276521010285.

Jaeschke, H. 2007. “Troglitazone Hepatotoxicity: Are We Getting Closer to Understanding Idiosyncratic Liver Injury?” *Toxicological Sciences* 97(1): 1–3. https://academic.oup.com/toxsci/article-lookup/doi/10.1093/toxsci/kfm021.

Jakovcevski, Mira, and Schahram Akbarian. 2012. “Epigenetic Mechanisms in Neurological Disease.”

Nature Medicine 18(8): 1194–1204. https://doi.org/10.1038/nm.2828.

Jastreboff, Ania M et al. 2022. "Tirzepatide Once Weekly for the Treatment of Obesity." *New England Journal of Medicine* 387(3): 205–16. https://doi.org/10.1056/NEJMoa2206038.

Jensen-Urstad, Anne P.L., and Clay F. Semenkovich. 2012. "Fatty Acid Synthase and Liver Triglyceride Metabolism: Housekeeper or Messenger?" *Biochimica et Biophysica Acta (BBA) - Molecular and Cell Biology of Lipids* 1821(5): 747–53. https://linkinghub.elsevier.com/retrieve/pii/S1388198111001879.

Jerbi, Jihène, Michael Springborg, Helena Den-Haan, and José P. Cerón-Carrasco. 2017. "S-Adenosyl- l -Methionine Analogs as Enhanced Methyl Donors: Towards Novel Epigenetic Regulators." *Chemical Physics Letters* 690: 74–81. https://linkinghub.elsevier.com/retrieve/pii/S0009261417309776.

Ji, Cheng, and Neil Kaplowitz. 2003. "Betaine Decreases Hyperhomocysteinemia, Endoplasmic Reticulum Stress, and Liver Injury in Alcohol-Fed Mice." *Gastroenterology* 124(5): 1488–99.

Jiang, Li-Peng, and Hong-Zhi Sun. 2022. "Long-Chain Saturated Fatty Acids and Its Interaction with Insulin Resistance and the Risk of Nonalcoholic Fatty Liver Disease in Type 2 Diabetes in Chinese." *Frontiers in Endocrinology* 13. https://www.frontiersin.org/articles/10.3389/fendo.2022.1051807/full.

Jin, B., Y. Li, and K. D. Robertson. 2011. "DNA Methylation: Superior or Subordinate in the Epigenetic Hierarchy?" *Genes & Cancer* 2(6): 607–17. http://gan.sagepub.com/lookup/doi/10.1177/1947601910393957.

Jin, Wenxing et al. 2020. "Structural Basis for Pri-MiRNA Recognition by Drosha." *Molecular Cell* 78(3): 423-433.e5. https://linkinghub.elsevier.com/retrieve/pii/S1097276520301441.

Jo, Junghyo et al. 2009. "Hypertrophy and/or Hyperplasia: Dynamics of Adipose Tissue Growth." *PLoS computational biology* 5(3): e1000324–e1000324. https://pubmed.ncbi.nlm.nih.gov/19325873.

Johnson, Nicholas D. et al. 2021. "Differential DNA Methylation and Changing Cell-Type Proportions as Fibrotic Stage Progresses in NAFLD." *Clinical Epigenetics* 13(1): 152. https://clinicalepigeneticsjournal.biomedcentral.com/articles/10.1186/s13148-021-01129-y.

Jopling, Catherine L et al. 2005. "Modulation of Hepatitis C Virus RNA Abundance by a Liver-Specific MicroRNA." *Science* 309(5740): 1577–81. https://www.science.org/doi/abs/10.1126/science.1113329.

Kabir, Morvarid et al. 2005. "Molecular Evidence Supporting the Portal Theory: A Causative Link between Visceral Adiposity and Hepatic Insulin Resistance." *American Journal of Physiology-Endocrinology and Metabolism* 288(2): E454–61. https://doi.org/10.1152/ajpendo.00203.2004.

Kansra, Alvina R., Sinduja Lakkunarajah, and M. Susan Jay. 2021. "Childhood and Adolescent Obesity: A Review." *Frontiers in Pediatrics* 8. https://www.frontiersin.org/articles/10.3389/fped.2020.581461/full.

Karagkouni, Dimitra et al. 2018. "DIANA-TarBase v8: A Decade-Long Collection of Experimentally Supported MiRNA–Gene Interactions." *Nucleic Acids Research* 46(D1): D239–45. https://doi.org/10.1093/nar/gkx1141.

Kathirvel, Elango et al. 2010. "Betaine Improves Nonalcoholic Fatty Liver and Associated Hepatic Insulin Resistance: A Potential Mechanism for Hepatoprotection by Betaine." *American journal of physiology. Gastrointestinal and liver physiology* 299(5): G1068-77.

KATSURA, AKIKO et al. 2015. "MicroRNA Profiles Following Metformin Treatment in a Mouse Model of Non-Alcoholic Steatohepatitis." *International Journal of Molecular Medicine* 35(4): 877–84.

https://www.spandidos-publications.com/10.3892/ijmm.2015.2092.

Kehl, Tim et al. 2017. “About MiRNAs, MiRNA Seeds, Target Genes and Target Pathways.” *Oncotarget* 8(63): 107167–75. https://www.oncotarget.com/lookup/doi/10.18632/oncotarget.22363.

Kelly, T et al. 2008. “Global Burden of Obesity in 2005 and Projections to 2030.” *International Journal of Obesity* 32(9): 1431–37. https://www.nature.com/articles/ijo2008102.

Kendall, Timothy J et al. 2023. “An Integrated Gene-to-Outcome Multimodal Database for Metabolic Dysfunction-Associated Steatotic Liver Disease.” *Nature Medicine* 29(11): 2939–53. https://doi.org/10.1038/s41591-023-02602-2.

Kennedy, Lindsey L et al. 2016. “Knockout of MicroRNA-21 Reduces Biliary Hyperplasia and Liver Fibrosis in Cholestatic Bile Duct Ligated Mice.” *Laboratory Investigation* 96(12): 1256–67. https://linkinghub.elsevier.com/retrieve/pii/S0023683722014210.

Keshet, Rom, Peter Szlosarek, Arkaitz Carracedo, and Ayelet Erez. 2018. “Rewiring Urea Cycle Metabolism in Cancer to Support Anabolism.” *Nature Reviews Cancer* 18(10): 634–45. https://www.nature.com/articles/s41568-018-0054-z.

Khvorova, Anastasia, Angela Reynolds, and Sumedha D. Jayasena. 2003. “Functional SiRNAs and MiRNAs Exhibit Strand Bias.” *Cell* 115(2): 209–16. https://linkinghub.elsevier.com/retrieve/pii/S0092867403008018.

Kim, A. Young et al. 2015. “Obesity-Induced DNA Hypermethylation of the Adiponectin Gene Mediates Insulin Resistance.” *Nature Communications* 6(1): 7585. https://www.nature.com/articles/ncomms8585.

Kim, Kimyeong, and Haejin Yoon. 2023. “Gamma-Aminobutyric Acid Signaling in Damage Response, Metabolism, and Disease.” *International Journal of Molecular Sciences* 24(5).

Kim, Tae Hyun, Dong-Gyun Hong, and Yoon Mee Yang. 2021. “Hepatokines and Non-Alcoholic Fatty Liver Disease: Linking Liver Pathophysiology to Metabolism.” *Biomedicines* 9(12): 1903. https://www.mdpi.com/2227-9059/9/12/1903.

Kim, Young-Kook, and V Narry Kim. 2007. “Processing of Intronic MicroRNAs.” *The EMBO Journal* 26(3): 775–83. http://emboj.embopress.org/cgi/doi/10.1038/sj.emboj.7601512.

Kingwell, Katie. 2024. “NASH Field Celebrates ‘Hurrah Moment’ with a First FDA Drug Approval for the Liver Disease.” *Nature Reviews Drug Discovery*. https://www.nature.com/articles/d41573-024-00051-1.

Kirchner, Henriette, Megan E. Osler, Anna Krook, and Juleen R. Zierath. 2013. “Epigenetic Flexibility in Metabolic Regulation: Disease Cause and Prevention?” *Trends in Cell Biology* 23(5): 203–9. https://linkinghub.elsevier.com/retrieve/pii/S096289241200222X.

Klaus, Valentina S et al. 2021. “Correlation Guided Network Integration (CoNI) Reveals Novel Genes Affecting Hepatic Metabolism.” *Molecular metabolism* 53: 101295.

Klein Geltink, Ramon I, and Erika L Pearce. 2019. “The Importance of Methionine Metabolism.” *eLife* 8.

Kokkinos, Alexander et al. 2019. “Will Medications That Mimic Gut Hormones or Target Their Receptors Eventually Replace Bariatric Surgery?” *Metabolism* 100: 153960. https://linkinghub.elsevier.com/retrieve/pii/S0026049519301659.

Kolenda, Tomasz et al. 2020. “Good or Not Good: Role of MiR-18a in Cancer Biology.” *Reports of Practical Oncology & Radiotherapy* 25(5): 808–19. https://linkinghub.elsevier.com/retrieve/pii/S1507136720301061.

Koonen, Debby P.Y. et al. 2007. “Increased Hepatic CD36 Expression Contributes to Dyslipidemia Associated With Diet-Induced Obesity.” *Diabetes* 56(12): 2863–71. https://diabetesjournals.org/diabetes/article/56/12/2863/12984/Increased-Hepatic-CD36-Expression-Contributes-to.

Kozomara, Ana, Maria Birgaoanu, and Sam Griffiths-Jones. 2019. “MiRBase: From MicroRNA Sequences to Function.” *Nucleic Acids Research* 47(D1): D155–62. https://academic.oup.com/nar/article/47/D1/D155/5179337.

Kozomara, Ana, and Sam Griffiths-Jones. 2014. “MiRBase: Annotating High Confidence MicroRNAs Using Deep Sequencing Data.” *Nucleic Acids Research* 42(D1): D68–73. https://academic.oup.com/nar/article-lookup/doi/10.1093/nar/gkt1181.

Krause, Christin et al. 2020. “Multi-Layered Epigenetic Regulation of IRS2 Expression in the Liver of Obese Individuals with Type 2 Diabetes.” *Diabetologia* 63(10): 2182–93.

———. 2023. “Liver MicroRNA Transcriptome Reveals MiR-182 as Link between Type 2 Diabetes and Fatty Liver Disease in Obesity.” *bioRxiv*. https://www.biorxiv.org/content/early/2023/10/04/2023.10.02.560594.

Krützfeldt, Jan et al. 2005. “Silencing of MicroRNAs in Vivo with ‘Antagomirs.’” *Nature* 438(7068): 685–89. https://www.nature.com/articles/nature04303.

Kumarswamy, Regalla, Ingo Volkmann, and Thomas Thum. 2011. “Regulation and Function of MiRNA-21 in Health and Disease.” *RNA Biology* 8(5): 706–13. http://www.tandfonline.com/doi/abs/10.4161/rna.8.5.16154.

Lacal, Irene, and Rossella Ventura. 2018. “Epigenetic Inheritance: Concepts, Mechanisms and Perspectives.” *Frontiers in Molecular Neuroscience* 11. https://www.frontiersin.org/article/10.3389/fnmol.2018.00292/full.

Lambert, Samuel A et al. 2018. “The Human Transcription Factors.” *Cell* 172(4): 650–65. https://www.sciencedirect.com/science/article/pii/S0092867418301065.

Langin, Dominique. 2006. “Adipose Tissue Lipolysis as a Metabolic Pathway to Define Pharmacological Strategies against Obesity and the Metabolic Syndrome.” *Pharmacological Research* 53(6): 482–91. https://linkinghub.elsevier.com/retrieve/pii/S1043661806000478.

Lee, Gwo-Hwa et al. 1996. “Abnormal Splicing of the Leptin Receptor in Diabetic Mice.” *Nature* 379(6566): 632–35. https://www.nature.com/articles/379632a0.

Lee, R C, R L Feinbaum, and V Ambros. 1993. “The C. Elegans Heterochronic Gene Lin-4 Encodes Small RNAs with Antisense Complementarity to Lin-14.” *Cell* 75(5): 843–54.

Lee, Won Jun, and Bao Ting Zhu. 2006. “Inhibition of DNA Methylation by Caffeic Acid and Chlorogenic Acid, Two Common Catechol-Containing Coffee Polyphenols.” *Carcinogenesis* 27(2): 269–77. http://academic.oup.com/carcin/article/27/2/269/2476070/Inhibition-of-DNA-methylation-by-caffeic-acid-and.

Lee, Yoontae et al. 2004. “MicroRNA Genes Are Transcribed by RNA Polymerase II.” *The EMBO journal* 23(20): 4051–60.

Lee, Young-Yoon et al. 2023. “Structure of the Human DICER–Pre-MiRNA Complex in a Dicing State.” *Nature* 615(7951): 331–38. https://www.nature.com/articles/s41586-023-05723-3.

Lehnertz, Bernhard et al. 2003. “Suv39h-Mediated Histone H3 Lysine 9 Methylation Directs DNA Methylation to Major Satellite Repeats at Pericentric Heterochromatin.” *Current Biology* 13(14): 1192–1200. https://linkinghub.elsevier.com/retrieve/pii/S0960982203004329.

Lenz, Michael et al. 2020. “Adipose Tissue in Health and Disease through the Lens of Its Building Blocks.” *Scientific Reports* 10(1): 10433. https://www.nature.com/articles/s41598-020-67177-1.

Leonetti, Simone et al. 2020. “Glutamate–Serine–Glycine Index: A Novel Potential Biomarker in Pediatric Non-Alcoholic Fatty Liver Disease.” *Children* 7(12): 270. https://www.mdpi.com/2227-9067/7/12/270.

Lewis, Benjamin P., Christopher B. Burge, and David P. Bartel. 2005. “Conserved Seed Pairing, Often Flanked by Adenosines, Indicates That Thousands of Human Genes Are MicroRNA Targets.” *Cell* 120(1): 15–20. https://linkinghub.elsevier.com/retrieve/pii/S0092867404012607.

Li, Bo et al. 2023. “Downregulation of MicroRNA-145a-5p Promotes Steatosis-to-NASH Progression through Upregulation of Nr4a2.” *Journal of Hepatology* 79(5): 1096–1109. https://www.sciencedirect.com/science/article/pii/S0168827823049796.

Li, Chi, and Yangchao Chen. 2015. “Small and Long Non-Coding RNAs: Novel Targets in Perspective Cancer Therapy.” *Current Genomics* 16(5): 319–26. http://www.eurekaselect.com/openurl/content.php?genre=article&issn=1389-2029&volume=16&issue=5&spage=319.

Li, Jie et al. 2019. “Prevalence, Incidence, and Outcome of Non-Alcoholic Fatty Liver Disease in Asia, 1999–2019: A Systematic Review and Meta-Analysis.” *The Lancet Gastroenterology & Hepatology* 4(5): 389–98. https://linkinghub.elsevier.com/retrieve/pii/S2468125319300391.

Li, Linsen et al. 2021. “Lipids and Membrane-Associated Proteins in Autophagy.” *Protein & Cell* 12(7): 520–44. https://academic.oup.com/proteincell/article/12/7/520/6724517.

Li, Shijie, Michael S. Brown, and Joseph L. Goldstein. 2010. “Bifurcation of Insulin Signaling Pathway in Rat Liver: MTORC1 Required for Stimulation of Lipogenesis, but Not Inhibition of Gluconeogenesis.” *Proceedings of the National Academy of Sciences* 107(8): 3441–46. https://pnas.org/doi/full/10.1073/pnas.0914798107.

Li, Yanlin et al. 2022. “Betaine Alleviates High-Fat Diet-Induced Disruptionof Hepatic Lipid and Iron Homeostasis in Mice.” *International Journal of Molecular Sciences* 23(11): 6263. https://www.mdpi.com/1422-0067/23/11/6263.

Li, Zhuozhuo et al. 2022. “Arginase: Shedding Light on the Mechanisms and Opportunities in Cardiovascular Diseases.” *Cell Death Discovery* 8(1): 413. https://www.nature.com/articles/s41420-022-01200-4.

Lim, Unhee, and Min-Ae Song. 2012. “Dietary and Lifestyle Factors of DNA Methylation.” *Methods in molecular biology (Clifton, N.J.)* 863: 359–76.

Lin, Fei et al. 2023. “Weight Loss Efficiency and Safety of Tirzepatide: A Systematic Review” ed. Inge Roggen. *PLOS ONE* 18(5): e0285197. https://dx.plos.org/10.1371/journal.pone.0285197.

Liu, Baohong, Yu Shyr, Jianping Cai, and Qi Liu. 2018. “Interplay between MiRNAs and Host Genes and Their Role in Cancer.” *Briefings in functional genomics* 18(4): 255–66.

Liu, Xiaojing et al. 2018. “Acetate Production from Glucose and Coupling to Mitochondrial Metabolism in Mammals.” *Cell* 175(2): 502-513.e13. https://linkinghub.elsevier.com/retrieve/pii/S0092867418311012.

Longo, Michele et al. 2019a. “Adipose Tissue Dysfunction as Determinant of Obesity-Associated Metabolic Complications.” *International journal of molecular sciences* 20(9): 2358. https://pubmed.ncbi.nlm.nih.gov/31085992.

———. 2019b. “Adipose Tissue Dysfunction as Determinant of Obesity-Associated Metabolic Complications.” *International Journal of Molecular Sciences* 20(9): 2358.

https://www.mdpi.com/1422-0067/20/9/2358.

Loomba, Rohit, Scott L. Friedman, and Gerald I. Shulman. 2021. "Mechanisms and Disease Consequences of Nonalcoholic Fatty Liver Disease." *Cell* 184(10): 2537–64. https://linkinghub.elsevier.com/retrieve/pii/S0092867421004943.

Loyer, Xavier et al. 2016. "Liver MicroRNA-21 Is Overexpressed in Non-Alcoholic Steatohepatitis and Contributes to the Disease in Experimental Models by Inhibiting PPARα Expression." *Gut* 65(11): 1882–94. https://gut.bmj.com/lookup/doi/10.1136/gutjnl-2014-308883.

Lu, Shelly C. et al. 2001. "Methionine Adenosyltransferase 1A Knockout Mice Are Predisposed to Liver Injury and Exhibit Increased Expression of Genes Involved in Proliferation." *Proceedings of the National Academy of Sciences* 98(10): 5560–65. https://pnas.org/doi/full/10.1073/pnas.091016398.

Lujambio, Amaia et al. 2008. "A MicroRNA DNA Methylation Signature for Human Cancer Metastasis." *Proceedings of the National Academy of Sciences* 105(36): 13556–61. https://pnas.org/doi/full/10.1073/pnas.0803055105.

Luo, Liping, and Meilian Liu. 2016. "Adipose Tissue in Control of Metabolism." *Journal of Endocrinology* 231(3): R77–99. https://joe.bioscientifica.com/view/journals/joe/231/3/R77.xml.

Ma, Xinran, Dongmei Wang, Wenjun Zhao, and Lingyan Xu. 2018. "Deciphering the Roles of PPARγ in Adipocytes via Dynamic Change of Transcription Complex." *Frontiers in Endocrinology* 9. https://www.frontiersin.org/article/10.3389/fendo.2018.00473/full.

Maciejewski, Matthew L. et al. 2016. "Bariatric Surgery and Long-Term Durability of Weight Loss." *JAMA Surgery* 151(11): 1046. http://archsurg.jamanetwork.com/article.aspx?doi=10.1001/jamasurg.2016.2317.

Makris, Georgios et al. 2024. "Expression and Function of the Urea Cycle in Widely-Used Hepatic Cellular Models." *Journal of Inherited Metabolic Disease* n/a(n/a). https://doi.org/10.1002/jimd.12701.

Małodobra-Mazur, Małgorzata, Aneta Cierzniak, Krzysztof Kaliszewski, and Tadeusz Dobosz. 2021. "PPARG Hypermethylation as the First Epigenetic Modification in Newly Onset Insulin Resistance in Human Adipocytes." *Genes* 12(6): 889. https://www.mdpi.com/2073-4425/12/6/889.

Martin, Fergal J et al. 2023. "Ensembl 2023." *Nucleic Acids Research* 51(D1): D933–41. https://academic.oup.com/nar/article/51/D1/D933/6786199.

Martin, Hilary C et al. 2014. "Imperfect Centered MiRNA Binding Sites Are Common and Can Mediate Repression of Target MRNAs." *Genome Biology* 15(3): R51. http://genomebiology.biomedcentral.com/articles/10.1186/gb-2014-15-3-r51.

Martins-de-Souza, Daniel. 2014. "Proteomics, Metabolomics, and Protein Interactomics in the Characterization of the Molecular Features of Major Depressive Disorder." *Dialogues in clinical neuroscience* 16(1): 63–73.

Matoba, Yasuyuki et al. 2017. "Crystallographic and Mutational Analyses of Cystathionine β-Synthase in the H(2) S-Synthetic Gene Cluster in Lactobacillus Plantarum." *Protein science : a publication of the Protein Society* 26(4): 763–83.

Matsumoto, Shirou et al. 2019. "Urea Cycle Disorders—Update." *Journal of Human Genetics* 64(9): 833–47. https://doi.org/10.1038/s10038-019-0614-4.

McCarthy, John J. 2011. "The MyomiR Network in Skeletal Muscle Plasticity." *Exercise and Sport Sciences Reviews* 39(3): 150–54. https://journals.lww.com/00003677-201107000-00008.

McGlinchey, Aidan J et al. 2022. “Metabolic Signatures across the Full Spectrum of Non-Alcoholic Fatty Liver Disease.” *JHEP reports : innovation in hepatology* 4(5): 100477.

Medley, Jeffrey C, Ganesh Panzade, and Anna Y Zinovyeva. 2021. “MicroRNA Strand Selection: Unwinding the Rules.” *Wiley interdisciplinary reviews. RNA* 12(3): e1627.

Meier, Juris J., and Michael A. Nauck. 2015. “Incretin-Based Therapies: Where Will We Be 50 Years from Now?” *Diabetologia* 58(8): 1745–50. http://link.springer.com/10.1007/s00125-015-3608-6.

Melzner, Ingo et al. 2002. “Leptin Gene Expression in Human Preadipocytes Is Switched on by Maturation-Induced Demethylation of Distinct CpGs in Its Proximal Promoter.” *Journal of Biological Chemistry* 277(47): 45420–27. https://linkinghub.elsevier.com/retrieve/pii/S0021925819716494.

Merrell, Allyson J., and Ben Z. Stanger. 2016. “Adult Cell Plasticity in Vivo: De-Differentiation and Transdifferentiation Are Back in Style.” *Nature Reviews Molecular Cell Biology* 17(7): 413–25. https://www.nature.com/articles/nrm.2016.24.

Mohn, Fabio et al. 2008. “Lineage-Specific Polycomb Targets and De Novo DNA Methylation Define Restriction and Potential of Neuronal Progenitors.” *Molecular Cell* 30(6): 755–66. https://linkinghub.elsevier.com/retrieve/pii/S1097276508003584.

Molinaro, Angela, Barbara Becattini, and Giovanni Solinas. 2020. “Insulin Signaling and Glucose Metabolism in Different Hepatoma Cell Lines Deviate from Hepatocyte Physiology toward a Convergent Aberrant Phenotype.” *Scientific Reports* 10(1): 12031. https://www.nature.com/articles/s41598-020-68721-9.

Momeni, Kavoos, Saeid Ghorbian, Ehsan Ahmadpour, and Rasoul Sharifi. 2023. “Unraveling the Complexity: Understanding the Deconvolutions of RNA-Seq Data.” *Translational Medicine Communications* 8(1): 21. https://transmedcomms.biomedcentral.com/articles/10.1186/s41231-023-00154-8.

Mondal, Tanmoy et al. 2023. “Transcriptomics of MASLD Pathobiology in African American Patients in the Washington DC Area †.” *International Journal of Molecular Sciences* 24(23): 16654. https://www.mdpi.com/1422-0067/24/23/16654.

Monteys, Alex Mas et al. 2010. “Structure and Activity of Putative Intronic MiRNA Promoters.” *RNA (New York, N.Y.)* 16(3): 495–505.

Moore, Lisa D., Thuc Le, and Guoping Fan. 2013. “DNA Methylation and Its Basic Function.” *Neuropsychopharmacology* 38(1): 23–38.

Moosavi, Azam, and Ali Motevalizadeh Ardekani. 2016. “Role of Epigenetics in Biology and Human Diseases.” *Iranian biomedical journal* 20(5): 246–58. https://pubmed.ncbi.nlm.nih.gov/27377127.

Moraes, Paulo Alexandre et al. 2014. “Insulin Acutely Triggers Transcription of Slc2a4 Gene: Participation of the AT-Rich, E-Box and NFKB-Binding Sites.” *Life sciences* 114(1): 36–44.

Moslehi, Azam, and Zeinab Hamidi-Zad. 2018. “Role of SREBPs in Liver Diseases: A Mini-Review.” *Journal of clinical and translational hepatology* 6(3): 332–38.

Mottillo, Emilio P. et al. 2014. “Coupling of Lipolysis and de Novo Lipogenesis in Brown, Beige, and White Adipose Tissues during Chronic B3-Adrenergic Receptor Activation.” *Journal of Lipid Research* 55(11): 2276–86. https://linkinghub.elsevier.com/retrieve/pii/S0022227520349804.

Müller-Dott, Sophia et al. 2023. “Expanding the Coverage of Regulons from High-Confidence Prior Knowledge for Accurate Estimation of Transcription Factor Activities.” *Nucleic Acids Research*

51(20): 10934–49. https://doi.org/10.1093/nar/gkad841.

Müller, Fabrice A., and Shana J. Sturla. 2019. “Human in Vitro Models of Nonalcoholic Fatty Liver Disease.” *Current Opinion in Toxicology* 16: 9–16. https://linkinghub.elsevier.com/retrieve/pii/S2468202019300117.

Müller, Timo D, Matthias Blüher, Matthias H Tschöp, and Richard D DiMarchi. 2022. “Anti-Obesity Drug Discovery: Advances and Challenges.” *Nature Reviews Drug Discovery* 21(3): 201–23. https://doi.org/10.1038/s41573-021-00337-8.

Nagle, Cynthia A., Eric L. Klett, and Rosalind A. Coleman. 2009. “Hepatic Triacylglycerol Accumulation and Insulin Resistance.” *Journal of Lipid Research* 50: S74–79. https://linkinghub.elsevier.com/retrieve/pii/S0022227520305903.

Nakanishi, Kotaro. 2022. “Anatomy of Four Human Argonaute Proteins.” *Nucleic Acids Research* 50(12): 6618–38. https://academic.oup.com/nar/article/50/12/6618/6613925.

Namkoong, Sim et al. 2015. “The Integral Membrane Protein ITM2A, a Transcriptional Target of PKA-CREB, Regulates Autophagic Flux via Interaction with the Vacuolar ATPase.” *Autophagy* 11(5): 756–68. http://www.tandfonline.com/doi/full/10.1080/15548627.2015.1034412.

Naruse, Ken et al. 2018. “In Vitro Reconstitution of Chaperone-Mediated Human RISC Assembly.” *RNA* 24(1): 6–11. http://rnajournal.cshlp.org/lookup/doi/10.1261/rna.063891.117.

Neill, Meaghan Anne, Judy Aschner, Frederick Barr, and Marshall L Summar. 2009. “Quantitative RT-PCR Comparison of the Urea and Nitric Oxide Cycle Gene Transcripts in Adult Human Tissues.” *Molecular genetics and metabolism* 97(2): 121–27.

Neumann, Anne-Marie et al. 2021. “Restructuring of the Male Mice Peripheral Circadian Network after Bariatric Surgery.” *Journal of Endocrinology* 250(2): 67–79. https://joe.bioscientifica.com/view/journals/joe/250/2/JOE-20-0611.xml.

Ng, S. S., W. W. Yue, U. Oppermann, and R. J. Klose. 2009. “Dynamic Protein Methylation in Chromatin Biology.” *Cellular and Molecular Life Sciences* 66(3): 407. https://link.springer.com/10.1007/s00018-008-8303-z.

Nguyen, Tuan Anh et al. 2015. “Functional Anatomy of the Human Microprocessor.” *Cell* 161(6): 1374–87. https://linkinghub.elsevier.com/retrieve/pii/S0092867415005589.

Nishizawa, Hitoshi, and Iichiro Shimomura. 2019. “Fat Cell Lipolysis and Future Weight Gain.” *Journal of Diabetes Investigation* 10(2): 221–23. https://onlinelibrary.wiley.com/doi/10.1111/jdi.12950.

Nour, Nawal N. 2010. “Obesity in Resource-Poor Nations.” *Reviews in obstetrics & gynecology* 3(4): 180–84. http://www.ncbi.nlm.nih.gov/pubmed/21364850.

O’Brien, Jacob, Heyam Hayder, Yara Zayed, and Chun Peng. 2018. “Overview of MicroRNA Biogenesis, Mechanisms of Actions, and Circulation.” *Frontiers in Endocrinology* 9. https://www.frontiersin.org/articles/10.3389/fendo.2018.00402.

Of, Metabolism, and Fatty Acids. 1956. “Metabolism of Lipides1,2.”

Ogawa, Yuji et al. 2018. “Palmitate-Induced Lipotoxicity Is Crucial for the Pathogenesis of Nonalcoholic Fatty Liver Disease in Cooperation with Gut-Derived Endotoxin.” *Scientific Reports* 8(1): 11365. https://www.nature.com/articles/s41598-018-29735-6.

Okano, Masaki, Daphne W Bell, Daniel A Haber, and En Li. 1999. “DNA Methyltransferases Dnmt3a and Dnmt3b Are Essential for De Novo Methylation and Mammalian Development.” *Cell* 99(3): 247–57. https://linkinghub.elsevier.com/retrieve/pii/S0092867400816566.

Ospelt, Caroline. 2022. “A Brief History of Epigenetics.” *Immunology Letters* 249: 1–4.

https://www.sciencedirect.com/science/article/pii/S0165247822001055.

Park, Anna. 2014. “Distinction of White, Beige and Brown Adipocytes Derived from Mesenchymal Stem Cells.” *World Journal of Stem Cells* 6(1): 33. http://www.wjgnet.com/1948-0210/full/v6/i1/33.htm.

Patel, Mulchand S, Natalia S Nemeria, William Furey, and Frank Jordan. 2014. “The Pyruvate Dehydrogenase Complexes: Structure-Based Function and Regulation.” *The Journal of biological chemistry* 289(24): 16615–23.

Petersen, Max C., and Gerald I. Shulman. 2018. “Mechanisms of Insulin Action and Insulin Resistance.” *Physiological Reviews* 98(4): 2133–2223. https://www.physiology.org/doi/10.1152/physrev.00063.2017.

Pfaffl, M W. 2001. “A New Mathematical Model for Relative Quantification in Real-Time RT-PCR.” *Nucleic acids research* 29(9): e45.

Pham, Tho X., and Ji-Young Lee. 2017. “Epigenetic Regulation of Adipokines.” *International Journal of Molecular Sciences* 18(8): 1740. http://www.mdpi.com/1422-0067/18/8/1740.

Poletto, Ana Cláudia et al. 2015. “Reduced Slc2a4/GLUT4 Expression in Subcutaneous Adipose Tissue of Monosodium Glutamate Obese Mice Is Recovered after Atorvastatin Treatment.” *Diabetology and Metabolic Syndrome* 7(1): 1–6.

Polyzos, Stergios A et al. 2012. “Serum Homocysteine Levels in Patients with Nonalcoholic Fatty Liver Disease.” *Annals of hepatology* 11(1): 68–76.

Ponnaluri, V.K. Chaithanya, Pierre-Olivier Estève, Cristian I. Ruse, and Sriharsa Pradhan. 2018. “S-Adenosylhomocysteine Hydrolase Participates in DNA Methylation Inheritance.” *Journal of Molecular Biology* 430(14): 2051–65. https://linkinghub.elsevier.com/retrieve/pii/S0022283618304121.

Pouwels, Sjaak et al. 2022. “Non-Alcoholic Fatty Liver Disease (NAFLD): A Review of Pathophysiology, Clinical Management and Effects of Weight Loss.” *BMC Endocrine Disorders* 22(1): 63. https://bmcendocrdisord.biomedcentral.com/articles/10.1186/s12902-022-00980-1.

Project, ENCODE. 2012. “An Integrated Encyclopedia of DNA Elements in the Human Genome.” *Nature* 489(7414): 57–74. http://www.nature.com/articles/nature11247.

Quinn, Connor, Mario C Rico, Carmen Merali, and Salim Merali. 2022. “Dysregulation of S-Adenosylmethionine Metabolism in Nonalcoholic Steatohepatitis Leads to Polyamine Flux and Oxidative Stress.” *International journal of molecular sciences* 23(4).

Qume, Michelle, and Leslie J Fowler. 1996. “Effects of Chronic Oral Treatment with GABA-Transaminase Inhibitors on the GABA System in Brain, Liver, Kidney, and Plasma of the Rat.” *Biochemical Pharmacology* 52(9): 1355–63. https://www.sciencedirect.com/science/article/pii/S0006295296004546.

Rahmani, Elior et al. 2019. “Cell-Type-Specific Resolution Epigenetics without the Need for Cell Sorting or Single-Cell Biology.” *Nature Communications* 10(1): 3417. https://doi.org/10.1038/s41467-019-11052-9.

Rai, Kunal et al. 2008. “DNA Demethylation in Zebrafish Involves the Coupling of a Deaminase, a Glycosylase, and Gadd45.” *Cell* 135(7): 1201–12. https://linkinghub.elsevier.com/retrieve/pii/S0092867408015171.

Ramasamy, Deepa, Arunagiri Kuha Deva Magendhra Rao, Thangarajan Rajkumar, and Samson Mani. 2021. “Non-CpG Methylation—a Key Epigenetic Modification in Cancer.” *Briefings in Functional Genomics* 20(5): 304–11. https://academic.oup.com/bfg/article/20/5/304/6329163.

Ramirez, Alfred K. et al. 2020. “Single-Cell Transcriptional Networks in Differentiating Preadipocytes Suggest Drivers Associated with Tissue Heterogeneity.” *Nature Communications* 11(1): 2117. https://www.nature.com/articles/s41467-020-16019-9.

Rauluseviciute, Ieva et al. 2023. “JASPAR 2024: 20th Anniversary of the Open-Access Database of Transcription Factor Binding Profiles.” *Nucleic Acids Research* 52(D1): D174–82. https://doi.org/10.1093/nar/gkad1059.

Reneau, James et al. 2018. “Effect of Adiposity on Tissue-Specific Adiponectin Secretion” ed. Andrew Wolfe. *PLOS ONE* 13(6): e0198889. https://dx.plos.org/10.1371/journal.pone.0198889.

de Rie, Derek et al. 2017. “An Integrated Expression Atlas of MiRNAs and Their Promoters in Human and Mouse.” *Nature Biotechnology* 35(9): 872–78. https://www.nature.com/articles/nbt.3947.

Rinella, Mary E. et al. 2023. “A Multisociety Delphi Consensus Statement on New Fatty Liver Disease Nomenclature.” *Journal of Hepatology* 79(6): 1542–56. https://linkinghub.elsevier.com/retrieve/pii/S016882782300418X.

Rodrigues, Pedro M et al. 2023. “MiR-21-5p Promotes NASH-Related Hepatocarcinogenesis.” *Liver International* 43(10): 2256–74. https://doi.org/10.1111/liv.15682.

Rohde, Kerstin et al. 2019. “Genetics and Epigenetics in Obesity.” *Metabolism* 92: 37–50. https://www.sciencedirect.com/science/article/pii/S0026049518302257.

Romeo, Stefano et al. 2008. “Genetic Variation in PNPLA3 Confers Susceptibility to Nonalcoholic Fatty Liver Disease.” *Nature genetics* 40(12): 1461–65.

Ross, Stuart A, and Jean-Marie Ekoé. 2010. “Incretin Agents in Type 2 Diabetes.” *Canadian family physician Medecin de famille canadien* 56(7): 639–48. http://www.ncbi.nlm.nih.gov/pubmed/20631270.

Ruby, J. Graham, Calvin H. Jan, and David P. Bartel. 2007. “Intronic MicroRNA Precursors That Bypass Drosha Processing.” *Nature* 448(7149): 83–86. https://www.nature.com/articles/nature05983.

Rytka, Julia M., Stephan Wueest, Eugen J. Schoenle, and Daniel Konrad. 2011. “The Portal Theory Supported by Venous Drainage–Selective Fat Transplantation.” *Diabetes* 60(1): 56–63. https://diabetesjournals.org/diabetes/article/60/1/56/15089/The-Portal-Theory-Supported-by-Venous-Drainage.

Sakabe, Kaoru, Zihao Wang, and Gerald W. Hart. 2010. “β- N -Acetylglucosamine (O-GlcNAc) Is Part of the Histone Code.” *Proceedings of the National Academy of Sciences* 107(46): 19915–20. https://pnas.org/doi/full/10.1073/pnas.1009023107.

Sakers, Alexander, Mirian Krystel De Siqueira, Patrick Seale, and Claudio J. Villanueva. 2022. “Adipose-Tissue Plasticity in Health and Disease.” *Cell* 185(3): 419–46. https://linkinghub.elsevier.com/retrieve/pii/S0092867421014549.

Salvoza, Noel C., David C. Klinzing, Juliet Gopez-Cervantes, and Michael O. Baclig. 2016. “Association of Circulating Serum MiR-34a and MiR-122 with Dyslipidemia among Patients with Non-Alcoholic Fatty Liver Disease” ed. Manlio Vinciguerra. *PLOS ONE* 11(4): e0153497. https://dx.plos.org/10.1371/journal.pone.0153497.

Samuel, Varman T. et al. 2007. “Inhibition of Protein Kinase Cε Prevents Hepatic Insulin Resistance in Nonalcoholic Fatty Liver Disease.” *Journal of Clinical Investigation* 117(3): 739–45. http://www.jci.org/cgi/doi/10.1172/JCI30400.

Sana, Jiri, Petra Faltejskova, Marek Svoboda, and Ondrej Slaby. 2012. “Novel Classes of Non-Coding RNAs and Cancer.” *Journal of Translational Medicine* 10(1): 103. https://translational-medicine.biomedcentral.com/articles/10.1186/1479-5876-10-103.

Sangiao-Alvarellos, Susana et al. 2020. “Metabolic Recovery after Weight Loss Surgery Is Reflected in Serum MicroRNAs.” *BMJ Open Diabetes Research & Care* 8(2): e001441. https://drc.bmj.com/lookup/doi/10.1136/bmjdrc-2020-001441.

Santoro, Anna, Timothy E. McGraw, and Barbara B. Kahn. 2021. “Insulin Action in Adipocytes, Adipose Remodeling, and Systemic Effects.” *Cell Metabolism* 33(4): 748–57. https://linkinghub.elsevier.com/retrieve/pii/S1550413121001261.

Sarna, Lindsei K., Yaw L. Siow, and Karmin O. 2015. “The CBS/CSE System: A Potential Therapeutic Target in NAFLD?” *Canadian Journal of Physiology and Pharmacology* 93(1): 1–11. http://www.nrcresearchpress.com/doi/10.1139/cjpp-2014-0394.

Saxonov, Serge, Paul Berg, and Douglas L. Brutlag. 2006. “A Genome-Wide Analysis of CpG Dinucleotides in the Human Genome Distinguishes Two Distinct Classes of Promoters.” *Proceedings of the National Academy of Sciences* 103(5): 1412–17. https://pnas.org/doi/full/10.1073/pnas.0510310103.

Sbodio, Juan I, Solomon H Snyder, and Bindu D Paul. 2019. “Regulators of the Transsulfuration Pathway.” *British Journal of Pharmacology* 176(4): 583–93. https://bpspubs.onlinelibrary.wiley.com/doi/10.1111/bph.14446.

Schamberger, Anita, Balázs Sarkadi, and Tamás I. Orbán. 2012. “Human Mirtrons Can Express Functional MicroRNAs Simultaneously from Both Arms in a Flanking Exon-Independent Manner.” *RNA Biology* 9(9): 1177–85. http://www.tandfonline.com/doi/abs/10.4161/rna.21359.

Schult, Philipp et al. 2018. “MicroRNA-122 Amplifies Hepatitis C Virus Translation by Shaping the Structure of the Internal Ribosomal Entry Site.” *Nature Communications* 9(1): 2613. https://www.nature.com/articles/s41467-018-05053-3.

Schulz, W. A., C. Steinhoff, and A. R. Florl. “Methylation of Endogenous Human Retroelements in Health and Disease.” In *DNA Methylation: Development, Genetic Disease and Cancer*, Springer Berlin Heidelberg, 211–50. http://link.springer.com/10.1007/3-540-31181-5_11.

Schweinberger, Bruna M., and Angela T. S. Wyse. 2016. “Mechanistic Basis of Hypermethioninemia.” *Amino Acids* 48(11): 2479–89. http://link.springer.com/10.1007/s00726-016-2302-4.

Seok Roh, Yoon et al. 2016. “G-Aminobutyric Acid Promotes Methionine-Choline Deficient Diet-Induced Nonalcoholic Steatohepatitis.” *Journal of biomedical research* 31(1): 65–73.

Shabkhizan, Roya et al. 2023. “The Beneficial and Adverse Effects of Autophagic Response to Caloric Restriction and Fasting.” *Advances in Nutrition* 14(5): 1211–25. https://linkinghub.elsevier.com/retrieve/pii/S2161831323013443.

Shao, Mingmei et al. 2022. “Application of Metabolomics in the Diagnosis of Non-Alcoholic Fatty Liver Disease and the Treatment of Traditional Chinese Medicine.” *Frontiers in Pharmacology* 13. https://www.frontiersin.org/articles/10.3389/fphar.2022.971561/full.

Sheedy, Frederick J. 2015. “Turning 21: Induction of MiR-21 as a Key Switch in the Inflammatory Response.” *Frontiers in Immunology* 6. http://journal.frontiersin.org/article/10.3389/fimmu.2015.00019/abstract.

Sheka, Adam C. et al. 2020. “Nonalcoholic Steatohepatitis.” *JAMA* 323(12): 1175. https://jamanetwork.com/journals/jama/fullarticle/2763297.

Shen, Kexin et al. 2019. “The Dual Functional Role of MicroRNA-18a (MiR-18a) in Cancer Development.” *Clinical and translational medicine* 8(1): 32.

Shen, Wen et al. 2020. “Homocysteine-Methionine Cycle Is a Metabolic Sensor System Controlling

Methylation-Regulated Pathological Signaling." *Redox Biology* 28: 101322. https://linkinghub.elsevier.com/retrieve/pii/S2213231719309589.

Shen, Wenwen et al. 2014. "Epigenetic Modification of the Leptin Promoter in Diet-Induced Obese Mice and the Effects of N-3 Polyunsaturated Fatty Acids." *Scientific Reports* 4(1): 5282. https://www.nature.com/articles/srep05282.

Shen, Yang et al. 2022. "Tumor-Suppressive and Oncogenic Roles of MicroRNA-149-5p in Human Cancers." *International Journal of Molecular Sciences* 23(18). https://www.mdpi.com/1422-0067/23/18/10823.

Shook, Brett A. et al. 2020. "Dermal Adipocyte Lipolysis and Myofibroblast Conversion Are Required for Efficient Skin Repair." *Cell Stem Cell* 26(6): 880-895.e6. https://linkinghub.elsevier.com/retrieve/pii/S1934590920301053.

Sievert, Helen, Christin Krause, Cathleen Geißler, et al. 2021. "Epigenetic Downregulation of FASN in Visceral Adipose Tissue of Insulin Resistant Subjects." *Experimental and clinical endocrinology & diabetes : official journal, German Society of Endocrinology [and] German Diabetes Association* 129(9): 674–82.

Sievert, Helen, Christin Krause, Cathleen Geiβler, et al. 2021. "Epigenetic Downregulation of FASN in Visceral Adipose Tissue of Insulin Resistant Subjects." *Experimental and Clinical Endocrinology and Diabetes* 129(9): 674–82.

Simón, Jorge, María Luz Martínez-Chantar, and Teresa C. Delgado. 2021. "Glutamine, Fatty Liver Disease and Aging." *Aging* 13(3): 3165–66. https://www.aging-us.com/lookup/doi/10.18632/aging.202666.

Singh, Omkar, Drew Pratt, and Kenneth Aldape. 2021. "Immune Cell Deconvolution of Bulk DNA Methylation Data Reveals an Association with Methylation Class, Key Somatic Alterations, and Cell State in Glial/Glioneuronal Tumors." *Acta Neuropathologica Communications* 9(1): 148. https://actaneurocomms.biomedcentral.com/articles/10.1186/s40478-021-01249-9.

Skat-Rørdam, Josephine, David Højland Ipsen, Jens Lykkesfeldt, and Pernille Tveden-Nyborg. 2019. "A Role of Peroxisome Proliferator-Activated Receptor γ in Non-Alcoholic Fatty Liver Disease." *Basic & Clinical Pharmacology & Toxicology* 124(5): 528–37. https://doi.org/10.1111/bcpt.13190.

Smith, Kerri. 2015. "Epigenome: The Symphony in Your Cells." *Nature*. https://doi.org/10.1038/nature.2015.16955.

Song, Tongxing, and Shihuan Kuang. 2019. "Adipocyte Dedifferentiation in Health and Diseases." *Clinical Science* 133(20): 2107–19. https://portlandpress.com/clinsci/article/133/20/2107/220930/Adipocyte-dedifferentiation-in-health-and-diseases.

Song, Ziyi, Alus M. Xiaoli, and Fajun Yang. 2018a. "Regulation and Metabolic Significance of De Novo Lipogenesis in Adipose Tissues." *Nutrients* 10(10): 1–22.

Song, Ziyi, Alus Xiaoli, and Fajun Yang. 2018b. "Regulation and Metabolic Significance of De Novo Lipogenesis in Adipose Tissues." *Nutrients* 10(10): 1383. http://www.mdpi.com/2072-6643/10/10/1383.

Stadler, Julia T., and Gunther Marsche. 2020. "Obesity-Related Changes in High-Density Lipoprotein Metabolism and Function." *International Journal of Molecular Sciences* 21(23): 8985. https://www.mdpi.com/1422-0067/21/23/8985.

Stavast, Christiaan, and Stefan Erkeland. 2019. "The Non-Canonical Aspects of MicroRNAs: Many

Roads to Gene Regulation." *Cells* 8(11): 1465. https://www.mdpi.com/2073-4409/8/11/1465.

Stefan, Norbert, and Hans-Ulrich Häring. 2013. "The Role of Hepatokines in Metabolism." *Nature Reviews Endocrinology* 9(3): 144–52. https://www.nature.com/articles/nrendo.2012.258.

Stephenson, Kristen et al. 2018. "Updates on Dietary Models of Nonalcoholic Fatty Liver Disease: Current Studies and Insights." *Gene Expression* 18(1): 5–17. https://www.ingentaconnect.com/content/10.3727/105221617X15093707969658.

Sui, Guangchao et al. 2002. "A DNA Vector-Based RNAi Technology to Suppress Gene Expression in Mammalian Cells." *Proceedings of the National Academy of Sciences* 99(8): 5515–20. https://pnas.org/doi/full/10.1073/pnas.082117599.

Sun, Qing-Feng et al. 2022. "Potential Blood DNA Methylation Biomarker Genes for Diagnosis of Liver Fibrosis in Patients With Biopsy-Proven Non-Alcoholic Fatty Liver Disease." *Frontiers in Medicine* 9. https://www.frontiersin.org/articles/10.3389/fmed.2022.864570/full.

Sun, Shengyi, Yewei Ji, Sander Kersten, and Ling Qi. 2012. "Mechanisms of Inflammatory Responses in Obese Adipose Tissue." *Annual Review of Nutrition* 32(1): 261–86. https://www.annualreviews.org/doi/10.1146/annurev-nutr-071811-150623.

Swapna Sasi, U S, G Sindhu, and K.G. Raghu. 2020. "Fructose-Palmitate Based High Calorie Induce Steatosis in HepG2 Cells via Mitochondrial Dysfunction: An in Vitro Approach." *Toxicology in Vitro* 68: 104952. https://linkinghub.elsevier.com/retrieve/pii/S0887233320305026.

Takeuchi, Kazuharu, and Karen Reue. 2009. "Biochemistry, Physiology, and Genetics of GPAT, AGPAT, and Lipin Enzymes in Triglyceride Synthesis." *American Journal of Physiology-Endocrinology and Metabolism* 296(6): E1195–1209. https://www.physiology.org/doi/10.1152/ajpendo.90958.2008.

Tehlivets, Oksana et al. 2013. "S-Adenosyl-L-Homocysteine Hydrolase and Methylation Disorders: Yeast as a Model System." *Biochimica et biophysica acta* 1832(1): 204–15.

Thaker, Vidhu V. 2017. "GENETIC AND EPIGENETIC CAUSES OF OBESITY." *Adolescent medicine: state of the art reviews* 28(2): 379–405. http://www.ncbi.nlm.nih.gov/pubmed/30416642.

Thiagarajan, Prarthana, and Guruprasad P. Aithal. 2019. "Drug Development for Nonalcoholic Fatty Liver Disease: Landscape and Challenges." *Journal of Clinical and Experimental Hepatology* 9(4): 515–21. https://linkinghub.elsevier.com/retrieve/pii/S0973688319300635.

Thyagarajan, Baskaran, and Michelle T. Foster. 2017. "Beiging of White Adipose Tissue as a Therapeutic Strategy for Weight Loss in Humans." *Hormone Molecular Biology and Clinical Investigation* 31(2). https://www.degruyter.com/document/doi/10.1515/hmbci-2017-0016/html.

Tonoli, Hélène, and J. Carl Barrett. 2005. "CD82 Metastasis Suppressor Gene: A Potential Target for New Therapeutics?" *Trends in Molecular Medicine* 11(12): 563–70. https://linkinghub.elsevier.com/retrieve/pii/S1471491405002297.

Toraño, Estela G et al. 2016. "The Impact of External Factors on the Epigenome: In Utero and over Lifetime." *BioMed research international* 2016: 2568635.

Torres, Jorge-Luis et al. 2022. "PPAR-γ Gene Expression in Human Adipose Tissue Is Associated with Weight Loss After Sleeve Gastrectomy." *Journal of Gastrointestinal Surgery* 26(2): 286–97. https://linkinghub.elsevier.com/retrieve/pii/S1091255X23003207.

TORRES, LUIS et al. 2000. "Liver-specific Methionine Adenosyltransferase MAT1A Gene Expression Is Associated with a Specific Pattern of Promoter Methylation and Histone Acetylation: Implications for MAT1A Silencing during Transformation." *The FASEB Journal* 14(1): 95–102.

https://onlinelibrary.wiley.com/doi/abs/10.1096/fasebj.14.1.95.

Tryndyak, Volodymyr P. et al. 2011. “Coupling Global Methylation and Gene Expression Profiles Reveal Key Pathophysiological Events in Liver Injury Induced by a Methyl-deficient Diet.” *Molecular Nutrition & Food Research* 55(3): 411–18. https://onlinelibrary.wiley.com/doi/10.1002/mnfr.201000300.

Tsai, Wei-Chih et al. 2012. “MicroRNA-122 Plays a Critical Role in Liver Homeostasis and Hepatocarcinogenesis.” *Journal of Clinical Investigation* 122(8): 2884–97. http://www.jci.org/articles/view/63455.

Tsang, Wing Pui, and Tim Tak Kwok. 2009. “The MiR-18a* MicroRNA Functions as a Potential Tumor Suppressor by Targeting on K-Ras.” *Carcinogenesis* 30(6): 953–59. https://academic.oup.com/carcin/article-lookup/doi/10.1093/carcin/bgp094.

Turchinovich, Andrey, and Barbara Burwinkel. 2012. “Distinct AGO1 and AGO2 Associated MiRNA Profiles in Human Cells and Blood Plasma.” *RNA Biology* 9(8): 1066–75. http://www.tandfonline.com/doi/full/10.4161/rna.21083.

Varga, Tamas, Zsolt Czimmerer, and Laszlo Nagy. 2011. “PPARs Are a Unique Set of Fatty Acid Regulated Transcription Factors Controlling Both Lipid Metabolism and Inflammation.” *Biochimica et Biophysica Acta (BBA) - Molecular Basis of Disease* 1812(8): 1007–22. https://linkinghub.elsevier.com/retrieve/pii/S0925443911000494.

Vogel, Kara R et al. 2018. “Succinic Semialdehyde Dehydrogenase Deficiency, a Disorder of GABA Metabolism: An Update on Pharmacological and Enzyme-Replacement Therapeutic Strategies.” *Journal of inherited metabolic disease* 41(4): 699–708.

Waddington, C H. 2011. “The Epigenotype.” *International Journal of Epidemiology* 41(1): 10–13. https://doi.org/10.1093/ije/dyr184.

Waddington, Conrad H. 1953. “Epigenetics and Evolution.” In *Symp. Soc. Exp. Biol*, , 186–99.

Walsh, C. P., and G. L. Xu. “Cytosine Methylation and DNA Repair.” In *DNA Methylation: Basic Mechanisms*, Berlin/Heidelberg: Springer-Verlag, 283–315. http://link.springer.com/10.1007/3-540-31390-7_11.

Walsh, Colum P., J. Richard Chaillet, and Timothy H. Bestor. 1998. “Transcription of IAP Endogenous Retroviruses Is Constrained by Cytosine Methylation.” *Nature Genetics* 20(2): 116–17. https://www.nature.com/articles/ng1098_116.

Wanders, Ronald J.A., and Hans R. Waterham. 2006. “Biochemistry of Mammalian Peroxisomes Revisited.” *Annual Review of Biochemistry* 75(1): 295–332. https://www.annualreviews.org/doi/10.1146/annurev.biochem.74.082803.133329.

Wang, Tiannan et al. 2020. “Current Understanding of Glucose Transporter 4 Expression and Functional Mechanisms.” *World Journal of Biological Chemistry* 11(3): 76–98. https://www.wjgnet.com/1949-8454/full/v11/i3/76.htm.

Wang, Xiangyu et al. 2023. “A Comprehensive Review of the Family of Very-Long-Chain Fatty Acid Elongases: Structure, Function, and Implications in Physiology and Pathology.” *European Journal of Medical Research* 28(1): 532. https://eurjmedres.biomedcentral.com/articles/10.1186/s40001-023-01523-7.

Wang, Xiaowei, and Issam M. El Naqa. 2008. “Prediction of Both Conserved and Nonconserved MicroRNA Targets in Animals.” *Bioinformatics* 24(3): 325–32. https://academic.oup.com/bioinformatics/article/24/3/325/253469.

Wang, Xin-Yue et al. 2023. “Effect of Liver Transplantation with Primary Hyperoxaluria Type 1: Five

Case Reports and Review of Literature." *World Journal of Clinical Cases* 11(5): 1068–76. https://www.wjgnet.com/2307-8960/full/v11/i5/1068.htm.

Wang, Yu-Ping, and Kuo-Bin Li. 2009. "Correlation of Expression Profiles between MicroRNAs and MRNA Targets Using NCI-60 Data." *BMC Genomics* 10(1): 218. http://bmcgenomics.biomedcentral.com/articles/10.1186/1471-2164-10-218.

Wang, Yu et al. 2022. "Acetyl-CoA Carboxylases and Diseases." *Frontiers in Oncology* 12(March): 1–10.

Watanabe, M et al. 1995. "Mice Deficient in Cystathionine Beta-Synthase: Animal Models for Mild and Severe Homocyst(e)Inemia." *Proceedings of the National Academy of Sciences* 92(5): 1585–89. https://www.pnas.org/doi/abs/10.1073/pnas.92.5.1585.

Whitlock, Gary et al. 2009. "Body-Mass Index and Cause-Specific Mortality in 900 000 Adults: Collaborative Analyses of 57 Prospective Studies." *Lancet (London, England)* 373(9669): 1083–96.

WHO. "Link to WHO - Global Obesity and Overweight Data." https://www.who.int/news-room/fact-sheets/detail/obesity-and-overweight.

Wiering, Leke, Pallavi Subramanian, and Linda Hammerich. 2023. "Hepatic Stellate Cells: Dictating Outcome in Nonalcoholic Fatty Liver Disease." *Cellular and Molecular Gastroenterology and Hepatology* 15(6): 1277–92. https://linkinghub.elsevier.com/retrieve/pii/S2352345X23000292.

Williams, Emma L. et al. 2009. "Primary Hyperoxaluria Type 1: Update and Additional Mutation Analysis of the AGXT Gene." *Human Mutation* 30(6): 910–17. https://onlinelibrary.wiley.com/doi/10.1002/humu.21021.

Willmer, Tarryn, Rabia Johnson, Johan Louw, and Carmen Pheiffer. 2018. "Blood-Based DNA Methylation Biomarkers for Type 2 Diabetes: Potential for Clinical Applications." *Frontiers in Endocrinology* 9. https://www.frontiersin.org/article/10.3389/fendo.2018.00744/full.

Wilson, Camella G. et al. 2016. "Hepatocyte-Specific Disruption of CD36 Attenuates Fatty Liver and Improves Insulin Sensitivity in HFD-Fed Mice." *Endocrinology* 157(2): 570–85. https://academic.oup.com/endo/article/157/2/570/2422650.

Wishart, D. S. et al. 2007. "HMDB: The Human Metabolome Database." *Nucleic Acids Research* 35(Database): D521–26. https://academic.oup.com/nar/article-lookup/doi/10.1093/nar/gkl923.

Witte, Nicole et al. 2015. "The Glucose Sensor ChREBP Links De Novo Lipogenesis to PPARγ Activity and Adipocyte Differentiation." *Endocrinology* 156(11): 4008–19. https://academic.oup.com/endo/article/156/11/4008/2422738.

Wu, C.-t., and J R Morris. 2001. "Genes, Genetics, and Epigenetics: A Correspondence." *Science* 293(5532): 1103–5. https://doi.org/10.1126/science.293.5532.1103.

Wu, Yan-Lin et al. 2023. "Epigenetic Regulation in Metabolic Diseases: Mechanisms and Advances in Clinical Study." *Signal Transduction and Targeted Therapy* 8(1): 98. https://doi.org/10.1038/s41392-023-01333-7.

Xia, Jianguo, Nick Psychogios, Nelson Young, and David S Wishart. 2009. "MetaboAnalyst: A Web Server for Metabolomic Data Analysis and Interpretation." *Nucleic Acids Research* 37(suppl_2): W652–60. https://doi.org/10.1093/nar/gkp356.

Xie, Shaoping et al. 1999. "Cloning, Expression and Chromosome Locations of the Human DNMT3 Gene Family." *Gene* 236(1): 87–95. https://linkinghub.elsevier.com/retrieve/pii/S0378111999002528.

Xu, Yang et al. 2015. “A Metabolic Stress-Inducible MiR-34a-HNF4α Pathway Regulates Lipid and Lipoprotein Metabolism.” *Nature Communications* 6(1): 7466. https://www.nature.com/articles/ncomms8466.

Yamakawa, Natsuko et al. 2014. “Novel Functional Small RNAs Are Selectively Loaded onto Mammalian Ago1.” *Nucleic Acids Research* 42(8): 5289–5301. https://academic.oup.com/nar/article-lookup/doi/10.1093/nar/gku137.

Yang, Wenjing et al. 2022. “ARHGAP24 Represses β-Catenin Transactivation-Induced Invasiveness in Hepatocellular Carcinoma Mainly by Acting as a GTPase-Independent Scaffold.” *Theranostics* 12(14): 6189–6206. https://www.thno.org/v12p6189.htm.

Yao, Tatsuma, and Yuta Asayama. 2017. “Animal-cell Culture Media: History, Characteristics, and Current Issues.” *Reproductive Medicine and Biology* 16(2): 99–117. https://onlinelibrary.wiley.com/doi/10.1002/rmb2.12024.

Yi, Rui, Yi Qin, Ian G Macara, and Bryan R Cullen. 2003. “Exportin-5 Mediates the Nuclear Export of Pre-MicroRNAs and Short Hairpin RNAs.” *Genes & development* 17(24): 3011–16.

Yu, Hsin-Hsien et al. 2022. “Exendin-4 Attenuates Hepatic Steatosis by Promoting the Autophagy-Lysosomal Pathway” ed. Si Qin. *BioMed Research International* 2022: 1–7. https://www.hindawi.com/journals/bmri/2022/4246086/.

Yu, Songtao et al. 2003. “Adipocyte-Specific Gene Expression and Adipogenic Steatosis in the Mouse Liver Due to Peroxisome Proliferator-Activated Receptor Γ1 (PPARγ1) Overexpression.” *Journal of Biological Chemistry* 278(1): 498–505. https://linkinghub.elsevier.com/retrieve/pii/S0021925819312980.

Zabielski, Piotr et al. 2018. “The Effect of High Fat Diet and Metformin Treatment on Liver Lipids Accumulation and Their Impact on Insulin Action.” *Scientific Reports* 8(1): 7249. https://www.nature.com/articles/s41598-018-25397-6.

Zeng, Qin et al. 2024. “A Negative Feedback Loop between TET2 and Leptin in Adipocyte Regulates Body Weight.” *Nature Communications* 15(1): 2825. https://www.nature.com/articles/s41467-024-46783-x.

Zhang, Shasha et al. 2019. “Metabolic Engineering for Efficient Supply of Acetyl-CoA from Different Carbon Sources in Escherichia Coli.” *Microbial Cell Factories* 18(1): 130. https://microbialcellfactories.biomedcentral.com/articles/10.1186/s12934-019-1177-y.

Zhang, Xinchao, Yue Zhang, Chaofu Wang, and Xu Wang. 2023. “TET (Ten-Eleven Translocation) Family Proteins: Structure, Biological Functions and Applications.” *Signal Transduction and Targeted Therapy* 8(1): 297. https://www.nature.com/articles/s41392-023-01537-x.

Zhang, Yongjie et al. 2024. “Glutamine Prevents High-Fat Diet-Induced Hepatic Lipid Accumulation in Mice by Modulating Lipolysis and Oxidative Stress.” *Nutrition & Metabolism* 21(1): 12. https://nutritionandmetabolism.biomedcentral.com/articles/10.1186/s12986-024-00784-1.

Zhao, Yixin, Xu Shen, Tian Tang, and Chung-I Wu. 2017. “Weak Regulation of Many Targets Is Cumulatively Powerful—An Evolutionary Perspective on MicroRNA Functionality.” *Molecular Biology and Evolution* 34(12): 3041–46. http://academic.oup.com/mbe/article/34/12/3041/4259870.

Zhou, Ting et al. 2023. “Restoring Skeletal Muscle Mass as an Independent Determinant of Liver Fat Deposition Improvement in MAFLD.” *Skeletal Muscle* 13(1): 23. https://skeletalmusclejournal.biomedcentral.com/articles/10.1186/s13395-023-00333-z.

Zhou, Y et al. 2012. “The Betaine-GABA Transporter (BGT1, Slc6a12) Is Predominantly Expressed in

the Liver and at Lower Levels in the Kidneys and at the Brain Surface." *American journal of physiology. Renal physiology* 302(3): F316-28.

Zhu, Yuezhi, Jen Kit Tan, Sok Kuan Wong, and Jo Aan Goon. 2023. "Therapeutic Effects of MicroRNAs on Nonalcoholic Fatty Liver Disease (NAFLD) and Nonalcoholic Steatohepatitis (NASH): A Systematic Review and Meta-Analysis." *International journal of molecular sciences* 24(11).

Zhu, Zhixian et al. 2023. "In-Depth Analysis of de Novo Lipogenesis in Non-Alcoholic Fatty Liver Disease: Mechanism and Pharmacological Interventions." *Liver Research* 7(4): 285–95. https://www.sciencedirect.com/science/article/pii/S2542568423000648.

Zubiete-Franco, Imanol et al. 2016. "Methionine and S-Adenosylmethionine Levels Are Critical Regulators of PP2A Activity Modulating Lipophagy during Steatosis." *Journal of Hepatology* 64(2): 409–18. https://www.sciencedirect.com/science/article/pii/S0168827815006224.

van Zwol, Willemien, Bart van de Sluis, Henry N. Ginsberg, and Jan Albert Kuivenhoven. 2024. "VLDL Biogenesis and Secretion: It Takes a Village." *Circulation Research* 134(2): 226–44. https://www.ahajournals.org/doi/10.1161/CIRCRESAHA.123.323284.

9. Appendix

9.1. Abbreviations

Supplementary Table 1: List of abbreviations

Abbreviation	Full name
ABAT	4-aminobytyrate aminotransferase
ACACA	acetyl-CoA carboxylase alpha
ACC1/ACACA	acetyl-CoA decarboxylase A
ACC2/ACACB	acetyl-CoA decarboxylase B
ACLY	ATP citrate lyase
ACO1	aconitase 1
ACS	acetyl-CoA synthetase
ACSL	acyl-CoA synthetase
ACTH	adrenocorticotropic hormone
AGO	Argonaute protein
AGPAT	acylglycerolphosphate acyltransferase
AGXT	serine-glyoxylate transaminase
AID	activation-induced cytidine deaminase
ALDH5A1	aldehyde dehydrogenase 5 family member A1
ALT	alanin aminotransferase
AMD1	adenosylmethionine decarboxylase 1
APC	adipocyte precursor cell
APOBEC	apolipoprotein B mRNA-editing enzyme complex
ARG1	argniase 1
ASL	argininosuccinate lyase
ASS1	argininosuccinate synthase 1
AST	aspartate aminotransferase
AT	adipose tissue
ATP	adenosyl triphosphate
BAT	brown adipose tissue
BeAT	beige adipose tissue
BGT1	betaine/GABA transporter 1
BHMT	betaine homocysteine methyltransferase
bisDNA	bisulfite-converted DNA
bisPCR	bisulfite PCR
BMI	body mass index
BSA	bovine serum albumin
CBS	cystathionine beta synthase
CD36	cluster of differentiation 36
ChIP	chromatin immunoprecipitation
ChREBP	carbohydrate response element binding protein
CIC	citrate-isocitrate carrier
CO2	carbon dioxide
CoNI	correlation oriented network integration
CPS1	carbamoylphsophate synthetase 1
cr	caloric restriction

CS	citrate synthase
CTH	cystathionine gamma lyase
CTL4	choline transporter-like protein 4
DAG	diacylglycerol
DEG	differentially expressed gene
DEM	differentially enriched metabolite
DGAT	acyl-CoA :diacylglycerol transferase
DHFR	dihydrofolate reductase
DIO	diet-induced obesity
DLAT	dihydrolipoyl transacetylase
DMR	differentially methylated region
DNA	deoxyribonucleic acid
DNL	de novo lipogenesis
DNMT	DNA methyltransferase
ECH	enoyl-CoA hydratase
ELOVL	fatty acid elongase
ex-4	exendin 4
FABP	fatty acid binding protein
FASN	fatty acid synthase
FATP2	fatty acid transport protein 2
FATP5	fatty acid transport protein 5
FFA	free fatty acid
FH1	fumarate hydratase 1
G3P	glycerol-3-phosphate
GABA	gamma-aminobutyric acid
GCLC	glutamate-cysteine ligase catalytic subunit
GCLM	glutamate-cysteine ligase modifier subunit
GIP	glucose-dependent insulinotropic polypeptide
GLP-1	glucagon-like peptide 1
GLS2	glutaminase 2
GLUT1	glucose transporter 1
GLUT4	glucose transporter 4
GOT1	glutamic-oxaloacetic transaminase 1
GPAT	glycerol-3-phosphate acyltransferase
GPC1	glypican 1
GRID1	glutamate receptor delta-1
GRN	gene regulatory network
HADH	3-hdydroxyacyl-CoA dehydrogenase
HbA1c	hemoglobin A1c
HCC	hepatocellular carcinoma
HCV	hepatitis C virus
hfd	high-fat diet
hsa	human
IDH1	isocitrate dehydrogenase 1
IDH2	isocitrate dehydrogenase 2
IGF1	insulin-like growth factor 1
INSR	insulin receptor
iPSC	induced pluripotent stem cell
IRS1	insulin receptor substrate 1

IRS2	insulin receptor substrate 2
KAD	keto-acid dehydrogenase
KAT	3-ketoacyl-CoA thiolase
KO	knock out
LCFA	long chain fatty acid
LCG	local controlling gene
LEP	leptin
lncRNA	long non-coding RNA
LRP6	low-density-lipoportein receptor related protein 6
LXR	liver X-receptor
lyso-P	lysophosphatidate
MASH	metabolic dysfunction-associated steatohepatitis
MASLD	metabolic dysfunction-associated steatotic liver disease
MAT1A	methionine adenosyltransferase 1 A
MC4R	melanocortin-4 receptor
MCAD	acyl-CoA dehydrogenase
MDH1	malate dehydrogenase 1
MGAT	acyl-CoA:monoacylglycerol acyltransferase
miRISC	miRNA-induced silencing complex
miRNA	micro-RNA
MLXIPL	MLX-interacting protein-like
mmu	murine
mRNA	messenger RNA
MSEA	metabolite set enrichment analysis
MSH	melanocyte-stimulating hormone
MTAP	methylthioadenosine phosphorylase
MTHFR	methylenetetrahydrofolate reductase
MTTP	microsomal triglyceride transfer protein
NADPH	nicotinamide adenine dinucleotide phosphate H (protonated)
NAFLD	non-alcoholic fatty liver disease
NASH	non-alcoholic steatohepatitis
NCD	noncommunicable disease
OGDH	2-oxoglutarate dehydrogenase complex
OTC	ornithine transcarbamylase
PAP	phosphatidate phsphohydrolase
PDC	pyruvate dehydrogenase complex
PDHA1	pyruvate dehydrogenase E1 subunit alpha 1
PH1	Primary Hyperoxaluria Type 1
piRNA	piwi-interacting RNA
PKCε	protein kinase Cε
PLCG1	phospholipase C gamma 1
PNPLA3	ptatin-like phospholipase domain-containing protein 3
PPARG	peroxisome proliferator-activated receptor gamma
PS	phosphatidate
RNA	ribonucleic acid
RNAi	RNA interference
RNAseq	RNA sequencing
ROI	region of interest
RT-qPCR	real-time quantitative polymerase chain reaction

SAH	S-adenosylhomocysteine
SAM	S-adenosylmethionine
SAT	subcutaneous adipose tissue
SDHA	succinate dehydrogenase complex flavoprotein subunit A
SHMT2	serine hydroxymethylatransferase 2
siRNA	small interfering RNA
SLC14A2	solute carrier family 14 member 2
SLC25A15	solute carrier family 25 member 15
SLC27A2	solute carrier family 27 member 2
SLC27A5	solute carrier family 27 member 5
SLC2A1	solute carrier family 2 member 1
SLC2A2	solute carrier family 2 member 2
SLC2A4	solute carrier family 2 member 4
SLC44A4	solute carrier family 44 member 4
SLC6A12	solute carrier family 6 member 12
SNP	single nucleotide polymorphism
snRNA	small nuclear RNA
SP1	specificity protein 1
SREBF1	sterol regulatory element binding transcription factor 1
SUCLA2	succinate-CoA ligase ADP-forming subunit beta
SUCLG2	succinate-CoA ligase GDP-forming subunit beta
T2D	type 2 diabetes
TAG	triacylglycerol
TCA	trichloroacetic acid cycle/ citrate cycle
TDG	thymine DNA glycosylase
TET	ten-eleven translocation family proteins
TF	transcription factor
THRb	thyroid hormone receptor beta
TNFa	tumor necrosis factor alpha
TRBP	Transactivation response element RNA-binding protein
tRNA	transfer RNA
UCD	urea cycle disorder
UCP1	uncoupling protein 1
UTR	untranslated region
VAT	visceral adipose tissue
VLCFA	very long chain fatty acid
VLDL	very-low density lipoportein
vsg	vertical sleeve gastrectomy
WAT	white adipose tissue
WGBS	whole-genome bisulfite sequencing
WHO	World Health-Organization
XPO5	exportin 5
ZNF714	zinc finger protein 714

9.2. Supplementary figures

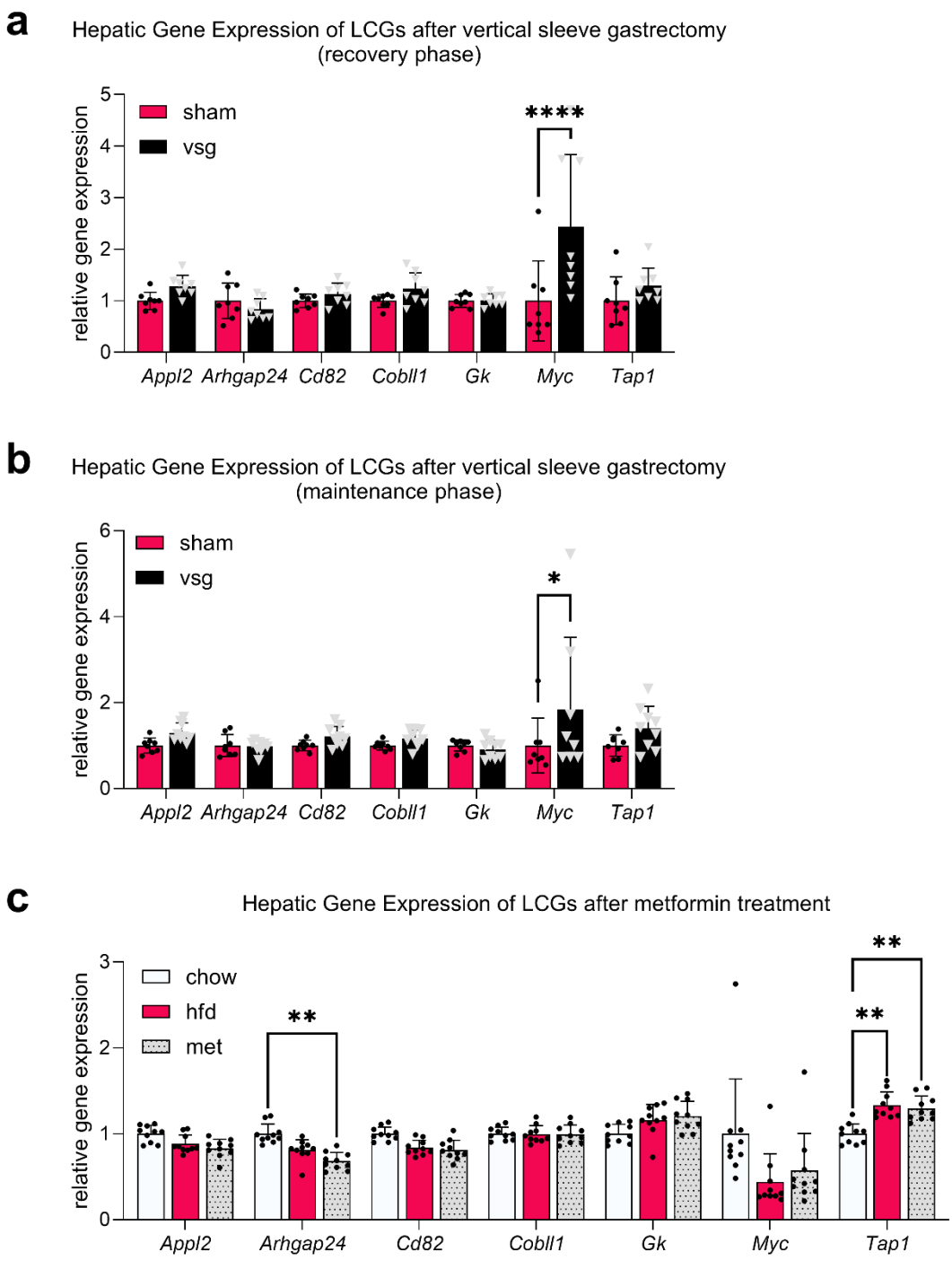

Supplementary Figure 1: Hepatic gene expression of remaining LCGs after vertical sleeve gastrectomy and metformin treatment.

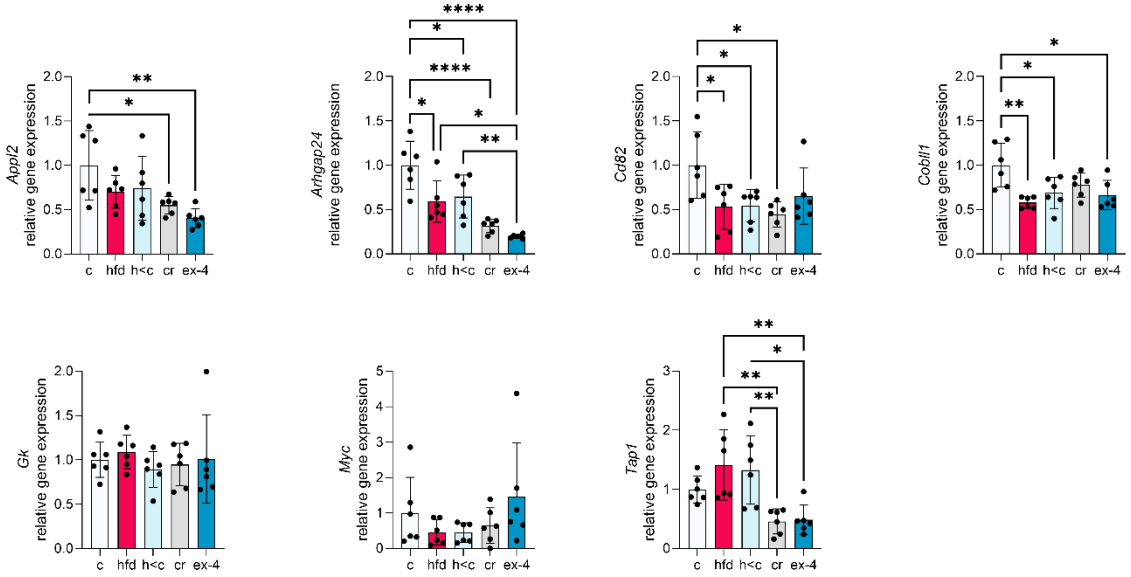

Supplementary Figure 2: Hepatic gene expression of remaining LCGs in intervention studies after diet-switch (h<c), caloric restriction (cr) and exendin-4 treatment (ex-4.)

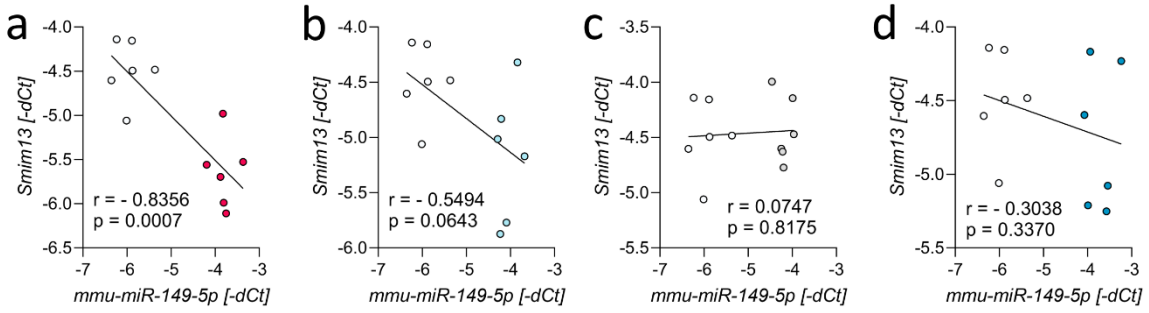

Supplementary Figure 3: Sub cohort Pearson correlation analysis from weight-loss intervention models of hepatic mmu-miR-149-5p expression with hepatic Smim13 gene expression. a: Pearson correlation of chow and hfd-fed animals. b: Pearson correlation of chow and diet-switch animals. c: Pearson correlation of chow and caloric restricted animals. d: Pearson correlation of chow and exendin-4 treated animals.

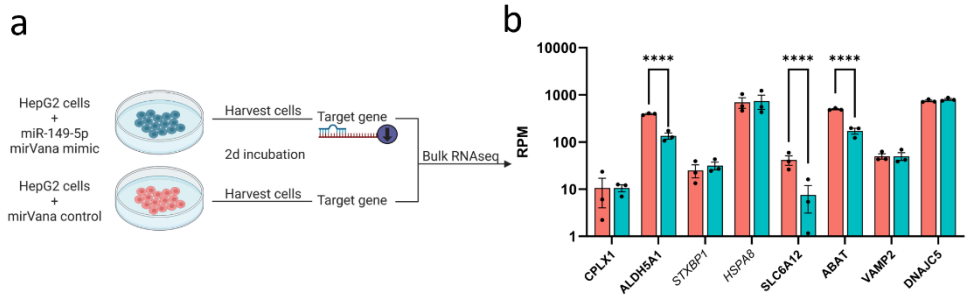

Supplementary Figure 4: Overexpression of miR-149-5p in HepG2 cells. a: Transfection protocol for miR-149-5p overexpression in HepG2 cells using mirVana mimics. b: Genes annotated to the GABA synthesis, release, reuptake and degradation REACTOME term, which are expressed in human liver (REACTOME ID: R-HSA-888590).

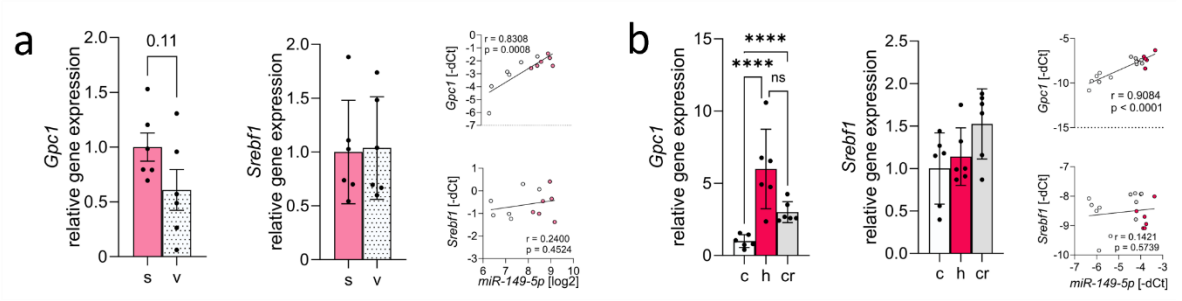

Supplementary Figure 5: Expression and Pearson correlation analysis for vsg intervention cohort and caloric restriction cohort. a: Gpc1 & Srebf1 gene expression and correlation with mmu-miR-149-5p expression in vsg and sham mice. b: Gpc1 & Srebf1 gene expression and correlation with mmu-miR-149-5p expression in caloric restricted (cr), hfd or chow (c) mice.

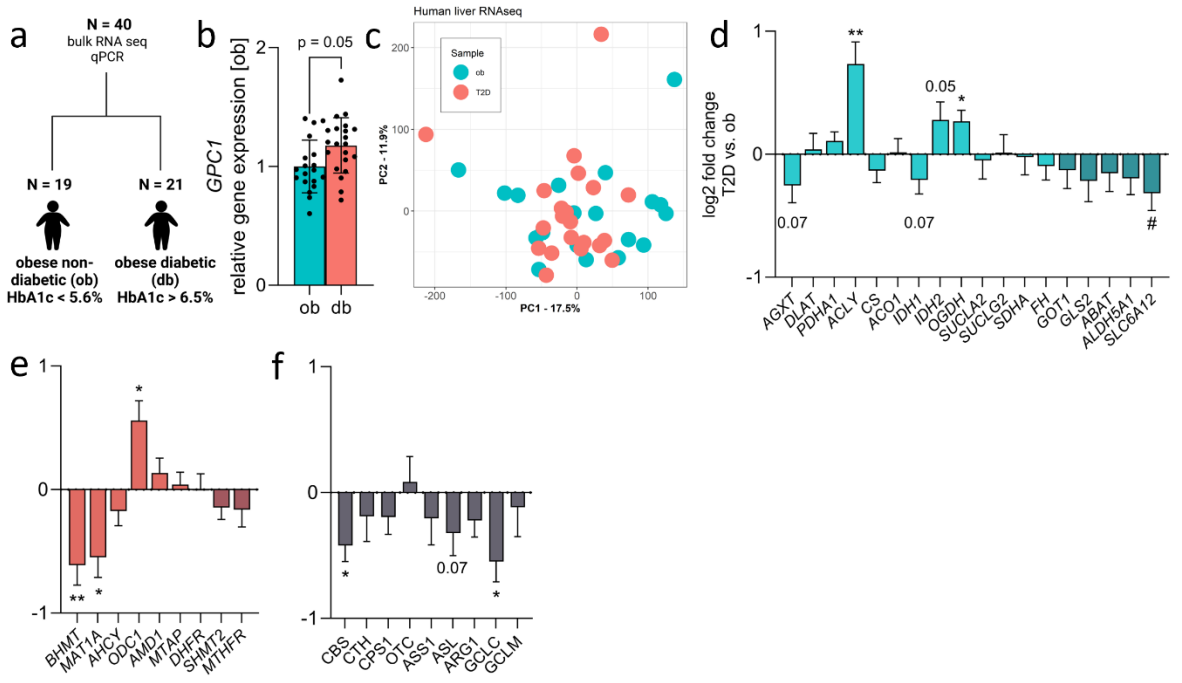

Supplementary Figure 6: Human liver cohort bulk-mRNA sequencing analysis of metabolic pathways genes. a: Cohort size and parameters according to ADA criteria. b: GPC1 gene expression from RNA sequencing data. c: Principal component analysis of bulk-mRNA sequencing. d – f: Log2 fold changes of metabolic pathway genes involved in TCA and GABA shunt (d), one-carbon metabolism (e) and urea cycle (f).

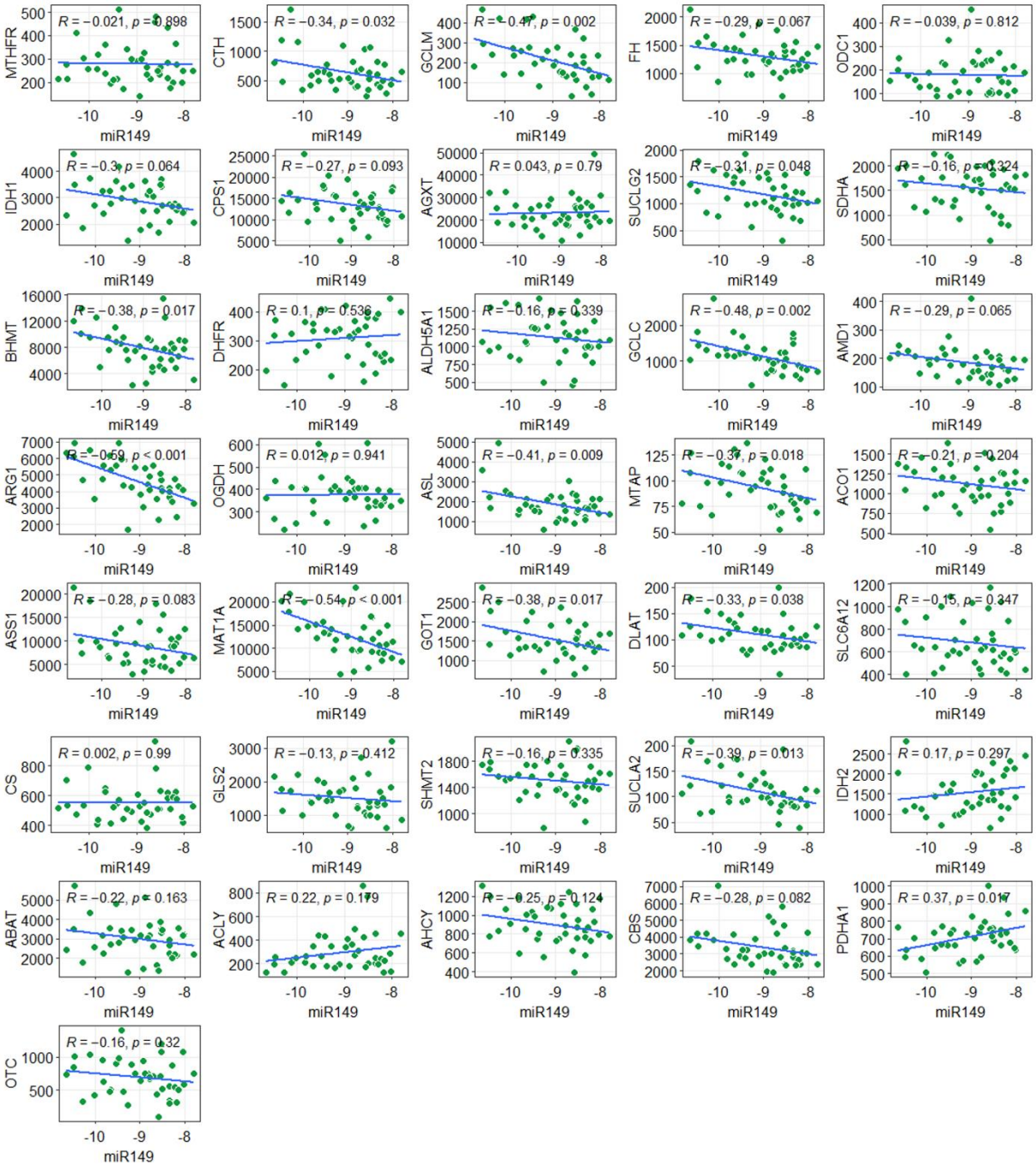

Supplementary Figure 7: Single Pearson correlations of metabolic pathway genes from mRNA-sequencing with hsa-miR-149-5p expression, which are shown in the dandelion plot Figure 27d Figure 25

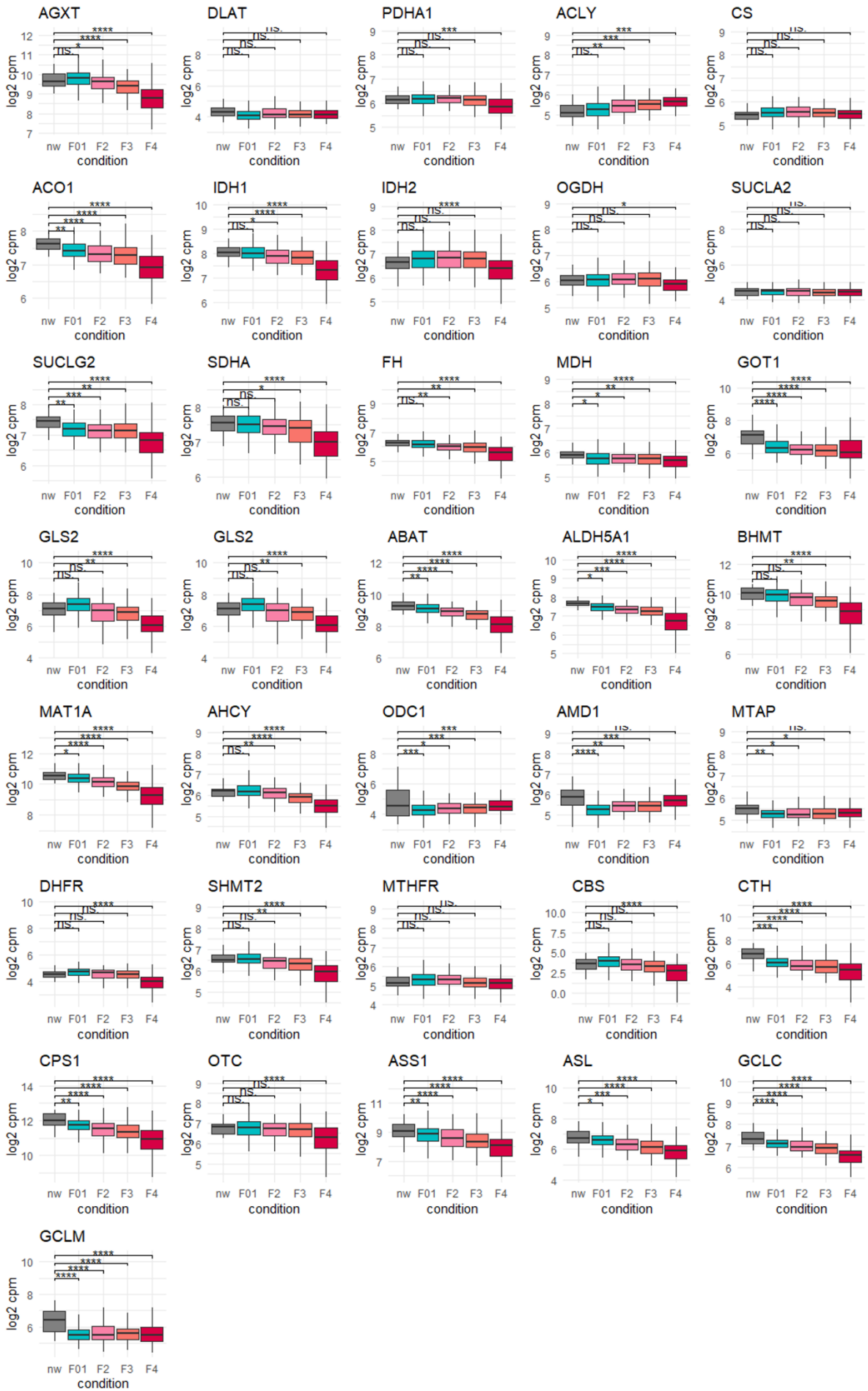
AGXT
DLAT
PDHA1
ACLY
CS
ACO1
IDH1
IDH2
OGDH
SUCLA2
SUCLG2
SDHA
FH
MDH
GOT1
GLS2
GLS2
ABAT
ALDH5A1
BHMT
MAT1A
AHCY
ODC1
AMD1
MTAP
DHFR
SHMT2
MTHFR
CBS
CTH
CPS1
OTC
ASS1
ASL
GCLC
GCLM
log2 cpm
condition
nw F01 F2 F3 F4

Supplementary Figure 8: Hepatic gene expression data of metabolic pathway genes of the SteatoSITE cohort. nw = normal weight controls, F01 = fibrosis stage 0 and 1, F2 = fibrosis stage 2, F3 = fibrosis stage 3, F4 = fibrosis stage 4.

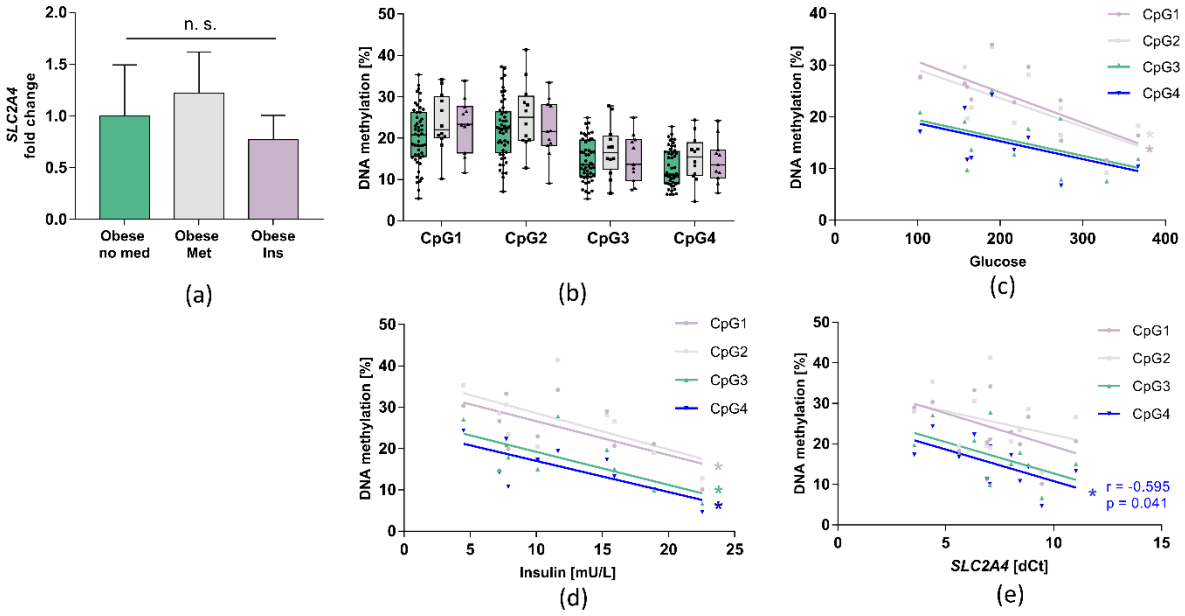

Supplementary Figure 9: Sub cohort analysis of SLC2A4 gene expression and DNA methylation in VAT of obese subjects, which receive no medication (Obese no med: n = 56), metformin (Obese Met: n = 15) or insulin (Obese Ins: n = 11). a: SLC2A4 gene expression in VAT. b: SLC2A4 DNA methylation in VAT. c: Pearson correlation of DNA methylation with basal glucose levels in Obese Ins subjects. d: Pearson correlation of DNA methylation with basal insulin levels in Obese Met subjects. e: Pearson correlation of DNA methylation with SLC2A4 gene expression in Obese Met subjects.

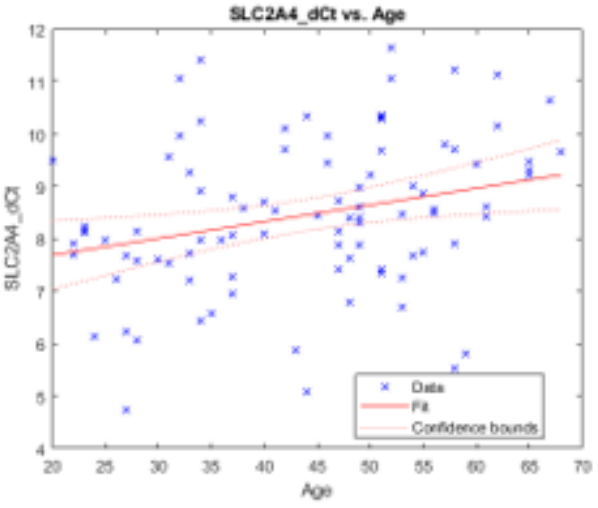

Supplementary Figure 10: Step-wise regression model excluding DNA methylation as predictor for *SLC2A4* gene expression

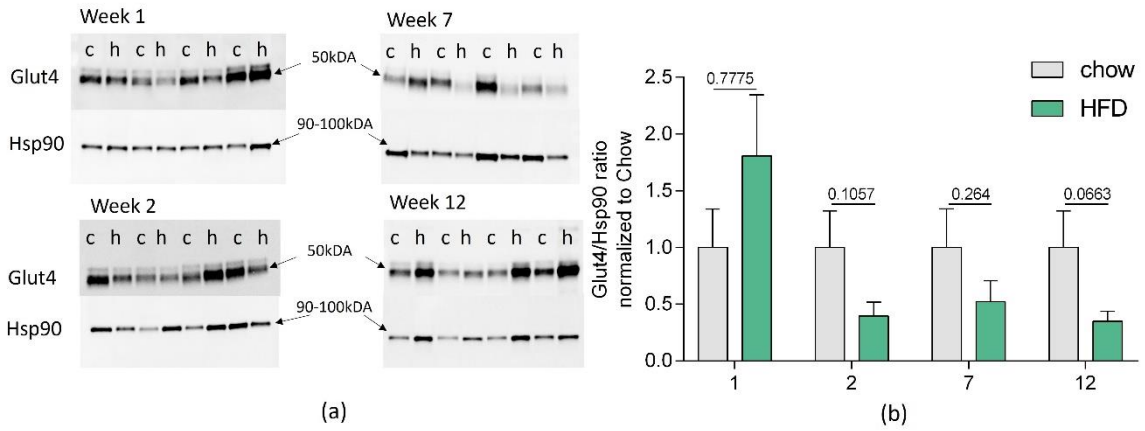

Supplementary Figure 11: Western Blot analysis of GLUT4 protein levels in VAT of chow and hfd-animals at week 1, 2, 7 and 12. a: Representative images of the HRP-signal. 4 animals per group are shown. b: Normalized GLUT4 protein levels to each chow week (n = 8).

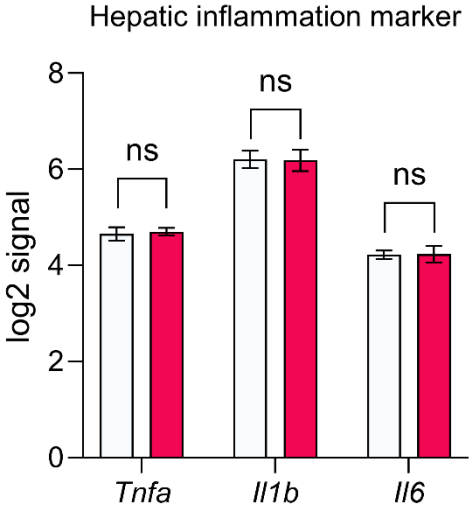

Supplementary Figure 12: Gene array signals of inflammation marker from liver of DIO mice.

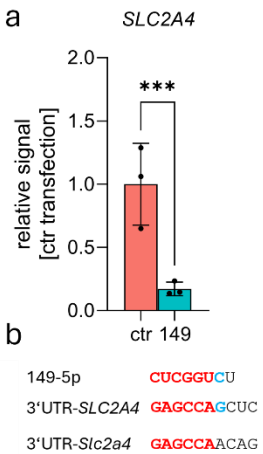

Supplementary Figure 13: SLC2A4 expression from bulk-mRNA sequencing after hsa-miR-149-5p overexpression. a: Relative reads per million normalized to control-mimic transfection. b: Seed prediction and match pairing of miR-149-5p to human (*SLC2A4*) and murine (*Slc2a4*) 3'UTR.

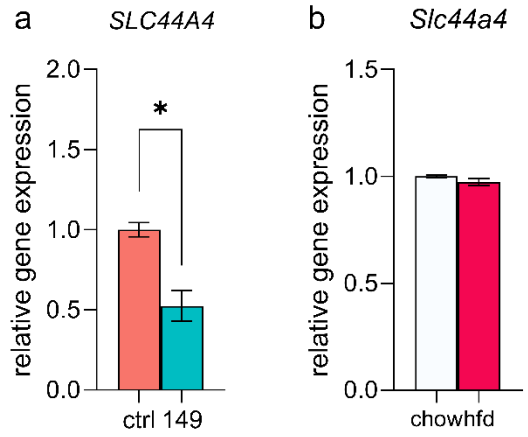

Supplementary Figure 14: Choline transporter *SLC44A4* gene expression in HepG2 cells and liver of DIO mice. a: *SLC44A4* gene expression in HepG2 cells after miR-149-5p overexpression (n = 3, mean ± SD). b: Slc44a4 gene expression in liver of DIO mice fed a hfd or standard chow diet for 12 weeks (chow: n = 7, hfd: n = 8, mean array signal normalized to chow ± SD).

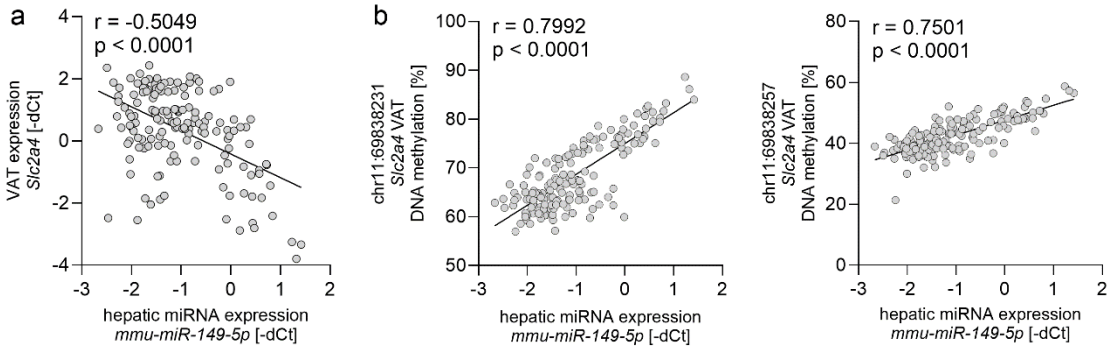

Supplementary Figure 15: Pearson correlation of hepatic mmu-miR-149-5p expression with Slc2a4 gene expression in VAT (a) and Slc2a4 DNA methylation (b). This emphasizes a potential common regulating factor of Slc2a4 gene expression and mmu-miR-149-5p expression.

9.3. Supplementary tables

Supplementary Table 2: miRNA sequences

miRNA name	Species	Sequence
mmu-miR-21a-5p	mmu	UAGCUUAUCAGACUGAUGUUGA
hsa-miR-21-5p	hsa	UAGCUUAUCAGACUGAUGUUGA
mmu-miR-149-5p	mmu	UCUGGCUCCGUGUCUUCACUCCC
hsa-miR-149-5p	hsa	UCUGGCUCCGUGUCUUCACUCCC

Supplementary Table 3: Pearson correlation of mmu-miR-149-5p expression with metabolic pathway genes from liver of DIO mice at week 12.

Gene	Pearson r	p	significant	Cycle
Dlat	-0.389	0.1692	ns	TCA
Pdha1	0.5058	0.065	ns	TCA
Aco1	-0.08805	0.7647	ns	TCA
Idh1	-0.2368	0.4151	ns	TCA
Idh2	-0.2429	0.4028	ns	TCA
Ogdh	-0.4949	0.072	ns	TCA
Sucla2	-0.2573	0.3744	ns	TCA
Suclg2	0.4704	0.0896	ns	TCA
Sdha	-0.1717	0.5573	ns	TCA
Fh1	-0.4662	0.0929	ns	TCA
Mdh1	**-0.5739**	**0.0319**	*	**TCA**
Cs	0.2835	0.326	ns	TCA
Acly	-0.09852	0.7376	ns	TCA
Agxt	**-0.8169**	**0.0004**	***	**TCA**
Got1	**-0.675**	**0.0081**	**	**GABA**
Gls2	**-0.7192**	**0.0037**	**	**GABA**
Abat	**-0.8317**	**0.0002**	***	**GABA**
Aldh5a1	**-0.7678**	**0.0013**	**	**GABA**
Slc6a12	**-0.8658**	**<0,0001**	****	**GABA**
Cbs	**-0.6111**	**0.0203**	*	**urea**
Cth	**-0.7601**	**0.0016**	**	**urea**
Cps1	**-0.8537**	**0.0001**	***	**urea**
Otc	**-0.5499**	**0.0416**	*	**urea**
Ass1	**-0.7237**	**0.0034**	**	**urea**
Asl	**-0.6916**	**0.0061**	**	**urea**
Arg1	**-0.6315**	**0.0154**	*	**urea**
Bhmt	0.5289	0.0518	ns	methionine
Mat1a	-0.1223	0.6769	ns	methionine
Ahcy	**-0.8327**	**0.0002**	***	**methionine**
Odc1	**0.7031**	**0.005**	**	**methionine**
Amd1	0.1334	0.6495	ns	methionine
Mtap	0.0954	0.7456	ns	methionine
Dhfr	-0.09914	0.736	ns	folate
Shmt2	0.1819	0.5336	ns	folate
Mthfr	0.2577	0.3738	ns	folate

Supplementary Table 4: Data sets of ChIP-sequencing from ENCODE

ChIP-Type	Accession ID	Cell type
SREBF1	GSM935627	HepG2
PPARG	GSE95940	HepG2
H3K4me1	GSM798321	HepG2
H3K4me3	GSE96248	HepG2
SP1	GSE104247	HepG2

Supplementary Table 5: Top 50 significant differentially expressed genes after hsa-miR-149-5p overexpression in HepG2 cells sorted ascending by padj

GeneName	baseMean	log2FoldChange	lfcSE	stat	pvalue	padj
AKAP12	1648.942	2.624562	0.166463	15.76664	5.28E-56	5.93E-52
PEG3	1268.697	-3.44749	0.219166	-15.73	9.42E-56	5.93E-52
ANKRD1	1840.559	2.465829	0.180266	13.67882	1.36E-42	5.71E-39
EBP	277.153	-3.20641	0.244953	-13.0899	3.76E-39	1.19E-35
SHMT2	299.9403	-2.63364	0.209748	-12.5562	3.67E-36	9.26E-33
SAT1	2456.928	1.941428	0.155433	12.49045	8.42E-36	1.77E-32
IER3	4053.553	2.138736	0.17154	12.46787	1.12E-35	2.01E-32
XXbac-BPG252P9.10	3896.998	2.125231	0.171415	12.39818	2.67E-35	4.21E-32
SOX4	957.0548	2.111385	0.184504	11.44355	2.53E-30	3.55E-27
KRTAP3-1	96.29352	4.480333	0.394516	11.35653	6.88E-30	8.67E-27
MT2A	3376.319	2.216816	0.199618	11.10531	1.18E-28	1.35E-25
JAG1	696.3268	2.215361	0.200773	11.03416	2.61E-28	2.75E-25
CLDN1	449.4094	2.331612	0.218757	10.65845	1.59E-26	1.54E-23
MET	223.3122	2.59506	0.248028	10.46276	1.28E-25	1.15E-22
KRT19	3103.909	1.899734	0.19053	9.970782	2.05E-23	1.72E-20
RBP1	188.4491	2.595456	0.264865	9.799169	1.14E-22	8.94E-20
MARCKSL1	210.9086	-2.79291	0.285702	-9.7756	1.43E-22	1.06E-19
NABP1	193.573	2.263719	0.235049	9.630823	5.93E-22	3.93E-19
TRIB1	626.1589	1.766855	0.183366	9.635688	5.65E-22	3.93E-19
RNASEH1	194.4042	-2.29682	0.24034	-9.55655	1.22E-21	7.67E-19
STRADB	91.99085	-3.31061	0.346644	-9.55048	1.29E-21	7.75E-19
RHOB	1101.5	1.680442	0.17617	9.538761	1.45E-21	8.28E-19
ODAM	98.92733	-2.96496	0.314104	-9.43942	3.75E-21	2.05E-18
NKD1	513.3187	-1.97583	0.209626	-9.42548	4.28E-21	2.25E-18
TRNP1	559.3015	1.82342	0.195166	9.342929	9.37E-21	4.72E-18
S100A6	624.8271	1.912638	0.205376	9.312879	1.24E-20	6.03E-18
CPLX2	181.8452	-2.31727	0.250212	-9.2612	2.02E-20	9.43E-18
RALBP1	196.2213	-2.38367	0.25868	-9.21476	3.12E-20	1.4E-17
FADS1	606.6627	-1.85125	0.201856	-9.17116	4.68E-20	2.03E-17
GUCD1	261.1107	-2.29906	0.251893	-9.12715	7.03E-20	2.95E-17
EFNA1	332.3126	-1.88363	0.209186	-9.00456	2.17E-19	8.8E-17
OGFR	235.523	-2.37858	0.267261	-8.89984	5.59E-19	2.2E-16
ERBB3	292.3478	-1.96939	0.223714	-8.80316	1.33E-18	5.08E-16
THYN1	121.0619	-2.50145	0.285699	-8.75555	2.03E-18	7.53E-16
S100A16	714.6792	1.791141	0.205136	8.731466	2.51E-18	9.05E-16
TIMP1	259.8067	1.986325	0.230145	8.630748	6.1E-18	2.13E-15
SQRDL	139.8881	2.323913	0.272422	8.530577	1.46E-17	4.78E-15
CTCF	437.0277	-1.75736	0.205972	-8.532	1.44E-17	4.78E-15
KRT23	179.5476	2.382014	0.279292	8.528757	1.48E-17	4.78E-15
MCL1	967.7176	2.362487	0.278037	8.497014	1.95E-17	6.13E-15
KAT6A	210.4136	-2.06317	0.244605	-8.43472	3.32E-17	1.02E-14
SH3RF1	193.7432	2.004705	0.238294	8.412742	4.01E-17	1.2E-14
PSIP1	173.589	-1.99306	0.237249	-8.4007	4.44E-17	1.3E-14
EPB41	102.4034	-2.43066	0.28947	-8.39692	4.58E-17	1.31E-14
FAM32A	444.3112	1.589411	0.189477	8.388424	4.93E-17	1.38E-14
TBL1X	387.6469	-1.55463	0.18545	-8.38305	5.16E-17	1.41E-14

ITGA2	435.7174	1.621705	0.193616	8.375899	5.48E-17	1.47E-14
PCSK9	140.8646	-2.72578	0.328253	-8.3039	1.01E-16	2.64E-14
BEX1	347.8344	-1.57939	0.190754	-8.27969	1.23E-16	3.18E-14
RPIA	172.2659	-2.13863	0.258394	-8.27662	1.27E-16	3.19E-14

Supplementary Table 6: Statistics of genes from metabolic pathways after hsa-miR-149-5p overexpression in HepG2 cells

GeneName	baseMean	log2FoldChange	lfcSE	stat	pvalue	padj
AGXT	45.42337	-1.259893	0.4289	-2.9377	3.31E-03	2.93E-02
DLAT	183.02551	0.404031	0.2798	1.4439	1.49E-01	3.90E-01
PDHA1	368.85132	0.146470	0.2087	0.7019	4.83E-01	7.33E-01
ACLY	745.57794	-0.860555	0.1676	-5.1337	2.84E-07	1.16E-05
CS	519.64534	-0.063973	0.2030	-0.3151	7.53E-01	8.95E-01
ACO1	257.64419	-0.114766	0.2156	-0.5324	5.94E-01	8.09E-01
IDH1	1466.22462	-1.345418	0.2353	-5.7190	1.07E-08	6.37E-07
IDH2	277.65277	-1.285321	0.2109	-6.0945	1.10E-09	8.23E-08
OGDH	155.42815	0.690580	0.2608	2.6474	8.11E-03	5.57E-02
SUCLA2	63.42587	-0.210543	0.3147	-0.6690	5.04E-01	7.47E-01
SUCLG2	210.25026	0.609787	0.2695	2.2625	2.37E-02	1.19E-01
SDHA	231.06834	0.196447	0.2187	0.8981	3.69E-01	6.44E-01
MDH1	843.97541	-0.275115	0.1710	-1.6085	1.08E-01	3.20E-01
GOT1	453.89314	0.731589	0.1849	3.9570	7.59E-05	1.40E-03
GLS2	37.33002	-0.178751	0.4293	-0.4164	6.77E-01	8.54E-01
ABAT	330.82993	-1.538140	0.2253	-6.8261	8.73E-12	1.07E-09
ALDH5A1	260.95777	-1.541427	0.2298	-6.7070	1.99E-11	2.16E-09
SLC6A12	24.11471	-2.493992	0.6627	-3.7633	1.68E-04	2.64E-03
MAT1A	419.02305	-1.190274	0.1867	-6.3745	1.84E-10	1.58E-08
AHCY	715.88583	-0.249229	0.2120	-1.1754	2.40E-01	5.13E-01
ODC1	1000.41253	0.608857	0.2272	2.6802	7.36E-03	5.23E-02
MTAP	99.74858	1.769319	0.3381	5.2333	1.67E-07	7.11E-06
DHFR	105.71074	-1.126933	0.2739	-4.1148	3.87E-05	7.91E-04
SHMT2	299.94031	-2.633645	0.2097	-12.5562	3.67E-36	9.26E-33
MTHFR	18.16532	-0.695547	0.6077	-1.1446	2.52E-01	5.28E-01
CBS	259.1426	-0.606473	0.2186	-2.7743	5.53E-03	4.26E-02
CTH	23.28822	0.517428	0.5476	0.9449	3.45E-01	6.22E-01
CPS1	53.83854	-0.592172	0.3894	-1.5208	1.28E-01	3.55E-01
ASS1	110.83492	-0.419818	0.2823	-1.4871	1.37E-01	3.71E-01
ASL	151.14567	0.079240	0.2756	0.2875	7.74E-01	9.06E-01
GCLC	164.34417	0.276427	0.2245	1.2315	2.18E-01	4.85E-01
GCLM	157.08101	0.173200	0.2484	0.6972	4.86E-01	7.35E-01

Supplementary Table 7: Top 50 significant differentially expressed genes from liver of obese subjects with and without type 2 diabetes sorted ascending by padj

GeneName	baseMean	log2FoldChange	lfcSE	stat	pvalue	padj
PADI1	27.0121	5.366996	0.736743	7.284759	3.22E-13	4.6E-09
FABP4	58.17636	2.528824	0.348557	7.255117	4.01E-13	4.6E-09
EEF1A2	13.97517	5.138419	0.721871	7.1182	1.09E-12	8.36E-09

CYP2C19	1037.692	-1.33769	0.189253	-7.06827	1.57E-12	8.99E-09
PHLDA3	30.94956	1.866997	0.265571	7.030131	2.06E-12	9.46E-09
DPPA4	9.184489	-1.49557	0.219431	-6.81568	9.38E-12	3.58E-08
ITGBL1	52.84738	2.421908	0.365317	6.629609	3.37E-11	1.1E-07
MROH7	53.62721	-1.80926	0.277549	-6.51871	7.09E-11	2.03E-07
THY1	49.71046	2.197098	0.341009	6.442936	1.17E-10	2.98E-07
LPL	12.4118	3.118516	0.508656	6.130895	8.74E-10	1.82E-06
COL1A1	536.1491	1.715356	0.279266	6.142373	8.13E-10	1.82E-06
SUSD2	23.23813	1.67165	0.279619	5.978307	2.25E-09	4.31E-06
DCDC1	94.10695	-1.07222	0.180124	-5.95267	2.64E-09	4.65E-06
RP11-334E6.12	12.13986	2.172266	0.367697	5.907759	3.47E-09	5.68E-06
ANXA2	404.1442	1.16563	0.198658	5.867531	4.42E-09	6.76E-06
LOXL4	44.93499	2.032911	0.347439	5.851136	4.88E-09	7E-06
PTPRD	115.4798	-0.94465	0.162245	-5.82237	5.8E-09	7.48E-06
RP11-442H21.2	121.3268	1.463839	0.2515	5.820437	5.87E-09	7.48E-06
DDIT4	185.9782	1.49314	0.258323	5.780119	7.46E-09	9.01E-06
CYP2C8	21978.82	-0.81971	0.143137	-5.72675	1.02E-08	1.17E-05
ACHE	27.90937	1.745865	0.305623	5.712482	1.11E-08	1.22E-05
SH3PXD2A	962.168	-1.21084	0.213086	-5.68238	1.33E-08	1.38E-05
AEBP1	363.736	1.478489	0.262779	5.626369	1.84E-08	1.76E-05
LOXL1	14.48549	1.935159	0.343863	5.627705	1.83E-08	1.76E-05
FAM129B	207.4255	0.860318	0.153625	5.60012	2.14E-08	1.96E-05
COL1A2	492.9334	1.489214	0.266796	5.581844	2.38E-08	1.97E-05
STMN2	15.5085	4.764692	0.853903	5.5799	2.41E-08	1.97E-05
DERL3	51.10171	1.415994	0.253246	5.591372	2.25E-08	1.97E-05
ZMAT3	107.3304	1.220401	0.219413	5.562109	2.67E-08	2.11E-05
NIPAL2	81.95443	0.767952	0.138373	5.549853	2.86E-08	2.18E-05
DPYSL2	265.319	0.882994	0.159731	5.528014	3.24E-08	2.4E-05
C9orf66	3.078708	3.059645	0.55567	5.506228	3.67E-08	2.63E-05
TREM2	13.04061	3.202073	0.588073	5.445024	5.18E-08	3.57E-05
WFDC2	8.152781	1.751603	0.321912	5.441249	5.29E-08	3.57E-05
ZCCHC9	205.0217	-0.52464	0.097574	-5.37688	7.58E-08	4.96E-05
LGALS3	114.0435	1.195276	0.223432	5.349608	8.81E-08	5.61E-05
RP11-465B22.3	15.84272	1.563045	0.293544	5.324731	1.01E-07	6.26E-05
CYP3A43	366.9282	-1.23329	0.233022	-5.2926	1.21E-07	7.28E-05
MOXD1	17.16526	2.271748	0.431472	5.265105	1.4E-07	8.24E-05
AACS	48.27708	1.012513	0.193555	5.231145	1.68E-07	9.66E-05
DOCK8	79.10639	1.09832	0.210316	5.222244	1.77E-07	9.88E-05
ANXA2P2	169.8592	1.252594	0.241323	5.190532	2.1E-07	0.000114
EFEMP1	81.68256	1.867326	0.36044	5.180678	2.21E-07	0.000118
ADCY10	92.25608	-0.8391	0.162106	-5.17622	2.26E-07	0.000118
THBS2	100.7035	1.655497	0.320454	5.166104	2.39E-07	0.000122
MIR4435-1HG	27.02369	1.496381	0.290384	5.153115	2.56E-07	0.000128
AEN	64.70497	1.075538	0.209598	5.131424	2.88E-07	0.00014
COL4A2	247.2768	1.381265	0.269543	5.124469	2.98E-07	0.000143
SNTB1	987.0485	-0.51549	0.100839	-5.11206	3.19E-07	0.000143
RP11-612B6.2	128.8124	-0.53425	0.104458	-5.11447	3.15E-07	0.000143

Supplementary Table 8: Statistics of genes from metabolic pathways in liver of obese subjects with and without type 2 diabetes

GeneName	baseMean	log2FoldChange	lfcSE	stat	pvalue	padj
AGXT	23147.01973	-0.253530	0.140397	-1.805804	0.070949	0.265176
DLAT	109.28871	0.038222	0.131869	0.289849	0.771932	0.900587
PDHA1	706.43851	0.107689	0.073852	1.458167	0.144794	0.394268
ACLY	290.85293	0.732488	0.179769	4.074605	0.000046	0.003387
CS	549.13182	-0.134515	0.096566	-1.392990	0.163623	0.422637
ACO1	1111.77128	0.015320	0.111481	0.137425	0.890695	0.955596
IDH1	2841.07122	-0.207859	0.115293	-1.802870	0.071409	0.266229
IDH2	1524.5839	0.279304	0.146162	1.910924	0.056014	0.231860
OGDH	372.5426	0.266980	0.091020	2.933215	0.003355	0.044098
SUCLA2	108.21795	-0.050297	0.151420	-0.332169	0.739762	0.885543
SUCLG2	1163.46965	0.012694	0.146926	0.086398	0.931150	0.973245
SDHA	1542.42308	-0.024022	0.143455	-0.167453	0.867013	0.946499
MDH1	873.16613	0.073964	0.111131	0.665554	0.505696	0.745181
GOT1	1525.77526	-0.129971	0.148878	-0.873005	0.382661	0.650386
GLS2	1503.90994	-0.216966	0.168635	-1.286602	0.198233	0.467885
ABAT	2958.28778	-0.153432	0.150306	-1.020794	0.307352	0.586682
ALDH5A1	1118.77422	-0.196447	0.131622	-1.492514	0.135565	0.380347
SLC6A12	677.86418	-0.317336	0.139737	-2.270943	0.023150	0.139664
BHMT	7933.5601	-0.613597	0.161069	-3.809525	0.000139	0.006461
MAT1A	12529.77218	-0.549420	0.161287	-3.406473	0.000658	0.016327
AHCY	892.02588	-0.174868	0.117613	-1.486814	0.137064	0.382587
ODC1	175.85613	0.558540	0.159012	3.512558	0.000444	0.013083
MTAP	92.10549	0.040095	0.100328	0.399638	0.689423	0.859295
DHFR	305.25704	0.003665	0.123346	0.029711	0.976298	0.990806
SHMT2	1494.79534	-0.145877	0.096995	-1.503962	0.132591	0.375312
MTHFR	277.70364	-0.162949	0.140754	-1.157687	0.246992	0.525600
CBS	3364.28411	-0.421814	0.126733	-3.328380	0.000874	0.019442
CTH	638.62383	-0.189513	0.199535	-0.949775	0.342227	0.617954
CPS1	13411.55545	-0.194873	0.137077	-1.421626	0.155135	0.410654
OTC	682.30011	0.084070	0.201284	0.417666	0.676191	0.852631
ASS1	8973.75885	-0.204302	0.212802	-0.960055	0.337027	0.613300
ASL	1858.41893	-0.322620	0.179230	-1.800038	0.071855	0.267094
ARG1	4564.35961	-0.222596	0.131669	-1.690579	0.090917	0.302590
GCLC	1126.4446	-0.547942	0.161617	-3.390371	0.000698	0.016897
GCLM	208.69035	-0.116346	0.234068	-0.497060	0.619147	0.819541

Supplementary Table 9: Top 50 significant differentially expressed genes from week 12 livers of DIO mice sorted ascending by FDR adjusted p-val

Gene Symbol	Linear Fold Change	P-val	FDR P-val
Stap1	5.585395	1.04E-18	6.85E-14
Ces2a	-5.80877	5.14E-15	8.47E-11
Fabp2	4.172964	4.41E-15	8.47E-11
Cyp2b9	1033.702	3.73E-15	8.47E-11
Gpc1	2.810412	7.41E-15	9.78E-11

Agpat9	2.209734	9.74E-15	1.03E-10
Cd36	9.041596	1.10E-14	1.03E-10
Slc13a2	-3.034302	2.33E-14	1.92E-10
Vnn1	23.03889	7.49E-14	5.49E-10
Themis	4.683929	1.01E-13	6.64E-10
Adgrf1	-23.76655	1.44E-13	6.79E-10
Gstp2	-3.745286	1.22E-13	6.79E-10
Gstp1	-3.713239	1.40E-13	6.79E-10
Itih5	-2.68555	1.94E-13	8.51E-10
Ccl9	-3.257534	6.30E-13	2.60E-09
Lect2	2.338962	9.80E-13	3.80E-09
Cyp3a16	-2.915349	1.41E-12	5.00E-09
Mogat1	1.854893	1.44E-12	5.00E-09
Ech1	1.731583	2.50E-12	7.86E-09
Slco2a1	-3.414843	3.46E-12	1.04E-08
Cyp3a41b; Cyp3a41a	-4.247314	3.62E-12	1.04E-08
Myh10	-1.725698	5.01E-12	1.38E-08
Mfsd2a	43.02732	5.36E-12	1.41E-08
Gm3934	-3.468428	6.39E-12	1.62E-08
Cyp3a11	-5.263453	6.81E-12	1.66E-08
Csad	-10.21818	7.80E-12	1.71E-08
Acpp	-2.203163	8.04E-12	1.71E-08
Ctse	1.912286	8.00E-12	1.71E-08
Bdh1	2.001182	7.43E-12	1.71E-08
Cyp3a41a; Cyp3a41b	-4.115294	8.84E-12	1.74E-08
Pnldc1	2.100471	8.97E-12	1.74E-08
Samd9l	2.240238	8.97E-12	1.74E-08
Tpm2	1.682786	9.53E-12	1.79E-08
1810055G02Rik	4.149409	1.04E-11	1.91E-08
Irf6	-2.202884	1.13E-11	2.01E-08
Cyp3a44	-3.957213	1.25E-11	2.17E-08
Hmgcs2	1.662681	1.47E-11	2.49E-08
Cyp2c55	-6.470305	1.53E-11	2.53E-08
Acot2	6.760123	1.87E-11	3.01E-08
Pex11a	3.377643	2.14E-11	3.36E-08
Pdzrn3	2.20983	3.20E-11	4.91E-08
Eci1	1.918575	4.00E-11	6.00E-08
Vwa8	2.14711	4.56E-11	6.69E-08
Cdh1	-3.81363	8.27E-11	1.16E-07
Cyp2c70	-3.063162	8.23E-11	1.16E-07
Acmsd	-5.897377	8.98E-11	1.21E-07
Mgll	2.835695	8.91E-11	1.21E-07
Pctp	2.786451	1.04E-10	1.37E-07
C730002L08Rik	3.335368	1.21E-10	1.56E-07
Gm20262	4.831977	1.23E-10	1.56E-07

Supplementary Table 10: Top 50 significant intracellular metabolites measured in LC-MS/MS from HepG2 cells overexpressing hsa-miR-149-5p sorted ascending by padj

Metabolite	log2FoldChange	pval	padj
Ornithine	1.0402	0.00068616	0.023558
1-Methylhistidine	0.59493	0.00067668	0.023558
Uridine	1.8581	0.00024987	0.023558
Pseudouridine	0.85248	0.001561	0.040195
3-Methylhistidine	0.42612	0.0019756	0.040697
N-Acetylglutamic acid	-0.38899	0.0025081	0.043056
Trimethyllysine	0.76263	0.0039964	0.058804
Isoleucine	0.61965	0.0066606	0.085755
Methionine sulfoxide	0.24017	0.0096519	0.11046
Citrulline	0.6002	0.010972	0.11301
Octanoylcarnitine	0.74793	0.013911	0.13026
Serine	-0.32523	0.028933	0.14191
Riboflavin	0.50243	0.028677	0.14191
Pyridoxine	0.25278	0.028501	0.14191
Nicotinamide	1.4963	0.028072	0.14191
Symmetric dimethylarginine	0.71237	0.026657	0.14191
Hypoxanthine	3.2096	0.025111	0.14191
Lysine	0.48979	0.024994	0.14191
Urate	0.62091	0.022247	0.14191
Prolylleucine	0.35013	0.019684	0.14191
Xanthine	0.22449	0.017806	0.14191
3-(4-Hydroxyphenyl)lactate	0.72211	0.030939	0.14485
Phosphocholine	0.33088	0.040596	0.16082
Urea	0.41587	0.040445	0.16082
Ureidopropionic acid	1.3784	0.039801	0.16082
Asymmetric dimethylarginine	0.39931	0.038372	0.16082
Carnosine	0.49743	0.044658	0.16428
Decanoylcarnitine	1.0473	0.043979	0.16428
Asparagine	0.56204	0.048206	0.17122
Palmitoylcarnitine	0.97357	0.049887	0.17128
Lauroylcarnitine	1.0709	0.06076	0.19557
Glycine	0.14556	0.058915	0.19557
Lactate	0.3072	0.06799	0.20597
Histidine	0.25642	0.066386	0.20597
Glutamyl-glutamine	-1.1959	0.073921	0.21754
Glutathione	0.34879	0.084609	0.24208
Pyridoxic acid	0.57702	0.094955	0.26434
Oxoproline	0.27791	0.10738	0.26975
Glutamic acid	0.21199	0.10607	0.26975
C6 sugar alcohol	0.65954	0.10497	0.26975
Leucylproline	0.4459	0.10065	0.26975
Alanine	0.32312	0.11542	0.27019
Aspartate	-0.39448	0.11376	0.27019
Adenosine	0.31782	0.1113	0.27019
Thiamine	0.36338	0.1233	0.27608
Acetylcarnitine	-0.57213	0.1233	0.27608

Acetylarginine	0.35451	0.12946	0.2837
Uridinediphospho-N-acetylglucosamine	-1.4303	0.13253	0.28439
Leucine	0.48207	0.14061	0.29556
Amino(iso)butyric acid	0.25561	0.15793	0.32534

Supplementary Table 11 Top 50 significant extracellular metabolites measured in LC-MS/MS from HepG2 cells overexpressing hsa-miR-149-5p sorted ascending by pval

Metabolite	Log2FoldChange	pval
Glycitein	-0.33319	0.0006884
Folic Acid	-1.2917	0.0085815
Pseudouridine	-0.37721	0.0087838
Putrescine	0.4536	0.012688
Choline	0.46784	0.017545
Xanthine	-0.36248	0.021886
Urate	-0.72897	0.023191
Malate	-0.090476	0.027302
Carnosine	0.24918	0.030514
5'-Methylthioadenosine	-0.54104	0.031613
Xanthosine	-0.42104	0.033492
Daidzein	-0.21293	0.033542
Palmitoyl sphingomyelin	-0.32155	0.039987
Phenylalanine	-0.15601	0.055098
C6 sugar alcohol	0.49311	0.064683
Acetylcarnitine	0.12916	0.073001
Butyrylcarnitine	-0.40256	0.086354
N-Acetylcytidine	-0.2191	0.087143
Histidine	-0.085247	0.08734
Succinate	0.18604	0.098547
Trimethylamine N-oxide	-0.18595	0.10125
Biotin	-0.58685	0.1043
Decanoylcarnitine	0.28166	0.11492
Pantothenic acid	-0.1902	0.11819
Riboflavin	-0.21012	0.13465
C5H12O5	-0.12496	0.13843
Kynurenic acid	-0.39182	0.13854
Valine	0.155	0.14536
Allantoin	0.25594	0.16114
Propionylcarnitine	-0.41657	0.16331
Serine	-0.26441	0.17391
Indoxyl sulfate	-0.15736	0.17902
7-Methylguanine	-0.18339	0.18463
Pyridoxamine	-0.2661	0.19746
Adenine	0.11958	0.23368
Deoxyinosine	-0.33296	0.24966
N-Acetylaspartic acid	-0.21377	0.25449
Glutamic acid	0.20858	0.25609
Glutamine	-0.14183	0.26009
Pyridoxine	-0.10715	0.26559

Glycolate	-0.08991	0.29305
Phosphocholine	-0.14141	0.3093
3-Hydroxy-3-methylglutarate	-0.14696	0.33074
Methionine sulfoxide	0.60473	0.35146
Asymmetric dimethylarginine	-0.10591	0.35387
Glycerophosphocholine	-0.11304	0.37046
Hydroxyglutaric acid	0.40156	0.39142
Pyruvate	-0.61662	0.39594
Citrulline	-0.10699	0.40437
Asparagine	0.16148	0.40488

Supplementary Table 12: Top 50 significant metabolites measured in LC-MS/MS from livers of DIO mice

Metabolite	**log2FoldChange**	**pval**	**pajusted**
Trigonelline	-9.2233	0.0001554	0.0012432
Stachydrine	-7.7677	0.0001554	0.0012432
Equol	-7.1712	0.0001554	0.0012432
Ergothioneine	-5.6881	0.0001554	0.0012432
Guanidinobutanoate	-5.0586	0.0001554	0.0012432
Ophthalmic acid	-2.5521	0.0001554	0.0012432
N-alpha-acetyl-lysine	-2.2806	0.0001554	0.0012432
Deoxycarnitine	-2.2623	0.0001554	0.0012432
Valine	-1.8512	0.0001554	0.0012432
Hydroxyproline	-1.7161	0.0001554	0.0012432
S-Adenosylhomocysteine	-1.376	0.0001554	0.0012432
Amino(iso)butyric acid	-1.154	0.0001554	0.0012432
Allantoin	-0.8831	0.0001554	0.0012432
Pantothenic acid	-0.84737	0.0001554	0.0012432
Sphingomyelin (d36:2)	0.75687	0.0001554	0.0012432
Guanidinoacetate	-1.853	0.0003108	0.0018648
Betaine	-1.4867	0.0003108	0.0018648
Glycine	-1.1914	0.0003108	0.0018648
Guanosine	-1.1268	0.0003108	0.0018648
Creatine	-0.91827	0.0003108	0.0018648
Phosphatidylcholine (34:3)	-0.72523	0.0006216	0.0032431
Adenosine	-0.67104	0.0006216	0.0032431
Uridinediphospho-N-acetylglucosamine	-0.63187	0.0006216	0.0032431
Butyrylcarnitine	-2.2366	0.0010878	0.005439
Thiamine	-0.81129	0.0018648	0.0086068
Acetylcarnitine	-0.72511	0.0018648	0.0086068
Ureidopropionic acid	1.8368	0.0029526	0.012654
Carnitine	-1.0075	0.0029526	0.012654
Riboflavin	-0.94127	0.004662	0.018648
3-Methylhistidine	-0.55615	0.004662	0.018648
Serine	-1.0826	0.006993	0.025429
Symmetric dimethylarginine	-0.65552	0.006993	0.025429
Pyruvate	-0.5927	0.006993	0.025429

Ornithine	-0.83074	0.010412	0.033768
N-Acetylhistidine	-0.81762	0.010412	0.033768
Isoleucine	-0.80019	0.010412	0.033768
Hydroxyglutaric acid	-0.69197	0.010412	0.033768
N-Amidinoaspartate	1.7812	0.014763	0.043209
Hexanoylcarnitine	-1.6664	0.014763	0.043209
Leucine	-0.80247	0.014763	0.043209
N-Acetylaspartic acid	-0.4189	0.014763	0.043209
N-Acetylserine	-1.2451	0.020668	0.051671
Octanoylcarnitine	-1.2281	0.020668	0.051671
Pyridoxamine	-1.168	0.020668	0.051671
Methionine	-0.51493	0.020668	0.051671
Xanthine	-0.51099	0.020668	0.051671
Glutamine	-0.43744	0.020668	0.051671
Cytidinemonophosphate	-0.38029	0.020668	0.051671
Citrulline	-0.89872	0.028127	0.067506
Propionylcarnitine	-0.50786	0.028127	0.067506

Supplementary Table 13: Estimates and parameters for the stepwise-regression model

Estimates β	Estimates value	P value
β_0	13.281	0.018501
β_1	0.0028359	0.045025
β_2	-0.014897	0.0050012
β_3	0.0086405	0.085903
β_4	0.0117	0.043468
β_5	-0.074511	0.015191
β_6	0.0059353	0.0043084
β_7	-0.013651	0.029534
β_8	0.035458	0.00058659
β_9	-0.032362	0.0032492

9.4. List of tables

9.5. List of supplementary tables

9.6. List of figures

9.7. List of supplementary figures

9.8. Supplementary information

9.8.1. pCpGL-basic vector map

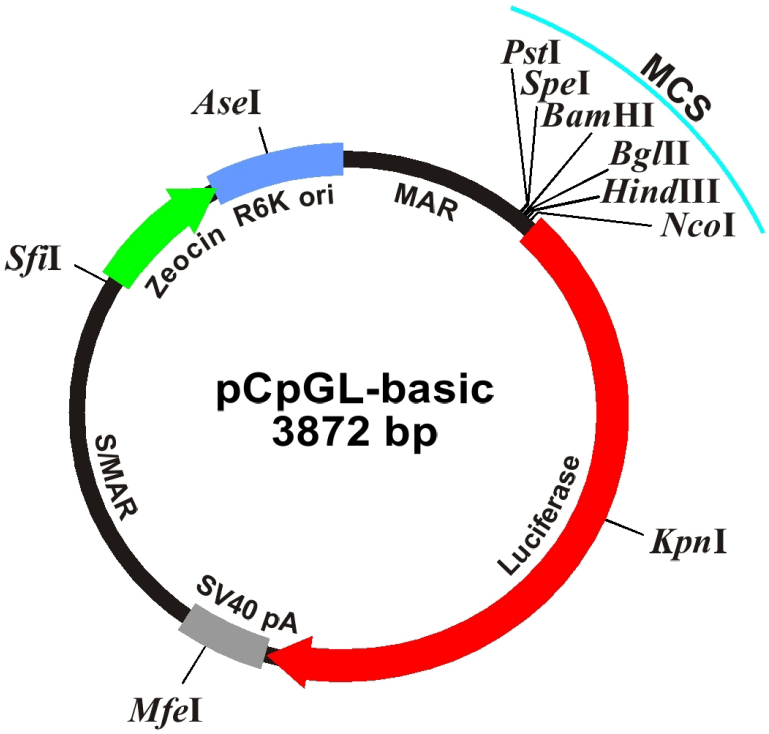

Curriculum vitae

Personal Details:

Name: Jan Hendric Britsemmer
eMail: jahe.brits@googlemail.com
ORCID ID: 0000-0001-5818-7750

Work and Professional Experience

March 2020 – May 2024	PhD student at the institute for human genetics, University of Lübeck, Germany associated with the graduate school GRK1957 ‚Adipocyte-Brain-Crosstalk' in the laboratory for Epigenetics and Metabolism (supervised by: Prof. Henriette Kirchner)
May 2019 -Jan 2020	Master thesis at the Fraunhofer Facility for marine Biotechnology, Lübeck, Germany with the topic ‚Effect of cold-atmospheric plasma on corneal wound healing in vitro and ex vivo'
Jan 2019 – May 2019	Internship at the Fraunhofer Facility for marine Biotechnology, Lübeck, Germany with the project ‚Effect of cold-atmospheric plasma on fibroblast differentiation'
Oct 2018 – Jan 2019	Internship at the Institute of molecular biology (IMB), Mainz, Germany with the project ‚βTrCP1 mutations on mPer1 binding in circadian clock rhythms' in the group of Prof. Eva Wolf

Academic education

Oct 2017 – Jan 2020	Master studies in molecular life science (MLS) at the University of Lübeck, Germany
Oct 2014 – Sep 2017	Bachelor studies in bioscience at the Goethe University of Frankfurt am Main

Grants and Awards

2022:	Scholarship holder for the DZD Summer School in Stockholm, Sweden
2022:	DZD travel grant (400 €)
2022:	Scholarship holder of the DDG travel grant (400 €)
2022:	3rd place for the best paper award of the GRK 1957
2021:	DDG travel grant (80 €)